Confinement Effects on the Electronic and Optical Properties of Semiconductor Quantum Dots Revealed with Two-Dimensional Coherent Spectroscopy

by

Galan Moody

B.Sc., University of Colorado, 2008

M.Sc., University of Colorado, 2011

A thesis submitted to the

Faculty of the Graduate School of the

University of Colorado in partial fulfillment

of the requirements for the degree of

Doctor of Philosophy

Department of Physics

2013

This thesis entitled:
Confinement Effects on the Electronic and Optical Properties of Semiconductor Quantum Dots
Revealed with Two-Dimensional Coherent Spectroscopy
written by Galan Moody
has been approved for the Department of Physics

Steven T. Cundiff

David M. Jonas

Date

The final copy of this thesis has been examined by the signatories, and we find that both the content and the form meet acceptable presentation standards of scholarly work in the above mentioned discipline.

Moody, Galan (Ph.D., Physics)

Confinement Effects on the Electronic and Optical Properties of Semiconductor Quantum Dots Revealed with Two-Dimensional Coherent Spectroscopy

Thesis directed by Prof. Steven T. Cundiff

Confinement of electron-hole pairs (excitons) in semiconductor quantum dots (QDs) leads to novel quantum phenomena, tunable optical properties and enhanced Coulomb interactions, all of which are sensitive to the size, shape and material composition of the QDs. This thesis discusses our pursuit in unraveling the complex interrelation between morphology of a QD and its electronic and optical properties. A series of epitaxially-grown semiconductor nanostructures with different QD sizes and composition is studied using optical two-dimensional coherent spectroscopy (2DCS). With the unique capabilities of unambiguously identifying coupling between resonances, isolating quantum pathways and revealing homogeneous dephasing information in heterogeneous systems, 2DCS is a powerful tool for studying QD ensembles.

Of paramount importance is the exciton homogeneous line width, which is inversely proportional to the dephasing time. As the dephasing time sets the duration for which coherence is maintained, knowledge of the principal dephasing mechanisms in QDs is essential. 2D spectra of excitons in weakly-confining GaAs QDs reveal that elastic exciton-phonon coupling and intra-dot exciton-exciton interactions are responsible for line width broadening beyond the radiative limit, and the interaction strength of both mechanisms increases for decreasing QD size. These results are compared to those obtained from InAs QDs, which exhibit an order-of-magnitude larger confinement, to illustrate the role quantum confinement plays in exciton dephasing.

The lowest energy optical transitions in semiconductor QDs are modified by confinement-enhanced Coulomb interactions, such as exchange-mediated coupling between excitons and correlation effects that can lead to bound and anti-bound states of two excitons. 2D spectra particularly sensitive to these interactions reveal that the electron and hole wave functions - and therefore the

strength of Coulomb interactions - are sensitive to variations in QD size for the GaAs ensemble. In the InAs QDs, however, the wave functions are remarkably independent of the details of confinement, leading to similar electronic and optical properties for all QDs. To provide additional insight, the spectra are modeled using perturbative density matrix calculations, and the results are compared to many-body calculations to reveal the significance of the strength and nature of Coulomb interactions on the optical properties of QDs.

Acknowledgements

I am extremely grateful for the opportunities that have been available to me while being part of the Cundiff group at JILA. I have had the pleasure of working on fascinating research projects with many wonderful people, without whom completion of this thesis would not have been possible.

First and foremost, my advisor, Steve Cundiff, has been a wonderful mentor. I cannot thank him enough for providing a positive and intellectually stimulating research environment that has enabled me to mature both scientifically and personally. I am grateful for Steve's constant guidance, encouragement and trust in me through the many challenges I have encountered. In addition to all of the opportunities and support that Steve has provided in the lab, his willingness to send me to many conferences has been extremely motivating and has had an energizing effect on my research. I strive to emulate Steve's approach and attitude towards science, which I hope to replicate with my colleagues when I leave JILA.

I am grateful to David Jonas, Dan Dessau, Andreas Becker and Markus Raschke for agreeing to be on my Comps III and PhD committees. Dan Dessau has been especially generous for co-advising my undergraduate research and being on my honors thesis committee.

The research presented in this thesis would never have been completed without the encouragement and support of past and present members of the Cundiff group with whom I've had the pleasure to interact. They have all provided a positive and entertaining environment and have been an excellent team. When I joined the Cundiff group as an undergraduate, Alan Bristow helped me develop the necessary skill set to be successful in scientific research. His enthusiastic approach towards research was very encouraging and has had a lasting effect on me. When I was confronted

with challenges or questions that I struggled to answer, Jared Wahlstrand was extremely patient and helpful in finding a solution with me, and I thank him for that. After I joined the 2D project as a graduate student, Alan was very helpful in introducing me to the concept of multi-dimensional spectroscopy, and I also learned a great deal while working with Xingcan Dai and Denis Karaiskaj. I am extremely grateful for the opportunity to work with Mark Siemens, who, in his short time with the Cundiff group, propelled our research to new levels and facilitated our understanding of the fundamentals of 2D spectroscopy. The 2D project has been a collaborative effort and would not be possible without contributions from the rest of the 2D team, including Tianhao Zhang, Hebin Li, Rohan Singh, Travis Autry, and Gaël Nardin. Hebin, Rohan, Travis and Gaël have also been kind enough to proof read my thesis and provide important feedback, and I thank them for that. I am also grateful to have had the chance to interact and work with many other Cundiff group members who have helped out in one way or another, including Andrew Funk, Soobong Choi, Ryan Smith, John Willits, Andrew Hunter, Charlie Bevis, Matthew Day, Takeshi Suzuki and Bo Sun.

An important aspect of our project is collaboration with many other research groups. I would like to thank Rich Mirin (NIST), Dan Gammon and Allan Bracker (U.S. Naval Research Laboratory) and Manfred Bayer and Ilya Akimov (Technische Universität Dortmund) for providing high quality quantum well and quantum dot samples. I have especially enjoyed working with Manfred and Ilya, who have been particularly engaged in our project and were also kind enough to host me during my visit to Germany. We have also had a number of visiting fellows who have contributed in many aspects to our research. Mackillo Kira (University of Marburg) has provided important insight into the interpretation of our 2D results, and our conversations about many different aspects of life are always a pleasure. Andrew Kortyna's (Lafayette College) visit was a welcomed change of pace. I learned a great deal from his expertise in atomic physics, and I certainly enjoyed all the ski days we were able to take.

Anyone who is familiar with JILA is aware of the tremendous amount of support provided by the JILA administrative and technical staff. They are crucial to the success of every research project, and I thank them for their continued support. The 2D project would not be possible

without assistance from the machine shop (especially Kim Hagen and Hans Green), electronics shop (especially Terry Brown), computing (especially J.R. Raith), administrative staff (especially Loree Kaleth, Maryly Dole and Jeanne Nijhowne) and the supply office.

Finally, my non-JILA friends and family have provided unwavering encouragement, advice and support throughout my entire academic career, for which I will be forever grateful.

Contents

Chapter

Tables

Table

Figures

Figure

Chapter 1

Introduction

Advances in nanofabrication technologies in the past few decades have facilitated the realization of novel semiconductor nanostructures with properties tailored for specific applications. Nanostructures with spatial dimensions comparable to the de Broglie wavelength of charge carriers residing in the material are readily engineered with nanometer precision. At this length scale, quantum confinement effects modify the electronic and optical properties and interesting quantum phenomena emerge. Three-dimensional confinement of carriers in a quantum dot (QD) transforms the continuous optical spectrum of a bulk semiconductor into a size-tunable, atomic-like spectrum featuring a series of sharp peaks associated with discrete electronic transitions. Each peak can be attributed to a particular multi-particle complex, such as an electron-hole pair (exciton), correlated two-excitons (biexciton), a positively- or negatively-charged exciton (trion), as well as other excitonic states associated with higher energy levels in the QD. Coulomb interactions between electrons and holes are enhanced in QDs compared to nanostructures with additional spatial degrees of freedom, which can lead to significant modifications of the exciton properties. Moreover, confinement reduces the effects of external perturbations that can limit the radiative lifetime of excitonic resonances, which can be as long as nanoseconds at low temperature. These unique electronic and optical properties of QDs have been exploited for a wide range of applications, including quantum electronics and quantum information processing, optical communications, display technologies, solar energy harvesting and fluorescent labeling, to name a few. Of particular importance for many of these applications are the physical parameters characterizing the optical transitions, such as the

energies, transition line widths and dipole moments. These parameters are highly-sensitive to the QD size, shape and material composition, which are difficult to control during fabrication. QD fabrication methods are inherently statistical processes that result in an ensemble of QDs with a distribution of spectroscopic properties. Establishing a connection between the morphology of a QD and its electronic and optical properties is crucial for the successful implementation of many QD-based applications.

Insight into the effects of QD morphology on the spectroscopic properties of excitonic resonances has been developed in the last three decades using linear and nonlinear spectroscopies, which are reviewed in Section 1.1. These pioneering works have facilitated the design and fabrication of novel devices and applications exploiting quantum phenomena that arise from confinement in QDs, some of which are presented in Section 1.2. Despite significant progress in this field, numerous questions remain with regard to how morphology affects the electronic and optical properties and coherent-light matter interactions in semiconductor QDs. This thesis discusses our efforts to address some of these questions by implementing optical two-dimensional coherent spectroscopy (2DCS) of a series of epitaxially-grown semiconductor nanostructures with different QD sizes and material composition. 2DCS, an enhanced version of three-pulse four-wave mixing spectroscopy, offers several advantages for elucidating the complex nature of multi-particle interactions compared to conventional spectroscopic techniques, which are discussed in Section 1.3. Section 1.4 highlights our main findings and is followed by an outline of this Thesis in Section 1.5.

1.1 An Historical Perspective on Quantum Dots

The evolution of semiconductor growth techniques [1, 2] in the 1960's and 1970's enabled the fabrication of atomically-sharp heterojunction interfaces between materials with different electronic and optical properties. This breakthrough launched a new regime of semiconductor quantum physics in which quantum effects could be introduced and controlled through spatial variation of the nanostructure dimensions. Since the seminal work of Esaki and Tsu investigating transport properties of a quantum well (QW) superlattice [3, 4] and the observation of energy quantization

and tunneling effects in GaAs/AlGaAs QWs by Dingle *et al.* in 1975 [5], the physics of spatially-quantized systems has been studied extensively and new quantum phenomena have been observed. In the early 1980's, semiconductor lasers with a QW as the active medium were introduced [6, 7], and localization and interaction effects on electrons and holes confined in one-dimensional quantum wires were examined by Skocpol *et al.* [8]. At the same time, quantum size effects on the absorption spectrum of excitons confined in epitaxially-grown quasi-zero-dimensional quantum boxes were revealed by Ekimov and Onushchenko [9] and in colloidal nanocrystals by Brus [10, 11]. Motivated by these ground breaking studies, Reed *et al.* provided the first indirect evidence of energy quantization in 1986, and coined the term "quantum dot" (QD) to describe the zero-dimensional quantum boxes [12]. Follow-up studies by Reed *et al.* revealed discrete peaks in resonant tunneling spectra, providing direct evidence of the atomic-like density of states in zero-dimensional QDs [13].

These pioneering works led to a sharp rise in the number of research groups interested in epitaxially-grown semiconductor QDs. The majority of studies in the following decade revolved around characterizing the fundamental electronic and optical properties of QDs and developing new fabrication techniques. Initial experiments investigated QDs that were formed through electron-beam lithography of narrow GaAs/AlGaAs [14] and InGaAs/InP [15] QWs. The lowest energy optical transition of these etched QDs was revealed through ensemble photoluminescence (PL) measurements [14, 15]. The optical and electronic properties could be tuned through application of external fields and were characterized by measuring Zeeman splittings of electronic states [16], resonant tunnel coupling between QDs [17] and QD charging with multiple electrons [18, 19, 20]. Calculations of the linear and nonlinear optical properties [21, 22], confinement effects on exciton formation and Coulomb correlations [23] and the influence of field effects [24] aided in the interpretation and understanding of the experiments; however significant inhomogeneity of the QD properties due to size dispersion hindered direct comparison between theory and experiments on QD ensembles.

A major milestone was achieved in 1992 when Brunner *et al.* demonstrated for the first time μ-PL spectra from a *single* GaAs/AlGaAs QD formed from laser-induced thermal interdiffusion of

a narrow QW nanostructure [25]. As the QD lateral dimensions became comparable to the exciton Bohr radius in bulk GaAs, discrete spectral lines appeared in the PL spectrum, demonstrating that they measured the atomic-like spectrum of an exciton in a single dot. They further improved their growth technique by instead interrupting the epitaxial growth process of a narrow QW, allowing the gallium and arsenide atoms to diffuse to nucleation sites, naturally forming monolayer interfacial islands known as interfacial fluctuation QDs (IFQDs) [26]. Their worked spurred a revolution in single dot fabrication and characterization, allowing for more-easily-controlled, systematic studies of size effects on the QD properties. Within two years Gammon *et al.* measured the excited-state spectrum of a single IFQD [27], the temperature dependence of the exciton homogeneous linewidth [28] and the exchange interaction in asymmetric dots [29].

In parallel to the development of GaAs IFQDs, significant progress was being made towards the fabrication of semiconductor QDs using other material combinations, including InSb, GaSb, AlSb [30], CdTe [31, 32, 33], ZnTe [34, 35], and more commonly, In(Ga)As [36, 37, 38], typically grown on a GaAs substrate using the Stranski-Krastanow (SK) method [39, 40]. So-called InGaAs/GaAs self-assembled QDs (SAQDs) would form naturally to alleviate strain introduced in the InGaAs layer from the InGaAs/GaAs lattice mismatch. Similar to the GaAs IFQD studies, InGaAs SAQDs were quickly characterized through examination of the electronic structure and carrier relaxation dynamics [41, 42], excitonic localization [43], and size-effects on the exciton exchange interaction [44, 45], biexciton binding energy [45] and homogeneous line width [46].

By the late 1990s, the fabrication and characterization of epitaxially-grown semiconductor QDs had advanced to the point that QD-based devices were realizable. The seminal studies highlighted in this Section have been crucial to the successful demonstration of a wide range of QD-based technologies, which are presented in the following Section. Despite the rapid progress in this field in the first 25 years, numerous questions remain with regard to how QD morphology affects the electronic and optical properties and coherent light-matter interactions in semiconductor QDs. The performance of QD-based devices relying on these interactions is typically limited by multiple effects that are not adequately understood: 1) short coherence and relaxation times due to interactions of

the charge carriers with each other and the local environment; 2) sensitivity of the QD properties on size and confinement, which is difficult to eliminate or control within the tolerances necessary for optimal device operation; and 3) the presence of many-body interactions that often dominate the linear and nonlinear optical response. Over the last decade, significant progress in experimental and theoretical QD-based research – some of which are discussed in this Section and the next – stems from the efforts to understand these problems.

1.2 Applications using Quantum Dots

Semiconductor QDs are considered the solid-state equivalent of atomic systems, with perhaps a few notable advantages with regard to functional device design and performance. Compared to hot atomic vapors or cold gases, the versatility of QDs for a broad range of applications stems from the ability to tune their electronic and optical properties through changes in size and composition, their strong optical transition dipole moments, and the rapidly-evolving sophistication of deterministic single dot isolation, placement and incorporation into chip-scale devices. These advantages are apparent in the first applications of QDs as classical light sources and detectors. In the mid-1990's a temperature-insensitive, low current threshold, high gain semiconductor laser fabricated from a single InGaAs/GaAs QD layer was demonstrated by Shoji *et al.* [47]. Within one year wavelength-tunable devices operating at room temperature were developed [48, 49] and within five years optical gain and stimulated emission were demonstrated in colloidal nanocrystals [50]. The development of QD-based lasers, incoherent light sources [51] and photo-detectors [52, 53] paved the way for devices with probe and detection wavelengths ranging from the ultraviolet to the infrared, benefitting both fundamental science and commercial applications.

Nonclassical states of light can also be generated on demand using semiconductor QDs [54, 55, 56], enabling on-chip semiconductor quantum optics. To generate and probe the light characteristics, researchers pump a single QD with a low-intensity laser beam and analyze the PL statistics using a Hanbury-Brown-Twiss setup [57]. A measure of the second-order correlation function, $g^{(2)}$, provides the degree to which single photons are emitted from the QD. Variations of

this experiment can also be used to probe violations of Bell's inequality for evidence of entangled photon pairs. These nonclassical light states can be used to ascertain the quality, charge state, and energy level structure of the QDs under examination and can be used to manipulate or entangle spatially-isolated QDs.

Within five years of the first experiments on a single QD, Solomon *et al.* revealed that SK-grown InAs/GaAs SAQDs in adjacent layers would spatially align and couple through wave function tunneling if the inter-layer spacing was below a critical thickness [58]. Two years later Bonadeo *et al.* demonstrated coherent optical control of the excitonic wave function in a single GaAs/AlGaAs IFQD using phase-locked picosecond pulses to prepare and manipulate the exciton quantum state [59]. These two works led to a paradigm shift in the field of quantum optics and hinted at the possibility of QD-based quantum computation. Indeed, most of the DiVincenzo criteria [60] for quantum computation – namely, state preparation [61], coherent control and manipulation [62, 63, 64, 65], and state read out [66, 67, 68] – have been demonstrated in QDs. While these works demonstrate the promise of chip-scale quantum information, scalability beyond the few quantum bit (qubit) level has yet to be achieved. Some promising methods to overcome the scalability issue include resonant tunnel coupling [69, 70, 71] and dipole-dipole interactions [72] between QD molecules and coherently-controlling and entangling spatially-isolated QDs using single photons. Demonstrating a practical, scalable N-qubit register will lead to a revolution in the field of quantum information and is currently at the forefront of application-based QD research.

While epitaxially-grown semiconductor QDs are primarily used in opto-electronics, chemically-synthesized colloidal QDs (CQDs) have been developed for applications ranging from biological tagging [73] and DNA nanosensors [74] to photovoltaics [75]. In the past decade, CQDs have shown promise as absorbers for photovoltaic devices with the potential to increase the maximum attainable efficiency up to 66% [76]. Strong confinement in CQDs, which are generally much smaller than the bulk exciton Bohr radius, is expected to enhance photon-to-electron conversion efficiencies and suppress hot carrier relaxation mechanisms compared to bulk materials [75]. Moreover, the bandgap of CQDs can be tuned throughout the solar spectrum by varying their material

composition and size, and they can be easily incorporated into Graëtzel-like cells for large-scale fabrication. One promising, albeit controversial [77], approach to enhance the efficiency is to generate multiple electron-hole pairs from a single photon through carrier multiplication [78, 79]. Despite reported exciton-to-photon internal quantum efficiencies up to $\sim$ 300%, the external efficiencies of multiplication-enhanced schemes are presently much lower than first- and second-generation devices.

The applications presented in this Section, while not comprehensive, demonstrate the versatility of semiconductor QDs for optics, electronics, chemistry, and biology. To facilitate the design and fabrication of novel devices, the effects of QD morphology on the electronic and optical properties must be better understood. For example, a technical challenge limiting the scalability of QD-based quantum computation is the inability to systematically fabricate an ensemble of QDs with similar properties – variability in the growth and preparation processes result in significant inhomogeneity of the radiative lifetime, emission energy, and dipole moment. Furthermore, unlike atomic systems, many-body interactions play a significant role in the linear and nonlinear optical response of QDs. Understanding the influence of morphology on the intrinsic properties of excitons confined in QDs will lead to the development of predictable growth and fabrication techniques, facilitating progress in QD-based applications.

1.3 Optical Two-Dimensional Coherent Spectroscopy

Quantum size effects on the electronic and optical properties in QDs have been studied extensively using both linear and nonlinear ultrafast spectroscopic techniques. The traditional approach is to perform spectrally- or time-resolved μ-PL spectroscopy on single QDs, which are isolated by depositing metal apertures on the sample surface or by etching mesas that contain one or a few dots. Experiments are then performed on tens of dots, whose properties exhibit inhomogeneity from size and/or composition dispersion (for an excellent review see Ref. [80]). Single dot studies have revealed rich information about resonance energies [26], Coulomb interactions [81, 82, 83, 84, 85] and exchange interaction effects [44]; however, the influence of confinement on the optical

properties is often hidden by considerable dot-to-dot variation of the data for QDs emitting at a particular energy, perhaps arising from sample modifications to isolate single dots and from the limited number of dots probed for a particular study. These effects are avoided in ensemble measurements using nonlinear techniques such as transient pump-probe [86] or transient four-wave mixing (FWM) spectroscopies [87].

Although conventional FWM techniques have been particularly useful for studying QD ensembles because of their ability to separate homogeneity from inhomogeneity in limiting cases, there are a number of drawbacks. Multiple electronic transitions can be excited by broadband picosecond or femtosecond laser pulses, resulting in complicated dynamics and oscillatory beats in the FWM signal. Distinguishing between quantum-mechanical coupling or polarization interference contributions to the beats is often difficult or impossible [88]. In addition, the nonlinear optical response is averaged within the pulse spectrum; consequently, inhomogeneity can result in artifacts in the FWM signal, such as artificially fast dephasing of quantum beats. FWM signals averaged within the laser spectrum are also insensitive to sub-ensemble properties. In order to probe size-dependent properties, multiple FWM experiments must be performed for different excitation wavelengths tuned within the QD inhomogeneous distribution. Moreover, there is an intrinsic ambiguity in distinguishing between the effects of inhomogeneity, dephasing and correlations between transition energy fluctuations, which provide similar signatures in one-dimensional FWM signals [89]. The manifestation of many-body interactions, such as local field effects [90], excitation-induced dephasing [91], excitation-induced shift [92] and biexcitonic effects [93], is also similar in FWM magnitude measurements.

Optical two-dimensional coherent spectroscopy (2DCS), an extension of three-pulse transient FWM, is a powerful tool that can overcome many of these limitations [94]. An optical analog of multidimensional nuclear magnetic resonance (NMR) spectroscopy [95], 2DCS has been implemented in both the infrared and optical regimes to study the coherent nonlinear response of a multitude of complex systems [96]. In contrast to NMR, optical 2DCS can provide a snapshot of coherent dynamics on a femtosecond timescale and can be employed in a non-collinear geometry,

resulting in spatial isolation of a background-free signal. By recording the FWM signal along a specific phase-matched direction, distinct 2D spectra that are sensitive to specific dynamics and interactions can be generated using different temporal ordering of the excitation pulses and taking a Fourier transform of the signal with respect to different pulse delays. Compared to one-dimensional spectroscopies, 2DCS provides many advantages by coherently tracking the signal phase evolution while one of the pulse delays is scanned. Congested one-dimensional spectra are unfolded onto two dimensions, allowing identification of multiple contributing resonances to the nonlinear response, revealing the nature of coupling between resonances and separating quantum-mechanical coherent pathways. For a specific pulse time ordering in which a photon echo is emitted, inhomogeneous broadening manifests itself in the 2D spectrum as diagonal elongation, enabling an accurate and unambiguous measurement of the homogeneous line width. Indeed, within the last three years 2DCS has facilitated progress in our understanding of inhomogeneously broadened QD ensembles through measurements of electronic properties [97], exciton dephasing and relaxation dynamics [98, 99], exciton-exciton coherent coupling [100], $\chi^{(5)}$ optical nonlinearities [101], exciton-biexciton correlated broadening [102] and the electron-hole exchange interaction [103].

1.4 Review

Throughout the past decade, the Cundiff group has developed and implemented 2DCS [104] in the optical regime to study semiconductor QWs [105, 106, 107] and atomic vapors [108, 109, 110]. In recent years, we have applied 2DCS to examine semiconductor QD ensembles and we have achieved a number of important milestones. This Section gives a brief review of the QD 2DCS experiments performed in the Cundiff laboratory and highlights our main results. The experiments on the GaAs IFQDs were performed in collaboration with Mark Siemens (currently at the University of Denver), Alan Bristow (currently at West Virginia University), Xingcan Dai (currently at Tsinghua University), Denis Karaiskaj (currently at the University of South Florida), Steve Cundiff at the University of Colorado, and Allan Bracker and Daniel Gammon from the U.S. Naval Research Laboratory. The experiments on the InAs SAQDs were performed in collaboration with Rohan

Singh, Hebin Li, and Steve Cundiff at the University of Colorado, Dirk Reuter and Andreas Wieck at the University of Bochum, Allan Bracker and Dan Gammon, and Ilya Akimov and Manfred Bayer at the University of Dortmund.

1.4.1 2D Spectroscopy of Semiconductor Quantum Dot Ensembles

2DCS of semiconductor QDs is implemented using the JILA Multidimensional Optical Nonlinear SpecTRometer, or JILA MONSTR, designed and built by Bristow *et al.* in 2009 [111]. The apparatus consists of a set of folded and nested Michelson interferometers housed inside two thick aluminum plates and can maintain a pulse delay phase-stability of $\lambda/100$. We used this setup to perform experiments on three different QD samples: GaAs/AlGaAs IFQDs formed from monolayer interfacial fluctuations of a thin GaAs QW, and two InAs/GaAs SAQD samples which were thermally-annealed post-growth at either 900 °C or 980 °C. Impurities unintentionally-introduced during the growth of the InAs samples results in approximately half of the QDs being positively charged with a hole. Because of weaker dipole moments and only 10^5 - 10^6 QDs probed within the excitation laser spot size (compared to an excitation density of $\sim 10^9$ excitons/cm^2 typical for QW studies), the FWM signal from the QDs is typically much weaker than the laser scatter in the phase-matched direction and is therefore too weak to be observed even when using a lock-in amplifier to detect a frequency-modulated time-integrated FWM signal on a slow photodetector. However, 2DCS with phase cycling cancels scatter from the excitation lasers, enabling precise, background-free measurements of the optical properties and many-body interactions in the QD samples.

1.4.2 Isolating the Nonlinear Response of Excitons, Biexcitons and Trions

Upon optical excitation using broadband, femtosecond pulses, excitons, charged excitons (trions) and bound two-excitons (biexcitons) can be created. Exciton resonances appear in the 2D spectra on the diagonal and elongated along the diagonal by the inhomogeneous line width, whereas biexciton resonances appear as spectrally-isolated peaks red-shifted from the exciton resonances

by the biexciton binding energy [102]. Using a specific polarization scheme in which the second two pulses are cross-linearly polarized with respect to the first pulse and the detected signal, the biexciton nonlinear response is enhanced relative to that of the exciton because no quantum-mechanical pathways exist for the exciton for this polarization scheme based on the dipole transition selection rules. Surprisingly, for this polarization, a resonance on the diagonal is still present for all samples, albeit with a smaller amplitude and different homogeneous line width. For the InAs SAQDs, this peak is attributed to the presence of trions, which do not obey similar dipole transition selection rules as the exciton [101]. For the GaAs IFQDs, the weak diagonal peak is attributed to the presence of unbound two-excitons in the weakly-confining QDs, which is confirmed by the presence of two-exciton resonances in two-quantum 2D spectra. Through spectral selection and by taking advantage of the dipole selection rules, we have measured quantum size effects on the optical properties of the different excitonic states in these samples.

1.4.3 Coherent and Incoherent Dephasing Mechanisms

Rephasing one-quantum 2D spectra, for which the homogeneous and inhomogeneous line widths are separated, are generated by using a specific pulse time-ordering in which a photon echo is emitted after the third excitation pulse. Cross-diagonal slices of the spectra at a particular emission energy provide a measure of the homogeneous line width [112], inversely proportional to the dephasing time, whereas a diagonal slice gives the amount of inhomogeneity. Taking cross-diagonal slices throughout the inhomogeneous distribution provides a measure of the homogeneous line width for QDs with different resonance energies, i.e. QDs with different physical size. Seminal studies of the homogeneous line width in GaAs IFQDs had revealed that despite the expectation of a "phonon bottleneck", which would lead to smaller dephasing rates, significant dephasing mechanisms were still present, although the principal mechanism had yet to be established [28, 113]. Applying 2DCS to this system, we find that elastic exciton-phonon scattering is responsible for the line width broadening at low sample temperatures (< 35 K), which had been speculated but not directly observed beforehand [99]. By measuring the exciton-phonon scattering strength for the entire

ensemble, we find that excitons confined in smaller, higher-energy QDs couple more strongly to acoustic phonons, consistent with theoretical predictions. In addition, we demonstrate that with increasing excitation density and independent of the QW exciton population density, the dominant line width broadening mechanism is exciton-exciton scattering arising from excitons localized in the same dot.

At elevated temperatures (> 35 K), additional line width broadening arises from temperature-dependent dynamics of incoherent QW–QD population transfer [98]. 2DCS is aptly designed for this type of study, since signatures of incoherent coupling appear as spectrally-isolated peaks in the 2D spectra. We show that at low temperature and long delay times (~ 100 ps), excitons delocalized in the QW relax and become confined in the QDs, while at temperatures above 35 K, incoherent QD $\rightarrow$ QW excitation occurs. The QW–QD interaction dynamics are modeled using a set of rate equations that require QW–QD coupling, inter-band population decay, and exciton-bound heavy-hole spin flips to reproduce the data. These measurements, providing dynamic coupling probabilities and rates, could facilitate development of more sophisticated, fast, and efficient electro-optic devices relying on QW–QD interactions.

A similar exciton homogeneous line width temperature dependence behavior is measured for excitons confined in the InAs SAQDs. In contrast to the GaAs IFQDs, however, the exciton, trion and biexciton line widths are independent of QD emission energy (i.e. shape, size) and excitation density. We find that the extrapolated zero-temperature and zero-excitation-density line widths are $\approx 10 - 12$ μeV, which is larger than radiatively-limited line widths reported in the literature. To determine the source of additional line width broadening, we performed a series of measurements in which the population lifetimes are obtained with 30 neV resolution, which requires $\lambda/100$ phase-stabilization of the pulse delays for an optical-delay line translation of 15 cm and a data acquisition time of ~ 5 hours. The population decay rates are ~ 5 μeV for the exciton and trion - less than the homogeneous line widths - indicating that pure dephasing effects are important at low temperature and independent of excitation density [103]. One possible pure dephasing mechanism could be a fast fluctuating quantum-confined Stark shift arising from phonon-assisted trapping of charges near

the QDs [114].

1.4.4 Coulomb and Exchange Interactions

Using an alternating linearly-polarized excitation pulse sequence, we can generate a non-radiative Raman-like coherence between the two lowest-energy exciton spin states, which are coupled and energetically separated by the electron-hole exchange interaction. By monitoring the coherence oscillations and scanning the delay between the second and third pulses, we can generate a zero-quantum 2D spectrum that provides a measure of the population decay rate and isolates quantum pathways associated with the Raman-like coherences. While we do not observe any exchange-mediated fine-structure splitting between the bright exciton states for the GaAs IFQD ensemble, we find that the InAs SAQDs exhibit a bright state splitting of ~ 20 μeV for the entire ensemble, with a measurement uncertainty over an order of magnitude smaller than the scatter in typical single-dot experiments [103]. An analysis of the dephasing times and radiative lifetimes reveal that the inter-band coherence of the two lowest-energy bright exciton states experience nearly perfectly-correlated dephasing, which could aid in the development of devices relevant for quantum information applications that rely on long-lived spin coherence times.

2DCS is a powerful technique for exploring how Coulomb interactions are affected by the strength and nature of confinement, which we determined by measuring quantum size effects on the biexciton binding energy for the three samples [102]. While single-dot experiments have provided some insight in this regard, significant dot-to-dot scatter of the data has made agreement between theory and experiment elusive. For cross-linearly polarized excitation that enhances the relative biexciton amplitude, we show that for the InAs SAQDs, which have an in-plane confinement larger than 60 meV, the biexciton binding energy is unaffected by changes in QD size, likely resulting from post-growth thermal annealing of the samples. On the other hand, for confinement of ~ 10 meV in the GaAs IFQDs, the electron and hole wave functions are sensitive to changes in the confinement potential; consequently, the biexciton binding energy increases by 15% over the inhomogeneous line width. The data is simulated using perturbative density matrix calculations that include the effects

of inhomogeneity, dephasing, and correlated scattering of the biexciton and exciton transitions. A comparison of the results to microscopic calculations reported in the literature provides detailed information regarding how the strength and nature of confinement affects Coulomb interactions in QDs.

1.4.5 Higher-Order Nonlinear Effects

Using a cross-linearly polarized excitation pulse sequence and increasing the excitation pulse intensity to drive the InAs SAQD nonlinear response beyond the $\chi^{(3)}$ regime, an additional spectral feature, too weak to be observed in the time-integrated FWM signal, appears in the 2D rephasing spectrum and is attributed to the $\chi^{(5)}$ biexciton nonlinear response that is radiated in the FWM phase-matched direction [101]. This six-wave mixing signal radiates in the FWM direction only for nonlinear interactions in which one of the pulses acts three times. We model the nonlinear response using a perturbative expansion of the density matrix. For $\chi^{(3)}$, only a single quantum pathway contributes to the biexciton nonlinear response and agrees with our observations of the biexciton resonance at low pulse intensity. The biexciton $\chi^{(5)}$ nonlinear response can be constructed from a total of 12 quantum pathways, some of which contribute to the peak that appears at high intensity. These results demonstrate that although higher-order nonlinearities are often too weak to be observed in one-dimensional FWM experiments, they can be clearly and unambiguously identified using 2DCS. Further separation of the $\chi^{(5)}$ quantum pathways could be accomplished by using a variation of nonlinear spectroscopy that isolates the six-wave mixing signal [115, 116] in combination with higher-order multidimensional coherent spectroscopy [110].

1.5 Thesis Outline

This thesis is focused on revealing the influence of confinement on the electronic and optical properties of semiconductor QDs using optical 2DCS and is organized as follows. Chapter 2 discusses the physics of semiconductor QDs. The concept of excitons in semiconductors is introduced, followed by a discussion of the conditions for three-dimensional quantum confinement, the

optical properties of semiconductor QDs, relaxation and dephasing mechanisms, the morphology of the samples studied, and conventional measurement techniques. In Chapter 3, the development of IR and optical 2DCS from multidimensional NMR is reviewed. Then details of FWM in semiconductors, including an intuitive description of how to interpret FWM experiments, are discussed. General aspects of 2DCS, different types of 2D spectra, and advantages of the technique will be presented. The density matrix formalism and the optical Bloch equations will be introduced. In Chapter 4, technical aspects of implementing 2DCS for studying semiconductor QDs will be discussed in detail, including fundamental and technical challenges, active interferometric stabilization, FWM generation and detection in QDs, spectral interferometry, and generating and analyzing 2D spectra. A discussion of the experimental results will begin with confinement effects on exciton-phonon coupling in Chapter 5. Mechanisms for enhanced broadening in smaller QDs will be discussed, and the results from the GaAs IFQDs will be compared to those from the InAs SAQDs. In Chapter 6, results of our studies on the influence of confinement on many-body interactions will be presented and compared between the different QD samples. Calculations based on the optical Bloch equations are performed and qualitatively reproduce the measured spectra. Signatures of higher-order nonlinearities will also be presented. 2D spectra revealing QW–QD incoherent population transfer will be presented in Chapter 7 and implications from a rate-equation analysis will be discussed.

In addition, we have performed preliminary 2DCS experiments on CdSeTe/ZnS colloidal QDs, which will be discussed in Appendix A. A more detailed analysis of the perturbative expansion of the optical Bloch equations will be presented in Appendix B. In Appendices C and D, the MONSTR alignment procedure and our efforts in developing a second generation JILA MONSTR will be presented, respectively.

Publications and Conference Presentations Relevant to this Thesis

Peer-Reviewed Journal Publications

[7] G. Moody, R. Singh, H. Li, I. A. Akimov, M. Bayer, D. Reuter, A. D. Wieck, and S. T. Cundiff, "Correlation and dephasing effects on the non-radiative coherence between bright excitons in an InAs QD ensemble measured with 2D spectroscopy," Solid State Communications **163**, 65 (2013).

[6] G. Moody, R. Singh, H. Li, I. A. Akimov, M. Bayer, D. Reuter, A. D. Wieck, A. S. Bracker, D. Gammon, and S. T. Cundiff, "Influence of confinement on biexciton binding in semiconductor quantum dot ensembles measured with two-dimensional spectroscopy," Physical Review B **87**, 041304(R) (2013).

[5] G. Moody, R. Singh, H. Li, I. A. Akimov, M. Bayer, D. Reuter, A. D. Wieck, and S. T. Cundiff, "Fifth-order nonlinear optical response of excitonic states in an InAs quantum dot ensemble measured with two-dimensional spectroscopy," Physical Review B **87**, 045313 (2013).

[4] S. T. Cundiff, A. D. Bristow, M. E. Siemens, H. Li, G. Moody, D. Karaiskaj, X. Dai, and T. Zhang, "Optical Two-Dimensional Fourier Transform Spectroscopy of Excitons in Semiconductor Nanostructures," IEEE Journal of Selected Topics in Quantum Electronics **18**, 318 (2012).

[3] G. Moody, M. E. Siemens, A. D. Bristow, X. Dai, A. S. Bracker, D. Gammon, and S. T. Cundiff, "Exciton relaxation and coupling dynamics in a GaAs/AlGaAs QW and QD ensemble," Physical Review B **83**, 245316 (2011).

[2] G. Moody, M. E. Siemens, A. D. Bristow, X. Dai, D. Karaiskaj, A. S. Bracker, D. Gammon, and S. T. Cundiff, "Exciton-exciton and exciton-phonon interactions in an interfacial GaAs QD ensemble," Physical Review B **83**, 115324 (2011).

[1] M. E. Siemens, G. Moody, H. Li, A. D. Bristow, and S. T. Cundiff, "Resonance lineshapes in two-dimensional Fourier transform spectroscopy," Optics Express, **18**, 17699 (2010).

Conference Presentations

[12] G. Moody, R. Singh, H. Li, I. A. Akimov, M. Bayer, D. Reuter, A. D. Wieck, A. S. Bracker, D. Gammon, and S. T. Cundiff , "Confinement effects on biexciton binding in semiconductor quantum dots measured with 2D coherent spectroscopy," Quantum Electronics and Laser Science (QELS) Conference, San Jose, CA (2013).

[11] G. Moody, M. E. Siemens, A. D. Bristow, X. Dai, D. Karaiskaj, A. S. Bracker, D. Gammon, and S. T. Cundiff, "Revealing exciton dephasing and transport dynamics in semiconductor quantum well–quantum dot systems using optical 2D Fourier transform spectroscopy," Photonics West, Ultrafast Phenomena and Nanophotonics XVI, San Francisco, CA (2012).

[10] G. Moody, R. Singh, H. Li, I. A. Akimov, M. Bayer, D. Reuter, A. D. Wieck, and S. T. Cundiff , "Excitons, Biexcitons, and Trions in an InAs Quantum Dot Ensemble," 6th International Conference on Coherent Multidimensional Spectroscopy (CMDS), Berlin, Germany (2012).

[9] G. Moody, R. Singh, H. Li, I. A. Akimov, M. Bayer, D. Reuter, A. D. Wieck, and S. T. Cundiff , "Excitons, Biexcitons, and Trions in an InAs Quantum Dot Ensemble Studied with Optical Two-Dimensional Fourier-Transform Spectroscopy," XVIII International Conference on Ultrafast Phenomena, Lausanne, Switzerland (2012).

[8] G. Moody, R. Singh, H. Li, I. A. Akimov, M. Bayer, D. Reuter, A. D. Wieck, and S. T. Cundiff , "Multi-particle interactions in an InAs quantum dot ensemble studied with optical two-dimensional Fourier-transform spectroscopy," 10th International Conference on Excitonic Processes in Condensed Matter, Nanostructured and Molecular Materials (EXCON), Groningen, the Netherlands (2012).

[7] G. Moody, R. Singh, H. Li, I. A. Akimov, M. Bayer, D. Reuter, A. D. Wieck, and S. T. Cundiff , "Two-Dimensional Fourier-Transform Spectroscopy of Excitons, Biexcitons and Trions in an InAs QD Ensemble," 7th International Conference on Quantum Dots, Santa Fe, NM (2012).

[6] G. Moody, R. Singh, H. Li, I. A. Akimov, M. Bayer, D. Reuter, A. D. Wieck, and S. T. Cundiff , "Excitons, Biexcitons, and Trions in an InAs Quantum Dot Ensemble Studied with 2D Fourier-Transform Spectroscopy," Quantum Electronics and Laser Science (QELS) Conference, San Jose, CA (2012).

[5] G. Moody, M. E. Siemens, A. D. Bristow, X. Dai, D. Karaiskaj, A. S. Bracker, D. Gammon, and S. T. Cundiff, "Exciton dephasing and transport dynamics in a GaAs quantum well and quantum dot ensemble," Meeting on Fundamental Optical Processes in Semiconductors (FOPS), Lake Junaluska, NC (2011).

[4] G. Moody, M. E. Siemens, A. D. Bristow, X. Dai, D. Karaiskaj, A. S. Bracker, D. Gammon, and S. T. Cundiff, "Linewidth and Coupling of Interfacial GaAs Quantum Dots Studied with Optical 2D Fourier Transform Spectroscopy," 10th International Workshop on Nonlinear Optics and Excitation Kinetics in Semiconductors (NOEKS), Paderborn, Germany (2010).

[3] G. Moody, M. E. Siemens, A. D. Bristow, X. Dai, D. Karaiskaj, A. S. Bracker, D. Gammon, and S. T. Cundiff, "Linewidth and Coupling of Interfacial GaAs Quantum Dots Measured with Optical Two-Dimensional Fourier Transform Spectroscopy," XVII International Conference on Ultrafast Phenomena, Snowmass, CO (2010).

[2] G. Moody, M. E. Siemens, A. D. Bristow, X. Dai, A. S. Bracker, D. Gammon, S. T. Cundiff, "Temperature-Dependent Coupling of GaAs Quantum Well and Interfacial Quantum Dots Studied with Optical 2-D Fourier-Transform Spectroscopy," Quantum Electronics and Laser Science (QELS) Conference, San Jose, CA (2010).

[1] G. Moody, M. E. Siemens, A.D. Bristow, X. Dai, D. Karaiskaj, S.T. Cundiff, "Coherent Excitonic Resonances of Natural Quantum Dots Studied with Optical 2D Fourier-Transform Spectroscopy," APS Four Corners Section Meeting, Golden, CO (2009).

Other Peer-Reviewed Journal Publications

[7] R. Singh, T. M. Autry, G. Nardin, G. Moody, K. Pierz, M. Bieler, and S. T. Cundiff, "Anisotropic homogeneous linewidths of the heavy-hole exciton state in (110)-oriented GaAs quantum wells," submitted for publication.

[6] G. Nardin, G. Moody, T. A. Autry, R. Singh, H. Li, and S. T. Cundiff, "Coherent coupling in an asymmetric double InGaAs quantum well," in preparation.

[5] G. Moody, I. A. Akimov, R. Singh, H. Li, D. R. Yakovlev, M. Bayer, G. Karczewski, T. Wojtowicz, and S. T. Cundiff, "Exciton-trion coherent interactions in a CdTe/CdMgTe quantum well," in preparation.

[4] H. Li, A. P. Spencer, A. Kortyna, G. Moody, D. M. Jonas, and S. T. Cundiff, "Pulse propagation effects in optical 2D Fourier-transform spectroscopy: Experiment," in press at the Journal of Physical Chemistry A.

[3] H. Li, A. D. Bristow, M. E. Siemens, G. Moody, and S. T. Cundiff, "Unraveling quantum pathways using optical 3D Fourier-transform spectroscopy," Nature Communications **4**, 1390 (2013).

[2] H. Li, G. Moody, and S. T. Cundiff, "Reflection optical two-dimensional Fourier-transform spectroscopy," Optics Express **21**, 1687 (2013).

[1] D. B. Turner, P. Wen, D. H. Arias, K. A. Nelson, H. Li, G. Moody, M. E. Siemens, and S. T. Cundiff, "Persistent exciton-type many-body interactions in GaAs quantum wells measured using two-dimensional optical spectroscopy," Physical Review B **85**, 201303(R) (2012).

Chapter 2

Physics of Semiconductor Quantum Dots

QDs of various material composition and size can be fabricated using several techniques, with the primary distinction being between epitaxial growth methods and chemical synthesis. Among epitaxially-grown QDs, In(Ga)As/GaAs and GaAs/AlGaAs have been the most widely-studied, both of which are the focus of this thesis. The energies associated with quantum confinement can vary by more than an order of magnitude between GaAs and In(Ga)As QDs. Specifically, electrons and holes are confined by $\sim$ 10 meV in GaAs interfacial fluctuation QDs (IFQDs), which are therefore considered only quasi-zero-dimensional systems. Conversely, confinement in In(Ga)As self-assembled QDs (SAQDs) typically varies from tens to hundreds of meV, and thus can more realistically be considered the solid-state equivalent of atomic systems. Because of the different amounts of confinement, the electronic and optical properties are often calculated using different methods to try to capture the essential features. One of three theoretical frameworks are typically used to calculate the electronic bandstructure: an effective mass approach [117, 118], an empirical pseudopotential theory [119], or $\mathbf{k}\cdot\mathbf{p}$ theory [120, 121, 122]. All methods generally predict similar qualitative features, however some persisting discrepancies include the number of confined levels and the energies of those levels for a particular QD morphology.

In this Chapter, the physics of QDs are discussed in the context of the $\mathbf{k}\cdot\mathbf{p}$ theory approach for two reasons: 1) this method automatically considers piezoelectric effects arising from a lattice strain distribution, which can drastically alter the optical properties; and 2) our results on the influence of confinement on many-body interactions presented in Chapter 6 are directly compared

to theory performed by several groups that use the **k**·**p** method. In Section 2.1, condensed matter theory for bulk semiconductors is reviewed, followed by a discussion of Coulomb effects that lead to exciton formation. In Section 2.2, conditions for three-dimensional quantum confinement are introduced, followed by a discussion of how confinement influences the optical properties and many-body interactions in semiconductor QDs (Section 2.3). In Section 2.4, dephasing mechanisms relevant to the context of this thesis are discussed, with a primary focus on exciton-exciton and exciton-phonon interactions and incoherent population transfer mechanisms. Details of the samples under investigation are discussed in Section 2.5. Conventional spectroscopic methods used to probe the optical properties in QDs are reviewed in Section 2.6.

2.1 Semiconductor Bulk Bandstructure

Allowed optical transitions in atomic systems are governed by the light-matter interaction Hamiltonian, whose non-zero matrix elements are determined by the symmetry properties of the electronic wave functions [123]. In semiconductors, the electron wave functions are Bloch states that are written as the product of a slowly-varying envelope function, which matches the boundary conditions of the confining potential, and a periodic Bloch function that captures the periodicity of the underlying atomic potential [124]. To understand how three-dimensional confinement affects the semiconductor optical properties, condensed matter theory regarding bulk bandstructure will first be reviewed.

2.1.1 Periodic Potential Lattice and Bloch Wavefunctions

The Schrödinger equation for an electron in a bulk crystal lattice is

$$\hat{H} \cdot \Psi(\vec{r}) = \{\frac{-\hbar}{2m}\nabla^2 + U(\vec{r})\} \cdot \Psi(\vec{r}) = E \cdot \Psi(\vec{r}), \tag{2.1}$$

where $U(\vec{r})$ is the periodic crystal lattice potential so that $U(\vec{r}+\vec{R}) = U(\vec{r})$ for a lattice vector $\vec{R}$. Bloch's theorem then states that the energy eigenfunction for such a Hamiltonian, $\Psi_{n\vec{k}}(\vec{r})$, can be

written as the product of a plane wave envelope function and a periodic Bloch function, $u_{n\vec{k}}(\vec{r})$, that has the same periodicity of the underlying atomic potential, giving:

$$\Psi_{n\vec{k}}(\vec{r}) = e^{i\vec{k}\cdot\vec{r}} \cdot u_{n\vec{k}}(\vec{r}), \tag{2.2}$$

where $u_{n\vec{k}}(\vec{r}) = u_{n\vec{k}}(\vec{r}+\vec{R})$ and $\vec{k}$ is the plane wave vector in the crystal. $\vec{k}$, equivalent to the crystal momentum when multiplied by the reduced Planck's constant, is unique only up to a reciprocal lattice vector and therefore one only needs to consider $\vec{k}$ within the first Brillouin zone of the reciprocal lattice. The corresponding energy eigenvalues, $E_n(\vec{k}) = E_n(\vec{k}+\vec{K})$, are also periodic with periodicity defined by the reciprocal lattice vector $\vec{K}$. The index n identifies an energy band for which the energy varies continuously with $\vec{k}$. All unique values of $E_n(\vec{k})$ also occur for $\vec{k}$ within the first Brillouin zone. For a given $U(\vec{r})$ and $\vec{k}$, a number of solutions to Eqn 2.1 exist and are indexed by n.

In general, the dispersion relation $E(\vec{k})$ is complicated and is difficult to calculate. For direct-gap III-V semiconductors, such as (Al)GaAs and In(Ga)As, the dispersion relation is approximately quadratic at the center of the Brillouin zone ($\vec{k} = 0$); therefore an effective mass for the electron can be defined as is done for a free electron plane wave:

$$m_{eff} = \left(\frac{1}{\hbar^2}\frac{d^2E}{dk^2}\right)^{-1}. \tag{2.3}$$

The dispersion relation for an electron in the crystal is not the same for a free space electron, and therefore m_{eff} is usually different from the free-space electron mass. Up to this point, the Bloch theorem is simply a general statement of the wave function form in a periodic potential. Additional insight can be gained by making specific assumptions about the wave functions using the tight-binding approximation [124, 125] in which the electrons are tightly-bound to the atom to which they belong and only weakly interact with electrons in neighboring atoms. Using this approximation, one writes the total crystal Hamiltonian, $\hat{H}_{\vec{k}}$, as the sum of a single-atom Hamiltonian, $\hat{H}_0$, and a perturbation, $\Delta U(\vec{r})$, describing the interaction of neighboring atoms, giving:

$$\hat{H}_{\vec{k}} = \hat{H}_0 + \Delta U\left(\vec{r}\right). \tag{2.4}$$

The total wave function, $\Psi_{\vec{k}}(\vec{r})$, satisfies the total Hamiltonian $\hat{H}_{\vec{k}}$ and can be expanded in a basis of the single-atom wave functions:

$$\Psi_{\vec{k}}(\vec{r}) = \sum_{\vec{R}} e^{i\vec{k}\cdot\vec{r}}\phi\left(\vec{r} - \vec{R}\right), \tag{2.5}$$

where

$$\phi\left(\vec{r}\right) = \sum_{n} a_n \psi_n\left(\vec{r}\right). \tag{2.6}$$

In Eqn 2.6, $\phi(\vec{r})$ is the weighted sum of the atomic wave functions, $\psi_n(\vec{r})$, that satisfy the single atom Hamiltonian $\hat{H}_0$. The sum over $\vec{R}$ in Eqn. 2.5 then considers contributions from all units cells in the crystal lattice. The tight binding approximation requires that the overlap integrals of neighboring atomic wave functions are zero, establishing the orthogonality relation

$$\langle \psi_n\left(\vec{r}\right) | \psi_m\left(\vec{r} - \vec{R}\right)\rangle = \delta_{nm}\delta_{\vec{R},0}. \tag{2.7}$$

For the QD materials (indium, arsenide, and gallium) considered in this thesis, the outer shell electrons are in the s and p atomic orbitals with angular momentum $l = 0$ and $l = 1$, respectively. Therefore the sum in Eqn. 2.6 can be simplified to contain only s and p states. Using these wave functions, the relevant total eigenstates and eigenenergies can be determined by calculating the matrix elements of the total Hamiltonian

$$\langle \psi_n | \hat{H}_{\vec{k}} | \Psi_{\vec{k}} \rangle = E_{\vec{k}} \langle \psi_n | \Psi_{\vec{k}} \rangle, \tag{2.8}$$

which can be solved in principle. A general result for the dispersion relation of a bulk III–V direct-gap semiconductor is depicted in the bandstructure diagram in Fig. 2.1 for $\vec{k} \approx 0$.

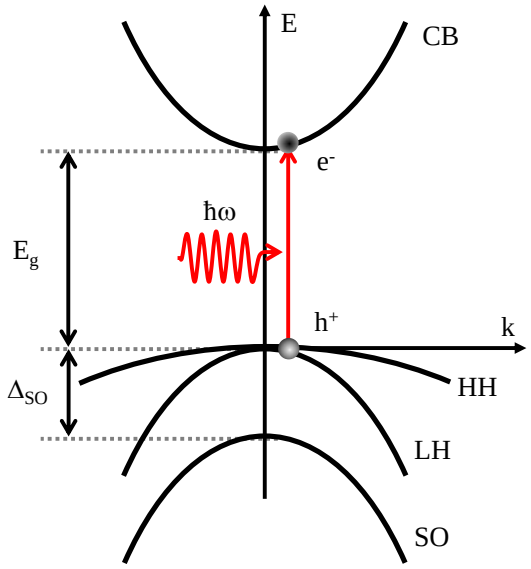

Figure 2.1: The conduction (CB) and heavy hole (HH), light hole (LH) and split off (SO) valence bands for a III–V direct-gap semiconductor. The bandgap, E_g, is the energy difference between the bottom of the conduction band and top of the HH and LH valence bands at $\vec{k} = 0$. The SO band is separated from the HH and LH valence bands by spin-orbit coupling energy, Δ_{SO}.

For bulk GaAs and In(Ga)As, the conduction band (CB) is s-like with zero orbital angular momentum (L) and a spin angular momentum (S) of $1/2 \cdot \hbar$. In terms of the total angular momentum state $|J, J_z\rangle$, where the total angular momentum is $J = L + S$, at $\vec{k} = 0$ the CB eigenstate is exactly $\Psi_C = |1/2, \pm 1/2\rangle$ in the tight-binding approximation. The valence bands are p-like with orbital angular momentum $L = 1$. Eigenstates for the heavy-hole (HH) band are $\Psi_{HH} = |3/2, \pm 3/2\rangle$ and for the light-hole (LH) band $\Psi_{LH} = |3/2, \pm 1/2\rangle$, and the two bands are degenerate at $\vec{k} = 0$. The split-off (SO) band eigenstates are $\Psi_{SO} = |1/2, \pm 1/2\rangle$ and the band is separated from the HH and LH bands by the spin-orbit interaction energy, Δ_{SO}. For both GaAs and In(Ga)As QDs, confinement shifts the LH and SO bands to an energy considerably lower than the HH band so that, to first order, these bands can be neglected. Therefore these bands will be ignored in the following discussions.

During optical excitation of a direct-gap semiconductor with a photon of sufficient energy

($\hbar\omega > E_g$), an electron (e-) is excited from the valence band to the conduction band, simultaneously creating a vacancy in the HH valence band, which is referred to as a "hole" (h+), shown in Fig. 2.1. Because the photon momentum is orders of magnitude smaller than that of the electron or hole, the optical transition is essentially vertical in Fig. 2.1 (i.e. the change in momentum, δk, is $\approx$ zero). For optical excitation high into the conduction band, the Coulomb interaction between the electron and hole can be treated as a perturbation [126]. In this case, the optical interaction is governed by the light-matter interaction Hamiltonian (in the dipole approximation) [123]

$$\hat{H}_{int}(t) = -\vec{\mu} \cdot \vec{E}(t), \tag{2.9}$$

where $\vec{\mu}$ is the transition dipole moment and $\vec{E}(t)$ is the electric field. The light-matter interaction strength is given by the matrix element $\mu_{ij} = \langle f|\vec{\mu} \cdot \hat{\varepsilon}|i\rangle$, where $|f\rangle$ and $|i\rangle$ are the conduction and valence band states, respectively, and $\hat{\varepsilon}$ is the electric field polarization vector. This matrix element determines the dipole transition selection rules for the system. The correct basis for states $|f\rangle$ and $|i\rangle$ is, in general, difficult to establish. The description of the eigenstates as pure total angular momentum states is only valid at $\vec{k} = 0$ for bulk materials. For $\vec{k} \neq 0$, eigenstates of the different bands mix.

When considering quantum confinement in QDs, the envelope wave function must satisfy the boundary conditions imposed by the confining potential – the envelope is no longer a plane wave but instead a linear combination of plane waves. Additionally, many-body effects, such as Coulomb interactions responsible for exciton formation, complicate the picture. Therefore, in order to properly determine the electron and hole wave functions and energies, a more complete theory that includes carrier-carrier interactions is necessary, which will be introduced in Section 2.3. In the following Section, excitonic effects on the optical properties in bulk materials are discussed.

2.1.2 Excitons in Semiconductors

For excitations close to the fundamental bandgap, Coulomb interactions between the electron and heavy hole can no longer be neglected. In this case, the attractive Coulomb force between the

electron and hole results in the formation of a bound state, known as an "exciton". The exciton can be treated as a "quasiparticle", and unbound electron-hole pairs are considered as continuum states [127]. The concept of a quasiparticle is convenient for describing the most basic excitations arising from weak perturbations. Typically, excitons have large oscillator strengths and dominate the linear optical properties of semiconductors near the band edge. However, the "residual" Coulomb forces not accounted for in exciton formation leads to interactions between excitons and induce a nonlinear response [127].

The exciton, considered the solid-state analog to the hydrogen atom formed by an electron and proton, can be described using a hydrogen-like energy level scheme. In the center-of-mass coordinates, the exciton has a reduced mass $\mu = m_e m_h/(m_e + m_h)$ and a total mass $M = m_e + m_h$, where m_e is the mass of the electron and m_h that of the hole. The internal energy of the exciton is then provided by the hydrogen-like analog:

$$E\left(n\right) = -\frac{E_R}{n^2}, \tag{2.10}$$

where E_R is the exciton form of the Rydberg constant (i.e. the binding energy of the exciton ground state) and n is the principle quantum number of the exciton. E_R depends on the reduced mass of the exciton and the background dielectric constant, ϵ:

$$E_R = \frac{\mu e^4}{2\epsilon^2\hbar^2} = \frac{\hbar^2}{2\mu a_B^2}, \tag{2.11}$$

where $a_B = \epsilon\hbar^2/\mu e^2$ is the exciton Bohr radius characterizing the spatial extent of the exciton in the semiconductor. The total energy of the exciton is then determined by its kinetic energy, the semiconductor bandgap, and the internal exciton energy [128]:

$$E\left(n, \vec{k}\right) = \frac{\hbar^2}{2M}|\vec{k}| + E_{\mathrm{g}} - \frac{E_R}{n^2}, \tag{2.12}$$

where $\vec{k} = \vec{k}_e + \vec{k}_h$ is the exciton center-of-mass wavevector. Excitons can typically be classified into two types: tightly-bound Frenkel excitons that are primarily localized to a unit cell [129, 130], and

Wannier-Mott excitons that extend over many unit cells [131]. Because of the small reduced mass and large dielectric constant in semiconductors, excitons are generally of the Wannier-Mott type and have large Bohr radii because of dielectric screening. Compared to the hydrogen atom, the exciton binding energy is orders of magnitude smaller. For example, for a bulk GaAs semiconductor at zero lattice temperature, $E_{\mathrm{g}} = 1.519$ eV, $m_e = 0.067 \cdot m_0$, $m_h = 0.51 \cdot m_0$ (where m_0 is the free electron mass), $\epsilon = 12.9$, $a_B = 11.6$ nm and $E_R \approx 4.8$ meV [132]. For bulk InAs at zero lattice temperature, $E_{\mathrm{g}} = 0.415$ eV, $m_e = 0.023 \cdot m_0$, $m_h = 0.41 \cdot m_0$, $\epsilon = 15.15$, $a_B = 36.9$ nm and $E_R \approx 1.3$ meV [132]. As the GaAs (InAs) lattice constant is 0.56 nm (0.61 nm), the electron and hole are separated by many lattice constants, confirming that the excitons are Wannier-type.

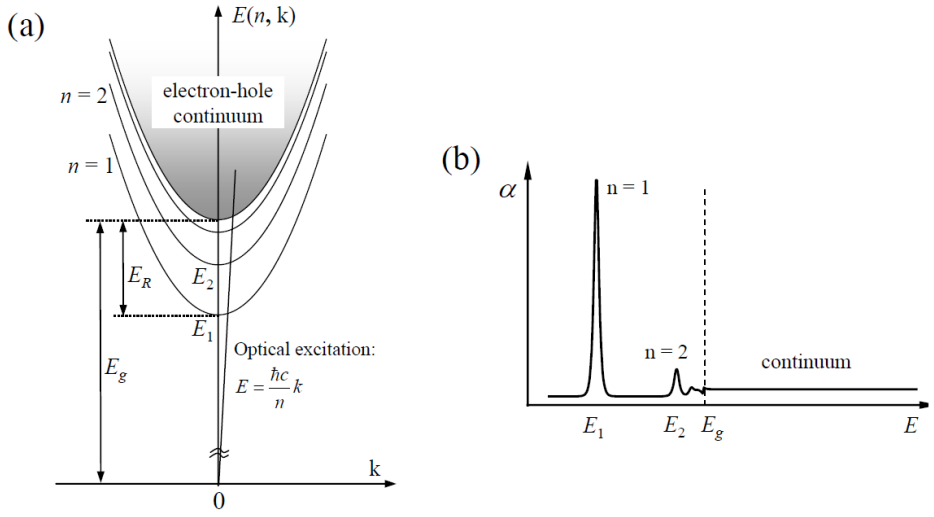

Figure 2.2: (a) The exciton dispersion relation and the photon line $E(k) = \hbar ck/n$. (b) A schematic figure of the exciton linear absorption spectrum with the ground state ($n = 1$), first excited state ($n = 2$) and the unbound electron-hole pair continuum labeled. This figure is reprinted from Zhang, T., "Optical two-dimensional Fourier transform spectroscopy of semiconductors," (Doctoral Dissertation) University of Colorado, Boulder (2008).

Instead of treating optical excitation as a two-particle process, as is shown in Fig. 2.1, a useful representation of the semiconductor system is the pair picture, shown in Fig. 2.2. In

Fig. 2.2(a), the exciton energy $E(n, \vec{k})$ is plotted versus the center-of-mass wavevector, $\vec{k}$. The origin corresponds to the crystal ground state, and the excited states correspond to excitons with $n = 1, 2, 3, \ldots$ and the unbound electron-hole continuum. An exciton can be excited by a photon characterized by the light line with energy $E(\vec{k}) = \hbar ck/n$, where c is the speed of light in vacuum and n is the semiconductor refractive index. This picture assumes weak exciton-photon coupling such that exciton-polariton effects can be ignored.

The center-of-mass momentum of an optically-created exciton is essentially zero compared to the size of the Brillouin zone since the photon momentum is negligibly small, thus $\vec{k} \approx 0$ in Eqn. 2.12. The effects of Coulomb interactions are apparent when considering the photon energies that can be absorbed. Unbound electron-hole pairs in the continuum can be created for photon energies greater than the fundamental bandgap. As the photon energy $\hbar\omega$ decreases to E_g, the continuum absorption approaches a finite value instead of decreasing to zero following a square-root behavior predicted for free-carriers. This enhanced absorption stems from Coulomb interactions between the electrons and holes, and the ratio of the Coulomb-enhanced absorption coefficient to that without Coulomb effects is known as the Sommerfeld enhancement factor [126, 128]. For photon energies $\hbar\omega \geq E_{\mathrm{g}} - E_R$, excitons can be created in the semiconductor. This effect is more clearly seen in the schematic low-temperature absorption spectrum shown in Fig. 2.2(b). Strong exciton absorption peaks corresponding to 1s ($n = 1$) and 2s ($n = 2$) hydrogen-like states appear below the bandgap, followed by a continuum of unbound electron-hole pairs. These results are quite different from what is expected when ignoring Coulomb interactions between electrons and holes and demonstrates how excitonic effects influence the band-edge linear absorption properties. The oscillator strength of an exciton with principle quantum number n relies on the electron-hole overlap integral and decreases as $1/n^3$. Experimentally, only excitons with $n \leq 3$ are usually observable because of the small exciton Rydberg constant E_R and various broadening and scattering effects that arise from exciton-exciton, exciton-free-carrier and exciton-phonon interactions.

2.2 Conditions for Three-Dimensional Quantum Confinement

Quantum confinement effects on the electronic and optical properties become important when the physical size of the confining potential becomes comparable to the de Broglie wavelength of the electrons or holes [133]. Considering the thermal motion of a particle of mass m along a single direction in a crystal with lattice temperature T, then the de Broglie wavelength is given by [133]

$$\lambda_{deB} = \frac{h}{\sqrt{mk_BT}}, \tag{2.13}$$

where k_B is the Boltzmann constant. For an electron in GaAs at room temperature (T = 300 K), λ_{deB} = 42 nm. This means that for nanostructures with spatial dimensions on the order of tens of nm, which are routinely grown using epitaxial techniques, quantum size effects will be important from room temperature down to liquid helium temperatures. In semiconductors, quantum confinement is provided by the discontinuity of the bandgap at interfaces. For structures that satisfy the confinement conditions set forth by Eqn. 2.13, the motion of electrons and holes is restricted and quantized along the confinement direction, giving rise to a series of discrete energy levels. This behavior is depicted in Fig. 2.3, which compares the density of states between the bulk, QWs, quantum wires, and QDs.

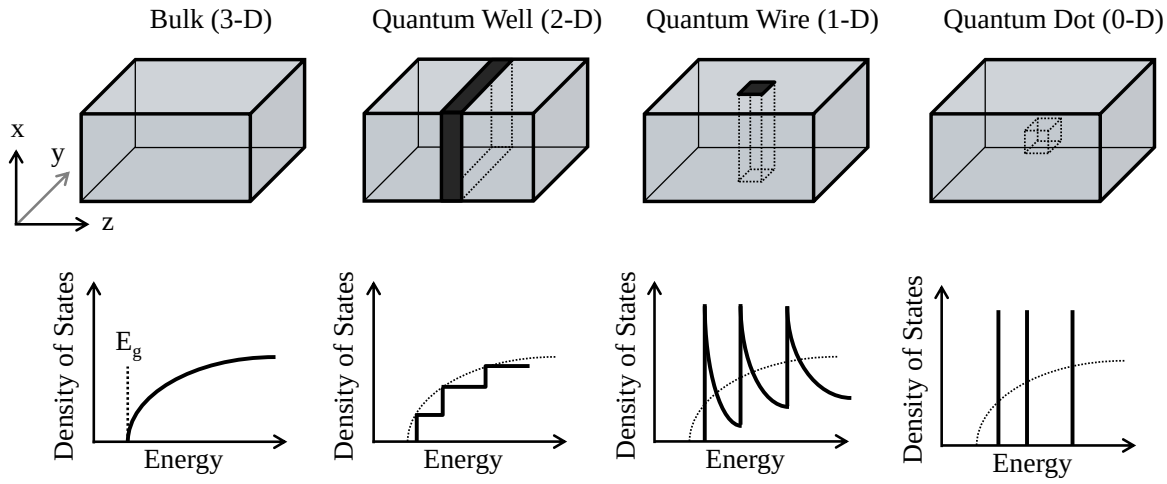

Figure 2.3: Density of states for particles with three (bulk), two (quantum well), one (quantum wire), and zero (quantum dot) spatial degrees of freedom.

Depending on the characteristics of the QD, e.g. epitaxially-grown versus chemically-synthesized, shape, composition gradients, etc., different models are used for the confinement potential Hamiltonian, with the most common being a simple quantum box with infinite or finite barriers, a spherical potential well, and a harmonic oscillator potential. These different models predict different eigenstates and eigenenergies; however they all predict qualitatively similar electronic and optical properties, in general. Quantization of the electron and hole spatial motion has three characteristic effects: 1) the effective band-edge is blue-shifted; 2) confinement forces the electron and hole to overlap, increasing the oscillator strength, and hence the radiative probability; and 3) as previously mentioned and depicted in Fig. 2.3, the density of states becomes discrete. Figure 2.4 demonstrates the energy level quantization from quantum confinement for a QD embedded in a matrix with a larger bandgap, as depicted in the right-most panel.

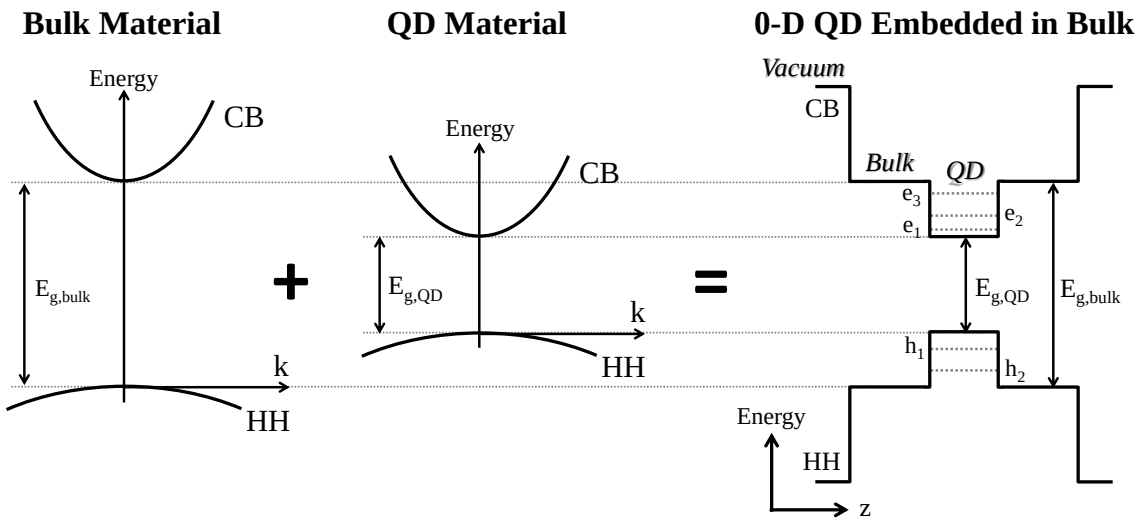

Figure 2.4: Energy level diagram of the HH and electron conduction band (CB) for bulk material with large bandgap, $E_{g,bulk}$, QD material with small bandgap, $E_{g,QD}$, and the 0-D nanostructure energy diagram with quantized QD states as a result of embedding the QD material into the bulk matrix.

If one considers, for example, a square well potential with a barrier height V_0 and a potential width L, then the minimum QD size allowed for the existence of a bound exciton state is $L_{min} = \pi\hbar/\sqrt{2\mu V_0}$, where μ is the exciton reduced mass. For QD sizes smaller than L_{min}, the exciton will be delocalized in the surrounding matrix in which the QD is embedded. Using the electron properties for GaAs and a confinement potential of 10 meV (which is typical for GaAs IFQDs), then $L_{min} \approx 25$ nm. Castella and Wilkins [134] demonstrated that for GaAs IFQDs with lateral dimensions 2-3 times L_{min}, the PL spectrum is split into two peaks with the lower-energy peak corresponding to excitons weakly-localized in the quasi-zero-dimensional QDs and the higher-energy peak corresponding to excitons delocalized in the underlying QW. Their observations are confirmed for the GaAs sample studied here, discussed in Section 2.5. For the InAs SAQDs, which exhibit a confinement energy ranging from 60 - 300 meV, then $L_{min} \approx 8 - 17$ nm. Referring back to the Bohr radii calculated in the previous Section for these materials, it is evident that in GaAs IFQDs, where $L_{min} > a_B$, excitons are weakly localized, whereas the strong confinement regime is realized

in InAs SAQDs, where $L_{min} < a_B$.

2.3 Optical Properties of Quantum Dots

The low temperature spectrum of a single or few QDs exhibits rich structure that is sensitive to the material composition, size and growth conditions. Large effort has been expended experimentally to characterize the electronic and optical properties of QDs using various linear and nonlinear techniques, and numerous theoretical models have been developed to try to reproduce the experiments. From experiments and theory, it is clear that the electronic and optical properties and the coherent optical response are influenced by two dominant effects [84]: 1) lattice-mismatch-induced strain that shifts the energy levels and can vary dot-to-dot [122]; and 2) Coulomb effects including direct pair-wise Coulomb interactions, analogous to a Hartree-Fock mean-field approximation, and Coulomb correlations beyond the mean-field limit [82]. In this Section, the optical properties of QDs will be discussed with references to the configuration interaction method and the $\mathbf{k}\cdot\mathbf{p}$ theory, which automatically account for strain and Coulomb interactions. The Section will be concluded with details of the samples investigated in this thesis, conventional spectroscopic measurement techniques, and motivation for implementing 2DCS to the study of semiconductor QDs.

2.3.1 Classification of Quantum Dots

Three-dimensional spatial confinement of electrons and holes in semiconductors can be accomplished using several techniques, with the most common relying on epitaxial-growth or chemical synthesis of a low-bandgap material embedded in another material with a higher bandgap. Other methods have been developed, including lithographically-patterning gate electrodes on a doped QW containing a two-dimensional electron gas or by using genetically-engineered viruses to organize inorganic nanocrystal arrays, although these techniques are not as relevant for ultrafast optical spectroscopy. Colloidal QDs (CQDs) can be chemically-synthesized from binary alloys such as CdSe, CdS, PbSe and PbS, or from ternary allows such as CdSeTe. CQDs usually exhibit a

complex optical spectrum that is inhomogeneously broadened by up to hundreds of meV from QD size dispersion occurring during synthesis. CQDs present a number of challenges for spectroscopic studies. For example, they typically have resonances at energies outside of the operating range of lasers and detectors that are commonly available. Furthermore, significant inhomogeneity and large energy separation between excited states make studying coherent and incoherent intraband dynamics in CQD ensembles difficult because of limited bandwidth of typical laser systems. Nonetheless, CQDs are interesting from both fundamental and applied perspectives [135] and preliminary 2DCS studies will be presented in Appendix A.

Epitaxially-grown QD ensembles, on the other hand, usually exhibit inhomogeneous line widths less than 100 meV and intraband energy level separation on the order of 10 meV. Epitaxial QDs can be separated into two classes: interfacial fluctuation QDs (IFQDs) that form "naturally" from monolayer changes in the width of a narrow QW, and self-assembled QDs (SAQDs) that form to alleviate lattice-mismatch-induced strain in a narrow QW in which two interfacing layers have dissimilar lattice constants by at least a few percent. The highest quality dots are usually grown by molecular beam epitaxy (MBE), where, for example, GaAs is deposited one atomic layer at a time on AlGaAs. If the GaAs layer is deposited uniformly, and then capped by another AlGaAs layer, the nanostructure would represent a QW. However, under specific growth conditions, which are detailed in Section 2.5 for the samples studied in this thesis, GaAs islands can form on top of a thin QW. The sample is then capped with an AlGaAs layer, encasing the islands, resulting in a QW–QD nanostructure, which is depicted in the schematic diagram in Fig. 2.5. The shape of the QD is sensitive to the growth conditions and can take the form of a truncated pyramid, lens, sphere or box, and due to material composition intermixing, the dots often have a linear composition gradient. For example, in In(Ga)As QDs, due to indium diffusion, the QDs tend to be indium-rich near the top and gallium-rich near the bottom, resulting in a slight (< 1 nm) displacement of the electron and hole wave functions along the growth direction, inducing a static electric dipole moment [136]. The main limitations of both IFQDs and SAQDs are the cost of fabrication and the lack of control over position of individual QDs. Site-controlled QDs can be fabricated by lithographically-patterning

the surface of a semiconductor substrate, such as bulk GaAs, and then growing QDs in the etched nano-imprints. The QD optical properties have so far been inferior compared to SAQDs, although significant progress in this area has been made in recent years [137]. Site-controlled growth has also been achieved using droplet epitaxy [138].

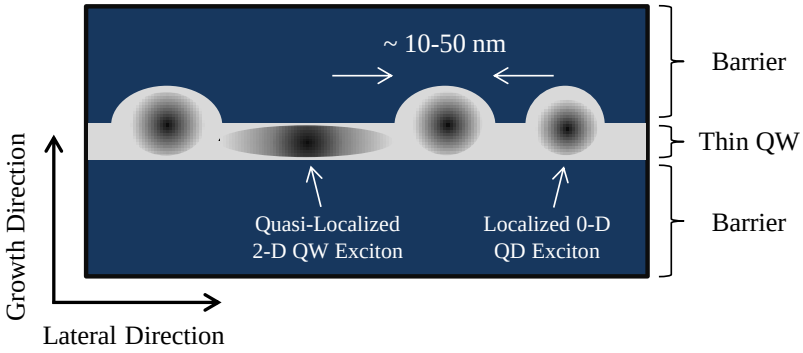

Figure 2.5: Schematic diagram of epitaxially-grown QDs on a narrow QW. Optical excitation can create 2-D excitons in the QW and 0-D excitons confined in the QDs.

The confinement potential for In(Ga)As SAQDs is typically hundreds of meV for the electron and less than 100 meV for the hole. Consequently, the electron-hole pair is bound more by the confinement potential than Coulomb interactions and the exciton pair-picture established in Section 2.1 is not as relevant as it is for QWs. This is not the case for GaAs IFQDs, in which the electron-hole pair is bound by $\sim$ 10 meV relative to 2-D excitons delocalized in the underlying QW. The results presented in Chapter 6 support the idea that Coulomb effects significantly influence, if not dominate, the nonlinear optical response of GaAs IFQDs. Moreover, despite strong confinement in the SAQDs, electron and hole interactions induce measurable changes of the optical properties, such as exchange-interaction-induced state splitting and bound biexciton effects.

2.3.2 Interband Optical Transitions

A distinct feature of three-dimensional confinement is the discrete energy level spectrum that supplants the continuous energy bands in lower-dimensionality materials. In the absence of band mixing effects, each bulk band gives rise to a series of discrete energy states. Due to strong spatial

confinement and different effective masses, the LH and SO bulk bands exhibit large energy shifts compared to the HH band and thus can be ignored. Continuing on the bandstructure framework established in Section 2.1, electrons in the conduction band have an s-like wave function (with total angular momentum along the growth direction of $J_z = 1/2$) while holes in the HH valence band are primarily p-like (with $J_z = 3/2$). Similar to the eigenstates for the bulk material, the wave function for a particle in a QD can be written in a slightly different form [139]:

$$\Psi_{n\vec{k}}(\vec{r}) = \sum_n F_n(\vec{r}) \cdot \psi_n(\vec{r}) \,. \tag{2.14}$$

The total wave function, $\Psi_{n\vec{k}}(\vec{r})$, is a product of an envelope function, $F_n(\vec{r})$, and the periodic Bloch functions $\psi_n(\vec{r})$. The envelope is required to satisfy the boundary conditions imposed by the QD confinement potential and therefore no longer has the form of a plane wave; it is often, however, written using a plane wave basis set. In contrast to the bulk total wave function, which has a well-defined crystal wave vector $\vec{k}$, the eigenstates of the QD are a linear combination of many $\vec{k}$'s. This is consistent with the Heisenberg uncertainty relationship $\delta_x \delta_{p_x} \geq \hbar/2$. When quantum confinement effects become important in three dimensions, δ_x decreases and therefore the distribution of crystal wave vectors $\Delta\vec{k}$ (i.e. δ_{p_x}) increases.

Numerous theoretical approaches are used to calculate accurate eigenstates and eigenenergies while including Coulomb effects, exchange interactions and strain, details of which can be found in Ref. [122] and references therein. One such approach to calculate the single particle states is to use the eight-band $\mathbf{k}\cdot\mathbf{p}$ theory [120, 122, 139], and then incorporate Coulomb and exchange effects using the configuration interaction method [84]. $\mathbf{k}\cdot\mathbf{p}$ theory assumes that the total wave function and eigenenergies are known at some wave vector $\vec{k}_0$ and then calculates the bandstructure perturbatively for $\vec{k}$ near $\vec{k}_0$. For strongly-confining QDs, $\vec{k}_0 = 0$ and the initial known wave functions consist of the s and p outer-most electron atomic states at $\vec{k} = 0$, which can be calculated using the tight-binding approximation described in Section 2.1. Confinement of the electron and hole wave functions in the QD requires multiple $\vec{k}$'s to construct the envelope wave function, and

this method is used to calculate the eigenstates and eigenenergies perturbatively for each $\vec{k}$. This method can automatically account for band mixing, which can result from strain and strain-induced piezoelectric fields.

While determining accurate eigenstates and eigenenergies requires rigorous calculations, the allowed optical transitions and dipole transition selection rules can be postulated without an intensive theoretical framework. Considering the light-matter interaction Hamiltonian under the dipole approximation (Eqn. 2.9), the optical transitions are governed by the matrix elements of $\langle f|\hat{H}_{int}|i\rangle$, where $|f\rangle$ and $|i\rangle$ are the final and initial electronic states. If the general form for the total wave function is used, assuming the envelope function varies slowly over a unit cell, then the light-matter interaction matrix elements are given by [139]

$$\langle f|\hat{H}_{int}|i\rangle \propto \sum_{nm} \int F_n(r) \cdot F_m(r)\, dr \int_{\Omega} \psi_n^*(r)\, \hat{\varepsilon} \cdot \nabla \psi_m(r)\, dr. \tag{2.15}$$

In this form, the envelope wave functions are general and therefore orthogonality has not yet been established for them. The integral of the Bloch functions over Ω is the transition dipole moment of an atom, thus the allowed interband optical transitions are governed by the atomic states that form the initial and final electronic states of the associated optical transition. Since the atomic states consist of primarily s-like and p-like wave functions, if only wave vectors near $\vec{k} \approx 0$ are considered, then the conduction and valence band ground states in the QD will consist of mostly s- and p-like states. This argument is consistent with the rigorous calculations in Ref. [122] in which, for example, the electron ground state is s-like with an integral probability of 0.89. In this simplified picture, one could calculate the allowed interband transitions using the atomic wave functions; however, the optical dipole transition selection rules are also affected by Coulomb and exchange interactions. Inclusion of these effects can be achieved by employing the configuration interaction method with basis states determined using the $\mathbf{k}\cdot\mathbf{p}$ theory. These effects will be reviewed in the next two sub-Sections.

2.3.3 Coulomb Effects: Excitons, Biexcitons and Trions

Regardless of whether the interaction energies associated with Coulomb effects are dominated by the confinement potential energies or not, the excitonic picture is a useful representation for epitaxially-grown QDs; however, it should be kept in mind that excitons in QDs are different from bulk excitons in several ways. First, a QD exciton cannot dissociate into an electron and hole, unless one of the charges leaves the QD, because the external confinement potential usually dominates over the Coulomb interactions. Second, excited exciton states in a QD are not states of the mutual Coulomb potential of interacting electrons and holes, but instead they are formed by the charge carriers residing in higher-lying single-particle states of the QD potential. Coulomb interactions between electrons and holes then modify the energetics of the few-particle states with respect to the sum of the energies of the individual single particles, and the resulting energy difference is considered the binding energy. For example, the exciton energy is given by $E_X = E_e + E_h - \Delta_X$, where E_e and E_h are the single-particle electron and hole energies and Δ_X is the binding energy due to renormalization from electron-hole Coulomb interactions. The biexciton energy would then be $E_B = 2 \cdot E_X - \Delta_B$, where Δ_B is the biexciton binding energy.

Single dot spectra reveal rich information about the energetics of various multi-particle states and their radiative decay dynamics. Excitons, bound and anti-bound two-excitons (biexcitons) and negatively or positively charged excitons (trions) are easily identified in PL spectra. In their representative ground states, for which only the lowest-energy electron and hole levels are occupied, these excitonic states would be degenerate if ignoring Coulomb interactions. Experimentally, this is not the case, and instead splitting of several meV are observed. The energetic ordering of the states is sensitive to the QD size, shape and composition; therefore a connection between QD morphology and the recombination energies of the excitonic states is difficult to establish. Experimentally, the energetics can be systematically characterized by recording many single-dot PL spectra for samples prepared using different growth methods, i.e. QDs with various morphology; however, significant dot-to-dot scatter of the data from single dot experiments and accurate characterization of the dot

size, shape and composition make comparison to theory difficult.

Nonetheless, certain fingerprints for specific QD morphology exist, such as the binding energies of the biexciton and trion relative to the exciton ground state [84]. Theorists often use this information to address the inverse problem: using the QD morphology as a fitting parameter, what QD structure would give rise to the measured optical spectrum? One common technique is to use the configuration interaction (CI) method [82, 83, 84, 85, 140]. CI is a linear variational technique for solving the few-particle Schrödinger equation in which the ground state energy, E, is minimized with respect to all normalized wave functions according to

$$E \equiv min\langle\Psi|\hat{H}|\Psi\rangle|_{\Psi}. \tag{2.16}$$

The exact ground state energy could, in principle, be found by minimizing Eqn. 2.16 with respect to all possible $|\Psi\rangle$, which is not computationally feasible. An alternative approach is to expand $|\Psi\rangle$ into a linear combination of Slater determinants constructed from the single-particle states. A Slater determinant is a convenient way to describe the wave function of a multi-fermionic system that satisfies the anti-symmetry requirements for the Pauli exclusion principle. For example, for two electrons at positions $\vec{r}_1$ and $\vec{r}_2$ in states χ_1 and χ_2, the anti-symmetric wave function would have the form $\Psi(\vec{r}_1, \vec{r}_2) = \{\chi_1(\vec{r}_1) \cdot \chi_2(\vec{r}_2) - \chi_1(\vec{r}_2) \cdot \chi_2(\vec{r}_1)\}/\sqrt{2}$. The corresponding Slater determinant would then be written as

$$\Phi = \frac{1}{\sqrt{2}} \begin{vmatrix} \chi_1(\vec{r}_1) & \chi_2(\vec{r}_1) \\ \chi_1(\vec{r}_2) & \chi_2(\vec{r}_2) \end{vmatrix}. \tag{2.17}$$

This expression can be generalized for an N-electron system:

$$\Phi\left(\vec{r}_1, \vec{r}_2, \ldots \vec{r}_N\right) = \frac{1}{\sqrt{N!}} \begin{vmatrix} \chi_1(\vec{r}_1) & \chi_2(\vec{r}_1) & \cdots & \chi_N(\vec{r}_1) \\ \chi_1(\vec{r}_2) & \chi_2(\vec{r}_2) & \cdots & \chi_N(\vec{r}_2) \\ \vdots & \vdots & \ddots & \vdots \\ \chi_1(\vec{r}_N) & \chi_2(\vec{r}_N) & \cdots & \chi_N(\vec{r}_N) \end{vmatrix}. \tag{2.18}$$

Using eight-band $\mathbf{k}\cdot\mathbf{p}$ theory, the single-particle states $\chi_i(\vec{r})$ can be calculated to form the basis for constructing the many-particle Slater determinant. The total wave function, $|\Psi_N^\alpha\rangle$, where N is the number of particles and α is the index for the few-particle state, can be written as a linear combination of all possible Slater determinants, $|\Phi_{i,j,k,...}\rangle$, that are constructed from the single-particle states, and is given by

$$|\Psi_N^\alpha\rangle = \sum_{i,j,k,...} C_{i,j,k,...}^\alpha |\Phi_{i,j,k,...}\rangle. \tag{2.19}$$

If the series contained an infinite number of terms, the wave function would be exact, which, of course, is not computationally tractable. Truncating the series to a single Slater determinant, for which all N particles are described by their ground-state wave functions, corresponds to what is known as the Hartree-Fock (HF) approximation. While this approximation still takes into account the exchange interaction, i.e. a special case of electron-electron correlation in which no two electrons can be in the same quantum state, satisfying the Pauli exclusion principle, and direct pair-wise Coulomb interactions, it cannot account for higher-order correlations of the collective system and consequently it underestimates the few-particle binding energies. To calculate the CI wave functions and eigenenergies, Eqn. 2.16 is solved using the wave functions from a truncated expansion of Eqn. 2.19. As an example, consider the positive trion, X^+, which consists of an electron (index i) and two holes (indices j and k). The ground-state configuration could be approximated as a linear combination of two Slater determinants [84],

$$|\Psi_3^{X^+}\rangle = \sum_{i=1}^{2} C_{i,1,2}^{X^+} |\Phi_{e_i h_j h_k}\rangle, \tag{2.20}$$

where the electron single-particle wave functions consist of the ground state ($i = 1$) and first excited state ($i = 2$) in this example. In practice, the CI wave functions and energies can be computed by multiplying both sides of the Schrödinger equation by the Slater determinant, Φ_i, inserting the wave function expansion from Eqn. 2.19, and then integrating the result, to give:

$$\begin{aligned}\sum_j \langle\Phi_i|\hat{H}|\Phi_j\rangle C_j^\beta &= \sum_j E_j\langle\Phi_i|\Phi_j\rangle C_j^\beta \\ &= \sum_j E_j\delta_{ij}C_j^\beta \\ &= E_i C_i^\beta. \end{aligned} \tag{2.21}$$

Equation 2.21 is the matrix representation of the component form of an eigenvalue problem. Thus determining the CI wave function and eigenenergies corresponds to finding the lowest energy eigenvalues of Eqn. 2.21. Typically the series can be truncated by using only one or two bound excited state wave functions to construct the Slater determinants. A more accurate approach [84] is to use a basis constructed from the wave functions of all bound states, which even itself only accounts for up to $\approx 80\%$ of the total interaction energies associated with the few-particle states in the QD [141]. Nonetheless, the results from this method have been effective for understanding the many-body configurations in epitaxial QDs, and are summarized in Fig. 2.6.

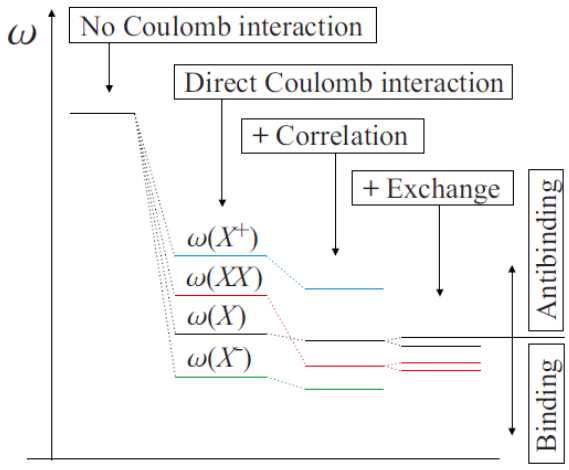

Figure 2.6: The evolution of few-particle recombination energies with increasing amount of correlation and electron-hole exchange. Without Coulomb effects, the exciton (X), positive (X^+) and negative (X^-) trions and the biexciton (XX) are degenerate. Only when direct Coulomb interactions, correlations and exchange are included do the few-particle energies accurately reproduce experiments. Reproduced from A. Schliwa, M. Winkelnkemper and D. Bimberg, Physical Review B **79**, 075443 (2009).

The results summarized in Fig. 2.6 highlight the importance of direct pair-wise Coulomb interactions (the HF approximation), correlations beyond the HF limit, and exchange interaction effects on the recombination energies of the few-particle states. The experimental results presented in Chapter 6 will be analyzed with regard to the CI simulations discussed in this sub-Section in order to understand how QW–QD confinement and QD size affect the few-particle interaction energies.

2.3.4 Electron-Hole Exchange Interaction: Exciton Fine-Structure

The theoretical framework introduced in the previous sub-Section automatically takes into account the effects of the electron-hole exchange interaction through the ground-state Slater determinant. Figure 2.6 demonstrates that electron-hole exchange interaction results in an energetic

splitting of both the exciton and biexciton states. While exchange effects are typically too weak to be observed in higher-dimensional systems, they are enhanced in QDs because confinement increases the electron-hole wave function overlap. The origin of the fine-structure splitting, and its connection to QD morphology, is more easily understood by explicitly writing the exchange energy, given by [44]

$$E_{exchange} = \int\int d^3r_1 d^3r_2 \cdot \Psi_X^* \left(\vec{r}_e = \vec{r}_1, \vec{r}_h = \vec{r}_2\right) \cdot \frac{1}{|\vec{r}_1 - \vec{r}_2|} \cdot \Psi_X \left(\vec{r}_e = \vec{r}_2, \vec{r}_h = \vec{r}_1\right), \tag{2.22}$$

where Ψ_X is the exciton wave function and $\vec{r}_{e,h}$ are the electron and hole spatial positions. The exchange integral is divided into two parts for calculations: 1) either real-space short- and long-range components; or 2) k-space analytical and non-analytical components. Considering the real-space decomposition, the short-range (long-range) component is given by the probability to find the electron and hole in the same (different) unit cell. First considering short-range exchange, the spin Hamiltonian for the electron-hole exchange interaction of an exciton is given by [142]

$$\hat{H}_{exchange} = -\sum_{i=x,y,z} \{a_i J_{h,i} S_{e,i} + b_i J_{h,i}^3 S_{e,i}\}, \tag{2.23}$$

where S_e and J_h are the electron and hole spins, a and b are the spin-spin coupling constants, and the quantization axis is chosen to be along the nanostructure growth direction, z. The single-particle basis from which excitons can be constructed consist of the HH valence band with total angular momentum $J_h = 3/2$ and $J_{h,z} = \pm 3/2$ and the electron conduction band with total angular momentum $S_e = 1/2$ and $S_{e,z} = \pm 1/2$. Writing the total angular momentum projected along z (M) in the pair-picture exciton basis, then $M = S_{e,z} + J_{h,z}$. The $|M| = 1$ states are optically-active (bright) excitons, since optical excitation of these states satisfies conservation of angular momentum. The $|M| = 2$ states are optically-inactive (dark) excitons and cannot couple to the light field [1] .

[1] These states are modified if the light-hole band is not ignored. In this case, heavy-hole–light-hole band mixing effects must be included and will result in a basis of eight total angular momentum states, which, for example, must be considered in colloidal QD samples.

Using the exciton basis $\{|+1\rangle, |-1\rangle, |+2\rangle, |-2\rangle\}$ and neglecting the x and y components that are linear in J_h because LH-HH mixing can be ignored, $\hat{H}_{exchange}$ has the following matrix form:

$$\hat{H}_{exchange} = \frac{1}{2}\begin{pmatrix} +\delta_0 & +\delta_1 & 0 & 0 \\ +\delta_1 & +\delta_0 & 0 & 0 \\ 0 & 0 & -\delta_0 & +\delta_2 \\ 0 & 0 & +\delta_2 & -\delta_0 \end{pmatrix}, \tag{2.24}$$

where the δ_i's are related to the coefficients in Eqn. 2.23 by: $\delta_0 = 1.5 \cdot (a_z + 2.25 \cdot b_z)$, $\delta_1 = 0.75 \cdot (b_x - b_y)$ and $\delta_2 = 0.75 \cdot (b_x + b_y)$ [44]. Because the matrix in Eqn. 2.24 is block diagonal, the bright and dark exciton states do not mix and they are separated in energy by δ_0. The following table summarizes the effects of the short-range exchange interaction on the eigenstates and eigenenergies of the bright and dark excitons:

D_{2d}		$< D_{2d}$	
$b_x = b_y$		$b_x \neq b_y$	
Energy	Eigenstate	Energy	Eigenstate
$+\frac{1}{2}\delta_0$	$\|-1\rangle$	$\frac{1}{2}(\delta_0 + \delta_1)$	$\frac{1}{\sqrt{2}}(\|+1\rangle + \|-1\rangle)$
$+\frac{1}{2}\delta_0$	$\|+1\rangle$	$\frac{1}{2}(\delta_0 - \delta_1)$	$\frac{1}{\sqrt{2}}(\|+1\rangle - \|-1\rangle)$
$\frac{1}{2}(-\delta_0 + \delta_2)$	$\frac{1}{\sqrt{2}}(\|+2\rangle + \|-2\rangle)$	$\frac{1}{2}(-\delta_0 + \delta_2)$	$\frac{1}{\sqrt{2}}(\|+2\rangle + \|-2\rangle)$
$\frac{1}{2}(-\delta_0 - \delta_2)$	$\frac{1}{\sqrt{2}}(\|+2\rangle - \|-2\rangle)$	$\frac{1}{2}(-\delta_0 - \delta_2)$	$\frac{1}{\sqrt{2}}(\|+2\rangle - \|-2\rangle)$

Table 2.1: Influence of the exchange interactions on the bright and dark exciton eigenstates for QDs with $\leq D_{2d}$ symmetry. When also considering long-range exchange effects, δ_0 is replaced by Δ_0 and δ_1 by Δ_1.

For QDs with in-plane rotational symmetry, belonging to the D_{2d} point group, angular momentum is a good quantum number and $b_x = b_y$. In this case, $\delta_1 = 0$ and the $|+1\rangle$ and $|-1\rangle$

states are eigenstates of $\hat{H}_{exchange}$. If rotational symmetry is broken somehow, such that $b_x \neq b_y$, angular momentum is no longer a good quantum number and the $|\pm 1\rangle$ states are mixed with each other. In this case, the eigenstates of $\hat{H}_{exchange}$ are symmetric ($\frac{1}{\sqrt{2}}[|+1\rangle + |-1\rangle] \equiv |H\rangle$) and anti-symmetric ($\frac{1}{\sqrt{2}}[|+1\rangle - |-1\rangle] \equiv |V\rangle$) linear combinations of the bright exciton states and are separated in energy by δ_1. Considering the relationship between linearly- and circularly-polarized light, the $|H\rangle$ and $|V\rangle$ states correspond to orthogonal linearly-polarized spin states. The energy splitting between the hybridized states of $|\pm 2\rangle$ is equal to δ_2 irrespective of the QD symmetry.

The long-range exchange interaction can be included by modifying the sub-block of the $|M| = 1$ excitons in Eqn. 2.24 to have the form

$$\begin{pmatrix} +\Delta_0 & +\Delta_1 \\ +\Delta_1 & +\Delta_0 \end{pmatrix}, \tag{2.25}$$

where $\Delta_0 = \delta_0 + \gamma_0$ and $\Delta_1 = \delta_1 + \gamma_1$. From this modification, it is apparent that the long-range exchange interaction further separates the bright and dark states by γ_0. For rotationally-symmetric QDs, $\gamma_1 = \gamma_x - \gamma_y = 0$, $\Delta_1 = 0$, and the $|\pm 1\rangle$ bright states are degenerate eigenstates of $\hat{H}_{exchange}$. For asymmetric dots, where Δ_1, δ_1, and γ_1 are nonzero, the long-range exchange further splits the mixed bright states. In general $\gamma_1 \gg \delta_1$, implying that the long-range exchange interaction is the dominant mechanism for mixing and splitting of the bright exciton states. This splitting is referred to in the literature as the exciton "fine-structure splitting" and will be represented by an energy Δ_{FSS} in this thesis.

Values of Δ_{FSS} reported in the literature range from $+1000$ to -100 μeV, where $\Delta_{FSS} > 0$ implies that $|V\rangle$ is higher in energy than $|H\rangle$. Although the dominant mechanism contributing to the breaking of the QD symmetry and nonzero Δ_{FSS} is still under debate, two competing mechanisms have been proposed [143]: 1) anisotropy in the QD shape arising from strain that is present during the epitaxial growth process; and 2) strain-induced piezoelectric fields. Both of these mechanisms are expected to induce anisotropy in the confinement potential, which typically aligns $|H\rangle$ and $|V\rangle$ along the [110] and [1$\bar{1}$0] crystal axes, respectively, for samples grown along the

[001] direction.

This discussion so far has assumed the QD is neutral, i.e. it does not contain any resident charge carriers. For charged QDs the energetics are different. As an example, consider the positive trion, X^+, for which the lowest energy state consists of two heavy-holes with opposite spin and a single electron with two possible spin orientations with all particles in their respective ground states. The trion can be considered as an electron interacting with the spin-singlet hole pair. For QDs exhibiting strong confinement, the electron and hole wave functions have similar spatial extent; thus the local hole spin density is zero. Consequently the electron-hole exchange interaction vanishes and $\Delta_{FSS} = 0$. In weakly-confining QDs and structures with higher dimensionality, the local spin density could be nonzero. This point will be revisited in Chapter 6, where results of ensemble measurements of Δ_{FSS} are discussed.

2.3.5 Relevant Energy Level Schemes and Dipole Transition Selection Rules

Based on the discussions in the previous sub-Sections, the energy level scheme for the ground state excitonic transitions in neutral, epitaxially-grown QDs is shown in Fig. 2.7. Excitonic states can be optically excited in both the underlying QW and the QDs. The single monolayer thickness difference between the QW and QDs red-shifts the QD resonance relative to the QW; however the in-plane lateral confinement blue-shifts the resonance, resulting in a net red-shift of the QD peak relative to the QW by an energy V_0. The QW and QD exciton states can be approximated as two separate two level systems, shown in Fig. 2.7(a). This picture is a simple way to visualize the QW–QD heterostructures; however the QW and QD are coupled predominantly through incoherent population transfer mechanisms and therefore Fig. 2.7(a) is only accurate when neglecting interactions. The preceding discussion regarding electron-hole exchange is summarized by the energy diagram shown in Fig. 2.7(b). When considering both short- and long-range exchange for an asymmetric confinement potential, the bright excitons mix and are energetically split by the fine-structure splitting, Δ_{FSS}.

In QDs for which $\Delta_{FSS} = 0$, the $|\pm 1\rangle$ bright exciton states can be excited using circularly-

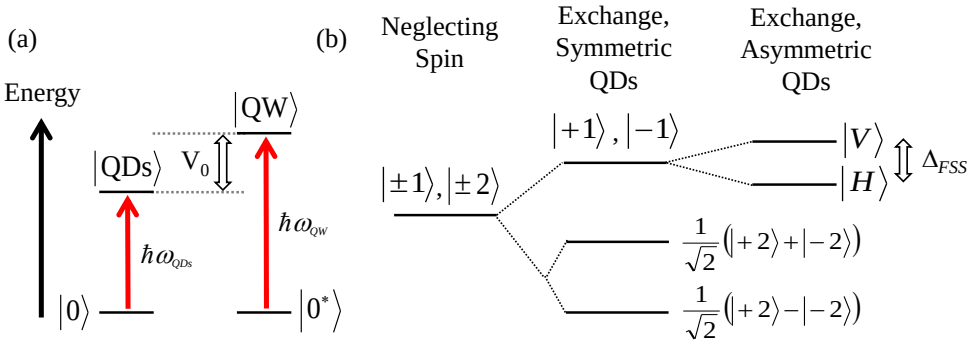

Figure 2.7: (a) Energy level diagram in the exciton picture indicating the crystal ground state for the QDs ($|0\rangle$) and QW ($|0^*\rangle$) and the corresponding QD ($|\text{QDs}\rangle$) and QW ($|\text{QW}\rangle$) exciton ground states separated by an energy V_0. (b) The QD bright excitons mix to form to orthogonal linearly-polarized states ($|H\rangle$ and $|V\rangle$) that are energetically separated by the fine-structure splitting, Δ_{FSS}, for an anisotropic confinement potential.

polarized photons with angular momentum $\sigma\pm$, depicted in the energy diagram in Fig. 2.8(a) for a neutral QD. Without interactions, the two exciton spin states can be considered two separate two-level systems, and the dipole transition selection rules for these transitions are governed by the symmetry of the HH and CB atomic Bloch functions discussed in sub-Section 2.3.2. Through a basis transformation, this energy scheme is equivalent to the "diamond level" scheme shown in Fig. 2.8(b) if $\Delta_{FSS} = \Delta_B = 0$. The two exciton states are coupled through the sharing of a common ground state. Moreover, both excitons can be excited to create a two-exciton with energy equal to twice the exciton energy. At first glance, coupling of the exciton states through the common ground state would lead to interactions between the two excitons, such as ground state bleaching nonlinearities; however nonlinearities arising from coherent pathways including the doubly-excited two-exciton state cancel the singly-excited nonlinearities such that all interactions between the $|+1\rangle$ and $|-1\rangle$ excitons cancel. This is expected, since a basis transformation of the independent two-level systems should not lead to interactions between them.

The "residual" Coulomb interactions between the excitons, which are the interactions beyond those responsible for exciton formation, lead to interactions between the excitons. Biexciton formation, in which the interaction energy between two excitons leads to a renormalization of their

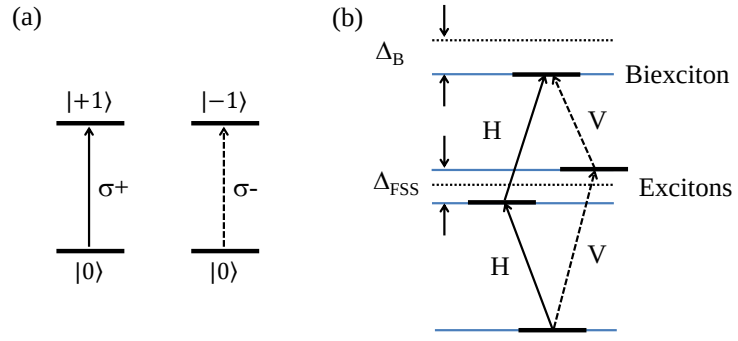

Figure 2.8: (a) Ground state exciton transitions when neglecting Coulomb and exchange interactions. The $|+1\rangle$ ($|-1\rangle$) exciton spin state can be excited by absorption of a $\sigma+$ ($\sigma-$) circularly-polarized photon. (b) Energy level diagram for a neutral, asymmetric QD, with the optical dipole transition selection rules labeled. $|H\rangle$ and $|V\rangle$ are separated by Δ_{FSS}, and the bound two-exciton (biexciton) is shown with a positive binding energy, Δ_B.

collective energy, and exchange effects that mix the circularly-polarized exciton spin states, break the symmetry of the diamond level scheme such that it is no longer equivalent to the independent two-level system picture. Many-body interactions lead to a modification of the optical dipole transition selection rules. The Hamiltonian basis states are no longer circularly-polarized exciton states, but are instead more easily described by the orthogonal linearly-polarized states $|H\rangle$ and $|V\rangle$. The selection rules are shown in the energy level diagram in Fig. 2.8(b). Pure $|H\rangle$ or $|V\rangle$ exciton states can be excited using linearly-polarized photons whose electric fields oscillate along either the minor or major axis of the asymmetric confinement potential. As previously mentioned, $|H\rangle$ and $|V\rangle$ tend to align along the two orthogonal in-plane crystal axes $[1\bar{1}0]$ and [110], respectively, for samples grown along [001]. For the experiments described in this thesis, photons linearly-polarized along these two axes are defined as having H and V polarization, respectively. Moreover, since the ground state of the biexciton – comprised of two electrons and two holes – is a singlet state, for QDs in the strong confinement regime, the local spin density is zero and the biexciton is insensitive to the exchange interaction. Therefore, the transition selection rules for the biexciton are similar to the exciton. As shown in Fig. 2.8(b), optical excitation of the QD using two linearly polarized photons can create a biexciton, which is in contrast to higher-dimensional systems in which two

opposite circularly-polarized photons are required [107, 144].

2.4 Decoherence and Relaxation Mechanisms

The unique optical properties of epitaxial QDs make them attractive for applications in opto-electronics and quantum information processing, some of which were introduced in Chapter 1. Successful implementation of many QD-based devices relies on maintaining coherence of the ground state exciton polarization for nanoseconds or longer. The homogeneous line width, γ, which is inversely proportional to the polarization dephasing time, T_2, can be broadened beyond the radiative recombination limit through numerous scattering mechanisms. Understanding the mechanisms responsible for dephasing – and the influence QD morphology has on them – is important for testing theoretical models and for enabling design of efficient and practical QD-based technologies.

The experiments performed for this thesis use a series of ultrafast optical pulses to excite and probe the electronic and optical properties of QDs. The electric field of each pulse creates an interband polarization with a phase determined by the field. Immediately after excitation, the polarization begins to dephase with the excitation field and phase coherence is lost in a time T_2. In the coherent regime, T_2 is limited only by the population decay time, T_1, which sets the ultimate timescale during which phase coherence is maintained [128]. Processes that alter the population – such as non-thermal scattering that redistributes the exciton energy or incoherent relaxation between resonances – inherently limit T_2. "Pure" dephasing processes that destroy the phase coherence without changing the population state include exciton-phonon scattering, exciton-exciton and exciton-carrier interactions. The polarization dephasing time is related to these decay and scattering processes through

$$\frac{1}{T_2} = \frac{1}{2T_1} + \frac{1}{T_2^*}, \tag{2.26}$$

where T_2^* is the pure dephasing time. This expression gives an upper limit on T_2 of $2T_1$ in the case that phase coherence is lost strictly through population decay. The homogeneous line width

of a single resonance is related to the dephasing time through $\gamma = \hbar/T_2$, in energy units. For a system consisting of multiple oscillators with the same energy, the polarization of every oscillator in the ensemble decays with the same rate T_2, and therefore the system can be characterized by a single homogeneous line width γ. In contrast, in an inhomogeneously broadened system, every oscillator has a slightly different energy and the distribution of energies can be characterized by a Gaussian function centered at an energy E_0 with an inhomogeneous line width γ_{inhom}. After optical excitation, the polarization of the ensemble decays faster than the polarization of each individual oscillator. Initially, all oscillators are in phase; however a phase distribution develops over time because of the different resonant energies, and the polarizations from the individual oscillators destructively interfere. The dephasing time of the ensemble can be characterized by a time constant $T_2^{'} \approx \hbar/\gamma_{inhom}$, which is shorter than the dephasing time T_2. Inhomogeneity can arise from disorder due to well width or alloy composition fluctuations in QWs. In QDs, the epitaxial growth processes are inherently statistical. Consequently each QD has a different size, shape and composition, resulting in a distribution of emission energies and optical properties of the ensemble. Nonlinear spectroscopic techniques are particularly suited to distinguish between these different broadening mechanisms and can provide a measure of the homogeneous line width even in the presence of strong inhomogeneity [145]. In the remainder of this Section, the dominant exciton dephasing mechanisms in epitaxial QDs are reviewed. Each mechanism will be discussed in more detail in the corresponding experimental results Chapter.

2.4.1 Exciton-Phonon Interactions

Of the numerous dephasing mechanisms, exciton-phonon interactions have garnered considerable attention both experimentally and theoretically. From fundamental arguments based on momentum and energy conservation, exciton-phonon interactions were predicted to be inhibited in QD systems because of the discrete nature of the density of states, leading to the so-called "phonon bottleneck" [113]. Thus, the interband polarizations were expected to be radiatively-limited at low-temperature. Furthermore, the line widths were expected to be insensitive to acoustic phonon

scattering since the energy levels of the QDs were large compared to the typical phonon energies. Nonetheless, a strong thermal component of the homogeneous line width has been observed; while this component was initially attributed to excitation of the exciton population to a higher-lying energy state through the absorption of a phonon or multiple phonons [28], subsequent studies using PL [146, 147, 148] and nonlinear spectroscopies [46, 149, 150] have provided evidence that inelastic activation of the exciton population cannot account for the dephasing. Instead, elastic exciton-phonon interactions, which leave the population state unchanged, are expected to dominate the line width broadening. The nature and strength of exciton-phonon scattering strongly depends on the confinement potential and surrounding QD environment [151, 152]. For QDs in the strong confinement regime, the emission line shape is characteristic of exciton-polaron mixed states, where the homogeneous line width is comprised of a narrow Lorentzian zero-phonon line (ZPL) superimposed onto a broad phonon sideband background. Conversely, excitons in weakly-confining QDs do not strongly couple to phonons and only the ZPL is observed. The line shape can be directly measured in single dot μ-PL spectroscopy. In nonlinear spectroscopies such as time-integrated FWM, the ZPL and broad background are manifest as slow and fast decay components, respectively, of the FWM signal with respect to the delay between the pulses. Moreover, the temperature dependence of the ZPL width and the relative weight of the ZPL component to the broad background component have exhibited linear and nonlinear behavior and the measurements vary significantly in the literature. To this end, a consistent scheme explaining the nature of the exciton-phonon interaction for QDs with different amount of confinement has not yet been fully developed.

2.4.2 Excitation-Induced Dephasing

Exciton-exciton and exciton-free carrier scattering can significantly influence the optical properties and coherent nonlinear optical response [153, 154, 155]. Wang *et al.* have demonstrated that in high-quality bulk GaAs, excitation-induced dephasing (EID) of the HH exciton is spin-independent and depends linearly on density for moderate excitation conditions [91, 156], so that $\gamma = \gamma_0 + \phi \cdot \gamma_{EID}$, where γ_0 is the zero-excitation line width and γ_{EID} is the rate of increase of the

homogeneous line width with average photon flux per pulse, ϕ, incident on the sample. This form of EID invokes a Markovian approximation, in which the full-time dependence of the EID process is neglected and is instead replaced by an instantaneous scattering event. Assuming memory-less scattering events is valid for bulk and QW systems, since continuous energy spectra of carriers provides a large phase space, ensuring energy and momentum conservation [157]. This approximation does not hold for QD structures, since the discrete density of states reduces the available phase space by restricting the number of allowed scattering transitions. Therefore a rigorous analysis that takes into account the frequency dependence of the EID scattering process, avoiding the Markovian approximation, is required to accurately describe EID in QDs. Nonetheless, calculations performed by Schneider *et al.* demonstrate that non-Markovian EID effects can be approximated by a linear dependence on the excitation density, albeit with a larger increase in the dephasing rate with excitation density. Compared to higher-dimensional structures, QDs are less sensitive to EID effects [157]; localization reduces the interaction strength between confined and free carriers and therefore EID plays a reduced role in the nonlinear optical response of QDs, but it cannot be ignored. Indeed, intradot carrier-carrier scattering and QW–QD interactions leading to dephasing of the interband optical polarizations determine the homogeneous broadening of QD-based lasers, where a high density of carriers is necessary for high optical gain [157, 158]. In quantum information applications, where single QDs act as qubits that can be coherently manipulated within the dephasing time T_2, intradot exciton-exciton and exciton-free carrier scattering damp Rabi oscillations and limit the time during which the exciton qubit can be coherently manipulated [159]. EID effects on the coherent nonlinear response of epitaxial QDs have been studied primarily through time-integrated FWM experiments [149, 160], where the FWM signal decays more rapidly under high excitation conditions. Since EID is sensitive to the relative carrier-carrier wave function overlap, γ_{EID} should be dependent on the amount of confinement and QD size. 2DCS experiments investigating the size-dependence of EID for both the GaAs IFQDs and In(Ga)As SAQDs will be discussed in Chapter 6.

2.4.3 Incoherent Population Transfer and Dynamical Broadening

Carrier transfer in low-dimensional semiconductor structures is interesting for the design of efficient and fast opto-electronic devices such as QD-based laser diodes. An important parameter for laser operation is the transfer rate of carriers from a reservoir or 2-D QW to localized QD states, which can limit the maximum achievable optical gain. Typically, high-energy free carriers relax or tunnel to the QD ground state in a time ranging from picoseconds [161, 162] to hundreds [163] of picoseconds, after which exciton-exciton, exciton-carrier and exciton-phonon interactions become important when the thermal energy is less than the exciton binding energy. From a fundamental standpoint, understanding population transfer of excitons between localized QDs and the underlying QW is interesting since the population lifetime of the interband optical polarizations, characterized by T_1, ultimately limits the dephasing time. Thus exciton population transfer can drastically affect applications where long-lived coherences are required. Similar to population transfer, dynamical broadening of the interband optical polarizations [114] – where the transition energy fluctuates with a characteristic timescale and amplitude from external perturbations – will also dephase the polarizations and limit T_2. These population dynamics have been measured using both PL and nonlinear spectroscopies; however distinguishing between the different mechanisms is difficult or impossible using 1-D techniques. 2DCS can unambiguously identify couplings between the QW and QDs and results will be presented in Chapter 7 for the GaAs IFQDs.

2.5 Sample Structure and Preparation

The samples discussed in this thesis are grown using molecular beam epitaxy (MBE) [2]. MBE usually takes place in an ultra-high vacuum (10^{-11} – 10^{-10} Torr), where ultra-pure elements, such as gallium and arsenic, are heated in separate effusion cells until they begin to sublimate. The gaseous elements are then adsorbed onto a substrate wafer, typically made of GaAs, which is held in the main chamber of the MBE system and acts as a seed crystal for growth of well-defined single-crystal layers. Each element cell temperature, cell shutter, the substrate temperature, and

the substrate rotation rate (required for uniform growth conditions across the entire substrate wafer) can be adjusted for precise growth of the nanostructures.

All samples studied in this thesis were grown on a [001]-oriented GaAs substrate. The GaAs IFQD sample was mounted onto a 0.25 inch diameter sapphire disk that is double-side AR-coated and is wedged by 1°. The substrate was removed for transmission measurements through mechanical lapping of the sample on lapping film with 5 μm grain size, until ≈ 10 μm of the substrate remained (e.g. the sample was, by eye, "infinitely thin"). The remaining substrate was removed via a wet chemical etch at room temperature using an H_2O_2 and NH_4OH solution with a pH ≈ 8. The In(Ga)As SAQD samples were also studied in transmission, however the substrate was left intact since the QD absorption energy is below that of the substrate. The sample was secured onto a 1 mm thick copper sheet with an aperture of 5 mm using rubber cement epoxy. Both samples were held in a liquid helium cold finger cryostat (Janis model ST100). The GaAs IFQD sample was provided by Dan Gammon and Allan Bracker at the Naval Research Laboratory. The InAs SAQD samples were provided by Ilya Akimov and Manfred Bayer from the Technical University of Dortmund, Germany, and were grown by Andreas Wieck and Dirk Reuter at the Ruhr-University of Bochum, Germany.

2.5.1 Interfacial Fluctuation Quantum Dots

The GaAs IFQD sample consists of a single 4.2 nm wide GaAs/$Al_{0.3}Ga_{0.7}$As QW with single monolayer (ML) interface fluctuations formed by 2 minute interruptions of the gallium flux during the epitaxial growth process (for detailed growth conditions, see Refs. [27, 28, 29]). For narrow QWs with widths similar to the one studied here, the fractional change in confinement along the growth direction from a ML width fluctuation is significant compared to the QW width and can result in a splitting of the optical spectrum into two peaks [134]. The higher-energy QW exciton states are weakly-localized by disorder on a length scale that is much larger than the mean separation between the ML fluctuations. The lower-energy resonance arises from excitons localized at the ML fluctuation sites, which form the IFQDs. Figure 2.9 shows a typical PL spectrum with the QD

ensemble red-shifted from the QW resonance by the in-plane confinement energy $V_0 \approx 10$ meV.

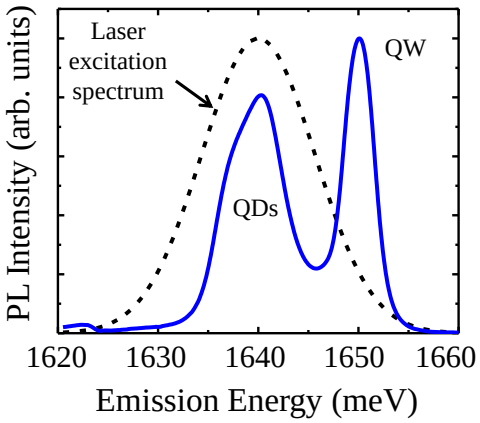

Figure 2.9: Typical PL spectrum (blue solid line) excited with 633 nm laser light. The center of the QD ensemble is red-shifted from the QW resonance by an in-plane confinement energy of $V_0 \approx 10$ meV. The laser excitation spectrum used in the experiments is indicated by the black dashed line.

Based on the analysis of 3-D confinement on bound states given in Section 2.2, the QDs have lateral dimensions of $30 - 40$ nm. A distribution of QD sizes results in an inhomogeneous line width of ≈ 3 meV full-width at half-maximum (FWHM). The QW excitonic resonance has a similar inhomogeneous line width due to a distribution of disorder length scales, which has been shown to be the origin of the mobility edge for dephasing and diffusion in 2-D semiconductor systems [164, 165]. Since the typical QD size is large than the exciton Bohr radius for bulk GaAs, excitons are only weakly-localized.

2.5.2 Self-Assembled Quantum Dots

Two In(Ga)As SAQD samples are investigated, both consisting of 10 quantum-mechanically isolated layers of QDs with GaAs barriers (details given in Ref. [166]). A thin layer of InAs was grown on top of GaAs. Strain builds as the InAs layer thickness increases because of the 7% lattice mismatch between InAs and GaAs. After a critical InAs layer thickness, the strain is relieved through the formation of islands, known as SAQDs, which rest on top of the underlying QW (often referred to as the "wetting layer"). The sample is then capped with a GaAs barrier to

form the QD/QW nanostructure. This process is repeated to form the other QD layers, with 50 nm GaAs layers separating them. Both samples have been thermally annealed post-growth – one at 900°C and the other at 980°C, both for 30 seconds. Annealing promotes indium diffusion so that a composition gradient forms across the dot, with affects the optical properties of the 900°C (980°C) sample in several ways [167, 166]: 1) the emission is blue-shifted to 1345 (1445) meV; 2) the inhomogeneous distribution is narrowed to $\sim$ 15 (10) meV FWHM; and 3) the ground state $\rightarrow$ QW in-plane confinement energy is decreased to $\sim$ 100 (60) meV. Impurities unintentionally-introduced during the growth process result in some of the QDs containing a resident hole. A method to determine the fraction of charged dots will be discussed in Chapter 6. Figure 2.10 shows a typical PL spectrum of the 900°C sample with the exciton ground state (GS) and first excited state (ES) labeled. Adopted from nomenclature in atomic physics, these states are often referred to as the "*s*-shell" and "*p*-shell".

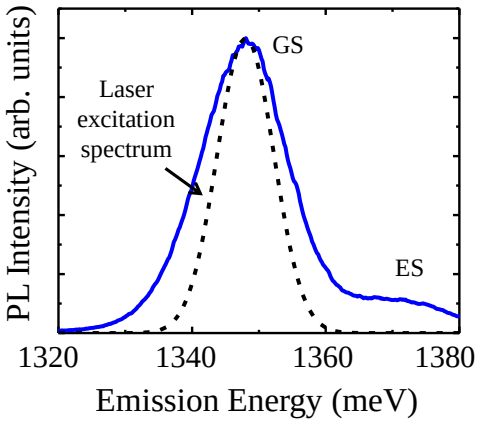

Figure 2.10: Typical PL spectrum (blue solid line) for the sample annealed at 900°C, excited with 633 nm laser light. The QD ensemble ground state (GS) emits at $\approx$ 1350 meV, and the first excited state (ES) is visible at $\approx$ 1370 meV. The laser excitation spectrum used in the experiments is indicated by the black dashed line.

2.6 Review of Conventional Experimental Techniques

A number of techniques have been devised for studying the electronic and optical properties of single dots and ensembles. A fundamental challenge in performing single dot spectroscopy

is separating the weak signal from the strong excitation laser pulses. The signal is enhanced by increasing the number of dots in ensemble measurements; however significant dispersion of the QD properties requires nonlinear techniques to isolate contributions from homogeneous and inhomogeneous effects. In this Section, a number of techniques used to investigate single dots and ensembles will be reviewed.

2.6.1 Photoluminescence Spectroscopies

Some of the first characterization studies of epitaxial QDs were performed using PL spectroscopy (for a representative list of experiments, see references in [99]). Single dots must be isolated in order to eliminate the effects of inhomogeneity. Electron-beam lithography and metal liftoff are often used to open a series a apertures in thin opaque aluminum or gold films deposited on the sample surface. Apertures ranging in diameter from 0.2 to 50 μm, spaced sufficiently apart so that only a single aperture is in the laser spot, are commonly used. The sample is then excited using non-resonant above-gap excitation with a power density below ≈ 100 W/cm^2 to avoid heating effects. Steady-state PL is detected in reflection through the same aperture using a triple spectrometer and charge coupled device (CCD) detector, which are necessary to eliminate pump light scatter. As shown in Fig. 2.11, PL from a 25 μm aperture exhibits broad, inhomogeneously-broadened peaks, indicative of radiative recombination of excitons in QWs with a single ML thickness difference [29]. With decreasing aperture size, discrete peaks appear in the PL spectrum are are attributed to excitons localized in the QDs.

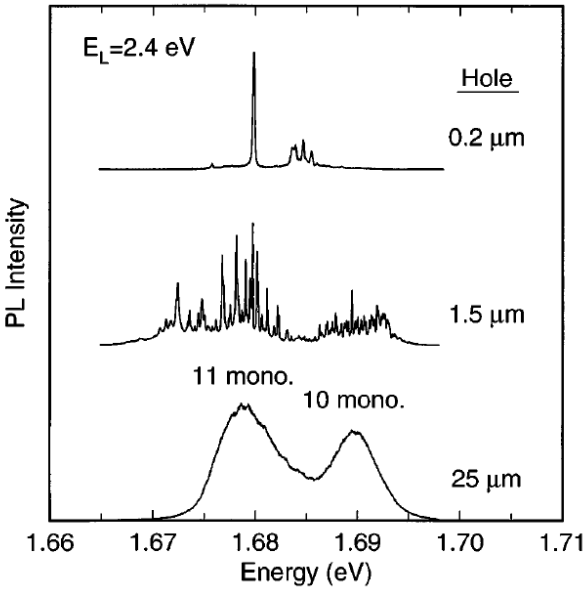

Figure 2.11: Non-resonant PL spectra from a GaAs IFQD sample. A thin aluminum film was deposited on the sample, and apertures of various diameter were formed to isolate regions containing different numbers of dots. For large apertures, broad PL from excitons delocalized in 11 ML and 10 ML thick QWs is observed. With decreasing aperture size, the spectrum evolves into a discrete set of peaks indicative of single dot emission. The laser excitation energy is $E_L = 2.4$ eV. Reproduced from D. Gammon, E. S. Snow, B. V. Shanabrook, D. S. Katzer, and D. Park, Physical Review Letters **76**, 3005 (1996).

By varying the excitation laser wavelength, a two-dimensional map correlating the PL emission and laser excitation energies reveals the excited states of the dots, and information regarding coupling between dots can be inferred. Time-resolved PL of single dots is achieved using pulsed laser excitation and detecting the PL through a monochromator and streak camera system to achieve picosecond time resolution [166]. Low excitation conditions are required to ensure that multiple excitons in one QD are not excited by a single excitation laser pulse.

Steady-state and time-resolved PL have facilitated progress in our understanding of the optical properties of single QDs. Recombination line widths and dynamics can reveal some of the processes that limit the radiative recombination lifetime and dephasing time of the ground and

excited states. A systematic study of different dots reveals the emission energy dependence (i.e. QD size dependence) of the optical properties, such as the recombination energies of different excitonic states. A critical drawback of single dot PL spectroscopies is the considerable dot-to-dot variation of the data for a particular emission energy, perhaps arising from modification of the local environment through the single dot isolation techniques. Patterning the sample using metal masks can introduce field effects that might shift the electronic bands or introduce charge carriers. Etching mesas that contain one or few dots [147] is an alternative to metal film deposition; however surface states and phonon scattering at the mesa boundaries can alter the linear and nonlinear response so that the intrinsic optical properties are not probed. Alternative single and ensemble QD characterization techniques that can eliminate some of these drawbacks are discussed in the following sub-Sections.

2.6.2 Resonance Fluorescence

Adapted from atomic physics experiments, resonant-fluorescence detection is suited to probing quantum statistics of QD emission and enables coherent optical control of a QD combined with quantum optical detection [168]. In resonant-fluorescence measurements, a pump resonantly excites an optical transition in the QD, and incoherent photon emission is detected. The technical challenge is to detect the emitted photons without the pump laser background. One method to reduce contributions from the pump is to detect the fluorescence normal to the sample and pump at large angles relative to the normal. This spatial filtering, along with detecting photons cross-linearly polarized relative to the pump, enables detection of single photons, although initial attempts using this method could not fully suppress the pump light. This method also requires a long focal length lens to focus the pump, increasing the spot size at the sample and reducing the intensity, thus increasing the probability of exciting multiple QDs and reducing the signal strength for the QD under examination.

Alternative geometries have enabled on- and near-resonance efficient detection. One scheme employs QDs embedded in a planar microcavity [169]. The pump laser is fiber-coupled into the

waveguide and the cavity forces the QD to emit along a specific direction, inherently enhancing the emission efficiency and suppressing the pump background. Another scheme is to excite and detect along the same direction normal to the sample surface using a high numerical-aperture lens, high-quality polarizer, and sharp spectral filter or dichroic mirror. This scheme inhibits detection at the pump frequency, but enables collection of single photons shifted by a small frequency from the pump. Using these techniques, researchers are devising methods to optically prepare, control and couple QDs embedded in photonic waveguides [170] and detect the single photon emission when exciting resonantly.

2.6.3 Photocurrent Detection

The photocurrent approach is advantageous compared to optical detection primarily because of its high detection efficiency. For example, in the case of optical detection, only 2% of the light can escape because of the large GaAs-air refractive index mismatch. Although low optical detection efficiency can be mitigated by incorporating single QDs into photonic structures or using a solid-immersion lens with a matched refractive index, the signal is ultimately detected through absorption in a slow photodiode or CCD, which have efficiencies below that of photocurrent detection. Figure 2.12 depicts the principles behind photocurrent detection, which was first demonstrated by Zrenner *et al.* in 2002 [66].

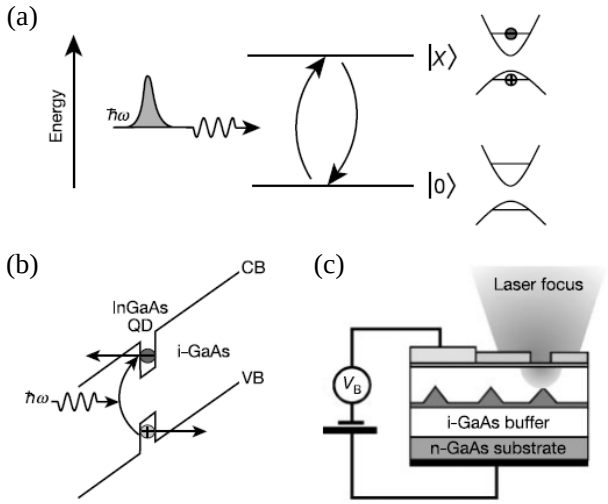

Figure 2.12: (a) Schematic view of an excitonic two-level system in the ground state of a semiconductor QD. (b) Intrinsic region of a biased single-QD photodiode. An optically-excited electron hole pair can tunnel out of the QD when the sample is biased, producing the deterministic photocurrent. (c) Schematic view of a single-QD photodiode, consisting of a GaAs n-i–Schottky diode. Optical access to a single QD is provided by a shadow mask. Reproduced from A. Zrenner, E. Beham, S. Stufler, F. Findeis, M. Bichler and G. Abstreiter, Nature **418**, 612 (2002).

A single QD is embedded in the intrinsic region of a photodiode structure. Resonant excitation creates an electron-hole pair that can tunnel out of the QD when the sample is biased. The carriers are detected as a change in the photocurrent of only a few pA. This method has been used primarily for coherent control experiments, where, for example, the exciton and biexciton quantum state can be manipulated [66, 171, 172] and hole spins can be prepared and detected [173]. Some apparent drawbacks of the technique originate from the limited coherence times due to the charge carrier tunneling required for detection. This can be mitigated, however, by gating the applied voltage, enabling dynamic control of the tunneling rate for both high detection efficiency and long coherence times [174]. The background photocurrent is proportional to the incident power (attributed to contributions from other dots in the structure at high power), requiring proper calibration of the photocurrents to isolate the single dot response. Moreover, the technique inherently

requires high-quality samples in photodiode structures, limiting the types of samples that can be studied. Care must also be taken to properly set the gate voltage so that the charges are removed from the sample between subsequent laser pulses; too slow of a tunneling rate could result in the presence of charge carriers when subsequent laser pulses arrive at the sample, which would shift the energy of the optical resonance and reduce the photocurrent signal.

2.6.4 Nonlinear Spectroscopies

The most widely-used techniques for time-resolved single dot characterization under resonant excitation are nonlinear spectroscopies, such as pump-probe-type measurements that detect the third-order nonlinear optical response of the QD. In most pump-probe experiments, the signal detected is the pump-mediated differential transmission or reflection of the probe. The interference between the third-order polarization, induced by the interaction of the pump and probe in the sample, with the probe can be spectrally-resolved using a monochromator, time-resolved through gated up-conversion techniques, or time-integrated using a slow detector and lock-in amplifier. In pump-probe experiments, the differential signal is proportional to the population inversion induced by the pump. The pump-probe delay, probe energy and probe polarization can be varied to resolve carrier relaxation, dephasing and spin dynamics, Coulomb-mediated dephasing and transition energy shifts, excited-state absorption, and biexciton formation, to name a few. For example, Lenihan *et al.* have measured the biexciton binding energy dependence on the exciton emission energy by pumping a subset of the inhomogeneously-broadened QD ensemble and tuning the spectrally-narrow probe energy to map out the excited-state absorption of the exciton $\rightarrow$ biexciton transition [86]. Pump-probe experiments can also be used to characterize the interband optical polarization dephasing rate by burning a spectral hole in the inhomogeneous distribution using a narrow pump pulse, and tuning a narrow probe pulse to map out the homogeneous line width of the transition [175]. The pump is amplitude modulated with frequency Δ_P and the probe is frequency modulated at Δ_{PR}. The pump and probe excite the QD ensemble, which is embedded in a waveguide geometry to enhance the light-matter interaction. The probe is interfered with a reference and their interfer-

ence is measured on a slow detector at the modulation difference frequency $\Delta_{mod} = \Delta_{PR} - \Delta_P$ using a lock-in amplifier. These methods are also effective for studying coherent control and manipulation of single QDs and have been demonstrated for a number of systems [176, 177, 178].

Time-resolved and time-integrated FWM techniques have enabled measurements of the optical properties of inhomogeneously-broadened ensembles with great success in revealing dephasing rates of the exciton coherence [149, 87]. In these experiments, details of which will be discussed in the following Chapter, the nonlinear interaction of the pump and probe pulses generates a nonlinear signal that is radiated in a background-free phase-matched direction. The signal can be time-resolved using nonlinear up-conversion techniques, spectrally-resolved, or more commonly, time-integrated using a slow detector and lock-in amplifier. The signal is recorded as the pump-probe delay is varied, and the decay of the signal provides a measurement of the dephasing rate. Interference between quantum pathways can give rise to beats in the FWM signal, and the period and damping of these beats can provide information regarding the intrinsic dephasing mechanisms in the sample. For example, Fig. 2.13 demonstrates the time-integrated FWM signal from InGaAs ensembles with different QW $\rightarrow$ QD confinement, V_0 [45]. At early times, fast oscillations corresponding to quantum interference of the ground state $\rightarrow$ exciton and exciton $\rightarrow$ biexciton transitions are observed. At longer times, slow oscillations corresponding to quantum interference between the interband transitions of the two bright exciton states $|H\rangle$ and $|V\rangle$ are present, with the beat period inversely proportional to Δ_{FSS}. These experiments demonstrate that the dephasing rate, biexciton binding energy and fine-structure splitting are sensitive to the level of confinement.

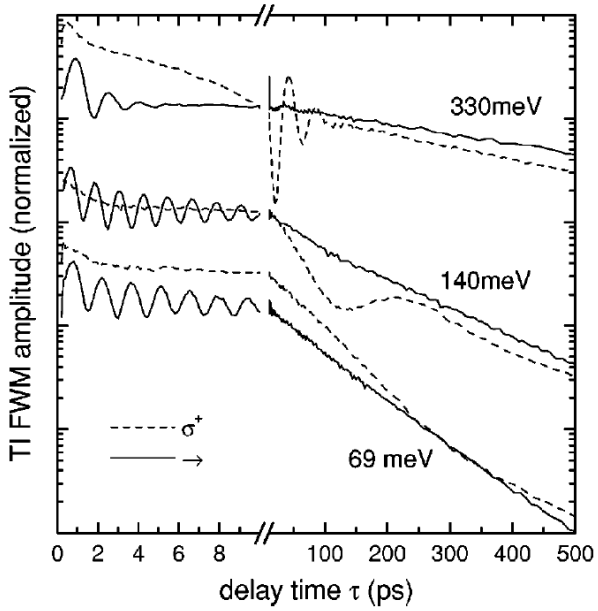

Figure 2.13: Time-integrated FWM amplitude versus delay, τ, between the two excitation pulses, for InGaAs QD samples with varying amounts of in-plane confinement energy, V_0. Beats at early time corresponding to interference between the exciton and biexciton quantum pathways, while oscillations corresponding to interference between the linearly-polarized bright excitons are observed at longer delays. Reproduced from W. Langbein, P. Borri, U. Woggon, V. Stavarache, D. Reuter, and A. D. Wieck, Physical Review B **69**, 161301(R) (2004).

While 1D FWM experiments, where the signal is recorded as a function of a single delay, have enhanced our understanding of confinement effects on the optical and electronic properties in QDs, they have several limitations that make interpretation of the data difficult or even impossible. For example, the nonlinear optical response of the QD ensemble is averaged over the excitation spectrum, thus 1D techniques are insensitive to the optical properties within the excitation laser bandwidth. Moreover, dispersion of the optical properties within the excitation laser bandwidth will result in artificially fast dephasing of the polarization and beats. FWM is also unable to reliably distinguish between the effects of inhomogeneity, dephasing and correlations between transition energy fluctuations of different states, which all contribute similarly to the FWM signal. Recently, optical 2DCS, which is an extension of FWM, has been implemented to study GaAs IFQDs [98, 99,

100] and In(Ga)As SAQDs [101, 102, 103]. This technique can overcome many of these limitations to simultaneously probe single-dot-like properties and ensemble interactions. Details of 2DCS, including the history of the technique, its implementation, and interpretation of the results, will be discussed in the following Chapter.

Chapter 3

Principles of Two-Dimensional Coherent Spectroscopy

Optical two-dimensional coherent spectroscopy (2DCS) is the optical analog of multidimensional nuclear magnetic resonance (NMR) that was developed in the 1970s [95]. Compared to conventional one-dimensional or non-Fourier transform techniques, 2DCS offers many advantages by tracking the phase evolution of the sample's nonlinear response with respect to two time delays. Precise knowledge of the phase enables a Fourier transform to be taken with respect to the delays, providing a correlation map of the nonlinear response with respect to two frequency dimensions. Congested one-dimensional spectra are unfolded onto two dimensions to allow for separation of inhomogeneous and homogeneous line widths, isolation of coherent pathways and identification of coupling between resonances. Moreover, the preservation of phase information enables the real and imaginary components of the nonlinear response to be separated, providing microscopic details not possible to obtain in magnitude measurements. These abilities make 2DCS a powerful technique for probing a material's electronic and optical properties, including dephasing mechanisms, population decay and transfer dynamics and many-body interactions. 2DCS has been implemented to study a multitude of complex systems, including liquids [179, 180], molecules [181, 182, 183, 184, 185, 186, 187], atomic vapors [108, 109, 110, 188], semiconductor QWs [106, 107, 189] and QDs [97, 98, 99, 100, 101, 102, 103].

In this Chapter, the development of optical 2DCS from NMR is first discussed in Section 3.1. In the following Section, the basic principles of four-wave mixing (FWM) are introduced, followed by an interpretation of the FWM experiments using the nonlinear optical response function to describe

the third-order macroscopic polarization (Section 3.3). The optical Bloch equation formalism is reviewed in Section 3.4, followed by an intuitive, sum-over-states diagrammatic approach to building the nonlinear response function (Section 3.5). This theoretical framework will aid in the discussion and interpretation of 2DCS. The transition from 1D to 2D spectroscopy is detailed in Section 3.6, including a discussion of the types of 2D spectra that can be generated, an intuitive interpretation of the spectra and advantages of the technique.

3.1 Development of IR and Optical 2D Spectroscopy

Multidimensional coherent spectroscopy was first implemented by the Ernst group in 1976 for NMR spectroscopy [190]. Soon after, it was clear that 2D NMR spectra contained valuable information that was not readily available from conventional NMR spectroscopies [191], such as cross peaks that revealed vibrational coupling between adjacent chemical bonds and spin coupling and transfer in molecules. These seminal works led to a heightened interest in multidimensional spectroscopy, and the technique was quickly extended to microwave frequency spectroscopy [192], 2D Raman spectroscopy of atomic vapors [193] and 2D infrared (IR) spectroscopy [194]. Similar to NMR studies, 2D IR spectroscopy revealed information about structural properties of molecules by probing the active vibrational modes and their coupling [183, 195]. 2D electronic spectroscopy was introduced by the Jonas group and was first implemented to study the dye IR144 in methanol [181]. In the last decade, 2D spectroscopy has been extended to the near-IR and optical regimes to study carrier dynamics and many-body effects in semiconductors. Some of the first studies investigated a disordered QW characterized by a bimodal inhomogeneous distribution and observed temporal oscillations in the time-resolved [88, 196] and spectrally-resolved [197] four-wave mixing (FWM) signals. These methods are based on measuring the FWM signal as a function of the delay between the excitation pulses; thus a 2D map correlating the time- or frequency-domain FWM signal with the pulse delay can be generated. There were two schools of thought regarding the temporal oscillations: either the beats originated from quantum interference between excitons or they were due to electromagnetic interference from two quantum-mechanically-uncoupled systems. Based on

a model in which the two effects could be distinguished by their temporal signatures, a conclusion was reached that the oscillations were indeed due to quantum interference, indicating that the transitions were coupled [88]. This problem was revisited using coherent excitation spectroscopy (CES), which relies on spectrally-resolving the FWM signal generated by a narrow bandwidth pulse preceding a second broad bandwidth pulse [198]. The FWM spectrum is recorded while the first pulse frequency is scanned, and peaks appear when the first pulse is in resonance with the optical transitions in the QW. The results from this experiment contradicted previous studies and claimed that the oscillations originated from the interference of the radiated fields of spatially-isolated excitons. 2D PL excitation spectra was developed for single QD spectroscopy, which provided information regarding incoherent energy transfer between GaAs IFQDs [29]. As in the context of NMR, "two-dimensional coherent spectroscopy" implies that the coherent phase evolution is preserved along two dimensions, either in the time domain so that a two-dimensional Fourier transform can be taken, or in the frequency domain. Therefore, these initial 2D studies of QWs and QDs, while elucidating some of the optical and electronic properties in semiconductors, are not considered 2DCS experiments since the 2D spectra are generated by incoherently stacking 1D spectra.

More recently, 2DCS has been implemented in the near-IR and optical regimes and has proven to be a powerful tool for unraveling the complex nonlinear optical response of semiconductors. In 2005, Borca *et al.* investigated the role of many-body effects and unbound electron-hole pairs on the nonlinear response of excitons in GaAs QWs [105]. Follow-up studies revealed that the dominant many-body interactions were excitation-induced dephasing and excitation-induced shift between excitons [106], and microscopic theories required Coulomb correlations beyond the Hartree-Fock mean field limit to reproduce the data [107]. 2D spectra particularly sensitive to many-body interactions revealed the role of mean-field interactions and higher-order Coulomb correlations on bound and unbound two-excitons in QWs [116, 199]. The power of 2DCS had not been extended to the study of QDs until recently. In the past few years, 2DCS has facilitated progress in our understanding of electronic properties [97], exciton dephasing and relaxation dynamics [98, 99], exciton-exciton

coherent coupling [100], $\chi^{(5)}$ optical nonlinearities [101], exciton-biexciton correlated broadening [102] and exciton fine-structure [103] in epitaxial and colloidal QDs.

3.2 Four-Wave Mixing

The dephasing dynamics in semiconductors typically occur on the timescale of picoseconds to tens of picoseconds, thus requiring ultrafast spectroscopic techniques to resolve them. Linear spectroscopy, for a limited number of cases, is sensitive to the dephasing rate; however the primary drawback of this technique is that it cannot distinguish between homogeneous and inhomogeneous broadening. This limitation is overcome using nonlinear techniques such as transient FWM and pump-probe spectroscopy, which can provide a measure of the homogeneous line width even in the presence of significant inhomogeneity. Nonlinear spectroscopic techniques require light with sufficient intensity such that the polarization induced in the sample can no longer be approximated as linearly-proportional to the incident electric field, but instead higher-power terms must be considered, i.e.,

$$P = \chi^{(1)} \cdot E + \chi^{(2)} \cdot E^2 + \chi^{(3)} \cdot E^3 + \cdots , \tag{3.1}$$

where P is the induced macroscopic polarization, E is the electric field of the incident light and $\chi^{(n)}$ is the n^{th}-order susceptibility. Equation 3.1 ignores the vector nature of E and P, which would require $\chi^{(n)}$ to have the form of an $n+1$ order tensor. The linear response of the system is approximated by truncating the series to include only the $\chi^{(1)}$ term, which determines the absorption and refractive index. For materials with inversion symmetry, the even orders of $\chi^{(n)}$ are zero, thus the lowest-order nonlinearity in these materials is due to the $\chi^{(3)}$ response. A material's $\chi^{(3)}$ response can be probed using transient FWM and pump-probe techniques for which two or three incident fields interact in the material to generate the nonlinear polarization. In the case of two fields, one of them acts twice. These techniques are most commonly applied in the time domain or a mixture of both time and frequency domains where, for example, the nonlinear signal

is spectrally-resolved while the pulse delay is varied.

In pump-probe experiments (often called transient absorption), a pump pulse injects a population that saturates a transition. A delayed probe pulse then experiences either reduced absorption at the same transition energy or can drive a stimulated emission process (both of which appear as a decrease in the absorption), or the probe can excite some of the population carriers to higher-lying states (which appears as an increase in absorption). The dynamics of these processes are mapped out by scanning the probe delay. As the population dynamics are measured, as opposed to the coherent dynamics, pump-probe is not considered coherent spectroscopy. This technique can still provide details about the coherent response by spectrally-resolving the differential probe signal, where the change in signal strength can arise from changes in the transition line width or energy and can provide a measure of the many-body interactions contributing to these phenomena.

The *coherent* nonlinear response can be probed using transient FWM techniques, of which there are many variations. In its most basic form, a FWM signal is generated through the nonlinear light-matter interaction using three pulses with similar frequency. The first pulse (A) incident on the sample, with wavevector $\mathbf{k}_{\mathrm{A}}$, induces a linear polarization, i.e. a coherent superposition between the ground and excited states. After a delay τ, the second pulse (B), with wavevector $\mathbf{k}_{\mathrm{B}}$, is incident on the sample and converts the polarization into a population. The population amplitude depends on the relative phase of the electric field of pulse B with respect to that of the polarization created by pulse A and varies across the sample at zero delay. The population is maximum when the two fields interfere constructively and is minimum where they interfere destructively, forming a dynamic population grating with an amplitude that varies across the sample with spatial period $\mathbf{k}_{\mathrm{B}} - \mathbf{k}_{\mathrm{A}}$. The third pulse ($C$) is incident on the sample with wavevector $\mathbf{k}_{\mathrm{C}}$ after a delay T with respect to pulse B. The polarization induced by this pulse scatters off the grating into the phase-matched direction $\mathbf{k}_{\mathrm{s}} = -\mathbf{k}_{\mathrm{A}} + \mathbf{k}_{\mathrm{B}} + \mathbf{k}_{\mathrm{C}}$, which is the FWM signal. In this case, detecting the signal along $\mathbf{k}_{\mathrm{s}}$ necessarily requires that pulse A acts as the conjugated pulse irrespective of time-ordering of the pulses.

The FWM signal depends on the pulse ordering and the pulse delays. The polarization gen-

erated by pulse A coherently evolves during the delay τ. Since the system is in a population state after pulses A and B are incident on the sample, incoherent population dynamics are associated with the delay T. Recording the FWM as either τ or T are varied thus provides essential information regarding coherent polarization dynamics or incoherent population relaxation and transfer dynamics. In a more complicated picture, additional processes in the sample can be probed, such as Raman-like coherences, and will contribute to the nonlinear FWM signal. Moreover, the pulse time ordering can be varied where, for example, pulse A is incident on the sample last. In this case, no FWM signal is expect to radiate along $\mathbf{k}_{\mathrm{s}}$ for a simple two-level system. This time ordering has been used to detect and study the influence of many-body interactions on the coherent nonlinear response [200]. A more complete description of the different pulse time orderings will be discussed in Section 3.6 in the context of 2DCS.

3.2.1 Types of FWM Experiments

A general FWM experimental setup is depicted in Fig. 3.1. The FWM signal is generated by three pulses with variable delays between the pulses, as described previously. The most common method to detect the signal is to record it on a slow detector for the integration of the signal intensity during the emission time, t. This time-integrated FWM (TI-FWM) signal is recorded while either the delay τ or T is varied and can be expressed as:

$$S_{\mathrm{TI}}(\tau, T) \propto \int_0^{+\infty} |P^{(3)}(\tau, T, t)|^2 dt, \tag{3.2}$$

where $P^{(3)}(\tau, T, t)$ is the macroscopic third-order polarization. For a homogeneously-broadened medium of independent two-level systems, in the approximation that the excitation pulses are infinitely short in time and in the Markovian limit, the TI-FWM signal has the form [201]

$$S_{\mathrm{TI}}(\tau, T) \propto \Theta(\tau)\,\Theta(T) \cdot e^{-2\gamma\tau} \cdot e^{-\Gamma_{gr}T}, \tag{3.3}$$

where $\Theta(x)$ is the Heaviside step function, γ is the homogeneous line width, and Γ_{gr} is the decay rate of the population grating visibility during T. The grating visibility is sensitive to population decay, spatial diffusion and spectral diffusion (which is often linked to spatial diffusion). The population decay rate and spatial diffusion can be distinguished by measuring, for example, the decay of the FWM signal with T for different angles between pulses A and B to measure the spatial diffusion coefficient.

If the system is inhomogeneously-broadened, the first-order polarization created by the first pulse will dephase more rapidly during τ than the homogeneous dephasing rate due to the oscillators in the ensemble having different resonance frequencies. If the first pulse is the conjugated pulse A, then the interactions of the second and third pulses with the system can reverse the phase evolution of the oscillators, resulting in rephasing of their polarizations during the time evolution after the third pulse. In this case, the FWM signal is emitted as a photon echo with a maximum amplitude at a time τ after the third pulse and a temporal duration inversely proportional to the inhomogeneous line width of the system. The TI-FWM signal of an inhomogeneously-broadened system for this pulse time-ordering has the form [201]

$$S_{\mathrm{TI}}(\tau, T) \propto \Theta(\tau)\,\Theta(T) \cdot e^{-4\gamma\tau} \cdot e^{-\Gamma_{gr}T}. \tag{3.4}$$

It is clear from Eqn. 3.4 that the signal decays with τ at a rate proportional to the homogeneous line width even in the presence of inhomogeneity. This aspect is one of the strengths of the FWM technique. However, in the case of moderate inhomogeneity where, for example, the homogeneous and inhomogeneous line widths are equal, the dephasing rate is ambiguously defined because the factor multiplying γ in Eqn. 3.3 and Eqn. 3.4 depends on the degree of inhomogeneity.

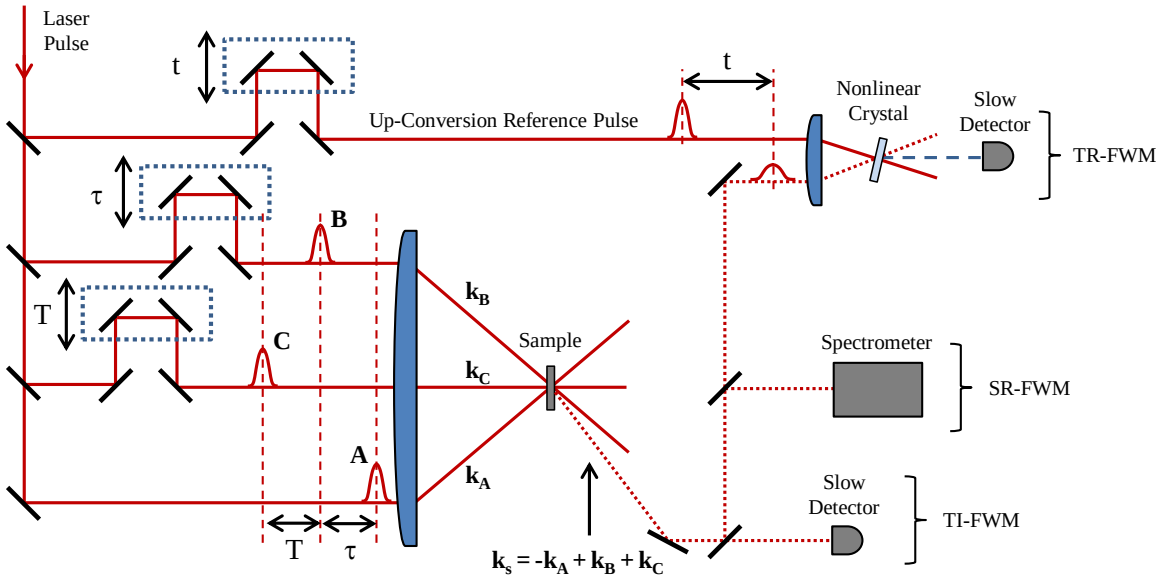

Figure 3.1: Schematic diagram of an experimental setup for time-integrated (TI), time-resolved (TR) and spectrally-resolved (SR) FWM signal detection.

Instead of using a slow detector to integrate the FWM signal, the signal can be measured via up-conversion with a reference pulse delayed by a time t in a nonlinear crystal to obtain the time-resolved FWM (TR-FWM) signal as a function of the emission time t. This signal can be expressed by:

$$S_{\mathrm{TR}}(\tau, T, t) \propto \int_{-\infty}^{+\infty} |P^{(3)}(\tau, T, t')|^2 \cdot |E_{ref}(t - t')|^2 dt', \tag{3.5}$$

where $E(t)$ is the reference pulse electric field. The FWM signal can also be measured by spectrally-dispersing the emitted field using a grating and detecting the different frequency components using a multi-channel CCD in a spectrometer (or using a slow detector and scanning the grating angle in a monochromator). The spectrally-resolved FWM (SR-FWM) signal has the form

$$S_{\mathrm{SR}}(\tau, T, \omega_t) \propto \int_{-\infty}^{+\infty} |P^{(3)}(\tau, T, t)|^2 e^{i\omega_t t} dt, \tag{3.6}$$

where ω_t is the emission frequency. Heterodyning the SR-FWM signal with a reference pulse enables measurement of the complex signal, i.e. with full phase information, for complete characterization

of the nonlinear signal. This is accomplished by interfering the FWM signal with a time-delayed reference pulse collinearly in a spectrometer. If the reference pulse amplitude and phase are well-characterized, then the FWM signal amplitude and phase can be extracted through Fourier analysis [202]. Details of this heterodyne technique will be presented in the following Chapter that discusses implementation of spectral interferometry for 2DCS.

3.3 Nonlinear Response Function

The macroscopic polarization induced by the nonlinear light-matter interaction is connected to the microscopic electronic couplings and dynamics in the sample through a multidimensional nonlinear response function [203]. In a three-pulse experiment, excitation pulses A, B and C are incident on the sample at absolute times t_{A}, t_{B} and t_{C}, respectively, so that the separation between pulses A and B is $\tau \equiv t_{\mathrm{B}} - t_{\mathrm{A}}$, between pulses C and B is $T \equiv t_{\mathrm{C}} - t_{\mathrm{B}}$, and the FWM signal is measured at a time $t = t_{\mathrm{s}}$ after pulse C (assuming $t_{\mathrm{A}} < t_{\mathrm{B}} < t_{\mathrm{C}}$). The pulse sequence and timing definitions are depicted in Fig. 3.2.

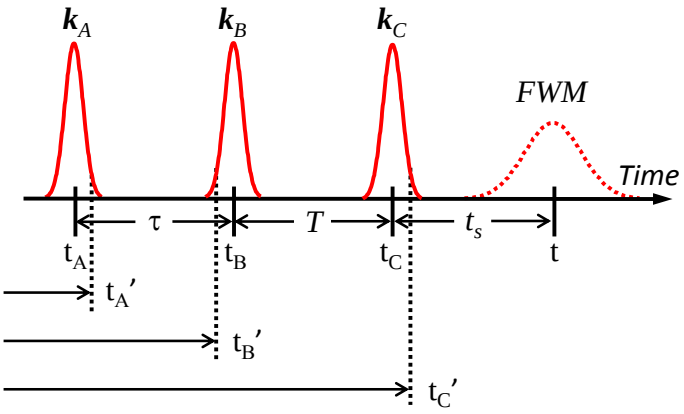

Figure 3.2: Excitation pulse sequence for three-pulse FWM experiments. Pulses with wavevectors $\mathbf{k}_{\mathrm{A}}$, $\mathbf{k}_{\mathrm{B}}$ and $\mathbf{k}_{\mathrm{C}}$ arrive at the sample as times t_{A}, t_{B} and t_{C}, respectively. Pulses A and B are separated by $\tau = t_{\mathrm{B}} - t_{\mathrm{A}}$, B and C by $T = t_{\mathrm{C}} - t_{\mathrm{B}}$, and the signal is measured at a time $t = t_{\mathrm{s}}$ after pulse C.

The electric field of each pulse is given by

$$\mathbf{E}_j(\mathbf{r},t) = [\varepsilon_j^+(t)\cdot e^{i(\mathbf{k}_j\cdot\mathbf{r}-\omega_j t)} + \varepsilon_j^-(t)\cdot e^{-i(\mathbf{k}_j\cdot\mathbf{r}-\omega_j t)}]\hat{\mathbf{e}}_j, \tag{3.7}$$

where $\mathbf{k}_j$, ω_j and $\hat{\mathbf{e}}_j$ are the wavevector, frequency and unit polarization vector of the j^{th} pulse ($j = A, B$ or C). $\varepsilon_j^+(t)$ ($\varepsilon_j^-(t)$) is the positive (negative) frequency component of the slowly-varying pulse envelope. Using this notation, the pulse sequence can be written as the sum of the three electric fields:

$$\mathbf{E}(\mathbf{r},t) = \sum_{j=A,B,C} \mathbf{E}_j(\mathbf{r}, t-t_j), \tag{3.8}$$

where pulse j arrives at the sample at time t_j. The total third-order polarization generated by the interaction of the three pulses in the material can be written as

$$\begin{aligned} P^{(3)}(\mathbf{r},t_\mathrm{A},t_\mathrm{B},t_\mathrm{C}) = \int_0^\infty\int_0^\infty\int_0^\infty \mathcal{R}^{(3)}(t_\mathrm{A}^{'},t_\mathrm{B}^{'},t_\mathrm{C}^{'})\cdot E_A(\mathbf{r},t_\mathrm{A}^{'}-t_\mathrm{A})E_B(\mathbf{r},t_\mathrm{B}^{'}-t_\mathrm{B}) \\ \times E_C(\mathbf{r},t_\mathrm{C}^{'}-t_\mathrm{C})\cdot dt_\mathrm{A}^{'}dt_\mathrm{B}^{'}dt_\mathrm{C}^{'}, \end{aligned} \tag{3.9}$$

where $\mathcal{R}^{(3)}$ is the third-order time-dependent response function of the system and $t_\mathrm{j}^{'}$ is the integration variable associated with pulse j. The n^{th} order response function $\mathcal{R}^{(n)}$ is calculated using time-dependent perturbation theory and can be expressed as a combination of $(n+1)^{th}$-order correlations of the dipole moment operator [204]. In general, a sum-over states expression for $\mathcal{R}^{(3)}$ can be derived for an arbitrary system.

In the limit of impulsive excitation, where the pulse envelope duration is short compared to the system dynamics and pulse delays, each pulse can be approximated as a Dirac delta function pulse in time. In this case, Eqn. 3.9 can be analytically evaluated and has the following form:

$$\begin{aligned} P^{(3)}(\mathbf{r},t,t_\mathrm{A},t_\mathrm{B},t_\mathrm{C}) = \mathcal{R}^{(3)}(t_\mathrm{A},t_\mathrm{B},t_\mathrm{C})\cdot\varepsilon_A^{\pm}\varepsilon_B^{\pm}\varepsilon_C^{\pm}\cdot e^{i(\pm\mathbf{k}_A\pm\mathbf{k}_B\pm\mathbf{k}_C)\cdot\mathbf{r}}\cdot e^{-i(\pm\omega_A\pm\omega_B\pm\omega_C)\cdot t} \\ \times e^{i(\pm\omega_A\pm\omega_B\pm\omega_C)\cdot t_\mathrm{C}}\cdot e^{i(\pm\omega_A\pm\omega_B)\cdot t_\mathrm{B}}\cdot e^{i(\pm\omega_A)\cdot t_\mathrm{A}}. \end{aligned} \tag{3.10}$$

Equation 3.10 includes all possible commutations of pulses A, B and C nonlinearly interacting in the sample. Each contribution produces a distinct FWM signal that radiates in the corresponding phase-matched direction $\mathbf{k}_{\mathrm{s}} = \pm\mathbf{k}_A \pm \mathbf{k}_B \pm \mathbf{k}_C$ after inserting $P^{(3)}$ into Maxwell's equations as a source term. Signals will emit in the phase-matched direction only if the sample size is larger than the wavelength of the excitation pulses and emitted signal; otherwise, a population grating cannot form across the sample and the signal will emit isotropically. Of the eight possible wavevectors for $\mathbf{k}_{\mathrm{s}}$, only four are independent, since $\mathbf{k}_{\mathrm{s}} = -\mathbf{k}_{\mathrm{s}}$ corresponds to the complex conjugate of $P^{(3)}$ and does not represent a unique physical process. The signal wavevector can then assume any of the four phase-matching values: $\mathbf{k}_{\mathrm{s,I}} = -\mathbf{k}_{\mathrm{A}} + \mathbf{k}_{\mathrm{B}} + \mathbf{k}_{\mathrm{C}}$, $\mathbf{k}_{\mathrm{s,II}} = \mathbf{k}_{\mathrm{A}} - \mathbf{k}_{\mathrm{B}} + \mathbf{k}_{\mathrm{C}}$, $\mathbf{k}_{\mathrm{s,III}} = \mathbf{k}_{\mathrm{A}} + \mathbf{k}_{\mathrm{B}} - \mathbf{k}_{\mathrm{C}}$ and $\mathbf{k}_{\mathrm{s,IV}} = \mathbf{k}_{\mathrm{A}} + \mathbf{k}_{\mathrm{B}} + \mathbf{k}_{\mathrm{C}}$.

For a given pulse time ordering, different physical processes in the sample will radiate along the different $\mathbf{k}_{\mathrm{s,j}}$ (where $j = I, II, III$ or IV). For example, if pulse A is incident on the sample first, followed by pulse B and then pulse C, the signal radiated along $\mathbf{k}_{\mathrm{s,I}}$ corresponds to the rephasing signal for which a photon echo is emitted from an inhomogeneously-broadened system at a time τ after pulse C. For this same pulse time-ordering, no signal is expected to radiate along the $\mathbf{k}_{\mathrm{s,III}}$ direction from a simple two-level system; the appearance of a signal along this direction for this pulse time ordering has been attributed to many-body interactions in the sample. One could probe the entire third-order nonlinear response by recording the FWM signal along all $\mathbf{k}_{\mathrm{s,j}}$'s. While this is rather straightforward for a two-pulse experiment, for two directions, recording all the signals is technically challenging and often not possible nor necessary (because they won't provide new information) for three-pulse experiments. Alternatively, the FWM signal can be measured along a single $\mathbf{k}_{\mathrm{s,j}}$, and multiple experiments using different time-orderings can be performed to probe different physical processes in the sample. The third-order polarization associated with the different pulse time-orderings can be obtained from a sum-over-states expression for the nonlinear response function. The response functions can be intuitively understood using a diagrammatic approach consisting of double-sided Feynman diagrams that represent the various coherent pathways. Before connecting the nonlinear response function to the diagrams, which are described in Section 3.5,

the optical Bloch equation formalism will first be reviewed in the next Section. The optical Bloch equations will aid in understanding how to construct and interpret the Feynman diagrams from an n^{th} order perturbative expansion of the equations of motion for the density matrix.

3.4 Optical Bloch Equation Formalism

The optical Bloch equations (OBEs) are convenient for interpreting the coherent nonlinear optical response of the light-matter interaction. They are more accurately applied to model atomic systems, where the energy structure is well characterized by a few atomic transitions [205]. For semiconductors, in which many-body effects (MBEs) often dominate the coherent nonlinear response, the OBEs encounter difficulties. To account for MBEs, the OBEs can be modified phenomenologically to incorporate different effects such as excitation-induced dephasing (EID), excitation-induced shift (EIS) and local field corrections (LFC) [92]. While phenomenological few-level models are often used because of their relatively easy implementation, significant progress has been made in the development of fundamental microscopic theory for semiconductors using density matrices as well as non-equilibrium Green's functions, which can account for Coulomb interactions between electrons and holes [203, 206, 207, 208]. Nonetheless, the basic form of the OBEs without modifications can help develop an intuitive understanding and interpretation of the 2DCS experiments. For a review and numerical analysis of the modified OBEs with MBEs, see Ref. [92].

3.4.1 Density Matrix and the Equation of Motion

The OBEs are derived using the density matrix formalism. The density matrix is useful for describing a quantum system of mixed states, that is, a statistical ensemble of pure states. Suppose a system may be found in state $|\psi_1\rangle$ with probability p_1, state $|\psi_2\rangle$ with probability p_2, and so forth, where $0 \leq p_n \leq 1$, $\sum_n p_n = 1$ and the $|\psi_n\rangle$'s are linear combinations of the pure basis states of the system, $|\phi_i\rangle$. The density matrix operator is then defined as [205]

$$\hat{\rho}(t) \equiv \sum_n p_n \cdot |\psi_n(t)\rangle\langle\psi_n(t)|, \tag{3.11}$$

where $|\psi_n(t)\rangle$ is the time-dependent wave function of state n with probability p_n. In terms of the eigenstates of the system, $|\psi_n(t)\rangle$ can be written as

$$|\psi_n(t)\rangle = \sum_i c_i(t)|\phi_i\rangle, \tag{3.12}$$

where $c_i(t)$ is the time-dependent coefficient for state $|\phi_i\rangle$. For a given state $|\psi_n(t)\rangle$, the elements of the density matrix, $\rho_{ij} = c_i(t) \cdot c_j^*(t)$, give the probability of the system being in a particular quantum state. The diagonal elements, $\rho_{ii} = |c_i(t)|^2$, give the probability of the system being in an eigenstate i, thus they are referred to as the population density. The off-diagonal elements, ρ_{ij} $(i \neq j)$, describe the probability to be in a coherent superposition (polarization) between states i and j. As an example, consider a single two-level system with ground state $|1\rangle$ and excited state $|2\rangle$. Suppose the wavefunction of the system has the form $|\psi(t)\rangle = c_1(t)|1\rangle + c_2(t)|2\rangle$. The density matrix is then given by:

$$\rho = \begin{pmatrix} \rho_{11} & \rho_{12} \\ \rho_{21} & \rho_{22} \end{pmatrix} = \begin{pmatrix} c_1c_1^* & c_1c_2^* \\ c_2c_1^* & c_2c_2^* \end{pmatrix}. \tag{3.13}$$

The diagonal element $\rho_{11} = |c_1|^2$ ($\rho_{22} = |c_2|^2$) is the population density of the ground state (excited state). The off-diagonal element $\rho_{12} = c_1c_2^* = \rho_{21}^*$ describes the coherence of the system. When considering an ensemble of independent two-level systems, the total system can be described using a summation of the pure case density matrices, given by Eqn. 3.13, weighted by the probability, p_n, of each individual system. The expectation value of any observable variable of the system can be expressed using the density matrix operator. For example, the expectation of the polarization operator $\hat{P}$ is given by:

$$\langle\hat{P}\rangle = \langle\psi(t)|\hat{P}|\psi(t)\rangle = \mathcal{T}r(P\rho(t)), \tag{3.14}$$

where $\mathcal{T}r$ represents the trace of an operator, i.e. the sum the operator's diagonal elements. For a system which can be described by a statistical ensemble of pure quantum states, the time dependence of the expectation value of the polarization is governed by the time evolution of the density matrix operator. Thus simulating the nonlinear response of a simple system amounts to analyzing the equations of motion for the density matrix. The equations of motion can be derived from the Schrödinger equation of the wavefunction and are given by:

$$\dot{\rho} = \frac{-i}{\hbar}[H, \rho], \tag{3.15}$$

where $[H, \rho] = H \cdot \rho - \rho \cdot H$. As currently written, Eqn. 3.15 does not include any relaxation or dephasing parameters. They can be added phenomenologically, resulting in a modified equation of motion whose matrix elements are [209]:

$$\dot{\rho}_{ij} = \frac{-i}{\hbar}\sum_{k}(H_{ik}\rho_{kj} - \rho_{ik}H_{kj}) - \Gamma_{ij}\rho_{ij}, \tag{3.16}$$

where $\Gamma_{ij} = (1/2)(\gamma_i + \gamma_j) + \gamma_{ij}^{ph}$, γ_i (γ_j) is the decay rate of state i (j) and γ_{ij}^{ph} is the coherence pure dephasing rate ($\gamma_{ij}^{ph} = 0$ for $i = j$). For a simple two-level system, the Hamiltonian is given by

$$H = H_0 + H_I = \begin{pmatrix} \hbar\omega_1 & V_{12} \\ V_{21} & \hbar\omega_2 \end{pmatrix}, \tag{3.17}$$

where H_0 is the free-particle Hamiltonian with eigenenergies $\hbar\omega_1$ and $\hbar\omega_2$ for states $|1\rangle$ and $|2\rangle$, respectively. The light-matter interaction Hamiltonian, under the dipole approximation, is given by $H_I = -\mu \cdot E(t)$. Only off-diagonal elements of H_I are nonzero due to parity of the eigenstates. Inserting H into the equation of motion for ρ gives a set of equations that describe the time evolution of the density matrix, commonly referred to as the OBEs. The OBEs are written as

$$\begin{aligned}
\dot{\rho}_{11} &= -\gamma_1 \cdot \rho_{11} + \frac{i}{\hbar} \cdot \mu_{12} E(t) \cdot (\rho_{12} - \rho_{21}) \\
\dot{\rho}_{22} &= -\gamma_2 \cdot \rho_{22} - \frac{i}{\hbar} \cdot \mu_{12} E(t) \cdot (\rho_{12} - \rho_{21}) \\
\dot{\rho}_{12} &= -\Gamma_{12} \cdot \rho_{12} + i\omega_0 \rho_{12} - \frac{i}{\hbar} \cdot \mu_{12} E(t) \cdot (\rho_{22} - \rho_{11}),
\end{aligned} \tag{3.18}$$

where $\omega_0 = (1/\hbar) \cdot (E_2 - E_1)$. Equation 3.18 can be used to describe coherent light-matter interactions in atomic systems. In order to account for MBEs in semiconductors, the equations are modified to include phenomenological terms for EID, EIS and LFC. In order to model these phenomena correctly, the modified OBEs need to be numerically solved. For the purpose of providing an intuitive understanding of 2DCS, however, these modifications are neglected. The equations of motion for the density matrix can be solved perturbatively in the limit of weak electric fields that are Dirac delta function pulses in time. Perturbation theory provides analytical solutions that will help to understand the relation between the light-matter interaction and the coherent nonlinear response in FWM experiments. The OBEs can be perturbatively solved by expanding them in terms of the Rabi frequency, $\Omega \equiv (\mu_{12} \cdot E)/\hbar$:

$$\begin{aligned}
\Omega &\rightarrow \alpha\Omega \\
\rho_{ij} &= \rho_{ij}^{(0)} + \alpha\rho_{ij}^{(1)} + \alpha^2\rho_{ij}^{(2)} + \cdots,
\end{aligned} \tag{3.19}$$

where α is assumed to be a small dimensionless parameter. These forms for Ω and ρ_{ij} are inserted into Eqn. 3.18 and equal powers of the coefficients α^n are collected. If we write the electric field as $E(t) = \hat{E}(t)\exp(-i\omega t) + \hat{E}^*(t)\exp(i\omega t)$ and $\rho_{ij}(t) = \hat{\rho_{ij}}(t)\exp(-i\omega t)$ for $i \neq j$, then the general expression for the n^{th}-order equation of motion for the density matrix, in the rotating wave approximation, is given by

$$\dot{\rho}_{ij}^{(n)} = -i\Delta_{ij} \cdot \rho_{ij}^{(n)} + \frac{i\mu}{2\hbar} \cdot \hat{E}(t) \cdot \rho_{kl}^{(n-1)}, \tag{3.20}$$

where $\Delta_{ij} \equiv \omega_i - \omega_j - i\Gamma_{ij}$. From this expression it becomes clear that the interaction of the

light field with the system increases the order of perturbation from $n-1$ to n. Furthermore, contributions to the polarization arise at odd orders of the applied field, whereas new contributions to the population arise at even orders. These two points are demonstrated in Fig. 3.3, where each arrow corresponds to a single interaction of the field with the system. Equation 3.20 can be integrated to give a general form for the n^{th}-order density matrix component $\rho_{ij}^{(n)}$. A diagrammatic approach using double-sided Feynman diagrams is useful for tracking the different orders of the density matrix and is introduced in the following Section.

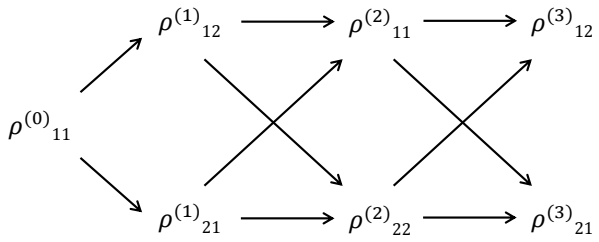

Figure 3.3: Schematic diagram representing the increase in perturbation order n with each light-matter field interaction. Even orders of the applied field produce populations, whereas odd orders generate polarizations.

3.5 OBEs Made Easy: Double-Sided Feynman Diagrams

In perturbation theory, the evolution of the density matrix elements can be tracked using double-sided Feynman diagrams. Each diagram corresponds to a coherent pathway in Liouville space. The diagrams are constructed by drawing vertical lines to track the "bra" and "ket" that form the density matrix operator, as depicted in Fig. 3.4. The left line represents the "ket" and the right line the "bra", with time increasing vertically upward. The incident light field is represented by the arrow, and the interaction of the field with the system is indicated by the vertex of the arrow with either the left or right vertical line. The light field interaction changes the density matrix state from $|i\rangle$ to $|j\rangle$. An arrow pointing to the right implies the light field has the form $E_j \cdot \exp(i\mathbf{k}_j \cdot \mathbf{r} - i\omega_j t)$, while an arrow pointing to the left means the light field contribution is

conjugated, with the form $E_j^* \cdot \exp(-i\mathbf{k}_j \cdot \mathbf{r} + i\omega_j t)$. An arrow pointing towards (away from) the vertical lines indicates absorption (emission) of a photon, driving the system from a lower (higher) energy state to a higher (lower) energy state. Thus the interaction of a field with amplitude E_j (E_j^*) with the "ket" state corresponds to an absorption (emission) process (the opposite is true for the "bra" state).

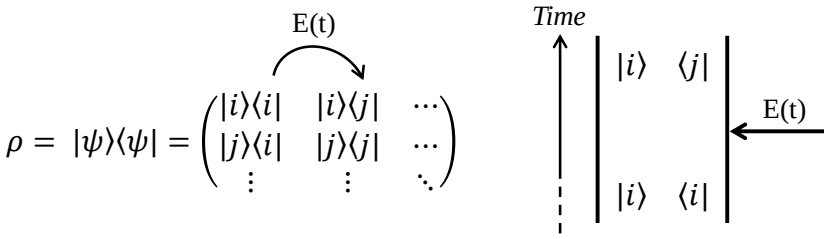

Figure 3.4: The light-matter field interaction changes either the "bra" or "ket" state of the density matrix. The double-sided Feynman diagram is shown for a conjugated field that interacts with the system in a population state i to induce a polarization between states i and j.

In the example given in Fig. 3.4, the time evolution of the density matrix element $\rho_{ij}^{(n)} = |i\rangle\langle j|$ depends on $\rho_{ii}^{(n-1)}$, the energy separation and dipole moment between states $|i\rangle$ and $|j\rangle$, the decay and dephasing rates, and the applied electric field as indicated in Eqn. 3.20. This equation can be integrated to give the n^{th}-order density matrix element and is shown in Fig. 3.5 for the four possible vertex types.

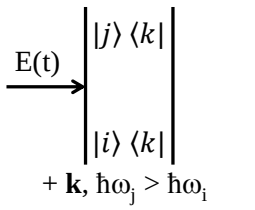

$$\rho_{jk}^{(n)} = \frac{i\mu}{2\hbar} e^{ik_n x} \int_{-\infty}^{t} \hat{E}_n(t')\, e^{-i\omega_n t'} e^{-i\Delta_{jk}(t-t')} \times \rho_{ik}^{(n-1)}(t')\, dt'$$

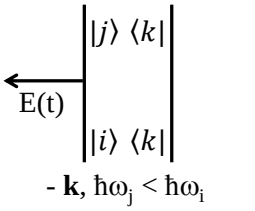

$$\rho_{jk}^{(n)} = \frac{i\mu}{2\hbar} e^{-ik_n x} \int_{-\infty}^{t} \hat{E}_n^{*}(t')\, e^{i\omega_n t'} e^{-i\Delta_{jk}(t-t')} \times \rho_{ik}^{(n-1)}(t')\, dt'$$

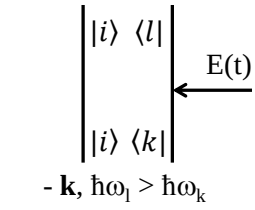

$$\rho_{il}^{(n)} = \frac{-i\mu}{2\hbar} e^{-ik_n x} \int_{-\infty}^{t} \hat{E}_n^{*}(t')\, e^{i\omega_n t'} e^{-i\Delta_{il}(t-t')} \times \rho_{ik}^{(n-1)}(t')\, dt'$$

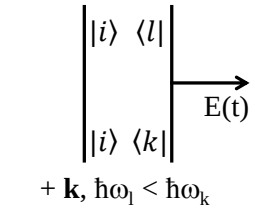

$$\rho_{il}^{(n)} = \frac{-i\mu}{2\hbar} e^{ik_n x} \int_{-\infty}^{t} \hat{E}_n(t')\, e^{-i\omega_n t'} e^{-i\Delta_{il}(t-t')} \times \rho_{ik}^{(n-1)}(t')\, dt'$$

Figure 3.5: The four possible double-sided Feynman diagram vertices and their corresponding integrals for calculating the density matrix elements.

Each order in the perturbation expansion can be characterized by a diagram containing one vertex, and n such diagrams are concatenated vertically in time to produce a diagram for the n^{th}-order component of the density matrix. The overall wavevector of the diagram is the sum of the individual wavevectors for each vertex. The sign of the diagram is $(-1)^m$, where m is the number of vertices on the right vertical line, since each interaction with the "bra" introduces a minus sign. The n^{th}-order component can be calculated using the integrals in Fig. 3.5. Calculating $\rho_{ij}^{(3)}$, for example, requires performing a triple integral over the applied field and previous orders of the density matrix. From the double-sided Feynman diagram, one can directly write down the mathematical form of the nonlinear response function using an appropriate set of translation

rules [204]. Once all Feynman diagrams for a particular phase-matched direction and pulse time-ordering are determined, the sum-over-states expression for the total nonlinear response can be obtained from the diagrams.

To illustrate how the double-sided Feynman diagrams can easily lead to a sum-over-states expression for $\mathcal{R}^{(3)}$, consider a system with a single ground state $|g\rangle$, singly-excited states $|e\rangle$ and $|e^{'}\rangle$, and doubly-excited state $|f\rangle$, which represents the QD system with two bright exciton states and a doubly-excited biexciton state presented in Chapter 2. When only considering the signal radiated along $\mathbf{k}_{\mathrm{s}} = -\mathbf{k}_{\mathrm{A}} + \mathbf{k}_{\mathrm{B}} + \mathbf{k}_{\mathrm{C}}$ and limiting the pulse sequence to the rephasing time ordering for which the conjugated pulse A arrives at the sample first, we can write three general double-sided Feynman diagrams, shown in Fig. 3.6.

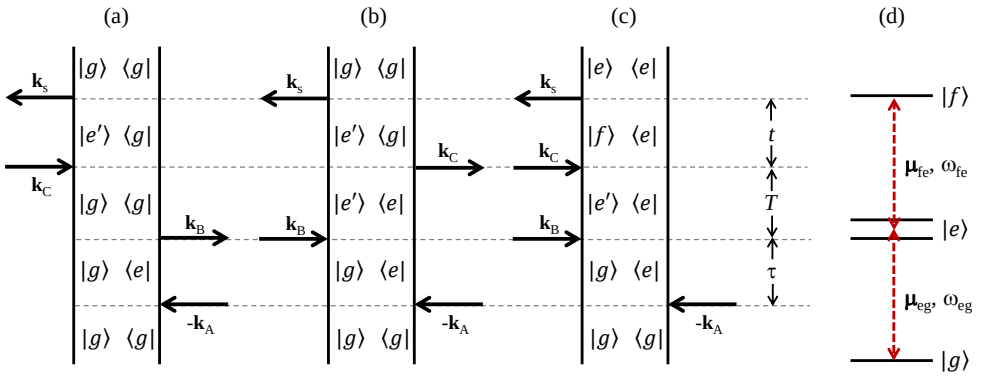

Figure 3.6: (a)-(c) Double-sided Feynman diagrams relevant for the FWM signal radiated along $\mathbf{k}_{\mathrm{s}} = -\mathbf{k}_{\mathrm{A}} + \mathbf{k}_{\mathrm{B}} + \mathbf{k}_{\mathrm{C}}$ for the rephasing pulse time ordering in which the conjugated pulse A arrives first. (d) The energy level scheme consists of a ground state, $|g\rangle$, singly-excited states, $|e\rangle$, and doubly-excited states $|f\rangle$.

The diagrams in Fig. 3.6 describe the processes of ground-state bleaching (a), excited-state emission (b) and excited-state absorption (c) [203]. For example, for the excited-state emission process in (b), the conjugated field A with wavevector $-\mathbf{k}_{\mathrm{A}}$ excites the "bra" from state $|g\rangle$ to state $|e\rangle$, inducing a polarization between these states. After a time τ, field B with wavevector

$\mathbf{k}_{\mathrm{B}}$ acts on the "ket" to induce a polarization between states $|g\rangle$ and $|e^{'}\rangle$, which places the system into a coherent superposition between states $|e^{'}\rangle$ and $|e\rangle$ during T. If $|e^{'}\rangle = |e\rangle$, then the frequency associated with this coherence is zero, and the system is instead in a population state of $|e\rangle$. After the delay T, field C with wavevector $\mathbf{k}_{\mathrm{C}}$ acts on the "bra" to drive it from state $|e\rangle$ to state $|g\rangle$. The system remains in a coherent superposition between states $|e^{'}\rangle$ and $|g\rangle$ during t. This coherent pathway is one contribution to the macroscopic polarization that will radiate as the FWM signal in the phase-matched direction $\mathbf{k}_{\mathrm{s}}$. From the three diagrams in Fig. 3.6, all the possible coherent pathways for the rephasing time ordering can be summed to obtain an expression for the nonlinear response function $\mathcal{R}^{(3)}$, which is given by [204]:

$$\begin{aligned}\mathcal{R}^{(3)} = \left(\frac{i}{\hbar}\right)^3 [& \\ & \sum_{e,e^{'}} (\boldsymbol{\mu}_{ge}\cdot\hat{\boldsymbol{e}}_1)(\boldsymbol{\mu}_{eg}\cdot\hat{\boldsymbol{e}}_2)(\boldsymbol{\mu}_{ge^{'}}\cdot\hat{\boldsymbol{e}}_3)(\boldsymbol{\mu}_{e^{'}g}\cdot\hat{\boldsymbol{e}}_4) e^{(i\omega_{eg}-\Gamma_{eg})\tau} e^{-\Gamma_{gg}T} e^{-(i\omega_{e^{'}g}+\Gamma_{e^{'}g})t} \\ & + \sum_{e,e^{'}} (\boldsymbol{\mu}_{ge}\cdot\hat{\boldsymbol{e}}_1)(\boldsymbol{\mu}_{ge^{'}}\cdot\hat{\boldsymbol{e}}_2)(\boldsymbol{\mu}_{eg}\cdot\hat{\boldsymbol{e}}_3)(\boldsymbol{\mu}_{e^{'}g}\cdot\hat{\boldsymbol{e}}_4) e^{(i\omega_{eg}-\Gamma_{eg})\tau} e^{-(i\omega_{e^{'}e}+\Gamma_{e^{'}e})T} e^{-(i\omega_{e^{'}g}+\Gamma_{e^{'}g})t} \\ & + \sum_{e,e^{'},f} (\boldsymbol{\mu}_{ge}\cdot\hat{\boldsymbol{e}}_1)(\boldsymbol{\mu}_{ge^{'}}\cdot\hat{\boldsymbol{e}}_2)(\boldsymbol{\mu}_{e^{'}f}\cdot\hat{\boldsymbol{e}}_3)(\boldsymbol{\mu}_{fe}\cdot\hat{\boldsymbol{e}}_4) e^{(i\omega_{eg}-\Gamma_{eg})\tau} e^{-(i\omega_{e^{'}e}+\Gamma_{e^{'}e})T} e^{-(i\omega_{fe}+\Gamma_{fe})t}],\end{aligned} \tag{3.21}$$

where $\boldsymbol{\mu}_{ij}$, $\omega_{ij} \equiv \omega_i - \omega_j$, and Γ_{ij} are the dipole moment, transition frequency and decay rate, respectively, of the transition $i \rightarrow j$. The result in Eqn. 3.21 can be inserted into Eqn. 3.10 to determine the total macroscopic polarization of the system, $P^{(3)}(\tau, T, t)$. The radiated FWM field can then be calculated by inserting the polarization into Maxwell's equations as a source term. These steps result in a simple expression that connects the spectrally-resolved emission to the macroscopic polarization, which is given by [210]:

$$E(\tau, T, \omega_t) = \frac{L}{2n(\omega_t)c\epsilon_0} i\omega_t P^{(3)}(\tau, T, \omega_t), \tag{3.22}$$

where L is the sample thickness, $n(\omega_t)$ is the frequency-dependent refractive index, c is the speed of

light and ϵ_0 is the vacuum permittivity. Equation 3.22 is valid only if absorption and propagation effects in the sample can be ignored.

3.6 2D Spectroscopy

Optical 2DCS is an enhanced version of transient FWM, in which the pulse delays are stepped with interferometric precision and the FWM complex field is measured through spectrally-resolved heterodyne detection. The technical details and challenges of implementing 2DCS are discussed in the next Chapter. In this Section, the principles of the technique are discussed and an intuitive description of the different types of 2D spectra is provided using the Feynman diagrams described in the previous Section.

2DCS based on three-pulse FWM can be experimentally implemented using a number of different methods, with the most common utilizing passive phase-stabilization of the pulse delays through common-path optics [211, 212, 213], pulse-shaping methods [214, 215], non-interferometric spectral intensity measurements [216], spectral phase calibration procedures [210] and active phase-stabilization using a reference laser and feedback electronics [104, 217]. For each of these variations, the geometric position and wavevectors of the pulses can be different, with perhaps the most common (and the one employed in the experiments discussed in this thesis) being the box geometry, depicted in Fig. 3.7(a). Three excitation pulses propagate along three corners of a square and are focused onto the sample with wavevectors $\mathbf{k}_\mathrm{A}$, $\mathbf{k}_\mathrm{B}$ and $\mathbf{k}_\mathrm{C}$. The third-order polarization, $P^{(3)}(\tau, T, t)$, generated by the nonlinear interaction of the three pulses in the sample radiates the FWM field that is detected in the phase-matched direction $\mathbf{k}_\mathrm{s} = -\mathbf{k}_\mathrm{A} + \mathbf{k}_\mathrm{B} + \mathbf{k}_\mathrm{C}$. Figure 3.7(c) shows the FWM and excitation beam spots on the collimating lens as viewed when looking towards the sample. The time ordering of the excitation pulses is shown in Fig. 3.7(b), where the delay between the first two pulses is τ, between the second and third pulses is T, and the signal is emitted during t.

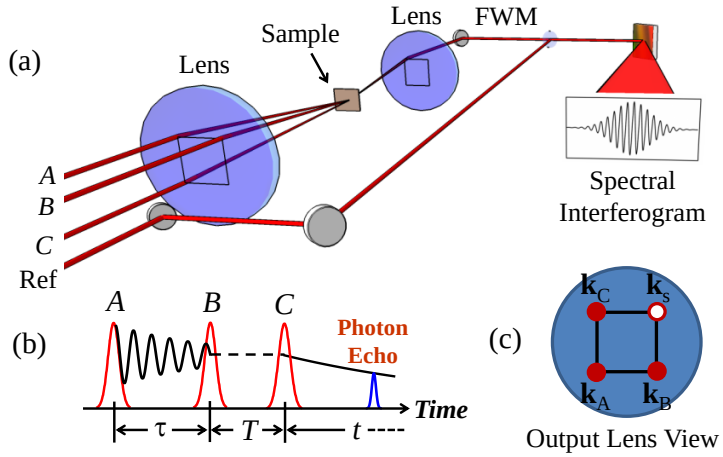

Figure 3.7: (a) Schematic of the excitation pulses propagating in the box geometry. The FWM signal is emitted in the phase-matched direction, $\mathbf{k}_s$. (b) Time ordering of the excitation pulses. (c) The FWM signal and excitation beam spots on the output lens as viewed looking towards the sample.

The FWM signal is measured by interfering it with a delayed reference pulse on a beam splitter, and their interference is spectrally-resolved using a spectrometer and multi-channel CCD. The FWM complex field is extracted using a simple algorithm that is discussed in the next Chapter. In standard 2DCS experiments, the electric field of the emitted FWM signal is presented as a 2D spectrum for which any two signal frequencies associated with the time delays are correlated. A 2D spectrum can be obtained from the emitted signal field, $E(\tau, T, t)$, by recording spectral interferograms while stepping one of the delays and taking a Fourier transform with respect to this delay. Since the Fourier transform with respect to t is implicit in the spectrally-resolved detection method, a Fourier transform with respect to τ produces a 2D spectrum with amplitude and phase characterized by

$$S(\omega_\tau, T, \omega_t) = \int_{-\infty}^{+\infty} E(\tau, T, \omega_t) e^{i\omega_\tau \tau} d\tau \tag{3.23}$$

for a fixed value of T. Similarly, if T is stepped for a fixed τ, the 2D spectrum is characterized by a complex amplitude $S(t, \omega_T, \omega_t)$. Using the relations between the nonlinear response function and

the radiated FWM field discussed in the previous Section, a 2D spectrum can be analyzed using the sum-over-states expressions for $\mathcal{R}^{(3)}$.

3.6.1 Types of 2D Spectra

Different microscopic processes in the sample can be probed by measuring the FWM signal along the phase-matched direction $\mathbf{k}_s$ for different permutations of the pulse time ordering, which are shown in Fig. 3.8. For each pulse sequence, a Fourier transform of the signal is taken with respect to two of the time delays, which are indicated by the labels "Axis 1" and "Axis 2".

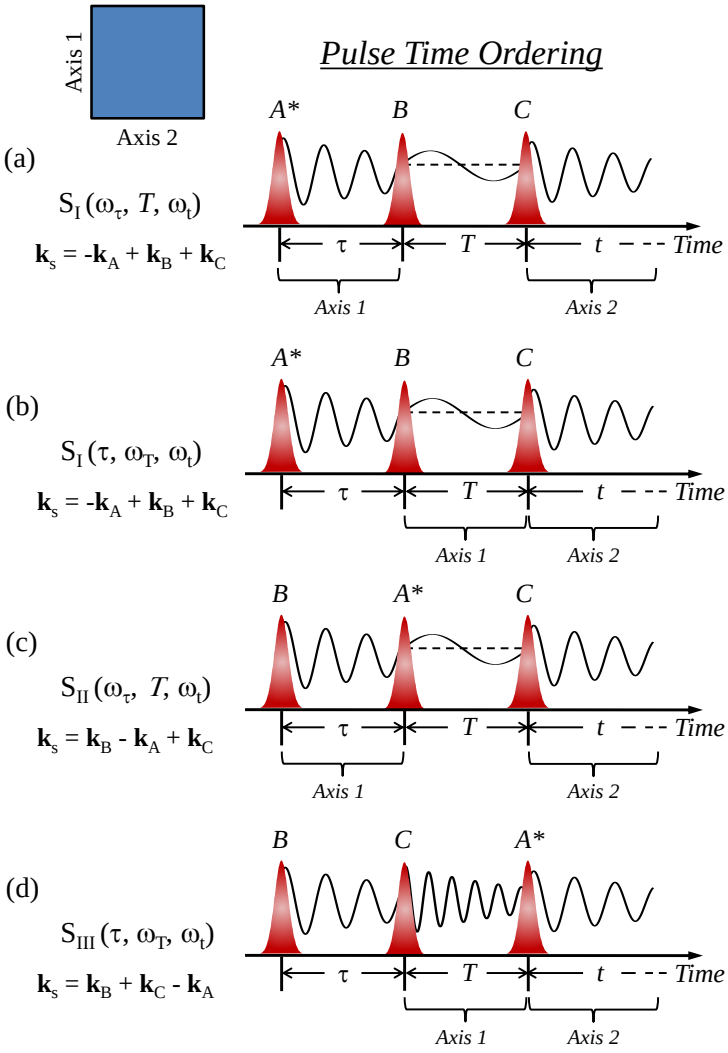

Figure 3.8: Schematic diagrams of the excitation pulse time ordering available for optical 2DCS three-pulse experiments. The rephasing pulse sequence is depicted in (a), where the conjugated pulse A is incident on the sample first, and the signal if Fourier-transformed with respect to τ and t. (b) is a variant of the sequence in (a), where instead the delay T is scanned to probe population dynamics and Raman-like coherences. The non-rephasing pulse sequence is depicted in (c), where the conjugated pulse comes second. (d) The two-quantum pulse sequence, where the conjugated pulse arrives last, is sensitive to many-body interactions. In each case, the signal is Fourier-transformed with respect to axes 1 and 2 to produce the corresponding 2D spectrum.

2D spectra for different excitation sequences are presented in this sub-Section for the four-

level energy scheme shown in Fig. 3.9, which consists of a ground state ($|g\rangle$), two singly-excited exciton states ($|H\rangle$ and $|V\rangle$) and a doubly-excited biexciton state $|B\rangle$. As mentioned in the previous Chapter, this energy scheme is relevant for the epitaxial QDs discussed in this thesis; therefore the analysis in this sub-Section will aid in interpreting the results presented in later Chapters.

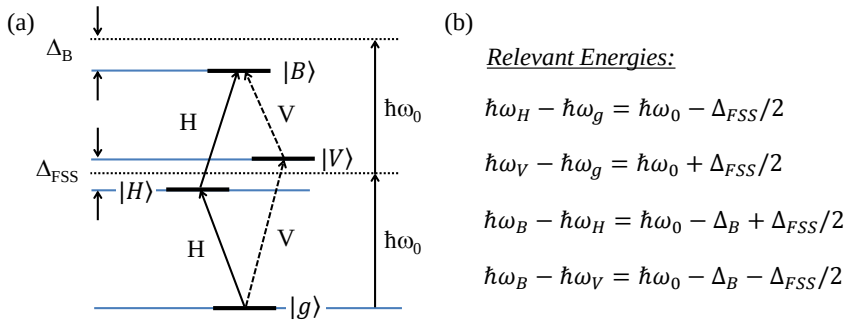

Figure 3.9: (a) The relevant energy level scheme used to model the nonlinear response from epitaxial QDs, consisting of the a ground state, $|g\rangle$, two singly-excited exciton states, $|H\rangle$ and $|V\rangle$, separated by the fine-structure splitting energy Δ_{FSS}, and a doubly-excited biexciton state $|B\rangle$ with binding energy Δ_B. The corresponding energies are indicated in (b).

As discussed in detail in Chapter 2, the four-level energy diagram in Fig. 3.9 is equivalent to two independent two-level systems if $\Delta_B = 0$. For the ensuing discussions, we consider nonzero Δ_{FSS} and Δ_B and follow the dipole transition selection rules as indicated in Fig. 3.9. The corresponding pulse sequence is indicated for each type of spectrum. The coherent pathways contributing to the 2D spectra are derived from the double-sided Feynman diagrams discussed in the previous Section. The spectra are calculated using the sum-over-states expressions for $\mathcal{R}^{(3)}$ for zero inhomogeneity so that the coherent pathways are more clearly resolved. The dipole moments for all transitions are equal to unity, all population relaxation rates are $\Gamma_{ii} = 0.05$ meV and all homogeneous line widths are $\Gamma_{ij} = 0.1$ meV. Typically for epitaxial QDs, $\Delta_B \gg \Delta_{FSS}$, which would result in most of the coherent pathways overlapping spectrally; thus for demonstration purposes we set $\Delta_{FSS} = 2$ meV and $\Delta_B = 3$ meV.

3.6.1.1 Rephasing One-Quantum Spectrum (S1)

A rephasing one-quantum spectrum $S_I(\omega_\tau, T, \omega_t)$ is generated using the pulse time ordering shown in Fig. 3.8(a) (the index i in S_i indicates the arrival order of the conjugated pulse A relative to the other pulses). The FWM signal is recorded while the delay τ between the first pulse A and pulse B is scanned and the delay T between pulses B and C is held fixed. The FWM signal field $E(\tau, T, \omega_t)$ is Fourier-transformed with respect to τ to generate the rephasing one-quantum 2D spectrum that correlates the excitation frequencies, ω_τ, with the emission frequencies, ω_t, in a two-dimensional map. Coherently tracking the phase of the signal as the delay τ is scanned with sub-cycle precision permits the Fourier transform operation of the emitted FWM field, thus congested one-dimensional spectra can be coherently unfolded onto two frequency dimensions.

The coherent pathways that contribute to the rephasing signal are indicated by the Feynman diagrams in Fig. 3.10(a)-(f) for pulse A linearly polarized along H and all possible polarization combinations of pulses B and C and the detected signal. Consider the diagram in Fig. 3.10(a), for which the polarization sequence is HHHH (where the sequence is defined as the polarization of pulses A, B, C and the detected signal, respectively). For this pathway, pulse A creates a coherent superposition between the ground state $|g\rangle$ and the excited state $|H\rangle$ that evolves as $e^{-i\omega_{gH}\tau}$, where $\omega_{gH} \equiv \omega_g - \omega_H < 0$. For an inhomogeneously-broadened ensemble, the oscillators evolve during τ with different frequencies and dephase. After a delay τ, pulse B converts the coherences into a ground state population, which does not accumulate phase during T but instead simply decays with a rate Γ_{gg}. After a delay T, the third pulse C converts the population back to a coherence between states $|H\rangle$ and $|g\rangle$, which evolves as $e^{-i\omega_{Hg}t}$. Comparing the phase evolution between τ and t, it is apparent that the coherences oscillate with negative frequency during τ and positive frequency during t because pulse A is conjugated. Phase evolution with opposite sign during τ and t enables the coherences to "rephase" at a time τ after pulse C, resulting in a photon echo signal with a temporal duration inversely proportional to the inhomogeneous line width (thus the reason this time ordering is referred to as the rephasing pulse sequence). The first- and third-order coherences

during τ and t, respectively, evolve with frequency of magnitude $\hbar\omega_H = \hbar\omega_0 - \Delta_{FSS}/2$; thus this coherent pathway contributes to the peak labeled (a) on the diagonal dashed line (indicating equal excitation and emission energies) in the simulated 2D spectrum shown in Fig. 3.10(g).

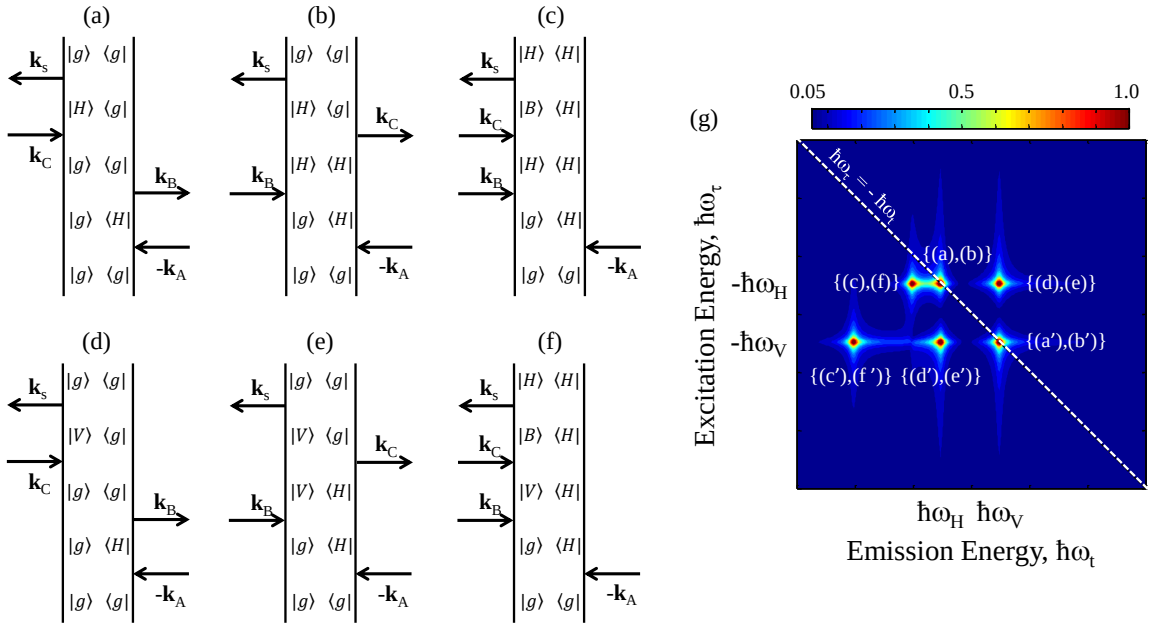

Figure 3.10: (a)-(f) Double-sided Feynman diagrams for the diamond level scheme consisting of the a ground state, $|g\rangle$, two singly-excited exciton states, $|H\rangle$ and $|V\rangle$, and a doubly-excited biexciton state $|B\rangle$. An additional six diagrams can be written if states $|H\rangle$ and $|V\rangle$ are swapped (referred to in the spectrum using the labels with "prime" notation), resulting in a total of 12 coherent pathways. The simulated 2D spectrum in (g) contains contributions from all possible coherent pathways irrespective of polarization; however specific pathways can be isolated by taking advantage of the dipole transition selection rules, as discussed in the text.

The remaining allowed coherent pathways are represented by the Feynman diagrams in Fig. 3.10(b)-(f). Only diagrams for which the first pulse is polarized along H are shown; an additional six diagrams can be written by interchanging $|H\rangle$ and $|V\rangle$, which are referred to in the 2D spectrum using the labels with "prime" notation. Thus a total of 12 coherent pathways can contribute to

the coherent nonlinear response in the rephasing pulse time ordering, which are shown in the 2D spectrum in Fig. 3.10(g). The vertical axis is plotted as negative energy since the first-order coherences induced by the conjugated pulse A oscillate with negative frequencies during τ compared to the third-order coherence frequencies during t. Two pathways (labeled (a) and (b) in Fig. 3.10) contribute to the peak at $|\hbar\omega_\tau| = \hbar\omega_t = \hbar\omega_H$ on the diagonal. They correspond to the system being in either a ground or excited state population during T. The peak labeled $\{(c),(f)\}$ arises from coherent pathways that involve excitation of the doubly-excited state $|B\rangle$. This peak is red-shifted from the diagonal peak along the emission energy axis by $\Delta_B - \Delta_{FSS}$ ($\Delta_B + \Delta_{FSS}$ for peak $\{(c^{'}),(f^{'})\}$). A third peak, corresponding to the Feynman diagrams (d) and (e), appears at the excitation energy of state $|H\rangle$ and emission energy of state $|V\rangle$. The three peaks labeled with the "prime" notation arise from similar processes where pulse A is linearly polarized along V instead of H.

The off-diagonal peaks arise from interactions in the system, since they indicate excitation at one energy and emission at another. The presence of these peaks is due to the bound biexciton energy shift Δ_B. From the Feynman diagrams it is clear that for $\Delta_B = 0$, the (f) and (c) coherent pathways destructively interfere with the (d) and (e) pathways (and same for "primed" notation) so that only two peaks remain in the 2D spectrum that correspond to the ground-state bleaching and excited-state emission nonlinearities. This is expected: for $\Delta_B = 0$, the four-level energy diagram in Fig. 3.9 is equivalent to two independent two-level systems through a basis transformation, which leaves the Hamiltonian unchanged. Thus, the nonlinear response for these two energy schemes would be similar and off-diagonal peaks indicative of coupling between the states would be absent.

An apparent advantage of performing 2DCS is the separation of the coherent pathways that give rise to the nonlinear optical response. For example, in one-dimensional spectrally-resolved FWM, which is the vertical projection of the 2D spectrum onto the emission axis, pathways (a), (b), (d$^{'}$) and (e$^{'}$) spectrally-overlap (similarly for (d), (e), (a$^{'}$) and (b$^{'}$)). Since these pathways originate from different microscopic processes, interpreting one-dimensional FWM measurements is often difficult or impossible. Not all pathways are isolated in the rephasing 2D spectrum, however –

each peak in the spectrum comprises two pathways. The diagonal peaks are easy to interpret since they arise from ground and excited state populations of the same transition. On the other hand, the off-diagonal peaks include contributions from both ground-state bleaching and Raman-like coherences between states $|H\rangle$ and $|V\rangle$ and thus extracting relevant parameters such as dephasing rates, dipole moments, and transition frequencies is not as straightforward. One can take advantage of the selection rules to isolate some of the pathways. For example, using an HVVH polarization sequence, the coherent pathway labeled (f) is isolated and the $|B\rangle \rightarrow |H\rangle$ transition emission properties can be probed. In practice, $\Delta_{FSS} \ll \Delta_B$, and so only two spectrally-resolvable peaks are measured. Nonetheless, certain coherent pathways can be isolated through the dipole selection rules.

3.6.1.2 Rephasing Zero-Quantum Spectrum (S1)

A rephasing zero-quantum spectrum $S_I(\tau, \omega_T, \omega_t)$ is generated using the same pulse time ordering as the rephasing one-quantum experiments, but instead scanning T while holding τ fixed and taking a Fourier transform of the emitted signal field with respect to T, as depicted in Fig. 3.8(b). A photon echo is still emitted at a time τ after pulse C; however the dynamics associated with population decay and Raman-like coherences can now be probed. The simulated $S_I(\tau, \omega_T, \omega_t)$ 2D spectrum is shown in Fig. 3.11.

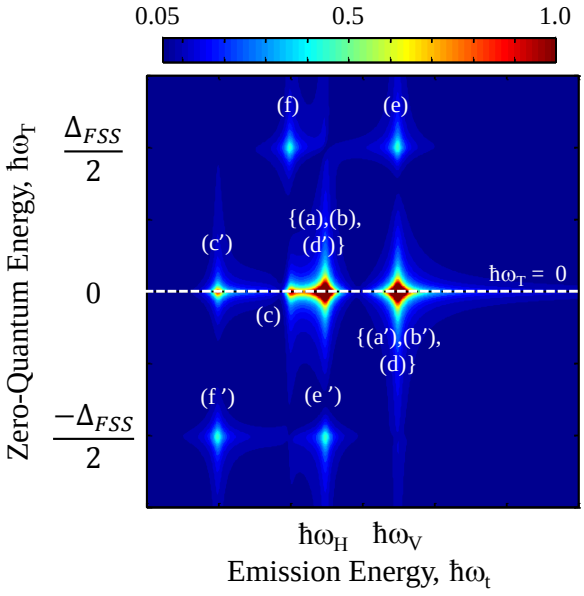

Figure 3.11: Simulated rephasing zero-quantum spectrum $S_I(\tau, \omega_T, \omega_t)$ that correlates the zero-quantum energy associated with T to the emission energy associated with t. The spectrum contains contributions from all coherent pathways, and the peak labels correspond to the same Feynman diagrams for the rephasing one-quantum spectrum $S_I(\omega_\tau, T, \omega_t)$. The amplitude has been saturated at half the maximum to enhance the cross peaks at $\hbar\omega_T \neq 0$.

Compared to the rephasing one-quantum spectrum, the zero-quantum spectrum more clearly isolates the coherent pathways associated with the biexciton transition and Raman-like coherences between states $|H\rangle$ and $|V\rangle$. One can also take advantage of the selection rules to isolate single peaks in the spectrum. For example, if Δ_{FSS} is smaller than the $|H\rangle \rightarrow |g\rangle$ and $|B\rangle \rightarrow |H\rangle$ homogeneous line widths, which is often the case experimentally, then the (f), (a), (b), (c) and (d$'$) pathways will overlap, inhibiting the ability to extract useful information. However, one can isolate the pathway associated with (f) by using an HVVH polarization sequence for which only this pathway is dipole-transition allowed. By using the transition selection rules to isolate certain quantum pathways, the parameters for specific peaks can be accurately measured. For example, the line widths along $\hbar\omega_T$ are associated with different relaxation processes depending on the coherent pathway and can provide additional insight into the dephasing mechanisms in the system that

cannot be obtained from the other 2D spectra. This aspect is discussed in more detail in Chapter 6.

3.6.1.3 Non-Rephasing One-Quantum Spectrum (S2)

Using three-pulse excitation allows for time ordering of the first two pulses to be interchanged, which is a capability not available in two-pulse experiments. A "non-rephasing" one-quantum spectrum $S_{II}(\omega_\tau, T, \omega_t)$ can be generated by impinging the sample first with pulse B, followed by the conjugated pulse A and then pulse C, as depicted by the timing sequence in Fig. 3.8(c). Pulse B is scanned earlier in time (increasing τ) while the FWM signal is recorded, and the emitted FWM field is Fourier-transformed with respect to τ. For this pulse time ordering, the phase accumulation occurs with similar sign for the first-order coherences during τ and third-order coherences during t. For a homogeneously-broadened system, the signal will decay with the homogeneous dephasing rate Γ_{ij}. If instead the line width is dominated by inhomogeneity, then the oscillators with different frequencies will dephase during τ and t and the signal decays in a time inversely proportional to the inhomogeneous line width. This behavior is in contrast to the rephasing pulse time ordering: the coherences no longer rephase and the emitted FWM signal is a free-polarization decay instead of a photon echo. The coherent pathways for this pulse time ordering are shown in Fig. 3.12(a)-(f) for pulse B linearly-polarized along H (as with the rephasing pulse time ordering, there are an additional six diagrams that correspond to interchanging $|H\rangle$ and $|V\rangle$ and are referred to using the "prime" notation). The corresponding 2D non-rephasing spectrum for zero-inhomogeneity is shown in Fig. 3.12(g).

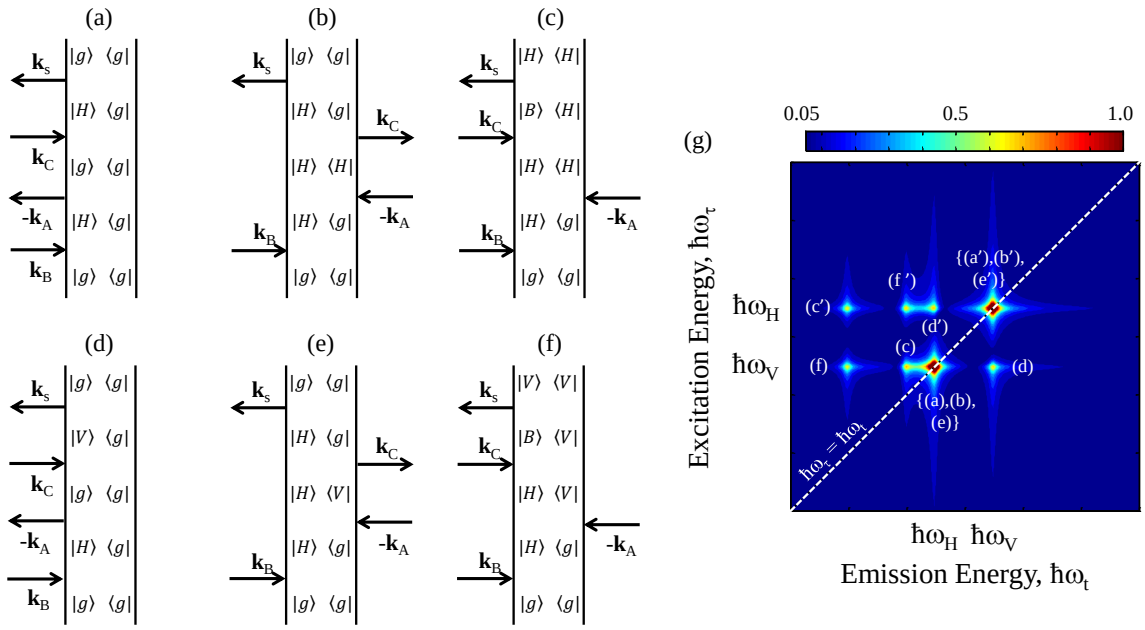

Figure 3.12: (a)-(f) Double-sided Feynman diagrams for the non-rephasing pulse sequence for the first pulse linearly-polarized along H. An additional six Feynman diagrams can be written for the first pulse polarized along V and are referred to using the "prime" notation. (g) The corresponding simulated 2D non-rephasing spectrum for the four-level energy structure containing contributions from all coherent pathways. The amplitude has been saturated at half the maximum to enhance the cross peaks.

The vertical axis in Fig. 3.12(g) is plotted as positive excitation energy $\hbar\omega_\tau$ since the coherences evolve with positive frequencies during τ for this pulse time ordering. The ground-state bleaching and excited-state emission pathways ($\{(a),(b)\}$, $\{(a)^{'},(b)^{'}\}$) overlap on the diagonal, similar to the rephasing zero- and one-quantum spectra. In this case the Raman-like coherence between states $|H\rangle$ and $|V\rangle$ associated with diagrams (e) and (e$^{'}$) are also on the diagonal, thus the diagonal peaks will oscillate with T at frequency $\Delta_{FSS}/\hbar$. In contrast to the rephasing one-quantum spectrum, the remaining pathways are spectrally-isolated. Thus the isolation of the majority of the coherent pathways can be achieved by performing these three types of 2DCS experiments. Further

isolation can be achieved by performing three-dimensional coherent spectroscopy for which the FWM signal is spectrally-resolved while both τ and T are scanned [110].

3.6.1.4 Two-Quantum Spectrum (S3)

A fourth-type of 2D spectrum, $S_{III}(\tau, \omega_T, \omega_t)$, can be generated using a pulse sequence in which the conjugated pulse A arrives at the sample last and the delay T is scanned instead of τ, as depicted by the timing sequence in Fig. 3.8(d). This pulse time ordering (for $\tau = 0$) is equivalent to the "negative" delay in two-pulse experiments for which no FWM signal is expected without considering many-body effects. The S_{III} spectrum is sensitive to many-body interactions in the system since the ground-state bleaching and excited-state emission pathways do not contribute. This idea is evident when considering the coherent pathways contributing to this signal, which are shown in Fig. 3.13(a)-(d). For the first pulse B polarized along the H transition, four pathways contribute to the nonlinear response. All pathways involve creating a coherence between states $|g\rangle$ and $|B\rangle$ from the interaction of the excitations created by the first two pulses.

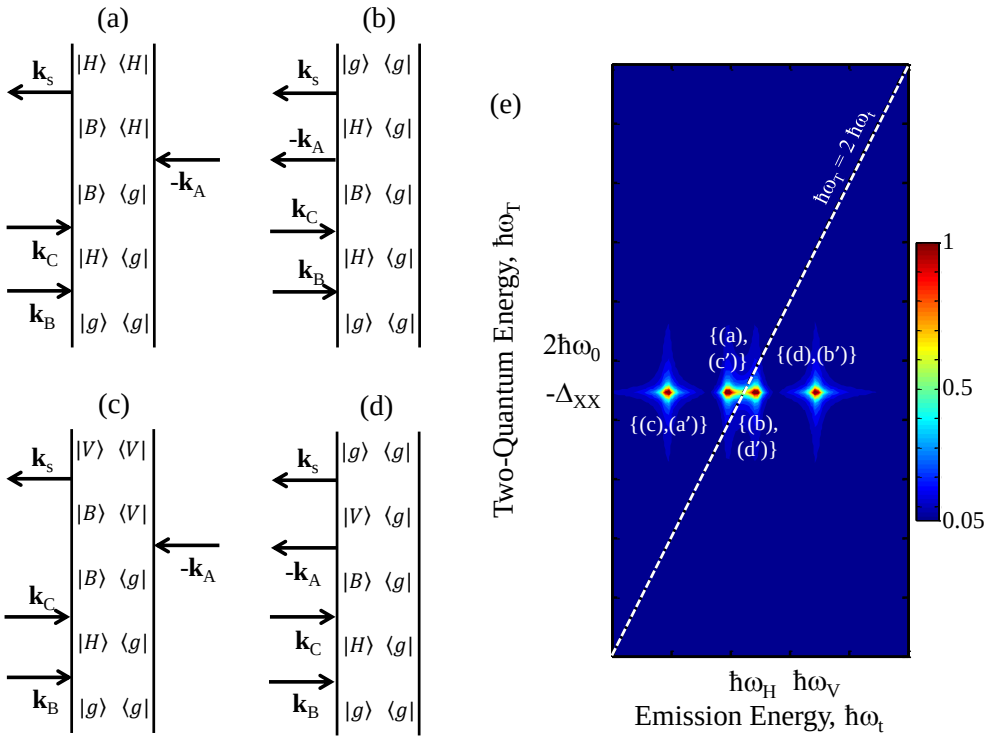

Figure 3.13: Double-sided Feynman diagrams for the two-quantum pulse time ordering. An additional four diagrams can be written by interchanging the $|H\rangle$ and $|V\rangle$ states and are labeled in the spectrum in (g) using the "prime" notation. The simulated spectrum contains contributions from all coherent pathways.

For a biexciton binding energy $\Delta_B = 0$, pathways (a) and (c) destructively interfere with pathways (d) and (b), respectively, and therefore the S_{III} field is zero. This is to be expected, since the energy level diagram for zero biexciton binding energy is equivalent to that of two-independent two-level systems for which no interaction-mediated signal is expected. The exciton-exciton interaction is modeled using the OBEs, in this case, by introducing a shift of the two-exciton energy. Generation of a "two-quantum" coherence can be intuitively understood by considering the excitation and interaction between two excitons: the first pulse B excites a coherence between states $|H\rangle$ and $|g\rangle$ of one exciton that evolves as $e^{-i\omega_{Hg}t'}$, where t' is the time after the arrival of the pulse. The second pulse C excites the same transition for another exciton, which also evolves as $e^{-i\omega_{Hg}t'}$.

The total phase evolution of the nonlinear signal occurs as $e^{-i2\omega_{Hg}T}$ during T, which is twice the frequency of a singly-excited exciton. Interactions between the two excitons can result in a renormalization of their collective energy such that the phase evolution evolves as $e^{-i(2\cdot\omega_{Hg}-\Delta_B)T}$, where the renormalization energy is Δ_B. Necessary for this mechanism to generate an S_{III} signal, the interaction must preserve phase coherence between the two excitons; otherwise, the phase evolution of the individual excitons would destructively interfere and the S_{III} signal would be zero.

A two-quantum spectrum is shown in Fig. 3.13(e) for similar simulation parameters as the zero- and one-quantum spectra. All peaks appear at a two-quantum energy of $2 \cdot \hbar\omega_0 - \Delta_B$. Each peak consists of two coherent pathways – one from initial excitation of the $|g\rangle \rightarrow |H\rangle$ transition and the other from the $|g\rangle \rightarrow |V\rangle$ transition – which are characterized by similar dipole moments, dephasing rates and energies during T and t and can therefore be considered equivalent. This type of spectrum provides a sensitive measure of the many-body effects on the renormalization energies and dephasing rates and has been implemented previously for both GaAs QWs [199, 218] and InGaAs coupled QWs [219]. S_{III} spectra of GaAs IFQDs will be presented in Chapter 6.

3.6.2 Interpreting 2D Spectra

In a 2D spectrum, individual resonances produce diagonal peaks and coupling between resonances produce off-diagonal peaks. This characterization allows for an intuitive way to identify the level system and type of coupling between resonances. Consider a system consisting of two independent transitions with energies $\hbar\omega_1$ and $\hbar\omega_2$, shown in Fig. 3.14(a). The corresponding 2D rephasing spectrum shown below the energy level diagram consists of two diagonal peaks at ($\hbar\omega_t = \hbar\omega_1$, $\hbar\omega_\tau = -\hbar\omega_1$) and ($\hbar\omega_2$, $-\hbar\omega_2$). As expected for two independent transitions, no off-diagonal coupling peaks are present. The diagonal peaks arise from both the ground-state bleaching and excited-state emission nonlinearities depicted by the diagrams in Fig. 3.10(a) and (b). If the two transitions share a common ground state, as shown by the "V" system in Fig. 3.14(b), then they can no longer be considered independent. In this case, two off-diagonal peaks appear at ($\hbar\omega_1$, $-\hbar\omega_2$) and ($\hbar\omega_2$, $-\hbar\omega_1$) and are attributed to the coherent pathways depicted by the (d) and (e)

Feynman diagrams in Fig. 3.10. Because the two transitions share a common ground state, excitation of one transition depletes the ground state population, which in turn affects the nonlinear optical response of the other transition.

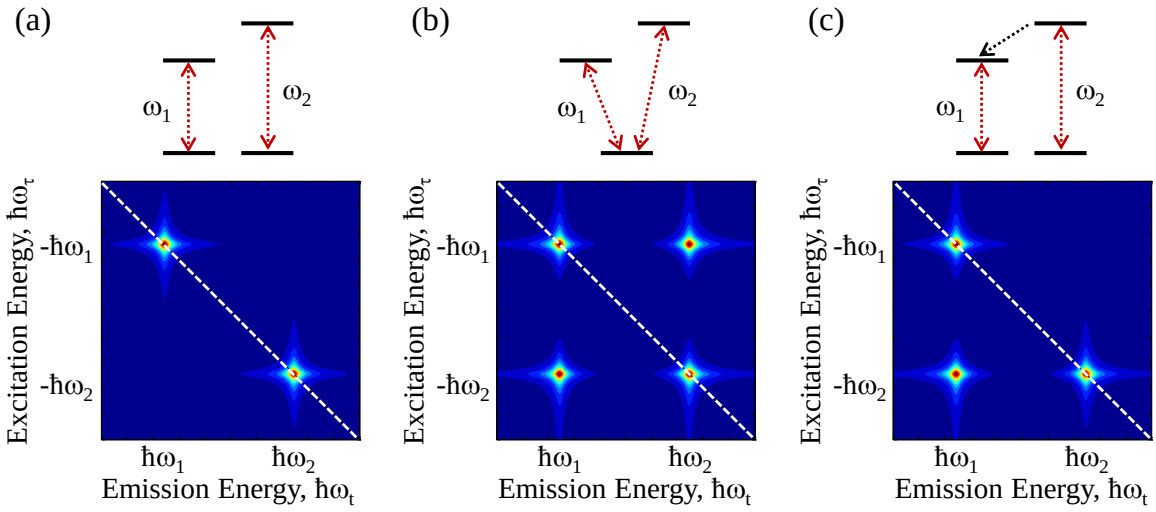

Figure 3.14: (a) Two independent two-level transitions and the corresponding 2D rephasing spectrum. (b) A three-level system with a common ground state and the corresponding 2D rephasing spectrum. (c) Two independent two-level systems that are coupled through incoherent relaxation from the higher-energy state to the lower-energy state, and the corresponding 2D rephasing spectrum.

The two systems and corresponding 2D rephasing spectra in Figs. 3.14(a) and (b) demonstrate the power of 2DCS: the technique can unambiguously identify whether resonances are quantum-mechanically coupled, whereas in one-dimensional spectroscopies such as linear absorption, PL and spectrally-resolved FWM, the two off-diagonal peaks would be hidden by the diagonal peaks. The nature of the coupling between transitions can also be identified using 2DCS. Consider a system of two two-level transitions that would otherwise be uncoupled if not for incoherent nonradiative population transfer from the higher-energy excited state to the lower-energy excited state, as shown in Fig. 3.14(c). This type of coupling would produce a single off-diagonal peak at energies $(\hbar\omega_1, -\hbar\omega_2)$. This cross-peak originates from excitation at the ω_2 transition and then incoherent

population relaxation to the ω_1 transition, after which the FWM signal is radiated. Because this is an incoherent process that affects populations, it occurs during the delay T for which phase coherence need not be maintained. The dynamics of this incoherent process can be mapped out by recording rephasing spectra for different delays T.

3.6.2.1 Lineshape Analysis

Up to this point, the systems considered have been homogeneously-broadened. In practice, most semiconductor samples studied are inhomogeneously-broadened either through disorder in QWs or dispersion in QD shape and composition. Various nonlinear spectroscopies have been used to study the line width broadening mechanisms in semiconductors, including TR- and TI-FWM [145]. The decay rate of a two-pulse TI-FWM signal can be connected to the homogeneous line width of a simple two-level system or for a sample dominated by inhomogeneity; however an accurate measurement of the homogeneous line width is difficult or impossible for samples exhibiting moderate inhomogeneity. In TR-FWM, the width of the emitted photon echo for an inhomogeneously-broadened sample provides an accurate measure of the inhomogeneity, and the decay of the echo with the two-pulse delay provides the homogeneous line width; however the echo may not be well-defined due to many-body interactions. It can also be distorted due to beating in the TR- or TI-FWM signal when multiple resonances are excited [220].

A glance at a rephasing 2D spectrum can give a qualitative sense of the inhomogeneity in a sample: for a given peak, the width in the cross-diagonal direction is associated with homogeneous broadening, whereas the width along the diagonal is related to the inhomogeneity in the sample. However, acquiring quantitative line width information is not so straightforward since, as is shown below, the line widths are coupled along both directions. Past work on 2D line shapes in NMR spectroscopy has focused on correlating the coupling between inhomogeneous and homogeneous broadening rather than understanding and isolating the individual contributions [95]. The coupling degraded the spectral resolution, which was enhanced using windowing functions at the expense of accurate line width measurements. An alternative approach implemented for molecular

systems considered both rephasing and non-rephasing signals together, which reduced the coupling [221]. From a theoretical approach, envelope line shapes were derived in the homogeneous and inhomogeneous limits from the Fourier transform of an absolute-value 2D time-domain solution of the OBEs [222]. Other theoretical work focused on correlations [223, 224] and many-body effects on the ratios of dephasing parameters [220] as opposed to determining a quantitative and physically meaningful relationship between the homogeneous and inhomogeneous line widths and the widths of a peak in the 2D rephasing spectrum.

We have established a quantitative connection between the homogeneous and inhomogeneous line widths and the cross-diagonal and diagonal widths in a 2D rephasing spectrum using analytical solutions to the OBEs [112]. In order to calculate the 2D spectral line shapes, we first consider the signal in the 2D time domain. Based on the OBE simulations discussed in the previous Chapter, the FWM signal for a single inhomogeneously-broadened resonance in the 2D time domain is

$$S_I(\tau, T=0, t) = S_I^0 e^{-(\gamma(t+\tau)+i\omega_0(t-\tau)+\sigma^2(t-\tau)^2/2)}\Theta(t)\Theta(\tau), \tag{3.24}$$

where S_I^0 is the amplitude at time zero, ω_0 is the center resonance frequency, γ is the homogeneous line width, σ is the inhomogeneous line width and the Θ's are unit step functions establishing that the signal cannot be emitted before the pulses arrive. A Gaussian distribution is used as the inhomogeneous broadening profile. The signal can be decomposed into a homogeneous decay along the photon echo direction, $t^{'} = t + \tau$, and an oscillation multiplied by a Gaussian envelope along the "anti-echo" direction, $\tau^{'} = t - \tau$, giving

$$S_I(\tau^{'}, T=0, t^{'}) = S_I^0 e^{-(\gamma t^{'}+i\omega_0\tau^{'}+\sigma^2\tau^{'2}/2)}\Theta(t^{'}-\tau^{'})\Theta(t^{'}+\tau^{'}). \tag{3.25}$$

Equation 3.25 is a more intuitive form to visualize the 2D time domain signal. The signal is shown in Fig. 3.15 in the 2D time (a) and frequency (b) domains. The signal is not completely separable along $t^{'}$ and $\tau^{'}$ due to the Θ functions enforcing causality. In order to extend these results to the frequency domain and derive analytical line shapes, we apply the projection-slice

theorem of Fourier transforms [225]. This theorem states that a Fourier transform of a projection in one domain is equivalent to a slice in the 2D Fourier pair plane. In this case, we project the 2D time domain signal onto $t^{'}$ and $\tau^{'}$, as illustrated in Figs. 3.15(c) and (d), respectively. A Fourier transform of these projections then provides the function for the line shape function of a slice along the $\omega_{t'}$ and $\omega_{\tau'}$ directions in the 2D spectrum, respectively.

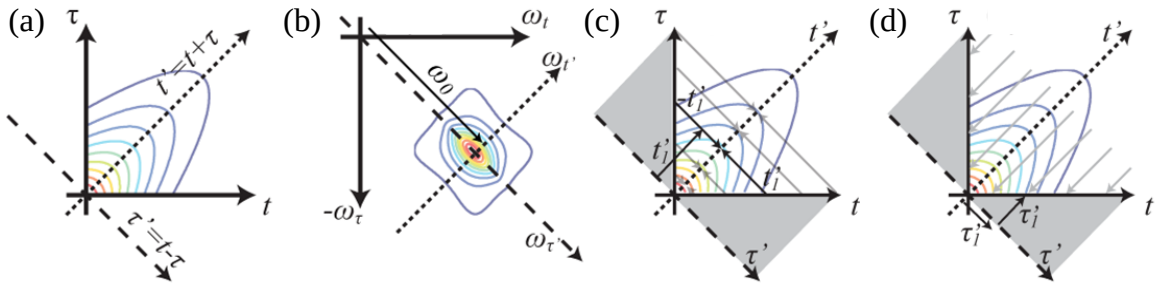

Figure 3.15: 2D spectrum in the (a) time and (b) frequency domains. (c) The Fourier transform of a projection of the 2D time domain signal onto the $t^{'}$ axis corresponds to a slice along $\omega_{t'}$ axis. (d) A similar analysis for $\tau^{'}$ corresponds to a slice along the $\omega_{\tau'}$ axis. The shaded regions correspond to areas of zero signal as enforced by causality.

In order to obtain an expression for slices in the 2D spectrum that cut through the resonance peak, we first invoke the Fourier shift theorem, which states that a shift in one domain is equivalent to a linear phase ramp in the Fourier pair domain. Therefore to slice through the resonance peak at ω_0 in the spectral domain, the 2D time domain signal must be multiplied by a linear phase term $e^{i\omega_0\tau^{'}}$. The time domain signal is then normalized (divide out S_I^0) and projected onto the $t^{'}$ and $\tau^{'}$ axis. The projection onto $t^{'}$ axis and centered at ω_0, as illustrated by Fig. 3.15(c), is written as

$$S_I^{proj}(t^{'}) = \int_{-\infty}^{\infty} S_I(\tau^{'},t^{'})d\tau^{'} = e^{-\gamma t^{'}} \int_{-t^{'}}^{t^{'}} e^{\sigma^2\tau^{'2}/2}d\tau^{'} = \frac{\sqrt{2\pi}}{\sigma}e^{-\gamma t^{'}}\,\mathrm{Erf}(\sigma t^{'}/\sqrt{2}), \tag{3.26}$$

where the integration limits are established by the causality conditions depicted by the shaded regions in Fig. 3.15(c) and Erf is the error function. A Fourier transform of this projection yields

the cross-diagonal line shape

$$S_I^{proj}(\omega_{t'}) = \frac{e^{(\gamma - i\omega_{t'}^2)^2/2\sigma^2}\mathrm{Erfc}\left(\frac{\gamma - i\omega_{t'}}{\sqrt{2}\sigma}\right)}{\sigma(\gamma - i\omega_{t'})}, \tag{3.27}$$

where $Erfc$ is the complementary error function. The 2D time domain signal projection onto the $\tau^{'}$ axis, illustrated in Fig. 3.15(d), is written as

$$S_I^{proj}(\tau^{'}) = \int_{-\infty}^{\infty} S_I(\tau^{'}, t^{'})dt^{'} = e^{\sigma^2\tau^{'2}/2}\int_{|\tau^{'}|}^{\infty} e^{-\gamma t^{'}}dt^{'} = \frac{1}{\gamma}e^{\sigma^2\tau^{'2}/2}e^{-\gamma|\tau^{'}|}. \tag{3.28}$$

The Fourier transform of this expression is given by the convolution ($*$) of the Fourier transforms of the Gaussian and exponential decay and yields the diagonal spectral line shape along $\omega_{\tau'}$:

$$S_I^{proj}(\omega_{\tau'}) = \left(\sqrt{\frac{2}{\pi\sigma^2}}e^{-\omega_{\tau'}^2/2\sigma^2}\right) * \left(\frac{1}{\gamma^2 + \omega_{\tau'}^2}\right) = \frac{\sqrt{2\pi}}{\gamma}\mathrm{Voigt}(\gamma, \sigma, \omega_{\tau'}), \tag{3.29}$$

where the Voigt profile is a convolution of a Gaussian profile and a Lorentzian profile. The expressions for the cross-diagonal and diagonal line widths in Eqns. 3.27 and 3.29, respectively, are valid for all values of γ and σ. Table 3.1 summarizes the line shapes for complex rephasing spectra, i.e. including the real and imaginary components.

While the expressions for the line shapes in Eqns. 3.27 and 3.29 are general, they take on familiar forms in certain limits. In the homogeneous limit for which the inhomogeneous line width is zero, both the diagonal and cross-diagonal slices of the rephasing amplitude spectrum are Lorentzian functions $L(\omega, \gamma) = \sqrt{2/\pi} \cdot (\gamma^2 + \omega^2)^{-1}$ with a FWHM equal to 2γ. In this limit, enforcing the time ordering (zero signal for $t, \tau < 0$) strongly affects the projections onto $t^{'}$ and $\tau^{'}$. It is the time ordering and consequent truncation of the 2D time domain signal that leads to the classic spectral star shape with Lorentzian width along both the diagonal and cross-diagonal directions.

In the opposite extreme case for which the line width is dominated by inhomogeneity ($\sigma \gg \gamma$), the cross-diagonal line shape becomes $\sqrt{L(\omega_{t'}, \gamma)}$ with a Lorentzian FWHM of 2γ, and the diagonal line shape is Gaussian $G(\omega_{\tau'}, \sigma) = \sigma^{-1} \cdot \exp(-\omega_{\tau'}^2/2\sigma^2)$ with line width σ. In this limit, the Gaussian

distribution characterizing the photon echo width in the time domain can be treated as a Dirac delta function so that the photon echo is restored along the diagonal $t^{'} = t + \tau$. The projection onto $t^{'}$ is purely homogeneous and the truncation of the signal at $\tau, t < 0$ due to time-ordering is negligible. The projection onto $\tau^{'}$ is a narrow Gaussian whose Fourier transform is a broad Gaussian along $\hbar\omega_{\tau'}$ in the 2D spectrum.

Spectral Line Shapes		**Real**		**Imaginary**		**Amplitude**	
		Shape	Width	Shape	Width	Shape	Width
Hom. Limit	Cross-Diag.	$\frac{d^2}{d^2\omega}L(\omega)$.	2γ (0-X)	$\frac{d}{d\omega}L(\omega)$	$\frac{2\gamma}{\sqrt{3}}$ (V-P)	$L(\omega)$	2γ
	Diag.	$L(\omega)$	2γ	–	–	$L(\omega)$	2γ
Inhom. Limit	Cross-Diag.	$L(\omega)$	2γ	$\frac{d}{d\omega}L(\omega)$	2γ (V-P)	$\sqrt{L(\omega)}$	2γ
	Diag.	$G(\omega)$	σ	–	–	$G(\omega)$	σ

Table 3.1: 2D rephasing spectral line shapes and widths (FWHM) in the homogeneous and inhomogeneous limits. Definitions: $L(\omega)$ = Lorentzian function; $G(\omega)$ = Gaussian function; γ = Lorentzian homogeneous line width; σ = Gaussian inhomogeneous line width; $0 - X$ = zero-crossing points; V–P = valley-to-peak.

Discussed in detail in Chapter 5, the inhomogeneous line width of a QD ensemble is typically orders of magnitude larger than the homogeneous line width; thus quantitative values of the dephasing rates and amount of inhomogeneity can be obtained using the expressions in the inhomogeneous limit. Moreover, since inhomogeneity arises from a distribution of QD sizes in the ensemble, one can can take cross-diagonal slices at different positions along the diagonal to obtain the homogeneous line width for various resonance energies within the inhomogeneous distribution. The signal amplitude at each resonant energy is the sum of the nonlinear response of all QDs emitting at that energy, which do not necessarily have similar physical properties such as shape and strain. Nonetheless, we show in Chapter 5 that the homogeneous line width at each energy is

consistent with the line widths obtained from single dot studies. This observation suggests that all QDs with a particular resonance energy can be described by one of the following: either 1) all the dots have similar physical properties, and therefore similar homogeneous line widths; or 2) dots with a distribution of properties contribute to the signal at a given energy, but their differences in shape, strain and local environment do not introduce a distribution of homogeneous line widths. Because the line width is dominated by inhomogeneity, the former scenario is more likely; any change in the dot properties shifts its resonance energy and contributes to inhomogeneous broadening so that each cross diagonal slice provides the homogeneous line width averaged over many dots with similar physical properties.

3.6.3 Advantages of the Technique

Besides the ability to isolate coherent pathways, identify resonance coupling mechanisms and separate inhomogeneity from homogeneity, 2DCS has additional capabilities that make it a powerful technique for studying semiconductors. One ability that is particularly useful is the preservation of phase information. By measuring the complex signal field, the technique inherently performs many other conventional spectroscopic experiments simultaneously. For example, a vertical projection along the $\hbar\omega_\tau$ axis provides the SR-FWM field from which the TR-FWM field can be extracted by taking an inverse Fourier transform with respect to ω_t. The TI-FWM signal can be extracted by integrating the spectrum along $\hbar\omega_t$ and taking an inverse Fourier transform with respect to ω_τ. Furthermore, multiplication of the probe field and the real part of the 2D signal integrated along ω_τ is equivalent to the spectrally-resolved differential transmission signal from a pump-probe experiment. Preservation of phase also enables decomposition of the complex signal field into its real and imaginary components that are connected by the Kramers-Kronig relation. A 2D spectrum with correct global phase has played an essential role in distinguishing between the microscopic mechanisms for different many-body interactions in semiconductor QWs [105, 106, 189, 199].

Another advantage of three-pulse 2DCS techniques in which the pulse time-ordering can be arbitrarily set is the ability to obtain the four different types of spectra discussed in this Section.

Each type of spectrum provides a unique picture into the dynamics and physical properties that govern the nonlinear response. By comparing the amplitudes, energies and line widths of all the peaks in the different types of spectra, one has the ability, for example, to distinguish between incoherent and coherent resonant coupling and ascertain the energy level structure [219, 226]. Moreover, with phase stability of each pulse delay, three-dimensional spectra can be generated to further isolate the coherent pathways, facilitating the pursuit of complete experimental characterization of the system Hamiltonian [110].

The 2DCS technique can also decouple the time and frequency resolutions imposed by the time-bandwidth product [210]. The time resolution in the experiment is determined by the excitation pulse width and the frequency resolution is limited by the maximum delay between the pulses. Consequently, 2DCS can capture the fast dynamics using femtosecond pulses with a frequency bandwidth that can span the spectral region of interest while being able to resolve the individual resonances. For example, using a Ti:Sapphire laser as the excitation source, one can probe dynamics on a tens of femtoseconds time scale. For pulse delays up to 1 ns (requiring a delay distance of 15 cm, which is easily achievable with current delay-stage technology), one can achieve a 1 GHz (4.1 μeV) spectral resolution. Zero-padding techniques can further enhance the resolution in certain circumstances.

These capabilities make 2DCS a powerful technique to study a diverse set of materials in biology, chemistry and atomic and semiconductor physics. Experimental implementation and the technical challenges associated with 2DCS in the near-IR and optical wavelengths are discussed in the next Chapter.

Chapter 4

Experimental Implementation of 2D Spectroscopy

Optical 2DCS experiments are commonly implemented using impulsive laser fields to probe the nonlinear optical response in the time domain or mixed time-frequency domains. The nonlinear signal is measured while the excitation pulse delays are varied, often using mechanical delay lines, glass prism wedges or pulse-shaping techniques. Due to the nature of the phase-sensitive measurements, stability of the pulse delays to $\approx \lambda/100$ or better is critical. Mechanical vibrations and drift of the optical mounts and inaccuracies in stepping of the pulse delays can degrade the nonlinear signal and introduce artifacts when generating a 2D spectrum. Compared to IR wavelengths, eliminating these detrimental effects is more difficult in the near-IR and optical regime because the relative phase fluctuations increase at shorter wavelengths, making the implementation of optical 2DCS challenging.

High phase stability and accurate pulse positioning for 2DCS experiments have been achieved using several methods, some of which were introduced in the previous Chapter. 2DCS was initially implemented in the Cundiff group using a free-space setup with active interferometric stabilization of the pulse delays in 2005 [104]. The technique was first applied to study semiconductor QWs, and Li *et al.* were able to distinguish between different many-body contributions to the nonlinear response more easily compared to one-dimensional spectroscopies [105, 106]. This work was instrumental in demonstrating that 2DCS could be performed in the optical regime using active stabilization; however the experimental setup had several limitations. Particularly, the delay between the second and third pulses, T, was not actively stabilized. Without stabilizing this delay,

the setup was not ideal for performing zero-quantum experiments to probe Raman-like coherences (although the setup could probe zero-quantum coherences if the frequencies were low enough). Moreover, the original setup was not able to generate a two-quantum spectrum, which is particularly sensitive to many-body interactions. These limitations are eliminated by the first generation JILA Multidimensional Optical Nonlinear SpecTROmeter, or JILA MONSTR, designed and built by Bristow *et al.* in 2009 [111]. This ultrastable platform is used to perform the experiments discussed in this thesis, with a few modifications for enhancing the signal-to-noise ratio from epitaxial QDs and optimizing the data acquisition time.

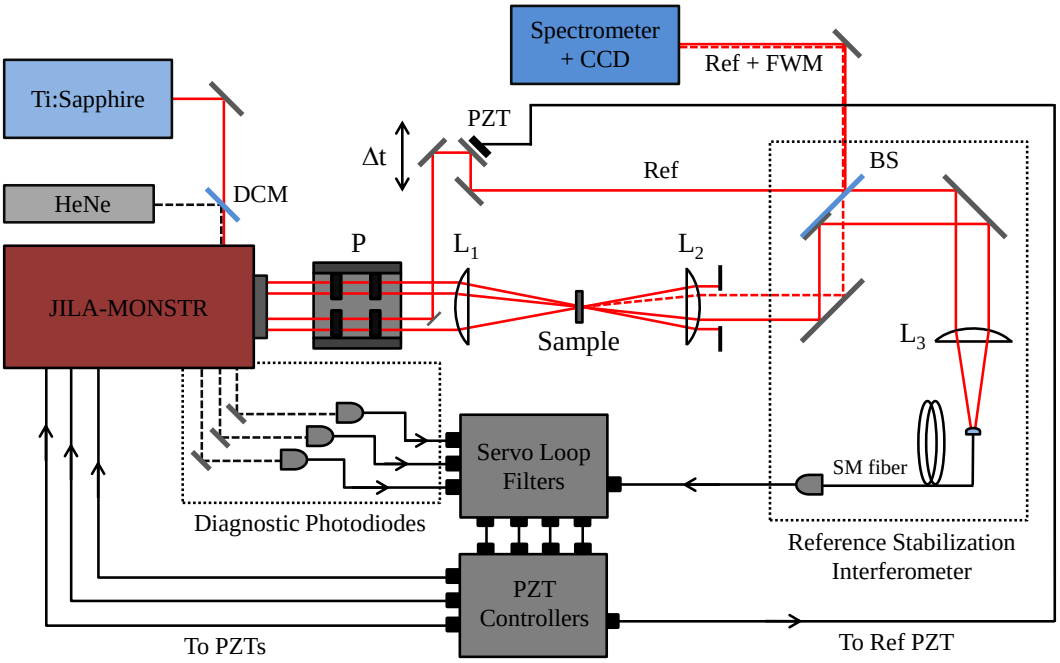

Figure 4.1: Schematic diagram of the 2DCS experimental setup with active stabilization. Three pulses propagating in the box geometry interact nonlinearly with the sample to generate a FWM signal that is interfered with a phase-stabilized reference pulse, and their interference is spectrally-resolved. Active phase stabilization is achieved by monitoring HeNe interference patterns from the MONSTR and using them as error signals for servo feedback loop filters that drive PZT actuators. The FWM signal/reference pulse delay is stabilized using an external servo loop. (DCM: dichroic mirror; BS: beam splitter with a reflective coating on one quadrant of one side; P: polarization optics consisting of $\lambda/2$ and $\lambda/4$ retarders, linear polarizers and liquid crystal phase modulators; L_1: focusing lens; L_2: collimating lens; PZT: piezo-electric actuator; Δ_t: adjustable reference/signal delay).

The apparatus consists of a set of nested and folded Michelson interferometers with mechanical delay stages that produce four pulses that are phase stabilized by electronic servo feedback loops, which are described in detail in Section 4.2. As depicted in the experimental schematic diagram in Fig. 4.1, three of the pulses are incident on the sample to generate the FWM signal

(Section 4.3), while the fourth pulse is routed around the sample and used as a reference pulse for heterodyne spectral interferometry, which requires an additional external interferometer to stabilize the reference/signal phase. Spectral interferometry using the reference pulse enables extraction of the FWM amplitude and phase, which is discussed in Section 4.4. The complex FWM signal is recorded while any of the pulse delays are scanned with interferometric precision, and a 2D spectrum is generated by taking a Fourier transform of the signal with respect to the scanned delay, as described in Section 4.5. Before discussing details of the apparatus and experiment, fundamental and technical challenges for implementing 2DCS to study semiconductor QDs are described in the following Section.

4.1 Fundamental and Technical Challenges

Optical 2DCS of semiconductor QDs is fundamentally difficult to implement because long pulse delays are required to probe the radiatively-limited dephasing time in epitaxial QDs, which has been measured to be as long as a few nanoseconds [46]. 2DCS methods based on pulse-shaping techniques are typically constrained by their spectral resolution to maximum pulse delays of tens of picoseconds [227]; other methods that delay the pulses using glass-wedges achieve even smaller delays. Thus, the only practical approach to sufficiently map out the decay of the FWM signal – providing a quantitative measurement of the homogeneous line width – is to delay the pulses using mechanical delay lines. The phase of the pulses must be stabilized to $\approx \lambda/100$ and the delays must be incremented in precise, equal steps in order to perform a numerical Fourier transform with respect to the varied delay. In the optical or near-IR regime, this stability criterium requires limiting the mechanical motion of the optical mounts to less than $\approx$ 5 nm, as is shown later in this Chapter. This limit is severely exceed when only using sturdy optics mounts and a protective box enclosing the experimental setup. The necessary phase stability and stepping precision can be achieved, however, using active stabilization with feedback electronics. Moreover, the stabilization must be maintained over the course of the experiment, which requires mechanical delays of $\approx$ 15 cm and data acquisition times up to $\approx$ 5 hours. These criteria are satisfied via active interferometric

stabilization in the JILA MONSTR, which is described in detail in the next Section.

Obtaining quantitative information from 2D spectra of epitaxial QDs is challenging because QDs have weaker dipole moments than QWs and the number of QDs excited within the pulse spot size (typically $\approx 10^5 - 10^6$) limits the maximum attainable signal-to-noise ratio. From a technical standpoint, non-resonant scatter of the excitation pulses into the FWM phase-matched direction tends to dominate the SR-FWM signal to the point that the signal cannot be identified. Modulating the excitation pulse amplitudes and detecting the TI-FWM signal on a slow detector using a lock-in amplifier does not increase the signal-to-noise ratio enough to detect the weak signal. Thus other techniques are required to optimize the signal strength and alignment of the collection optics, which are described in more detail in Section 4.3. Once the optics are aligned and the sample positioned properly for maximum FWM signal generation and detection, distinguishing between the laser scatter and FWM signal in the 2D spectrum is still difficult. The Fourier-transform operation can eliminate some of the noise in the spectral window of the signal; however the signal-to-noise ratio often remains too low to be able to extract useful quantitative information. Low signal-to-noise ratios can be mitigated by using phase-cycling algorithms that enhance the relative FWM signal strength at each pulse delay. Phase cycling involves toggling the phases of the excitation pulses at each delay between zero and π and then adding phased spectral interferograms appropriately to remove the pump scatter and enhance the FWM signal. Methods for performing phase cycling are discussed in Section 4.4.

4.2 Active Interferometric Stabilization using the JILA-MONSTR

The JILA-MONSTR [111] produces four phase-stabilized pulses whose delays and time ordering can be arbitrarily adjusted, as shown in the experimental setup diagrams in Fig. 3.8 in the previous Chapter and in more detail in Fig. 4.1. The excitation source is a mode-locked Ti:Sapphire oscillator that produces $\approx$ 100 fs pulses at a repetition rate of 76 MHz. The pulse center wavelength is tuned to either 756 nm for the GaAs IFQDs or above 900 nm for the InAs SAQDs with a spectral bandwidth of $\approx$ 10 nm FWHM. The femtosecond pulses are combined with the output

of a Helium-Neon (HeNe) CW laser on a dichroic mirror (DCM) so that they collinearly propagate into the MONSTR. The MONSTR consists of a set of nested Michelson interferometers shown in the schematic representation in Fig. 4.2. The input lasers are split by a 50:50 beam splitter so that fields of equal power are propagating in the two arms of an interferometer. Each arm of the interferometer is itself an interferometer, so that four replicas are generated by the nested interferometers. DCMs are placed at the end of each arm, which transmit the femtosecond pulses and reflect the HeNe laser. Delay stages are inserted into each arm so that the femtosecond pulse delays can be arbitrarily adjusted. The reflected HeNe beams recombine and exit the opposite port of the beam splitters and their interference is used as an error signal input for servo feedback electronics. The relative phase between pulse pair A–B and C–Ref and between all four pulses is monitored by detecting the corresponding HeNe interference pattern on a photodiode. Any deviation of the HeNe interference from the zero-crossing point corresponds to a change in the optical path length of one of the arms of the interferometer; this error signal is used as the input to a servo loop filter whose output drives a piezoelectric actuator (PZT) controller. The output of the PZT controller adjusts the voltage on a PZT that is attached to the back of one mirror in each interferometer (not shown in the schematic in Fig. 4.2). The loop filter provides negative feedback so that any change in the interferometer arm is compensated for by the PZT. Controlled through a computer interface, the servo loops are engaged to stabilize all pulse delays during acquisition of the FWM signal and they are disengaged to allow for scanning of the pulse delays.

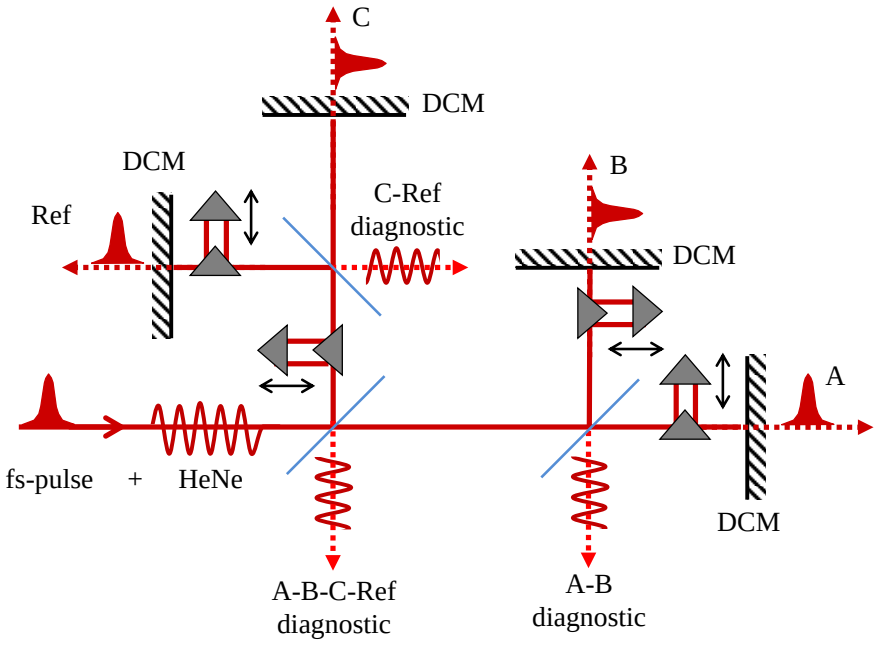

Figure 4.2: Schematic representation of the nested Michelson interferometers. Pulses A, B, C and Ref exit the interferometers through the dichroic mirrors (DCMs), while the collinearly propagating HeNe beams are reflected and exit the opposite ports of the beam splitters. The HeNe interference patterns are used as error signals for servo loop filters that stabilize the path lengths of the interferometers. The pulse delays are stepped with interferometric precision by disengaging the servo loops, after which the loops are re-engaged during data acquisition. In reality, the interferometer is designed so that a single DCM is used.

The scheme presented in Fig. 4.2 is implemented in the JILA-MONSTR, which is comprised of two decks that each contain the optics for an interferometer, and an additional interferometer is formed between the decks. Computer-aided design (CAD) drawings are shown for the lower and upper decks in Figs. 4.3(a) and (b), respectively. Each deck is milled from cast aluminum to house the optics for the interferometers. The lower deck supports the interferometer for pulses C and the Ref, while the upper deck for pulses A and B.

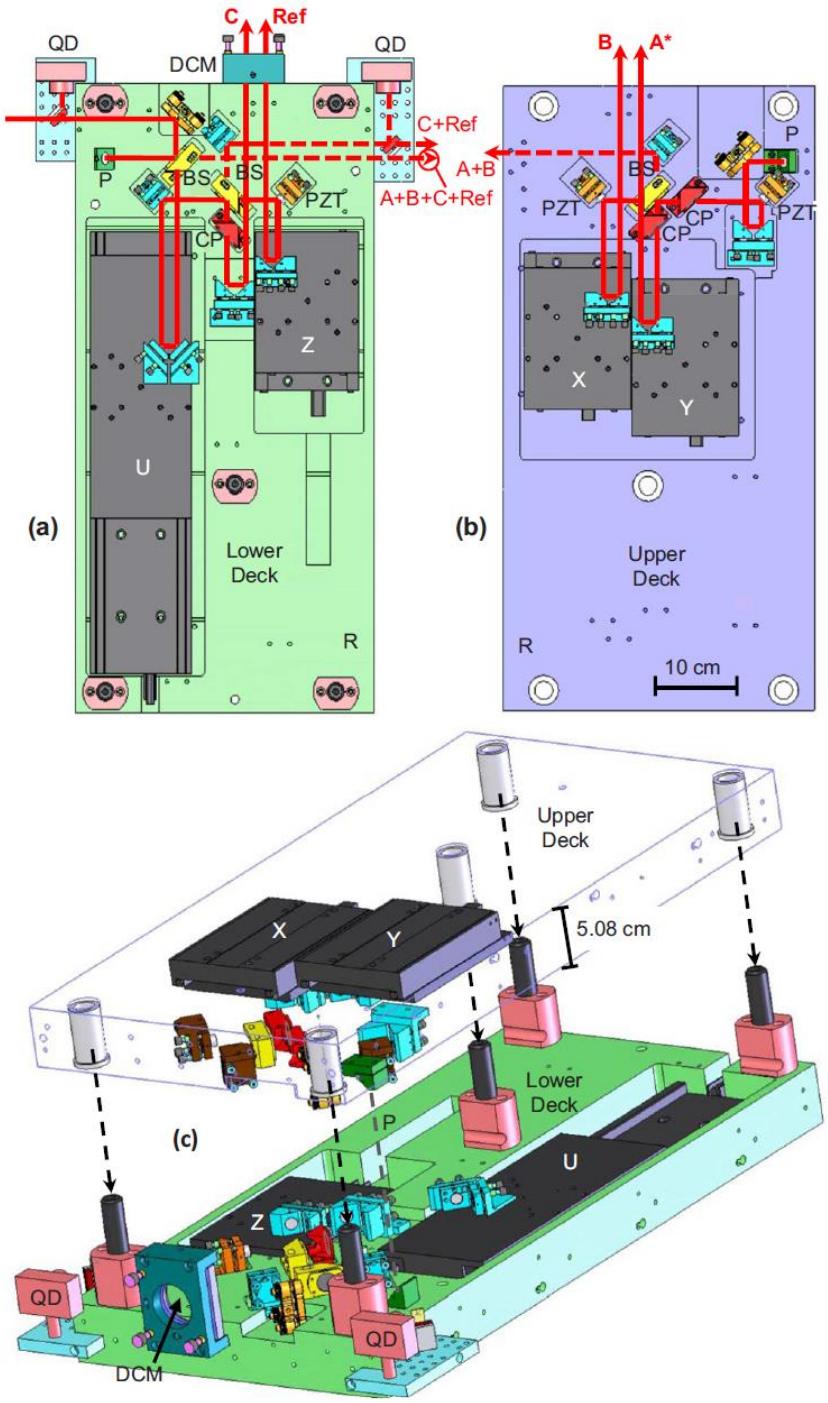

Figure 4.3: CAD drawings of the JILA-MONSTR. (a) The lower deck houses the interferometer for pulses C and Ref, while (b) the upper deck for pulses A and B. The entire assembly is formed by flipping and securing the upper deck onto the lower deck, shown in (c). (BS: beam splitter; CP: compensation plate; PZT: piezo-electric actuator; QD: quad-diode photodector; P: periscope mirrors; DCM: dichroic mirror). Reproduced from Bristow *et al.*, Review of Scientific Instruments **80**, 073108 (2009).

The long delay stage U enables 20 cm of travel and moves both C and Ref together with respect to the upper deck. The C–Ref delay can be adjusted using stage Z. A mirror mounted on a PZT controls the relative phase of pulse Ref with respect to C. The delays of pulses A and B are adjusted by stages Y and X (travel distance of 5 cm each) and the relative optical path length between the A–B and C–Ref interferometers is controlled by the PZT just before stage Y. All mirrors in the interferometers are silver protected by a dielectric from tarnishing. Each beam splitter consists of a broadband coating centered at 800 nm on a thin, low group velocity dispersion fused silica substrate. Compensation plates made from similar substrates are inserted to balance the dispersion. All optics are anti-reflection coated and held in custom mounts that minimize strain to prevent induced birefringence.

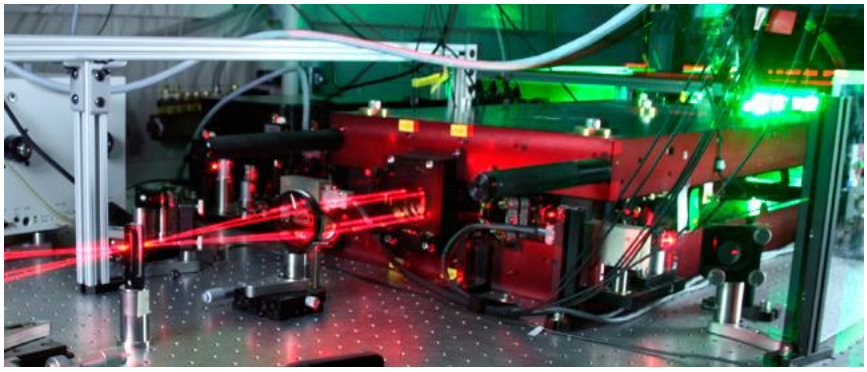

Figure 4.4: Photograph of the JILA-MONSTR. The lasers enter on at the right hand side of the picture, and the four output beams, propagating in the box geometry, are shown focusing to a single spot. Credit: Greg Kuebler and Alan Bristow.

The total assembly is formed by flipping and fastening the upper deck onto the lower deck, encompassing all the optics with a 5 cm gap between the decks, as shown in Fig. 4.3(c). The gaps along the side of the assembly are enclosed with panels to minimize the effects of air currents. After assembly, a 2" diameter DCM is attached to the front and acts as all the DCMs depicted in Fig. 4.2. The DCM transmits the femtosecond pulses and reflects the HeNe beams back into the MONSTR, completing the interferometer. The HeNe beams exit the MONSTR opposite the

entrance side, as depicted in Figs. 4.1 and 4.3. The femtosecond beams that perform the 2DCS experiment exit the MONSTR through the DCM and co-propagate along the four corners of a square with 1" sides. A photograph of the enclosed JILA-MONSTR highlighting the input beam on the right hand side and the four femtosecond beams focused through a lens is shown in Fig. 4.4. The alignment procedure for the MONSTR is described in Appendix C.

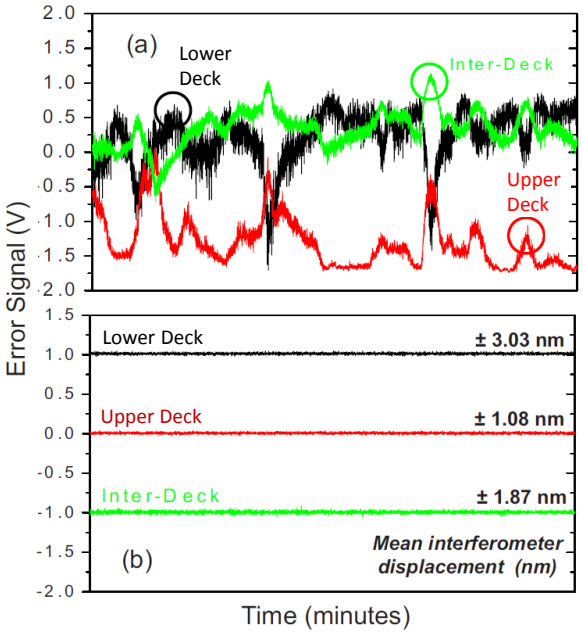

Figure 4.5: HeNe error signals for the lower-, upper-, and inter-deck interferometers recorded over approximately 10 minutes, without (a) and with (b) the servo loop filters engaged. The signals are offset from zero in (b) for clarity. Reproduced from Bristow *et al.*, Review of Scientific Instruments **80**, 073108 (2009).

The instability of the apparatus [111] when the servo loops are disengaged is evident from the characteristic error signals shown in Fig. 4.5(a). The signals are shown over a duration of ≈ 10 minutes. Within several minutes the path length difference of each interferometer drifts more than $\lambda/4$, resulting in a phase change $> 2\pi$ radians at the diagnostic port [1] . In comparison, with

[1] a factor of 1/4 arises from the HeNe double passing the stage once before and once after reflecting off the 2" DCM, so that a change in one interferometer arm of $\lambda/4$ corresponds to a phase change at the HeNe diagnostic output of 2π.

the servo loops engaged, the error signals are fixed at 0 V, as shown in Fig. 4.5(b) (the lower and inter-deck signals are offset by 1 and -1 V, respectively, for clarity). The error signal statistics follow a normal distribution with standard deviation that corresponds to less than ≈ 2 nm displacement for each interferometer [111]. This motion corresponds to better than $\lambda/100$ for the femtosecond pulse phase stabilization.

4.3 FWM Generation in Quantum Dots

The four pulses generated from this ultrastable platform propagate in the box geometry along the four corners of a 1" square. Using a 15 cm focal length lens (L1 in Fig. 4.1), three of pulses are focused onto the sample with wavevectors $\mathbf{k}_{\mathrm{A}}$, $\mathbf{k}_{\mathrm{B}}$ and $\mathbf{k}_{\mathrm{C}}$ to a spot size of ≈ 100 μm. The FWM signal generated by all three beams is detected in the phase-matched direction $\mathbf{k}_{\mathrm{s}} = -\mathbf{k}_{\mathrm{A}} + \mathbf{k}_{\mathrm{B}} + \mathbf{k}_{\mathrm{C}}$, which is the fourth corner of the square. As previously mentioned, specific types of 2D spectra are generated by choosing a specific pulse time ordering, scanning the appropriate delay, and taking a Fourier transform of the extracted FWM signal with respect to the scanned delay. In order to avoid contributions to the FWM signal from all coherent pathways at delays shorter than the pulse duration (where the pulse time ordering is ambiguous), the experiments are performed using a delay of 200 fs for the pulse pair this is not scanned. Specific coherent pathways are isolated by taking advantage of the dipole transition selection rules, which requires the ability to independently adjust the polarization state of each pulse. Placing the necessary polarization optics inside the MONSTR is not possible. Placing them after the MONSTR poses the risk of introducing unwanted vibrations that are not compensated for using the HeNe, which could degrade the signal-to-noise ratio and introduce artifacts in the 2D spectrum; however, we find that by placing all optics downstream from the MONSTR in sturdy, monolothic mounts, we are able to incorporate the necessary polarization optics without compromising the phase stability.

Before being focused by the lens, each pulse first passes through a half-wave plate and linear polarizer (all of which are held in a sturdy, monolithic mount as indicated by the component labeled P in Fig. 4.1) so that any arbitrary linear polarization state can be achieved. An auxiliary mount

housing four quarter wave plates can be attached to circularly-polarize the pulses. The pulses then propagate through a computer-controlled shutter assembly that enables selection of any pulse combination at the sample. After passing through the lens, the pulses are partially-reflected by a single-side AR coated window to form a replica focus that is imaged onto a CCD (purchased from *The Imaging Source Europe GmbH*, model #: DMK41BF02.H, not shown in the experimental setup figures; see Bristow *et al.* for details [228]). The replica focus serves two purposes [228]: 1) it can be used for all-optical retrieval of the global phase; and 2) the re-imaged spatial interference patterns between the pulses can be used for pair-wise calibration of zero delay between the pulses. For a given pulse pair, one pulse is scanned through the other, and the visibility of the spatial interference pattern can be used to determine the pulse widths and relative delays. The field correlations are fit to a sinusoidal function with a double Gaussian envelope and offset, and the delay associated with the peak amplitude is taken as the zero delay value.

The QD samples are held in a cold finger liquid helium flow cryostat for transmission experiments as discussed in Chapter 2. The sample position and downstream optics can be adjusted to optimize the signal-to-noise when detecting the SR-FWM signal. If the SR-FWM signal is too weak, the TI-FWM signal can be detected by modulating the amplitude of pulse A at Ω_A and B at Ω_B and measuring the signal using a slow detector and lock-in amplifier with reference frequency $\Omega_R = \Omega_A - \Omega_B$. Unfortunately neither of these methods are effective for the QD samples studied here because the laser scatter into the phase-matched direction dominates the signal; thus one cannot simply optimize the FWM signal by adjusting the sample and collection optics.

We can resolve this problem by instead optimizing a different FWM signal excited under slightly different conditions than those that will be used for the QD experiments. For the GaAs IFQDs, we blue-shift the excitation laser center wavelength by ≈ 5 nm so that the laser is resonant or nearly resonant with the QW heavy-hole exciton (recall that the QD–QW separation is 10 meV, as shown in PL spectrum from this sample in Fig. 2.9). Since the nonlinear response from the QW is significantly stronger than from the QDs, the SR-FWM signal can be optimized for this excitation wavelength. Tuning the laser back in resonance with the QDs does not affect the

alignment or focusing enough to require re-optimization and, in this case, the QD FWM signal is optimized (the pulse delay time zero values are acquired with the laser resonant with the QDs). A similar procedure is not possible for the InAs SAQD samples since QW–QD wavelength separation is too large to maintain similar alignment when tuning between them. Instead, we optimize the non-resonant FWM signal that is generated in the GaAs barrier for all pulses coincident in time [150]. The non-resonant signal, which lasts only when all three pulses temporally overlap, is orders of magnitude larger than the signal from the QDs. Optimizing this signal using the aforementioned procedures is straightforward and results in the largest FWM signal from the QDs. The experiments are then performed by setting the stationary pulse delay equal to 200 fs for the experiments.

4.4 FWM Detection: Fourier-Transform Spectral Interferometry

The FWM signal amplitude and phase is measured through spectral interferometry with a phase-stabilized reference pulse [202, 229]. To avoid pre-exciting the sample, the reference, which is derived from the fourth pulse exiting the MONSTR, is routed around the sample and recombined with the FWM signal on a beam splitter, shown in Fig. 4.1. Because the signal and reference do not share common path optics, an external interferometer is required to stabilize their relative phase. The final pulse incident on the sample (pulse C for the rephasing and non-rephasing experiments, pulse A for the two-quantum experiment) and a portion of the reference pulse are focused to a spot to form a spatial interference pattern at the entrance of a 6 μm core single-mode fiber, which acts as an aperture to select a narrow portion of the interference pattern. The interference amplitude is used as the error signal for an additional servo feedback loop, as described in the previous section. A mirror attached to a PZT in the reference path is controlled by the servo electronics to stabilize the interference. Since the final pulse and the FWM signal propagate on common optics, they both experience similar phase fluctuations. Stabilizing the reference phase with respect to the final pulse thus ensures that the reference and signal phase difference is stabilized. The reference and signal are combined on a beam splitter and collinearly-propagate into a 0.75 meter imaging spectrometer, where their interference is spectrally-resolved and detected using a CCD camera. The

thermo-electrically cooled CCD has a 1024×256 array of 25 μm pixels and a 16-bit dynamic range. The reference/signal delay is adjusted using a translation stage in the reference path. The delay, denoted Δ_t, is set so that a spectral interferogram with dense fringes is observed. The maximum number of fringes is limited by the spectrometer/CCD resolution, which is ≈ 0.01 nm (≈ 20 μeV) at a center wavelength of 800 nm.

The reference/signal spectral interferogram intensity can be written as [202]

$$|E_R(\omega_t) + E_s(\omega_t)|^2 = |E_R(\omega_t)|^2 + |E_s(\omega_t)|^2 + 2\mathcal{R}e\{E_s(\omega_t)E_R^*(\omega_t)\}, \tag{4.1}$$

where $E_s(\omega_t)$ and $E_R(\omega_t)$ are the FWM signal and reference electric fields, respectively. The power spectra of the FWM signal ($|E_s(\omega_t)|^2$), reference ($|E_R(\omega_t)|^2$) and their interference ($2\mathcal{R}e\{E_s(\omega_t)E_R^*(\omega_t)\}$ are shown in Fig. 4.6(a) for the GaAs IFQD sample with the laser tuned to resonantly excite the QW transition. The FWM signal amplitude and phase can be extracted from the interference term, shown in Fig. 4.6(b). This term is isolated by subtracting the signal and reference power spectra, which are taken before the experiment. The inverse Fourier transform of the interference term contains two terms that are time-reversed from each other and separated by a time $2\Delta_t$ in the time domain, given by

$$S(t) = \mathcal{F}^{-1}\{S(\omega_t)\} = f(-t - \Delta_t) + f(t - \Delta_t), \tag{4.2}$$

where $\mathcal{F}^{-1}$ is the inverse Fourier transform and the terms $f(-t - \Delta_t)$ and $f(t - \Delta_t)$ correspond to the peaks at negative and positive time, respectively, as shown in Fig. 4.6(c). Only the term $f(t - \Delta_t)$ satisfies causality and therefore the remaining features in the time domain signal are filtered using a Heaviside theta function $\Theta(t-\Delta_t)$. The remaining term is then Fourier transformed back to the frequency domain, multiplied by a phase factor $\exp(-i\omega_t\Delta_t)$ to remove the linear phase associated with the reference/signal delay and the reference amplitude is divided out, thus isolating the complex FMW signal electric field [202]:

$$E_s(\omega_t) = \frac{\mathcal{F}\{\Theta(t-\Delta_t)\mathcal{F}^{-1}\{S(\omega_t)\}\}e^{-i\omega_t\Delta_t}}{E_R^*(\omega_t)}, \tag{4.3}$$

where $\mathcal{F}$ is the Fourier transform operator. The extracted amplitude and phase of $E_s(\omega_t)$ are shown in Fig. 4.6(d) by the black solid and red dashed curves, respectively. The signal phase, $\phi_s(\omega_t)$, is measured relative to the reference phase, $\phi_R(\omega_t)$. $\phi_s(\omega_t)$ increases by π radians across the QW exciton resonance, as expected. If the reference phase varies with ω_t, it must first be characterized by an auxiliary spectral interferometry experiment using a pulse with known spectral phase, which can be obtained from FROG measurements [230]. An overall global phase offset is still unknown, however, and can be characterized through all-optical phase retrieval outlined in Ref. [228] or through a separate pump-probe experiment as described in Ref. [104]. Only amplitude measurements are presented in this thesis and therefore details of the phase retrieval algorithms are not further discussed.

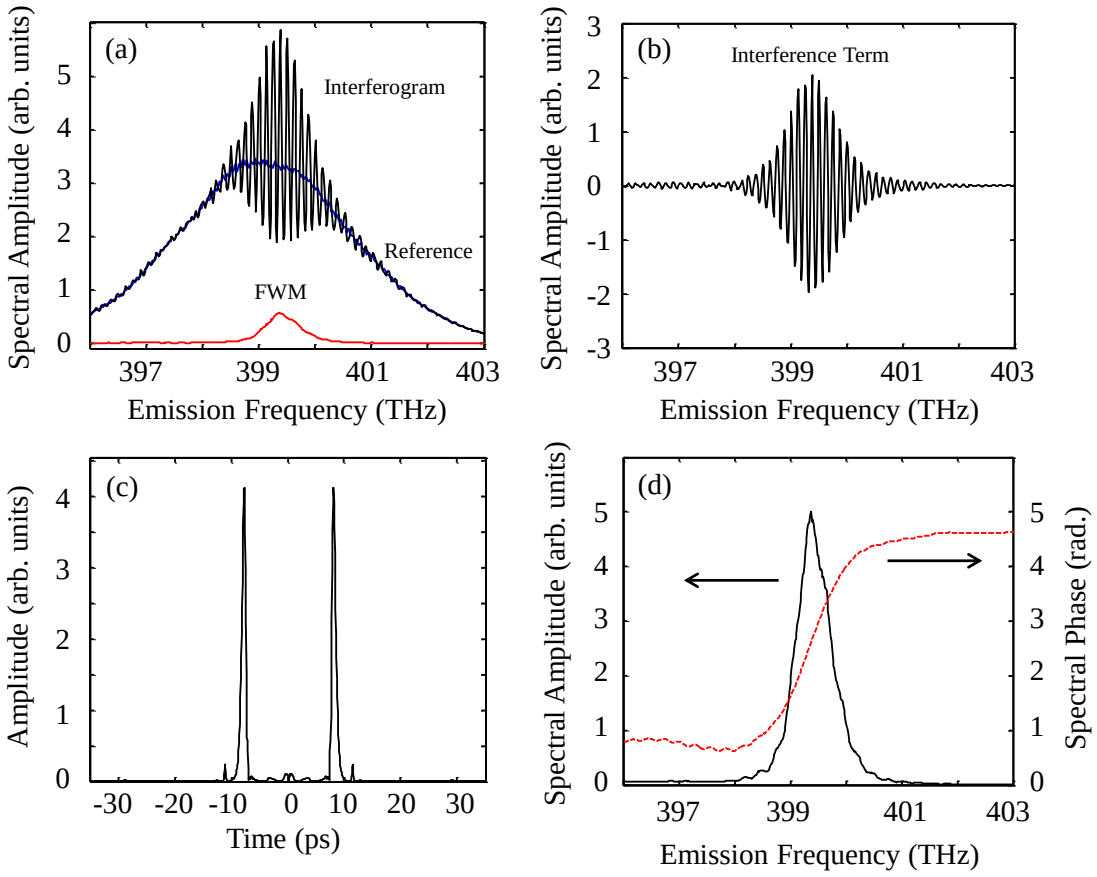

Figure 4.6: (a) Power spectra of the FWM signal, reference and their interference for the excitation pulses resonant with the QW exciton transition in the GaAs IFQD sample. (b) The interference term is isolated by subtracted the signal and reference power spectra from Eqn. 4.1. (c) The interference term is inverse Fourier-transformed into the time domain, which contains two terms time-reversed from each other. The term at positive times is isolated by multiplying the signal by a Heaviside theta function. (d) The positive time-domain signal is Fourier-transformed back to the frequency domain, multiplied by a phase factor to remove the linear reference/signal phase dependence, and divided by the reference amplitude. The retrieved FWM spectral amplitude (black solid line) and phase (red dashed line) are shown.

In practice, the FWM amplitude and phase retrieval algorithm as expressed by Eqn. 4.3 is robust when the signal-to-noise ratio is large enough such that the SR-FWM signal can be

distinguished from the background noise. For low signal-to-noise, correctly determining the delay Δ_t can be difficult, and noise that temporally overlaps with the time-domain signal will not be completely removed after it is Fourier transformed back to the frequency domain. In 2DCS spectra, scatter from the excitation lasers is observed along the diagonal in the single-quantum spectra because the pump is only self-coherent. The noise can be drastically reduced by using phase cycling techniques that eliminate laser light scatter, which were developed in NMR spectroscopy [95]. Phase cycling has been used in optical 2DCS experiments in which the pulses spatially-overlap and collinearly-propagate [188, 231] to remove noise and interference and to isolate specific quantum pathways. It has been used previously in non-collinear 2D techniques using pulse shapers [232]. We choose an alternative approach and use transmissive liquid crystal phase modulators (LCs) to toggle the phases of the first two excitation pulses incident on the sample. The LCs (purchased from Meadowlark Optics) can provide up to $\lambda/2$ retardance for wavelengths ranging from 450 nm to 1800 nm. The applied voltage to the LCs is modulated at a frequency of 4 kHz (square wave) centered at 0 ± 5 mV to avoid charge build-up that can cause damage. The modulation amplitude can be varied between 0 V and 10 V with a 20 ms response time and can be set to introduce either a 0π or 1π phase shift of the pulses. A 0π shift is defined for a modulation amplitude of 0 V. The voltage corresponding to a 1π phase shift is calibrated by monitoring the spatial interference pattern (using the replica focus discussed previously) between the pulse passing through the LC and any other pulse. The voltage is slowly ramped from 0 V to 5 V while the interference pattern is monitored, and the voltage at which the pattern has shifted by half a fringe (peak to trough) corresponds to the LC voltage for a 1π phase shift. This is repeated for the other LC and pulse so that the phases of the first two pulses incident on the sample can be toggled between 0π and 1π at each pulse delay[2] .

To understand how phase cycling eliminates laser light scatter, consider a rephasing one-quantum 2D experiment for which pulse A is incident on the sample first and interferograms are

[2] any two pulses could be used to perform the phase cycling algorithm; however if the phase of last pulse incident on the sample is toggled at each delay, the external interferometer servo loop would disengage, disrupting phase coherence. Thus we toggle the phase of the first two pulses.

recorded while the A–B delay τ is scanned. At any given τ, the spectral interferogram between the reference, FWM signal and scatter from pulse A (single pulse chosen for brevity) is given by

$$\begin{aligned} s_1 \equiv |E_R(\omega_t) + E_s(\omega_t) + E_A(\omega_t)|^2 = |E_R(\omega_t)|^2 + |E_s(\omega_t)|^2 + |E_A(\omega_t)|^2 \\ + 2\mathcal{R}e\{E_s(\omega_t)E_R^*(\omega_t) + E_s(\omega_t)E_A^*(\omega_t) + E_A(\omega_t)E_R^*(\omega_t)\}, \end{aligned} \tag{4.4}$$

where $E_R(\omega_t)$, $E_s(\omega_t)$ and $E_A(\omega_t)$ are the field amplitudes of the reference, FWM signal and pulse A scatter into the phase-matched direction, respectively, and the phase offsets are defined to be zero. The phase of the signal depends on both the phase associated with the nonlinear response, $\phi_{s,0}(\omega_t)$, and the phases of the excitation pulses, so that $\phi_s(\omega_t) = -\phi_A(\omega_t) + \phi_B(\omega_t) + \phi_C(\omega_t) + \phi_{s,0}(\omega_t)$. Toggling the phase of pulse A by 1π introduces a multiplicative $e^{\pm i\pi} = -1$ factor to the terms with $E_A(\omega_t)$ and $E_s(\omega_t)$, while toggling the phase of pulse B inverts the sign of only the terms with $E_s(\omega_t)$. Pump scatter can be eliminated by recording four interferograms (s_i) at each τ: $s_1 \rightarrow$ no phase shifts for any pulse; $s_2 \rightarrow 1\pi$ shift for pulse A; $s_3 \rightarrow 1\pi$ shift for pulses A and B; $s_4 \rightarrow 1\pi$ shift for pulse B. The corresponding interference terms are given by

$$\begin{aligned} s_2 &= 2\mathcal{R}e\{-1 \cdot E_s(\omega_t)E_R^*(\omega_t) + E_s(\omega_t)E_A^*(\omega_t) + -1 \cdot E_A(\omega_t)E_R^*(\omega_t)\} \\ s_3 &= 2\mathcal{R}e\{E_s(\omega_t)E_R^*(\omega_t) + -1 \cdot E_s(\omega_t)E_A^*(\omega_t) + -1 \cdot E_A(\omega_t)E_R^*(\omega_t)\} \\ s_4 &= 2\mathcal{R}e\{-1 \cdot E_s(\omega_t)E_R^*(\omega_t) + -1 \cdot E_s(\omega_t)E_A^*(\omega_t) + E_A(\omega_t)E_R^*(\omega_t)\}. \end{aligned} \tag{4.5}$$

(4.6)

The FWM/reference interference term is isolated by combining the interferograms according to: $s_{net} = (1/4)(s_1 + s_3 - s_2 - s_4) = 2\mathcal{R}e\{\cdot E_s(\omega_t)E_R^*(\omega_t)\}$. Combining phased interferograms this way will also cancel scatter from the other two pump pulses as well as any other nonlinear interactions that are not associated with the three-pulse FWM signal. The end result is an increase in the signal-to-noise ratio by up to a factor of 10^4 with negligible increase in the data acquisition time, since the LC response time (20 ms) is approximately an order of magnitude shorter than the

time required to increment the pulse delay. Moreover, the phase cycling algorithm automatically removes the power spectra of the reference, FWM signal and scattered laser light. The primary advantage of eliminating this step from the FWM field extraction procedure is that the FWM power spectrum, which depends on the pulse delays, no longer needs to be measured at each delay before data acquisition. Since the limiting factor for the data acquisition time is the mechanical motion of the delay stages, eliminating this step reduces the acquisition time by a factor of ≈ 2.

4.5 Generating and Analyzing 2D Spectra

A 2D data array is constructed by repeating the FWM signal extraction algorithm on the phase-cycled interferograms at each delay. The incremental adjustment of any one of the pulse delays is indicated by the flow chart in Fig. 4.7(a). Consider a rephasing one-quantum experiment that requires scanning the delay τ. At the start of the scan, a phase-cycled interferogram is acquired. Then the HeNe diagnostic error signal associated with the upper deck interferometer is measured (V_{err1}). Next the interdeck servo loop is disengaged, followed by the upper deck servo loop. The error signal of the upper deck interferometer is re-measured (V_{err2}) to determine the change in the path length difference (δ) of the upper deck after disengaging the loops, which is calculated using the expression $\delta = (\lambda/2\pi) \cdot \mathrm{asin}[V_{err2} - V_{err1}/V_0]$, where λ is the HeNe wavelength. V_0 is half the interferometer error signal peak-to-peak amplitude, which is set to 2 V_{pp} for all interferometers by adjusting the input gain on the servo loop filters. The delay stages are stepped in integer increments of the HeNe wavelength $\lambda/4$, since the servo loop filters are designed to lock the signal to a 0 V DC reference signal, which corresponds to the zero crossings of the HeNe interference diagnostic error signals. Each incremental step is adjusted by $\pm\delta$ to account for changes in the interferometer optical path length when the servo loop filters are disengaged. The delay stage Y is scanned a specified distance after which the HeNe error signal is re-measured (V_{err}) to check for glitches in the stepping and locking operations. The upper deck loop is re-engaged, followed by the inter-deck loop. A phase-cycled spectrum is acquired, and the process is repeated until the specified total number of spectra are measured.

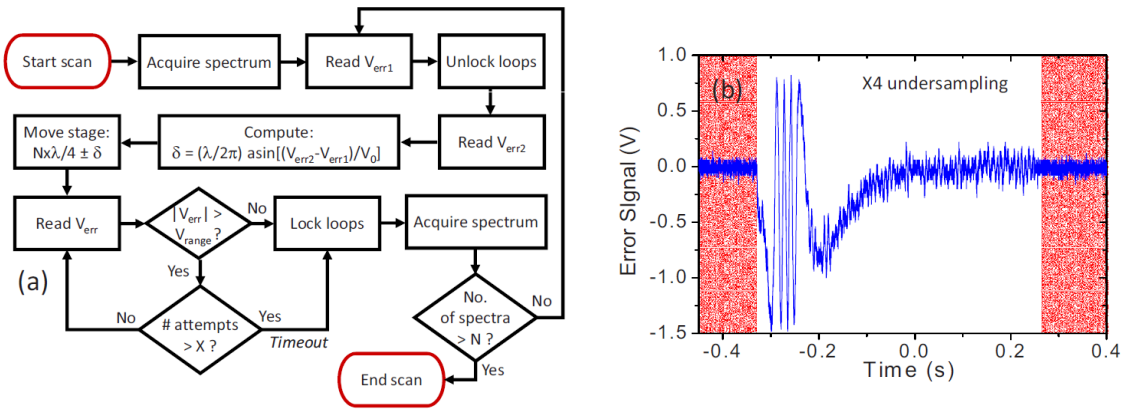

Figure 4.7: (a) Flow chart of the data acquisition and stage stepping algorithm. After a phase-cycled spectrum is acquired, the HeNe error signal is measured (V_{err1}). The servo loops are disengaged and the error signal is measured again (V_{err2}) to compute the change in optical path length ($\pm\delta$) after the loops are disengaged, where V_0 is half the peak-to-peak error signal. The stage steps the specified distance, the servo loops are re-engaged, the error signal is measured again (V_{err}) to check for glitches, and the process is repeated until the total specified number (N) of spectra are acquired. (b) HeNe error signal for stepping the delay τ by λ, corresponding to an undersampling ratio of four. The shaded regions indicate when the loop filter is engaged. Reproduced from Bristow *et al.*, Review of Scientific Instruments **80**, 073108 (2009).

An incremental stage distance of $\lambda/4$ corresponds to one fringe at the HeNe diagnostic photodiode and a $\Delta\tau = 1.06$ fs minimum delay of the femtosecond pulses. The Nyquist frequency associated with this delay is $f_{Nyq} = 1/2\Delta\tau = 473.61$ THz, which is the maximum frequency that can be accurately reconstructed without aliasing effects [233]. The most common signal reconstruction techniques produce the smallest of $f_{alias}(N) = |f - 2Nf_{Nyq}|$, where f is the frequency of the signal and N is any integer; satisfying the Nyquist criterion ensures that $f_{alias}(N = 0) = |f|$, i.e. the signal is properly sampled. Many of the semiconductor materials of interest studied with 2DCS have resonances centered at several hundred THz within a spectral window smaller than 10's of THz. In this case, aliasing can be exploited by appropriately undersampling the signal with a step size larger than 1.06 fs, enabling faster data acquisition. For example, the QW and QD transitions

in the GaAs IFQD sample are at 399 THz and 396.5 THz, respectively. Scanning the stages such that 32 HeNe fringes pass at the diagnostic photodiodes corresponds to a travel distance of 10.1 μm and a Nyquist frequency of $f_{Nyq} = 1/(2 \cdot 33.8\text{fs}) = 14.8$ THz. In this case, the lowest alias of the signal (centered at ≈ 398 THz) is $f_{alias}(N = 13) = |398 \text{ THz} - 2 \cdot 13 \cdot 14.81 \text{ THz}| = 12.5$ THz. Thus for this undersampling ratio the signal will appear at $\omega_\tau/2\pi = 12.5$ THz with a bandwidth of ± 2 THz, which lies below f_{Nyq} and will be properly reconstructed. In practice, the aliased signal is measured and this process is worked in reverse to reconstruct the correct spectrum by unfolding the image around the Nyquist frequency. The HeNe error signal shown in Fig. 4.7(b) corresponds to a stage translation of one HeNe wavelength so that four fringes (i.e. undersampling ratio of four) pass on the photodiode. The fast oscillations are from the motion of the stage when the servo loop is disengaged. After the stage motion has settled (within a couple hundred milliseconds), the servo loop filter is re-engaged for data acquisition (shaded regions). 2D spectra have been accurately reconstructed using undersampling ratios of up to 128, depending on the center frequency and bandwidth of resonances studied.

The total number of incremented delays is determined by the undersampling ratio and the signal decay rate. A windowing function is applied to the data with respect to the scanned delay so that the signal gradually decays to zero; otherwise, abrupt edges in the time domain would introduce oscillations in the frequency domain, and these truncation artifacts inhibit quantitative analysis of the 2D spectrum. The maximum delay is defined as the time at which the windowed signal accurately reproduces the real signal, so that if the signal has decayed below the minimum detection threshold at a time τ_{max}, then the maximum number of data points is $T_{max} = \tau_{max}/\Delta\tau = \tau_{max}/(N\lambda/4 \cdot 2 \cdot (1/c))$, where N is the undersampling ratio and c is the speed of light in vacuum. After all interferograms are recorded for the total specified number of delays, the complex FWM signal at each delay can be extracted using the procedure outlined by Eqn. 4.3. A 2D spectrum is generated by taking a Fourier transform of the data set with respect to the stepped delay. The procedure outlined in this section for scanning the delay τ is also used for scanning the other delays to generate all four types of 2D spectra.

Chapter 5

Influence of Confinement on Exciton-Phonon Coupling

In solid-state materials, carrier-phonon interactions are a significant source for loss of coherence. From fundamental arguments based on momentum and energy conservation, inelastic exciton-phonon scattering was expected to be inhibited in QDs because of the discrete nature of the density of states. This concept led to the prediction of a "phonon bottleneck" [113] and suggested that the homogeneous line width would be radiatively limited at low temperatures [28]. Moreover, the bottleneck effect was expected to prevent line width broadening at elevated temperatures, since the difference in excited state energy levels in the dots were large compared to the typical acoustic phonon energies. These ideas generated considerable interest and motivated numerous works examining environmental effects on the emission properties of QDs. Photoluminescence spectra of single dots revealed that the exciton-phonon coupling resulted in spectral line shapes that were comprised of a broad background superimposed onto a narrow Lorentzian, and the relative amplitude of the background compared to the Lorentzian depended on the material composition and size of the dots [28, 146, 147, 148]. Similar conclusions were drawn from FWM experiments on QD ensembles from which an initial fast decay of the signal was attributed to the broad background and a slow decay to the radiatively-limited homogeneous line width [150]. Common to all experiments was the observation of a strong thermal component of both the broad background and narrow Lorentzian line widths. Despite the bottleneck effect, the broadening has been attributed to phonon activation of the exciton to higher-lying energy levels [28, 146, 148]; however this idea is inconsistent with observations in other works, which have provided evidence

that inelastic scattering cannot account for the amount of broadening observed and instead pure exciton-phonon dephasing processes must be considered [147, 149, 150, 114].

These observations have stimulated numerous theoretical studies investigating the origins of the line shape and the strong thermal component to the homogeneous line width [151, 152]. Different approaches are used to describe the exciton-phonon interactions, most of which are modeled using deformation potential coupling of longitudinal acoustic phonon modes to the exciton states. In Section 5.1, a description of the exciton-phonon interaction mechanism and the main results from the models will be discussed. In Section 5.2, the temperature and dot size dependence of the GaAs IFQD homogeneous line widths extracted from 2D spectra will be presented. In Section 5.3, preliminary results and analysis of the ZPL temperature dependence of excitons in the InAs SAQDs will be presented.

5.1 Background

The workhorse for calculating exciton-phonon interactions has been the independent boson model, which allows for an exact analytical solution for the linear polarization [146] and third-order nonlinear response [234]. This model does not consider the exciton-phonon interaction as a perturbation, but instead considers new eigenstates arising from the mixing of discrete exciton states with a quasi-continuum of phonon modes. Transitions between these mixed states give rise to an exciton-phonon band which can describe the broad background observed in the QD emission spectra. The general Hamiltonian for the coupled exciton-phonon system is given by [146]

$$\hat{H} = E_0 c^\dagger c + \sum_{\vec{q}} \hbar\omega_{\vec{q}} (b_{\vec{q}}^\dagger b_{\vec{q}} + \frac{1}{2}) + c^\dagger c \sum_{\vec{q}} M_{\vec{q}} (b_{\vec{q}}^\dagger + b_{\vec{q}}), \tag{5.1}$$

where c and $b_{\vec{q}}$ ($c^\dagger$ and $b_{\vec{q}}^\dagger$) are the respective annihilation (creation) operators of the exciton, with energy E_0, and the phonon, with momentum $\vec{q}$ and energy $\hbar\omega_{\vec{q}}$. The first two terms are the exciton and phonon population energies of the system. The last term is the exciton-phonon interaction, whose strength is characterized by the matrix elements of $M_{\vec{q}}$. The ground state of the system is the

crystal lattice coupled to a phonon reservoir, shown in Fig. 5.1 as the lower-energy manifold. The higher-energy excited state manifold is an admixture of the pure exciton states with the phonon reservoir. In Fig. 5.1, only the crystal ground state manifold and the ground state exciton manifold are shown for a single phonon mode with wave vector $\vec{q}$. The phonon modes are assumed to be quantum harmonic oscillators with energy spacing between the n and $n+1$ levels equal to $\hbar\omega_{\vec{q}}$.

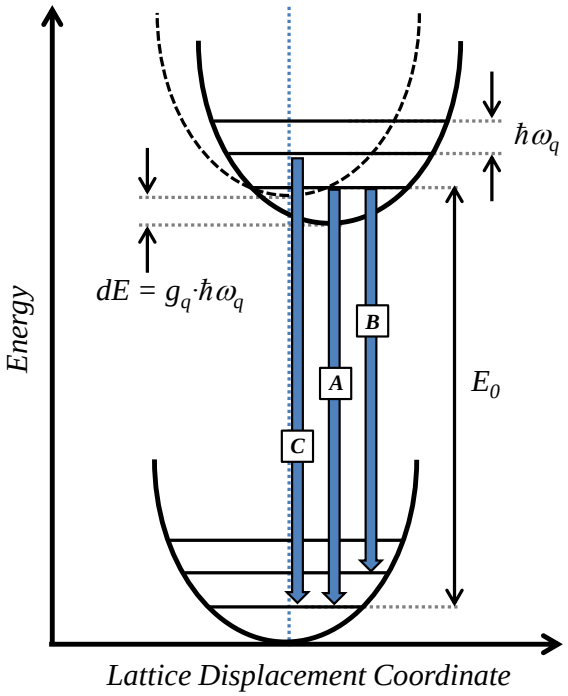

Figure 5.1: Schematic diagram of the exciton-phonon system for a specific phonon mode q with energy $\hbar\omega_q$ in the configuration coordinate space. The parabolas are harmonic potentials of the crystal lattice ground state and the exciton ground state with (solid lines) and without (dashed line) the exciton-phonon interaction. The interaction leads to an exciton-polaron shift dE. The transitions labeled A, B and C are examples of radiative recombination processes involving zero phonons (ZPL), one phonon emission and one phonon absorption, respectively.

Analytical solutions of the optical polarization based on the Hamiltonian in Eqn. 5.1 can be obtained when neglecting the off-diagonal elements of $M_{\vec{q}}$. This approximation ignores mixing of the excited exciton states and is valid only when the thermal energy, $k_b T$, is smaller than the exciton

energy level spacings. The primary effect of coupling of an exciton with phonon mode $\vec{q}$ is a change in the equilibrium lattice position, which shifts the exciton energy by the temperature dependent exciton-polaron energy $dE = M_{\vec{q}}^2/\hbar\omega_{\vec{q}} = g_{\vec{q}} \cdot \hbar\omega_{\vec{q}}$, where $g_{\vec{q}}$ is defined as the coupling constant of the exciton with phonon mode $\vec{q}$. As illustrated in Fig. 5.1, the exciton-polaron shift allows optical transitions between states with different phonon occupation numbers, two of which are labeled as transitions B and C in Fig. 5.1. Without the shift, the wave functions of the states connected by transitions B and C are orthogonal so that the transition dipole moment is zero. The transition labeled by A is called the zero-phonon line (ZPL), since it connects states in the upper and lower manifolds with similar phonon occupation numbers. The dipole moment for state A is non-zero even if $dE = 0$. Based on this simple picture, without specifying the exciton-phonon interaction mechanism, one can intuitively understand the origin of the emission line shapes of the QDs. The narrow Lorentzian, which is always present in the spectra, arises from the ZPL transitions, whereas the broad background arises from the transitions between states with different phonon quantum numbers. Thus, the sidebands will be present only when the exciton-polaron shift is large enough so that the dipole moment between states with different occupation numbers is comparable to that of the ZPL transition.

The matrix elements of $M_{\vec{q}}$ and the transition probabilities can be calculated by explicitly writing the form for the exciton-phonon interaction. Often, several assumptions are made beforehand. First, the dominant interaction term between excitons and phonons arises from the deformation potential coupling to longitudinal acoustic (LA) phonons [151], so transverse phonon modes, piezoelectric coupling and optical phonons are ignored. Moreover, the elastic properties of the QD are assumed to be similar to those of the surrounding matrix, so that bulk phonon modes can be used. Lastly, the QD confinement potential is either considered strongest in the growth direction and the QD shape assumed symmetric so that the the exciton wave function is isotropic in the transverse directions, or a spherical confinement potential and corresponding exciton wave functions are used. In either case, the exciton wave function can be characterized by a localization length parameter ξ. Coulomb interactions between the electron and hole are usually ignored. With

these assumptions, the diagonal matrix elements of $M_{\vec{q}}$ can be written, for an exciton state $|X\rangle$, as [151]

$$M_{\vec{q}} = \sqrt{\frac{\hbar|\vec{q}|}{2\rho u_s \nu}} \cdot (D_c\langle X|e^{i\vec{q}\cdot\vec{r}_e}|X\rangle - D_v\langle X|e^{i\vec{q}\cdot\vec{r}_h}|X\rangle), \tag{5.2}$$

where ρ is the mass density, ν is the quantization volume, and D_v (D_c) is the deformation potential of the valence (conduction) band. The deformation potential characterizes the carrier-phonon coupling strength and describes the change in the electronic band structure due to displacement of the lattice equilibrium coordinates. The acoustic phonon dispersion relation is assumed to be isotropic, i.e. $\omega(\vec{q}) = u_s \cdot q$, where u_s is the angular averaged sound velocity of the mode. Thus each phonon mode can be characterized by its wave vector modulus q and energy $\hbar\omega_q$. In this case, one can define an exciton-phonon coupling constant, $g(q)$, which is integrated over all directions of $\vec{q}$ and is related to the exciton-phonon coupling matrix through $g(q) = (M_q/\hbar\omega_q)^2$. Phonons with wave vectors equal to $q \sim 1/\xi$ interact most strongly with the excitons, so that phonons with energies greater than $\hbar\omega_q \approx 2\hbar u_s/\xi$ only weakly couple with the excitons. Using typical numbers for GaAs, for example, the deformation potential coupling of LA phonons with excitons is limited to phonons with energy less than ≈ 2 meV. Moreover, for weakly-confining QDs with large ξ, only phonons with small q interact with the excitons and the exciton-polaron shift is reduced compared to strongly-confining dots. In this case, the exciton-phonon background is narrow and hidden by the ZPL in the optical spectrum. Furthermore, the magnitude of $g(q)$ decreases for dots with large ξ, leading to a reduction in the broad background amplitude.

The exciton emission or absorption line shapes are dictated by the strength of the exciton-phonon coupling. The ZPL transition is allowed irrespective of the coupling strength, and the background is comprised of a continuum of transitions between states with different phonon occupation numbers. When modeling this phenomenon, the continuum of phonon modes is discretized into a set of N modes q_i, where each mode can be described by the diagram in Fig. 5.1 with a coupling constant $g(q_i)$. In this model, each transition between states with different phonon occupation

numbers is artificially broadened to have a similar line width as the ZPL. For example, Besombes *et al.* can accurately reproduce their photoluminescence line shapes using $N = 12$ phonon modes, and they only consider phenomenologically-broadened transitions between states that are different in the phonon occupation number by zero, one, and two [146].

A severe limitation of the independent boson model is that broadening of the ZPL can only be included phenomenologically. Being linear in the displacement coordinates and diagonal in the exciton states, the model only considers an impulsive excitation of a phonon cloud, which quickly decays into a finite lattice distortion that is constant during the subsequent time evolution of the polarization. This constant distortion, which is the origin of the exciton-polaron energy shift, introduces the phonon satellite peaks but cannot dephase the transitions. Thus the model cannot provide insight into the mechanisms responsible for the ZPL temperature dependence. This drawback can be mitigated by taking into account the off-diagonal elements of the carrier-phonon coupling term $M_{\vec{q}}$, i.e. phonon-assisted transitions of the exciton to higher-lying energy states. Calculations performed by Muljarov and Zimmermann show that by considering these elements, an exciton-phonon interaction term quadratic in the displacement coordinates appears [152]. This term can account for broadening of the ZPL through the temperature dependent phonon occupation, described by the Bose function $N_{\vec{q}} = 1/[\exp(\hbar\omega_{\vec{q}}/k_bT)-1]$. Similar to the independent boson model, their calculations set the wave vector limit for exciton-phonon coupling at $q \sim 1/\xi$. Their results demonstrate that the optical polarization quickly decays on a timescale $\xi/u_s \approx 1$ ps, which reflects the formation of the polaron cloud and provides the broad background in the optical spectrum. The resulting finite lattice distortion, however, is not completely stable because of the quadratic coupling term. This term describes scattering into the higher-lying energy states, which distorts the polarization and leads to an exponential decay. This exponential decay describes the narrow ZPL in the optical spectrum and is in agreement with the experiments on strongly-confining QDs [150].

In their calculations, Muljarov and Zimmerman clarify that their derivation is valid only if the relevant LA phonon energies are much smaller than the typical spacing between the exciton

energy levels, which implies that the phonon-assisted transitions between excited states are virtual and do not affect the exciton population state. Therefore the quadratic coupling is useful only for strongly-confining QDs, such as the InAs SAQDs, where the excited states are spaced by tens of meV and the acoustic phonon energies are less than a few meV. However, for the GaAs IFQDs, the acoustic phonon energies are comparable to the energy level spacing, invalidating this approach. Nonetheless, we show in the following sections that the temperature dependent broadening of the ZPL can still be described using the Bose function, which provides a measure of the typical energy of phonons strongly coupled to the excitons.

5.2 Zero-Phonon Line Broadening

2D rephasing amplitude one-quantum spectra acquired from the GaAs IFQDs using co-linear excitation and detection (HHHH) are shown in Figs. 5.2(a) and 5.2(b) for low (6 K) and high (50 K) temperature, respectively. The results discussed in this section are all performed using an excitation photon density at the sample of 1×10^{12} photons·pulse^{-1}·cm^{-2}, which is the maximum intensity while remaining in the $\chi^{(3)}$ regime and corresponds to ≈ 0.1 excitons excited per QD on average. Each spectrum features a QW (X_{QW}) and QD (X_{QD}) exciton peak, and a QW biexciton peak (B_{QW}) appears red-shifted along the emission energy axis from X_{QW} by the biexciton binding energy. A QD biexciton peak can be expected, but it is too weak to be observed using this polarization sequence. The peak of the excitation pulse spectrum is centered on X_{QD}. Both spectra are normalized to their maximum amplitude, and the contours in the spectrum in Fig. 5.2(b) are scaled so that the maximum plotted amplitude is equal to 0.1. As discussed in Chapter 3, the cross-diagonal line shape can be fit using a $\sqrt{Lorentzian}$ function, and the full-width at half-maximum (FWHM) of the fit is equal to twice the homogeneous line width, γ. The homogeneous line shapes (points) and the fits (solid lines) obtained at the maximum amplitude of the QD inhomogeneous distribution are shown in Figs. 5.2(c) and 5.2(d) for temperatures 6 K and 50 K, respectively.

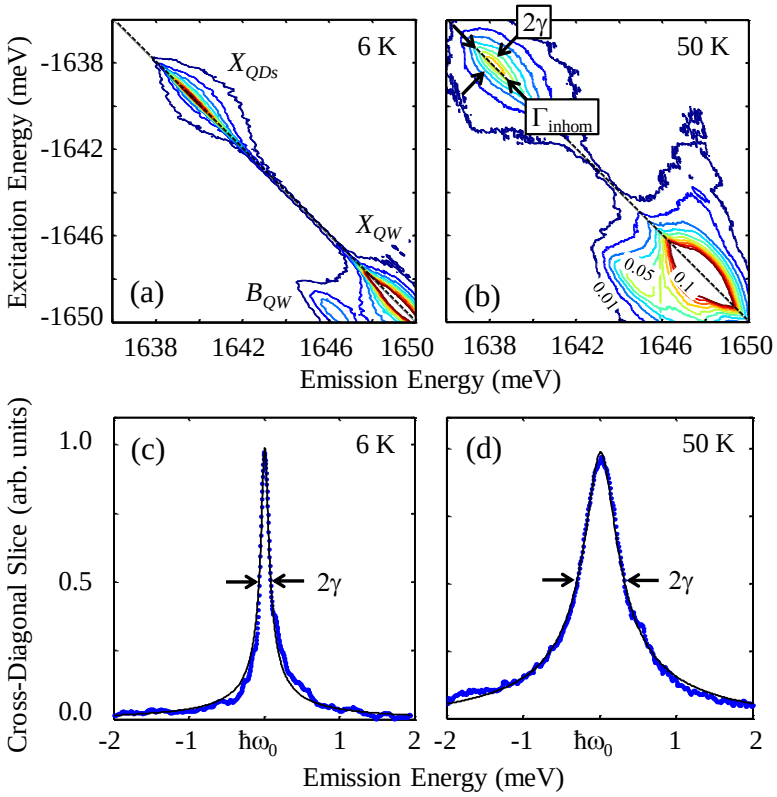

Figure 5.2: Normalized rephasing one-quantum amplitude spectra of the GaAs IFQD sample are shown for a sample temperature of (a) 6 K and (b) 50 K. Each spectrum features a QW (X_{QW}) and QD (X_{QD}) exciton peak and a QW biexciton peak (B_{QW}) red-shifted from X_{QW} by the biexciton binding energy. Cross-diagonal slices taken at the maximum amplitude of X_{QD} are shown for (c) 6 K and (d) 50 K, where the data (points) are fit using a $\sqrt{Lorentzian}$ function (solid line) with a FWHM equal to 2γ.

The fact that a $\sqrt{Lorentzian}$ function fits the line shapes well at both low and high temperature indicates that the broad phonon sidebands attributed to transitions between states with different phonon occupation numbers are absent; thus the FWHM of the fits provides a measure of the ZPL width. Figures 5.2(c) and 5.2(d) clearly show that the ZPL is broader at 50 K than 6 K. Figure 5.3(a) shows the projection of the QD signal onto the vertical axis (points), which gives the absorption line shape, with line center of the inhomogeneous distribution marked by the vertical arrows. With an increase in the temperature, the band-gap decrease red-shifts the inhomogeneous

distribution. The line shape at both temperatures is asymmetric with with a tail on the high-energy side of the distribution. In photoluminescence, a similar asymmetry was observed and was attributed to the lack of translational invariance of the excitons confined in the dots, which implies that the exciton wave function is described by a distribution of wave vectors centered around $\vec{k} = 0$. The optical density – which is proportional to the absorption spectrum – was derived by Schnabel *et al.* and calculated by Leosson *et al.* for a disordered potential with average confinement energy E_0 to be [235, 236]

$$\alpha(E) \propto \frac{1}{2\eta}\left[1 + \mathrm{erf}\left(\frac{E - E_0}{\sigma_E} - \frac{\sigma_E}{2\eta}\right)\right] \cdot e^{(\sigma_E/2\eta)^2 - (E-E_0)/\eta}, \tag{5.3}$$

where 'erf' is the error function, σ_E is the FWHM of the disordered confinement potential energy distribution, and $\eta = \hbar^2\Delta\vec{k}^2/2M$ is defined to be the localization energy parameter for a wave vector distribution $\Delta\vec{k}$ and exciton mass M. The model fits the projections in Fig. 5.3(a) well for both temperatures and is consistent with the idea that the excitons are weakly localized in the QDs. An advantage of performing 2DCS on the QDs is that the inhomogeneous and homogeneous line widths are uncoupled, enabling us to extract the homogeneous line width dependence on the QD resonance energy by taking cross-diagonal slices along the diagonal. The ZPL width dependence on the QD resonance energy is shown in Fig. 5.3(b) for a set of temperatures ranging from 6 K to 50 K. The line center of the inhomogeneous distribution at each temperature is indicated by the solid circles. The ZPL width increases with energy (decreasing QD size) across the inhomogeneous distribution for all temperatures, with the effect being more dramatic at elevated temperatures. Oscillations in the ZPL widths are due to time truncation artifacts of the FWM signal and are more pronounced at lower temperatures, where the signal dephases more slowly. At each temperature, a linear fit is performed (solid lines in Fig. 5.3(b)) and values from the fits are used in the subsequent discussion.

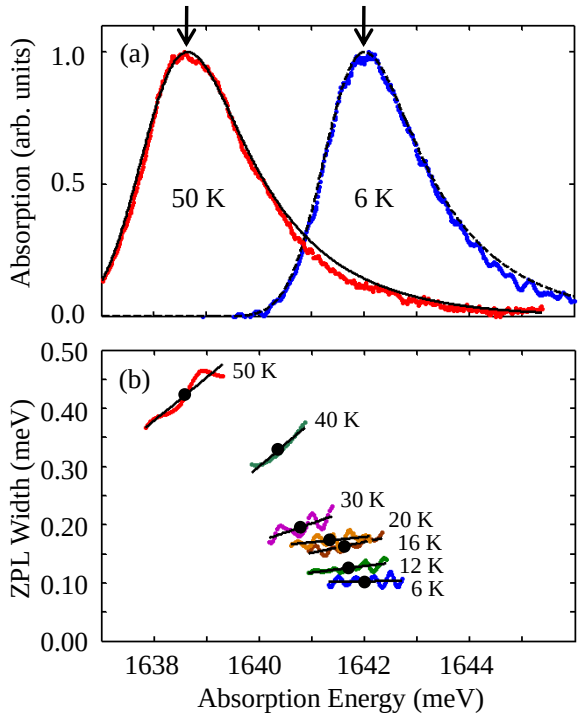

Figure 5.3: (a) The asymmetric absorption line shape, obtained by projecting the 2D amplitude rephasing spectrum onto the vertical axis. The line shapes (points) are reproduced using Eqn. 5.3 (solid line). Line center of the inhomogeneous distribution is marked by the vertical arrows. (b) The ZPL widths (points) within the FWHM of the inhomogeneous distribution for different sample temperatures. Line center of the inhomogeneous distribution at each temperature is marked by the larger solid circle. Linear fits (solid lines) are performed at each temperature.

The ZPL width temperature dependence is shown in Fig. 5.4(a) for QDs at line center of the inhomogeneous distribution (points). The temperature dependence is fit using a Bose function and offset, given by [28]

$$\gamma_\mu(T) = \gamma_\mu^* + \sum_{\nu>\mu} \gamma_{\mu\nu} \cdot N(E_{\mu\nu}, T), \tag{5.4}$$

where μ and ν are indices of the exciton ground state and higher-lying states, respectively, $N(E_{\mu\nu}, T) = 1/[\exp(E_{\mu\nu}/k_bT) - 1]$ is the Bose function that describes the phonon occupation of a single mode with energy $E_{\mu\nu}$, and $\gamma_{\mu\nu}$ is the coupling pre-factor characterizing the exciton-phonon interaction

strength. The first term in Eqn. 5.4 represents a temperature independent dephasing offset, while the second term describes the exciton-phonon interaction. A single term from the sum in Eqn. 5.4 is used to fit the data, shown in Fig. 5.4(a) as the solid line. The fit matches the data for an activation energy of $E_{12} = 4.4 \pm 0.8$ meV and an offset of $\gamma_1^* = 0.11 \pm 0.01$ meV. The offset is significantly larger than the radiatively-limited line widths reported in the literature for IFQDs, which are typically ten's of μeV. The significant low temperature broadening we observe arises predominantly through excitation-induced dephasing and is described in more detail in the next Chapter.

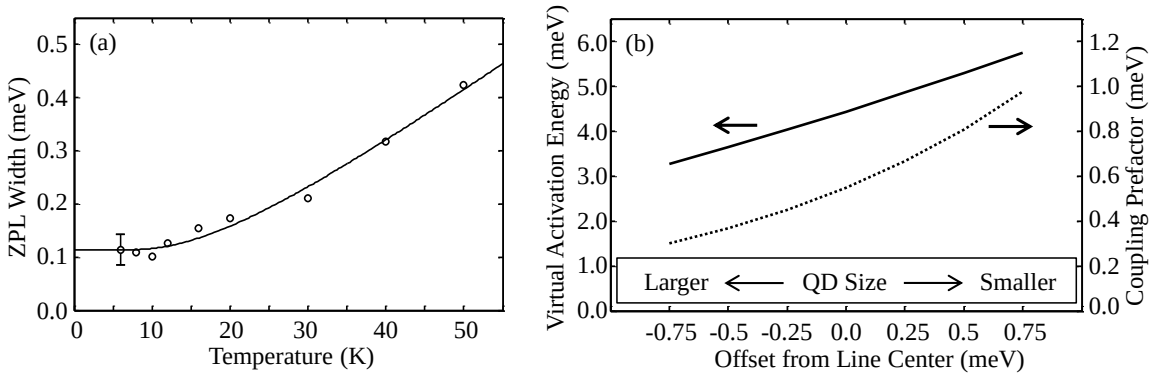

Figure 5.4: (a) Temperature dependence of the ZPL width measured at line center of the inhomogeneous distribution. The data (points) are fit with Eqn. 5.4 using a phonon energy $E_{12} = 4.4 \pm 0.8$ meV and an offset of $\gamma_1^* = 0.11 \pm 0.01$ meV. The absence of a phonon-activation peak in the data reveals that the dominant thermal broadening mechanism is virtual transitions between states, which is an elastic exciton-phonon scattering process. (b) The virtual activation energy (solid line) and coupling pre-factor characterizing the strength of the exciton-phonon interaction (dashed line) are shown for QDs with different resonance energies (sizes).

Since the model fits the data well and the phonon energy E_{12} is similar to the energy spacing between the exciton ground and excited states, one could speculate that the increase in the ZPL width with temperature stems from phonon-assisted excitation of the exciton to a higher-lying energy state. However, we can rule out this possibility since no additional features consistent with

this mechanism appear in the spectra. Since the inelastic activation mechanism is an incoherent process that would change the exciton population state, we can map out the dynamics of this process by measuring multiple rephasing one-quantum spectra at different delays T, during which time the system is in a ground or excited population state. If the exciton is excited to an energy level ≈ 4.4 meV higher, then a peak will appear blue-shifted along the emission energy axis by this energy at a time characteristic of the exciton-phonon scattering process. This peak would represent excitation at the exciton ground state energy and emission at the excited state energy. Spectra were taken for T up to 300 ps, which is almost an order of magnitude longer than the dephasing time, and no signatures of inelastic exciton-phonon scattering appear at this energy. This observation reveals that elastic pure dephasing from exciton-phonon scattering broadens the ZPL.

Intuitively, this result can be understood using the model based on virtual transitions between states proposed by Muljarov and Zimmermann discussed in the previous Section: the exciton-phonon scattering mechanism results in virtual transitions of the exciton either within the ground state or between the ground and excited states [151], which interrupts the coherence oscillations during τ and t and increases the dephasing rate. If the energy of phonons that strongly couple to the excitons, determined by the constant $g(q)$ discussed in the previous Section, is small relative to k_bT, then the temperature dependence exhibits a linear behavior since the Bose function can be approximated as $N(E,T) \approx k_bT/E$. This might occur when the energy level spacing of the excited states is much larger than the relevant phonon energies, so that only virtual transitions within the ground state occur. On the other hand, if the relevant phonon energies are similar to k_bT, the above approximation no longer holds. This behavior might occur when the relevant phonon energies are similar to the energy level spacing, so that virtual transitions between the ground and excited states are important. At elevated temperatures (> 35 K) and after long pulse delays ($T > 100$ ps), we observe incoherent transfer from the QD states to the delocalized QW states, which is an inelastic broadening mechanism that contributes to the ZPL width (discussed in detail in Chapter 7). However, the timescale of this process is almost an order of magnitude longer than the QD exciton dephasing time and the energy does not match the phonon activation energy

$E_{12} = 4.4$ meV from the fit to the data, so it cannot be responsible for the ZPL width broadening discussed in this Section.

This analysis is repeated as a function of energy offset from line center of the inhomogeneous distribution to characterize the dependence of the exciton-phonon interaction on the QD resonance energy (i.e. QD size). Figure 5.4(b) shows that the virtual activation energy, E_{12} (solid line), and the exciton-phonon interaction pre-factor, γ_{12} (dashed line), both increase with increasing exciton energy (decreasing QD size). An increase in E_{12} is a direct result of the ground-to-excited state energy separation increasing with decreasing QD size. The resonance energy dependence on the QD size is calculated by solving Schrödinger's equation for a finite three-dimensional box using an effective mass $M = 0.18 \cdot m_0$, where m_0 is the electron mass, and a binding potential of 10 meV. The QD size is adjusted until the emission spectrum matches results obtained from single dot photoluminescence spectra of a similar sample [27], which indicates that the typical QD in the sample has lateral dimensions of ≈ 40 nm. Changes in the QD size are mapped onto changes in the resonance energies, and the calculations reveal that the energy spacing between the exciton ground and first excited states changes by 1 meV for a change in the exciton ground state resonance energy of 0.8 meV, which agrees well with the slope of E_{12} in Fig. 5.4(b). The increase in γ_{12} for higher energy, smaller dots is consistent with Takagahara's work that predicts greater exciton-phonon coupling for smaller dots [151]. Intuitively, this result can be understood by considering that the exciton wave function in smaller dots is described by a larger $\Delta\vec{k}$, which in turn enables coupling of the exciton with more phonon modes.

5.3 Enhanced Exciton-Phonon Coupling in InAs SAQDs

The homogeneous line shapes from the GaAs IFQDs do not show any signs of the broad phonon sidebands, even at elevated temperatures. This result is not surprising, however, since excitons are only weakly-localized in the dots, so the amplitude of the coupling constant $g(q)$ is small. On the other hand, excitons are strongly-confined in the InAs SAQDs, which enhances the exciton-phonon interactions and alters the optical properties of the ground and first excited

state transitions. In this Section, preliminary results on our studies of the ZPL width broadening mechanisms in the InAs SAQD sample annealed at 900 °C are discussed and a model is proposed to explain the data.

5.3.1 Phonon Sidebands

2D one-quantum rephasing amplitude spectra are shown in Figs. 5.5(a)-(c) for a sample temperature of 10 K, 50 K and 70 K, respectively. The spectra are acquired using co-linearly polarized excitation and detection (HHHH) and an incident photon density of 3×10^{12} photons·pulse^{-1}·cm^{-2}, which is the maximum intensity of the incident pulses while remaining in the $\chi^{(3)}$ regime. At this intensity the estimated exciton density per QD is 0.1. Each spectrum features a single peak inhomogeneously broadened along the diagonal, and a weak peak red-shifted by the biexciton binding energy along the emission energy axis. Cross diagonal-slices taken at line center of the inhomogeneous distribution are shown in the bottom row of Fig. 5.5 for the three temperatures. Both neutral and charged excitons (trions) contribute to the nonlinear optical response for this polarization sequence. When using an HVVH polarization sequence, which is discussed in more detail in the next Chapter, no quantum pathways exist for the exciton, so any remaining signal on the diagonal dashed line is attributed to the trion nonlinear response. The signal for this polarization is two orders of magnitude weaker than for the HHHH polarization sequence; this result suggests that the trion contribution for the HHHH polarization scheme can be ignored since the signal is dominated by the exciton nonlinear response. In this case the parameters extracted from the spectrum describe the optical properties of excitons in neutral QDs. At 10 K, a single $\sqrt{Lorentzian}$ function is fit to the data, indicating that the line width is comprised of the ZPL transition only and is 12 μeV. At elevated temperatures, broad phonon sidebands appear and the ZPL broadens. The line shapes are fit to a triple $\sqrt{Lorentzian}$ function to account for the ZPL, the phonon sidebands and the weak biexciton peak.

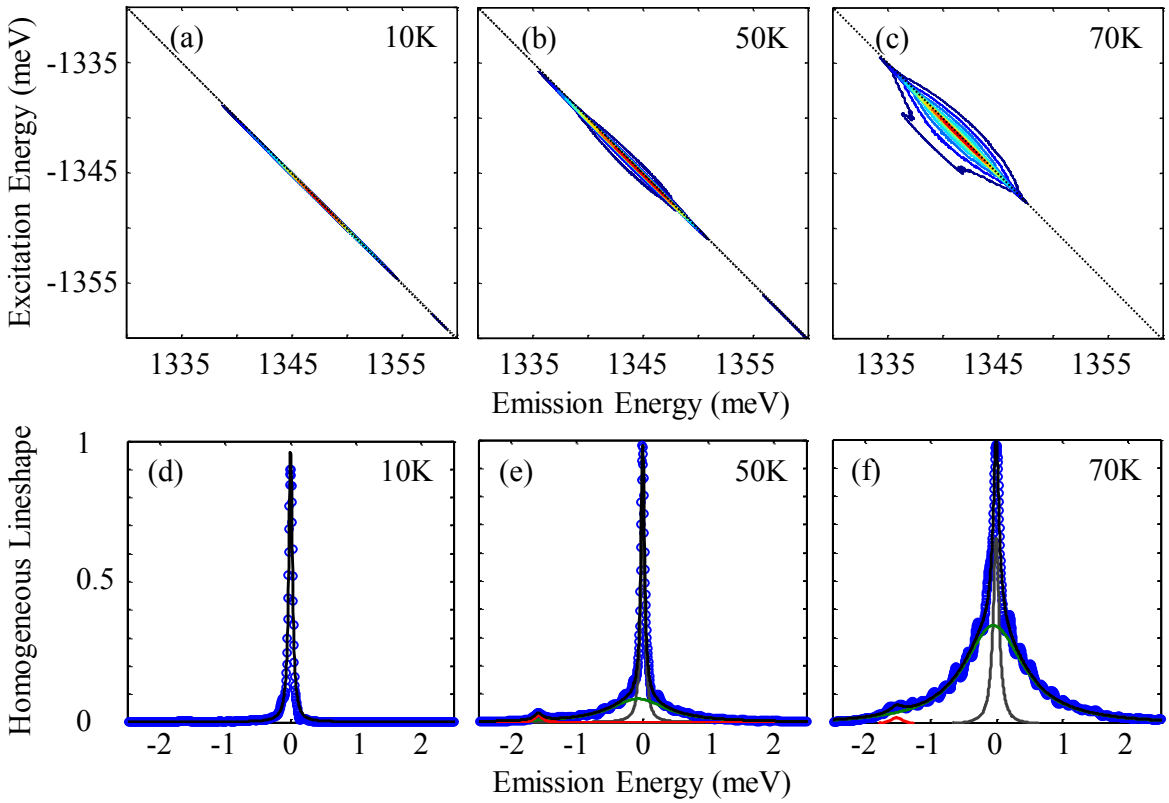

Figure 5.5: Normalized rephasing one-quantum amplitude spectra from the InAs SAQDs annealed at 900 °C for a sample temperature of (a) 10 K, (b) 50 K and (c) 70 K. The dominant peak in each spectrum is inhomogeneously-broadened along the diagonal and arises from the exciton nonlinear response. The corresponding homogeneous line shapes and fits are shown in the bottom row. At low temperature, a single $\sqrt{Lorentzian}$ function is used to fit the ZPL shape, whereas at elevated temperatures an additional $\sqrt{Lorentzian}$ function is necessary to fit the broad phonon background. A third function is used to fit the weak biexciton peak red-shifted from the diagonal peak at zero energy.

The appearance of the phonon sidebands confirms that the exciton-phonon coupling strength is greater in this sample compared to the GaAs IFQDs, so that now the transition dipole moment is significant between states with different phonon occupation numbers. The sidebands have been previously observed in both the linear emission spectrum from single dots and in the nonlinear

FWM response from QD ensembles. They are a manifestation of coupling between the different mixed exciton-phonon levels in the crystal ground state and exciton ground state manifolds (as shown in Fig. 5.1), which is analogous to coupling between the vibrational levels of the ground and excited state manifolds of a diatomic molecule or photosynthetic light-harvesting antennae [187]. A future area of interest is to perform a systematic study and analysis of the sideband amplitude, width and center frequency relative to those of the ZPL. For example, an asymmetry of the line shape can provide insight into thermalization effects of the ground and excited state manifolds. If the broad background in the photoluminescence emission spectrum is offset to lower energies compared to the ZPL, then one might conclude that the dominant optical transitions are between states with low phonon occupation numbers in the excited manifold and high occupation numbers in the ground state manifold. Similarly, if the absorption spectrum reveals that the background is blue-shifted relative to the ZPL, then only the zero phonon level of the ground state manifold is predominantly occupied. This information is readily available in the 2D spectra and can provide a deeper understanding into exciton-phonon interaction effects.

5.3.2 Excited State/Ground State Dephasing Mechanisms

The ZPL widths extracted from the $\sqrt{Lorentzian}$ fits to the cross-diagonal slices taken at line center of the inhomogeneous distribution are shown in Fig. 5.6(a) for the exciton ground state (GS, blue squares) and first excited state (ES, red circles). These states are separated in energy by ≈ 25 meV, which is too large for simultaneous excitation due to the limited laser bandwidth at the resonance energies. Each set of data were obtained with the laser tuned resonantly with the corresponding transition. The GS ZPL width is ≈ 12 μeV at low temperature and increases with temperature in a monotonic manner. The ES ZPL width is ≈ 25 μeV at low temperature and is insensitive to an increase in the temperature until ≈ 35 K, after which it increases similarly as the GS.

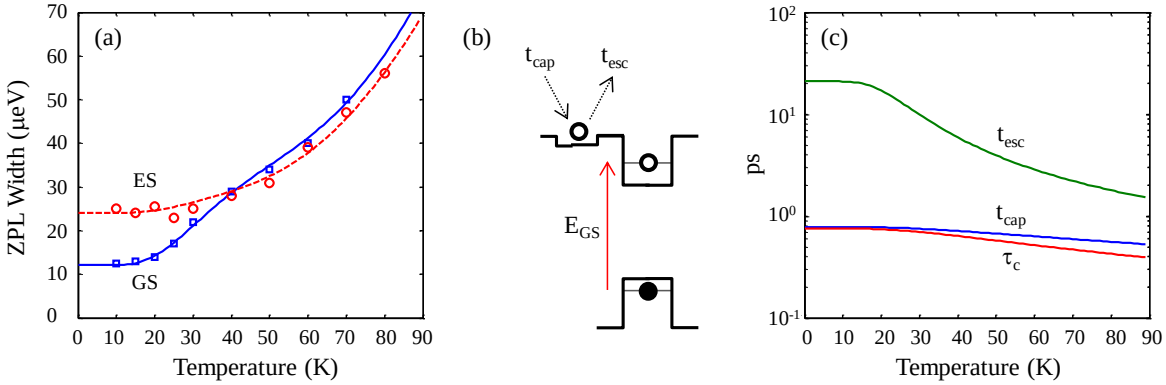

Figure 5.6: (a) The ZPL width temperature dependence of the exciton ground state (blue squares) and first excited state (red circles). The data is fit using the model described in the text, which includes effects from exciton-phonon scattering, phonon-assisted relaxation and the quantum confined Stark effect. (b) Schematic diagram of a charge trap near the QD. Fluctuations of the emission energy, E_{GS}, of an exciton in the ground state arise from the Stark effect associated with charges being captured and emitted from the trap with respective times t_{cap} and t_{esc}. (c) The charge capture and emission times and the fluctuation correlation time (τ_c) dependence on the sample temperature. At elevated temperatures, the correlation time decreases, with is reflected in the ZPL width broadening.

Insight into the phonon modes that couple strongly to the excitons could be obtained by analyzing the ZPL widths using the Bose function and offset given by Eqn. 5.4. However a comparison of the low temperature GS ZPL width (≈ 12 μeV) to the expected radiatively-limited line width of ≈ 3 μeV, based on population decay rate measurements, reveals that significant pure dephasing exists in the sample, independent of excitation density (excitation-induced dephasing effects and measurements of the population decay rate are discussed in detail in the following Chapter). The exciton-phonon interaction model described by Eqn. 5.4 cannot account for the additional pure dephasing at low temperature. One possible broadening mechanism could be the existence of a fluctuating environment arising from charges that are unintentionally introduced during the growth process, which become trapped in weakly-confining localization sites due to

unavoidable wetting layer/barrier interface roughness. The electric fields from localized charges in the vicinity of the QD induce a shift of the QD emission lines through the quantum confined Stark effect [114]. The QD resonance energy is randomized by the capture and escape of charges in the localization trap and the fluctuations can be characterized by a spectral modulation amplitude, Σ, and a timescale, τ_c. The characteristic parameters Σ and τ_c are determined by the proximity of the trap to the QD and the times associated with capture and escape of charges from the trap. This process is depicted in Fig. 5.6(b), where the characteristic charge trap and escape times are t_{cap} and t_{esc}, respectively. Calculations performed by Berthelot *et al.* demonstrate that in the slow modulation limit ($\Sigma\tau_c/\hbar \gg 1$), slow reservoir fluctuations are reflected in the QD spectrum, and the line shape is Gaussian with a FWHM give by $2\sqrt{2ln(2)}\Sigma$. In the opposite limit ($\Sigma\tau_c/\hbar \ll 1$), fast reservoir fluctuations are smoothed out and the line shape is narrowed into a Lorentzian with a FWHM given by $2\Sigma^2\tau_c/\hbar$. The random charge fluctuations result in transition energy shifts over time equal to $\delta E(t)$ around a mean resonance energy E_{GS}. Both Σ and τ_c are then computed by performing Monte Carlo simulations of the correlation function of the energy fluctuations, $X(t) = \langle \delta E(t)\delta E(0)\rangle$. The simulated results are well reproduced by the expressions [114]

$$\begin{aligned} \frac{1}{\tau_c} &= \frac{1}{t_{cap}} + \frac{1}{t_{esc}} \\ \Sigma &= \frac{\sqrt{N}\Delta}{\sqrt{\frac{t_{esc}}{t_{cap}}} + \sqrt{\frac{t_{cap}}{t_{esc}}}}, \end{aligned} \tag{5.5}$$

where N is the number of traps and Δ is the Stark shift. The saturation value of Σ is given by $\Sigma_s = \sqrt{N}\Delta/2$ and the temperature dependence of these expressions is reflected in t_{esc} and t_{cap}. The trapping of charges is associated with phonon emission and the escape process occurs through the absorption of phonons or through a carrier-carrier Auger mechanism, which is assumed to be temperature independent. These processes are related to the capture and escape times through

$$\begin{aligned}\frac{1}{t_{cap}} &= \sum_i \frac{1}{t_i}\left(1+\frac{1}{e^{E_i/k_bT}-1}\right)\\ \frac{1}{t_{esc}} &= \sum_i \frac{1}{t_i}\left(\frac{1}{e^{E_i/k_bT}-1}\right)+\frac{1}{t_A},\end{aligned} \tag{5.6}$$

where each term in the summation represents the carrier-phonon interaction involving phonons with average energy E_i and a characteristic scattering time t_i. The time t_A is the average Auger scattering time. Two terms from the summations corresponding to indices $i = 1, 2$ are necessary to reproduce the data. These expressions can be used to calculate the ZPL line width dependence on the fluctuating charge reservoir. Moreover, the ZPL width also depends on the exciton-phonon virtual activation process described in the previous Section, so that the total ZPL width of the GS exciton can be expressed as

$$\gamma_{GS} = \frac{\gamma_{pop}}{2} + \frac{2\Sigma^2\tau_c}{\hbar} + \frac{\hbar}{t_3}\left(\frac{1}{e^{E_3/k_bT}-1}\right), \tag{5.7}$$

where $\gamma_{pop}/2 = 3$ μeV is the radiatively-limited ZPL width and t_3 and E_3 are the average time and phonon energy corresponding to the exciton-phonon virtual activation mechanism. The results from this model are shown as the solid line in Fig. 5.6(a). The corresponding capture, emission, and fluctuation correlation times are shown in Fig. 5.6(c). The correlation time is ≈ 1 ps for all temperatures, which is similar to the results obtained by Berthelot *et al.* from a similar sample [114]. A short τ_c is also consistent with the idea that the transition energy fluctuations $\delta E(t)$ must be fast enough to dephase the interband optical coherences during τ and t, which occurs on a timescale of tens to hundreds of picoseconds. The ZPL temperature dependence of the ES exciton is modeled using a similar expression given by

$$\gamma_{ES} = \frac{\gamma_{pop}}{2} + \frac{2\Sigma^2\tau_c}{\hbar} + \frac{\hbar}{t_3}\left(1+\frac{1}{e^{E_3/k_bT}-1}\right) + \frac{\hbar}{t_4}\left(\frac{1}{e^{E_4/k_bT}-1}\right), \tag{5.8}$$

where the parameters t_4 and E_4 describe the ES exciton-phonon virtual activation behavior. The term corresponding to parameters t_3 and E_3 describes phonon-assisted relaxation from the ES to

the GS. The results from this model are shown as the dashed line in Fig. 5.6(a). The following table summarizes the parameters used in the expressions to fit the data.

	Σ_s	t_A	t_1	t_2	t_3	t_4	E_1	E_2	E_3	E_4
GS	0.39	21	0.9	6	1	-	8	36	25	-
ES	0.20	21	0.9	6	0.3	0.7	8	36	25	20

Table 5.1: Parameters used in the fits of the exciton ground state (GS) and first excited state (ES) ZPL widths. Σ_s and E_i are given in units of meV and t_i in units of ps.

The following assumptions have been made for fitting the data: 1) the ground and excited states have a similar radiatively-limited ZPL width [237]; 2) the characteristic charge carrier-phonon interaction times and energies are similar for both states; and 3) The phonon energy E_3 associated with the excited state $\rightarrow$ ground state relaxation process is equal to the energy separation of the states. The zero temperature ZPL widths set constraints on the values for t_A and the excited state phonon-assisted relaxation parameter t_3. Simultaneous fitting of the GS and ES ZPL widths based on these assumptions and constraints is sufficient to uniquely determine the values of the other parameters. Without the Auger scattering mechanism, the fits underestimate the zero-temperature offset of both states. An interesting result is the smaller saturation spectral modulation amplitude, Σ_s, for the ES compared to the GS, which implies a smaller Stark shift for the ES. In a simple picture, a larger Stark shift is expected for the ES exciton because weaker confinement typically leads to greater polarizability of the electron and hole wave functions; however, the exact form of the wave functions depends on the QD morphology, and several experimental and theoretical studies have shown that the GS exciton can experience a larger Stark shift for certain electric field orientations and strengths [238, 239].

The energies E_1 and E_2 likely describe charge carrier scattering with acoustic and optical phonons, respectively. Although the average phonon energy, E_3, associated with the GS exciton-phonon interaction mechanism is similar to the GS–ES energy separation, the scattering is likely

virtual in nature. An investigations of the GS–ES coupling is an interesting perspective for future experiments. An additional constraint on the parameters could be established by measuring the ES $\rightarrow$ GS relaxation rate, described by $(t_3)^{-1}$. The rate can be determined by repeating the rephasing one-quantum experiments using excitation pulses with sufficient bandwidth to simultaneously probe the GS and ES transitions. Incoherent population relaxation dynamics can be monitored by acquiring multiple spectra for different delays T. The fraction of the ES population relaxing to the GS would appear as a spectrally-isolated peak, and the relaxation time t_3 could be determined from a rate equation analysis of the peak amplitudes. ES population relaxation dynamics have been inferred from photoluminescence and TI-FWM studies. In photoluminescence, the ES dephasing time was measured for ≈ 100 dots and was less than 100 ps [240], corresponding to a minimum line width of ≈ 7 μeV. This width is almost an order of magnitude larger than for the GS and is attributed to phonon-assisted relaxation to the GS. More recently, TI-FWM experiments have revealed that the photon echo amplitude of excitons in the first ES exhibits a bi-exponential decay with a long decay time ≈ 1.1 ns, corresponding to a line width < 1 μeV that is comparable to that of the GS exciton [87, 237]. The discrepancy between the reported values is likely a result of different QD morphologies and therefore confinement energies and energy level separation. In the photoluminescence study, the QDs were comprised of $In_{0.5}Ga_{0.5}As/GaAs$ and emitted from $\approx 1250 - 1350$ meV, which was $200 - 100$ meV below the wetting layer emission energy. In the TI-FWM experiment, the QDs were comprised of InAs/GaAs that emitted around 1050 meV, which was 332 meV below the wetting layer. Moreover, the ES can exhibit a more complicated fine structure compared to the GS, which can alter the polarization selection rules [237]. Perhaps weaker confinement and smaller GS–ES energy separation is responsible for the enhanced ES $\rightarrow$ GS phonon-assisted relaxation that we observe. 2DCS is particularly suited for examining coupling between the exciton ground and excited states and could reveal the role of QD morphology on phonon-assisted transitions between excited states in QDs.

Chapter 6

Influence of Confinement on Many-Body Interactions

The finite confinement potential, discrete electronic density of states and long interband optical coherence times of semiconductor QDs are reminiscent of atomic systems, leading to the connotation of QDs as "artificial atoms". Despite some similarities, this simple picture becomes dramatically more complicated when the QD contains more than one charge, usually by means of optical excitation of single or multiple electron-hole pairs in neutral or charged QDs. Analytical methods adopted from atomic physics have been used to calculate the electronic and optical properties of dots embedded in a glass matrix, which exhibited nearly spherical shape with quasi-infinite confinement potential [11]. While this structure was more closely analogous to atomic systems, epitaxially-grown semiconductor QDs exhibit complex geometrical structure and are sensitive to environmental effects, which inhibit the possibility to accurately calculate the properties using analytical methods [84]. Several approximations have been made to simplify the geometry, including rectangular [241] and spherical [242] QD shapes and parabolic confinement potentials [243]; however these simplifications might introduce artificial properties that are not observed in real physical systems. Moreover, the electronic and optical properties depend on the interrelation between confinement effects and Coulomb interactions between multiple charges residing in the dot, which require more advanced calculation methods. For example, the properties of realistic QDs depend on the shape, composition, strain effects and piezoelectric fields, which all require numerical techniques to be taken into account properly.

Theoretical efforts have benefited from single-dot spectroscopy, which has been an extremely

powerful tool for measuring and characterizing the influence of confinement, material composition and shape on the QD optical properties (for a compilation of experiments results, see Ref. [84]). More recently, nonlinear techniques such as pump-probe and FWM have enabled studies of QD ensembles, although these methods have several limitations that have been discussed in previous Chapters. Regardless, previous works have revealed that the recombination energies of different excitonic states are sensitive to the morphology of the QDs. Calculations have demonstrated that Coulomb interactions, including exchange and correlation effects, are of large importance. For example, in Fig. 6.1, which is representative of the data obtained from many single-dot experiments, the binding energies of neutral (XX) and charged biexcitons (XX^+) and positive (X^+) and negative (X^-) trions are shown as a function of the exciton recombination energy for InAs/GaAs QDs, obtained from a single-dot photoluminescence spectroscopy experiment [244]. Clear trends are visible for the entire ensemble – specifically, the binding energies decrease with increasing recombination energy, or decreasing QD size[1] . Rodt *et al.* perform configuration interaction calculations using different numbers of electron and hole states confined in the QD. Their results indicate that with decreasing dot size, the number of confined levels decreases, the effects of Coulomb correlations beyond the HF level diminish, and the binding energies are reduced and can even be negative (i.e. blue-shifted with respect to the exciton), indicating the multi-particle configuration is in an "anti-binding" state but held together by confinement of a QD. For example, for exciton recombination energies below ≈ 1220 meV in their sample, the biexciton binding energy is positive (i.e. the biexciton $\rightarrow$ exciton recombination energy is red-shifted with respect to the exciton $\rightarrow$ ground state). With increasing exciton recombination energy, the biexciton binding energy decreases and flips sign.

[1] A positive binding energy corresponds to a red-shift in the recombination energy with respect to exciton $\rightarrow$ ground state recombination.

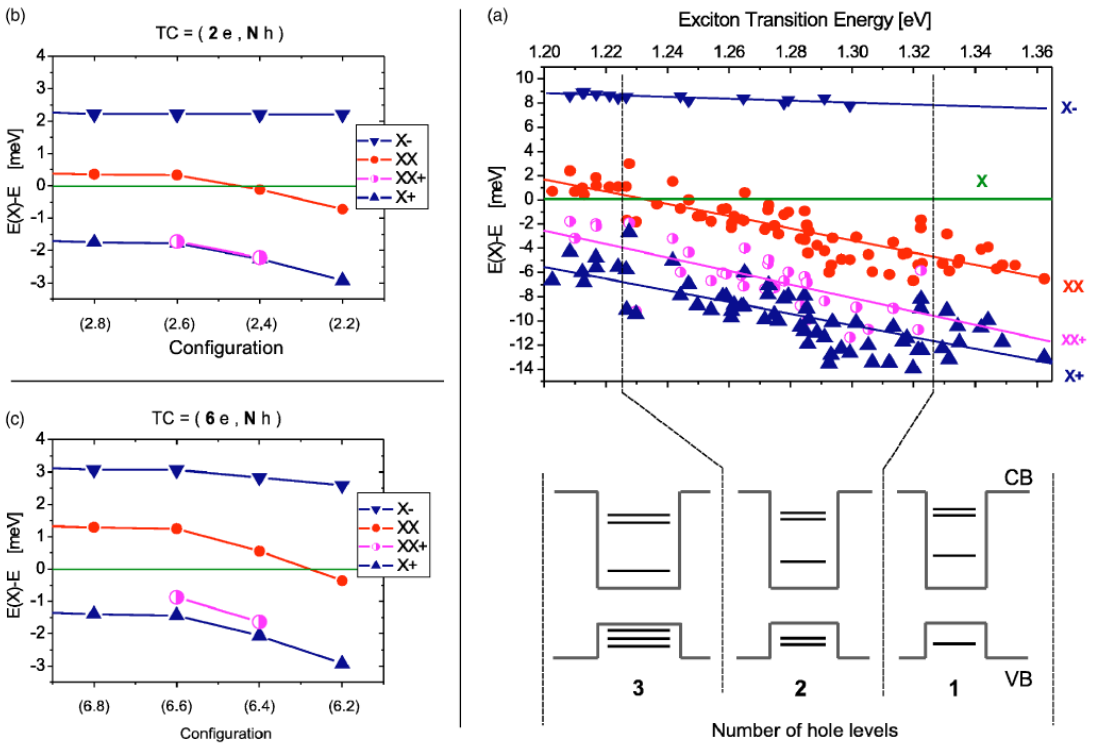

Figure 6.1: Comparison between the measured (a) and calculated (b),(c) relative recombination energies of the neutral (XX) and charged (XX^+) biexciton and positive (X^+) and negative (X^-) trions versus exciton recombination energy, E(X), in InAs/GaAs QDs. In the calculations, the total configuration, $TC = (\#e, \#h)$, comprises the number of electron ($\#e$) and hole ($\#h$) states confined in the dots. The calculations of the binding energies in (b) and (c), for which a positive binding energy corresponds to a red-shift of the transition energy with respect to the exciton recombination energy, are performed using two and six confined electron states, respectively, whereas the number of bound holes states is varied. Reproduced from Rodt. *et al.*, Physical Review B **71**, 155325 (2005).

The results presented in Fig. 6.1 clearly demonstrate that the binding energies, and therefore Coulomb effects, are sensitive to the QD size; however for single dot studies, significant dot-to-dot scatter of the data limits one's ability to compare experiment and theory only to samples whose optical properties vary significantly over a large energy range. For example, the calculated

recombination energies shown in Figs. 6.1(b) and 6.1(c) indicate that if the relative change in the number of bound hole levels in the QD is small, then the change in the biexciton binding energy is negligible; these small changes cannot be deduced from the data in Fig. 6.1(a) because of significant dot-to-dot variation at any given recombination energy. The large scatter of the data could be attributed to the limited number of dots probed, or perhaps to the sample modifications (aperture masks, etching mesas, etc.) necessary to isolate single QDs. Ensembles of dots can be probed using nonlinear techniques, which eliminate the need for sample modifications for single-dot isolation and dramatically increase the number of dots that can be probed. In this Chapter, our efforts to probe the effects of many-body interactions on the electronic and optical properties of QDs using 2DCS are discussed. The nonlinear response from excitons, biexcitons and trions can be independently analyzed by taking advantage of the dipole transition selection rules, which are discussed in Section 6.1. In Section 6.2, exciton-exciton scattering effects on the dephasing rates will be presented. In Section 6.3, 2DCS experiments probing the biexciton properties are discussed, and the results are compared to configuration interaction models in order to reveal the effects of confinement on Coulomb interactions between excitons. In Section 6.4, high-resolution 2D spectra probing exchange interaction effects are presented.

6.1 Isolating the Nonlinear Response from Excitons, Biexcitons and Trions

A quantitative analysis of the 2D spectra from the epitaxial QDs requires isolating specific coherent pathways that otherwise overlap because of inhomogeneity. Figure 6.2(a) and 6.2(b) shows typical rephasing one-quantum spectra of the InAs SAQDs annealed at 900 °C and of the GaAs IFQDs, respectively, taken at 10 K, an excitation intensity within the $\chi^{(3)}$ regime and collinear polarization (HHHH). The excitation field polarization direction is aligned along the $|H\rangle$ state for all samples. The orientation of the InAs sample is determined through an analysis of Δ_{FSS} acquired from the zero-quantum spectra, which is described in detail in Section 6.4. AFM images of a surface dot layer on the GaAs sample indicates that the average QD shape is slightly asymmetric along the [110] and [1$\bar{1}$0] crystal axes (H and V directions). The cleave planes of the sample are along

these directions, making alignment of the sample straightforward.

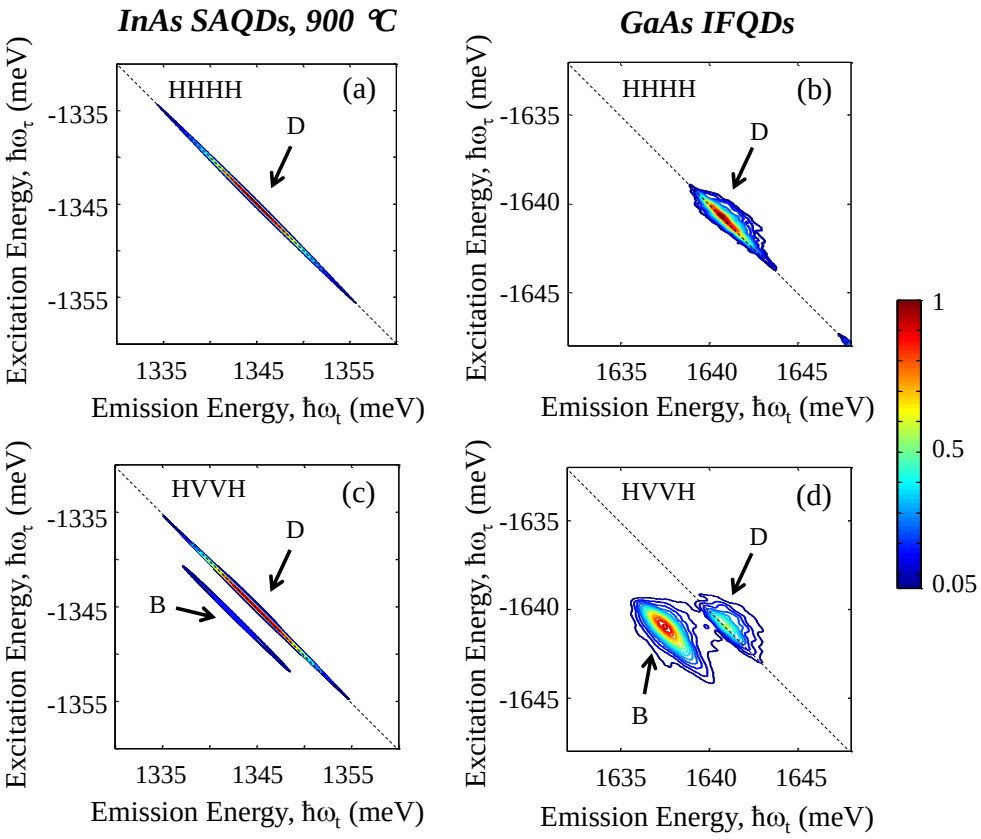

Figure 6.2: Rephasing one-quantum spectra taken at 10 K and low-excitation conditions. An HHHH excitation and detection polarization sequence is used for the InAs and GaAs QD spectra in (a) and (b), respectively. For the respective spectra from the InAs and GaAs dots in (c) and (d), an HVVH polarization sequence is used. The peaks labeled D are associated with excitons and trions and the peaks labeled B arise from biexciton contributions, as discussed in the text.

For collinear polarization, both spectra in Figs. 6.2(a) and 6.2(b) feature a single peak (D) elongated along the diagonal by the sample's respective inhomogeneous line width. When using a cross-linear polarization excitation and detection sequence (HVVH), an additional peak appears in the spectra shown in Figs. 6.2(c) and 6.2(d). Based on the dipole optical transition selection rules described in the previous Chapters, we can attribute the two peaks to either the exciton, biexciton,

or trion [101]. The diagonal peak in the spectra generated with an HHHH polarization sequence, for neutral QDs, arises from the ground-state bleach and excited-state emission nonlinearities of the exciton transition, described by the Feynman diagrams (a) and (b) in Fig. 3.10. The exciton $\rightarrow$ biexciton transition is also accessible with this polarization sequence and appears in the spectrum as a peak red-shifted along the emission energy axis, $\hbar\omega_t$, by the biexciton binding energy, Δ_B. For these samples and excitation conditions, the biexciton peak is too weak and the spectrum is dominated by the ground state $\rightarrow$ exciton transition so that only a single diagonal peak is present. In the case of charged QDs, excitation of the biexciton is forbidden due to Pauli blocking. Optical excitation creates an electron-hole pair that interacts with the resident charge to form a trion. The trion resonance appears as a diagonal peak spectrally-shifted along the diagonal from the exciton transition by the trion renormalization energy (either positive, i.e. binding, or negative, i.e. anti-binding, depending on the QD shape and composition and charge sign). The InAs SAQD ensemble contains both neutral and charged QDs, thus the diagonal peak for the HHHH polarization sequence is attributed to both excitons and trions. The fraction of charged QDs is estimated by noting that the third-order polarization and the ZPL width are proportional to the fourth and second powers of the dipole moment, respectively. We assume that a single dipole moment characterizes the quantum pathways leading to each excitonic state, and we use the radiatively-limited ZPL widths (discussed in the Section 6.4) to estimate the ratio of the dipole moments. By measuring the exciton (trion) peak amplitudes and line widths using the HHHH (HVVH) polarization sequence at low power (in the $\chi^{(3)}$ regime) and relating them through the dipole moments, we estimate that $\approx 50\%$ of the QDs are charged in the InAs SAQD sample annealed at 900 °C. This analysis requires normalizing the HHHH and HVVH spectra with respect to each other, which is done using the biexciton peak since the biexciton nonlinear response is expected to be the same for each polarization sequence (based on the Feynman diagrams in Chapter 3). A similar analysis is difficult for the InAs sample annealed at 980 °C since the biexciton contribution is too weak to extract the necessary parameters for the HHHH sequence. The GaAs IFQD sample exhibits no clear signatures indicating the presence of trions.

Using an HVVH polarization sequence, no quantum pathways exist for the exciton peak on the diagonal. Only one pathway associated with the biexciton $\rightarrow$ exciton emission is optically accessible (Fig. 3.10(f)), which is attributed to the peak labeled B in Figs. 6.2(c) and 6.2(d). The optical nonlinearities associated with the ground-state bleaching and excited-state emission are absent using this polarization, which enhances the biexciton relative amplitude in the spectrum. The presence of a diagonal peak for the InAs SAQDs is attributed to the dots that are charged with a hole. For charged QDs, the exchange interaction Hamiltonian is not diagonal using linearly-polarized basis states since only a single circularly-polarized transition is optically allowed due to Pauli blocking of one of the $|\pm 1\rangle$ transitions from the resident charge. Transforming the excitation and detection polarization states and the Feynman diagrams in Fig. 3.10 to a circular basis, assuming only one circularly-polarized transition is optically-allowed, one finds that the ground-state bleaching and excited-state emission nonlinearities for this single transition do not completely cancel and will result in a diagonal peak, which is associated with the trion. In the GaAs IFQD sample, the presence of the diagonal peak for this polarization sequence could indicate the presence of charged QDs; however two-quantum experiments discussed in Section 6.3 reveal the presence of unbound two-excitons in the dots. Unbound two-excitons can be described using similar pathways as the biexciton with a zero binding energy, which would appear as a peak on the diagonal in the rephasing spectrum. Therefore we conclude that the peaks in Fig. 6.2(d) originate from two-exciton interactions, and their ratio provides a measure of the degree to which the two excitons bind into a biexciton.

Isolation of specific quantum pathways using the dipole transition selection rules is possible only to the extent that the $|H\rangle$ and $|V\rangle$ basis states diagonalize the Hamiltonian. Mechanisms that mix the basis states, such as band mixing, can introduce effects that make interpretation of the results difficult. For example, if the light-hole band cannot be ignored, then the spin-independent Hamiltonian consists of eight basis states, which mix when considering the exchange interaction. The measurements of Δ_{FSS} discussed in Section 6.4 agree well with our assignment of the $|H\rangle$ and $|V\rangle$ basis states and assumption that band-mixing effects can be ignored.

6.2 Excitation-Induced Dephasing

Excitation-induced dephasing effects are usually detrimental for many applications, such as coherent control and manipulation of QDs for quantum information processing. The ZPL width has been shown to increase linearly with excitation density in GaAs IFQDs [149]; however few studies exist that have systematically investigated the influence of confinement on EID in QDs. The inset of Fig. 6.3(a) shows the EID behavior of the ZPL width at line center of the inhomogeneous distribution of the GaAs IFQDs, measured at a sample temperature of 6 K for co-linearly polarized excitation and detection (HHHH). As the average excitation power decreases from 1 mW/beam (1×10^{12} photons$\cdot$pulse$^{-1}\cdot$cm^{-2}) to zero, the ZPL width decreases linearly to an extrapolated zero excitation value of $\gamma = 31 \pm 10$ μeV, which is similar to the radiatively-limited ZPL width reported in the literature [28, 149, 245]. The similarity of our measurement and the ZPL widths obtained from single dot studies indicates that all QDs emitting at a particular resonance energy can be characterized by the same ZPL width measured using 2DCS.

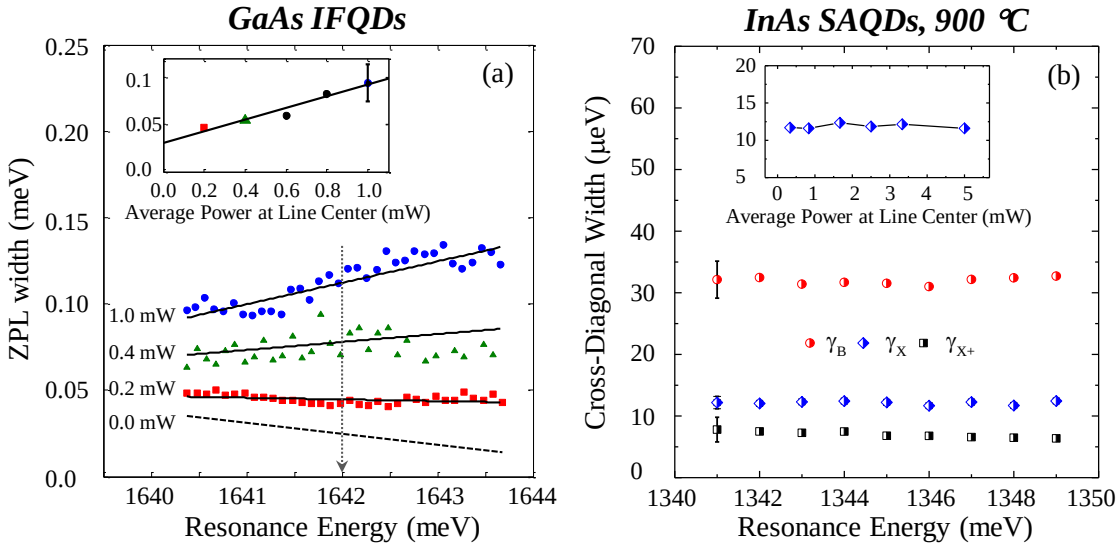

Figure 6.3: (a) The GaAs IFQD ZPL width dependence on the exciton recombination energy, measured for multiple excitation photon densities at a sample temperature of 6 K using co-linearly polarized excitation and detection (HHHH). The dashed line represents the extrapolated zero-excitation ZPL widths. The gray vertical arrow indicates line center of the inhomogeneous distribution. Inset: power dependence of the ZPL width at line center. The extrapolated zero excitation width is 31 ± 10 μeV. (b) Cross-diagonal line widths of the exciton (blue diamonds), biexciton (red circles) and trion (black squares) are shown as a function of resonance energy for the InAs SAQDs annealed at 900 °C. The widths are equal to the ZPL widths for the exciton and trion, whereas the biexciton width can be broadened through other mechanisms discussed in the text. No excitation-induced dephasing effects are observed within the $\chi^{(3)}$ regime, shown in the inset for the exciton ZPL width.

Measurements of the ZPL width at line center of the inhomogeneous distribution were repeated using a $4f$ grating pulse shaper to filter the excitation pulses such that excitons were not generated in the QW, and no change in the QD ZPL width values was observed. This is an interesting result: EID effects play a significant role in the dephasing of QD excitons as shown in the inset to Fig. 6.3(a), but effects from QW excitons are negligible. Thus, this many-body effect is governed by either intra- or inter-dot exciton-exciton interactions. Figure 6.3(a) shows the ZPL

width variation across the inhomogeneous distribution for three different average excitation powers and an extrapolation to zero excitation. Assuming that the low temperature, extrapolated zero power line widths are radiative lifetime broadened, the width should be proportional to the square of the optical transition dipole moment. Previous studies have found that the dipole moment is smaller for smaller QDs emitting at higher energy [246, 247], which is consistent with the negative slope for the zero excitation ZPL widths in Fig. 6.3(a). With increasing power, all ZPL widths increase and the slope flips from negative to positive. This behavior suggests that multiple excitons are excited within a given QD, and the interaction strength between these excitons increases with decreasing QD size due to greater exciton-exciton wave function overlap.

The exciton (blue diamonds), biexciton (red circles) and trion (black squares) cross diagonal line widths of the InAs SAQD sample annealed at 900 °C are shown in Fig. 6.3(b) for an average power of 5 mW/beam (2.5×10^{12} photons·pulse^{-1}·cm^{-2}). The trion and biexciton widths are extracted from the peaks in Fig. 6.4(a), discussed in detail in the next Section. The exciton line width was obtained using an HHHH polarization sequence and the trion and biexciton widths using an HVVH sequence. The data reveal that the line width of each excitonic state is independent of the emission energy. The cross diagonal widths of the exciton (12 ± 1 μeV) and trion (8 ± 2 μeV) are equal to their ZPL widths, whereas the width of the biexciton peak (32 ± 3 μeV) can be broadened beyond the homogeneous line width through auxiliary effects that are discussed in sub-Section 6.3.1. Interestingly, for excitation intensities within the $\chi^{(3)}$ regime, no EID effects are observed for the InAs SAQDs, shown for the exciton ZPL width in the inset to Fig. 6.3(b). Moreover, because of weak confinement in the GaAs IFQDs, the excitation density for a given QD is likely not limited by phase-space filling (Pauli-blocking), which is not the case for the strongly-confining InAs SAQDs.

6.3 Biexcitonic Effects

Recall from Chapter 3 that the nonlinear optical response of bound biexcitons appear in a 2D rephasing one-quantum spectrum as spectrally-isolated peaks. Moreover, using the dipole transition selection rules, the biexciton nonlinear response can be isolated and its optical properties – including

the binding energy and dephasing rate – can be unambiguously measured. Normalized 2D rephasing one-quantum amplitude spectra are shown in Fig. 6.4 for the InAs SAQDs annealed at 900 °C (a) and 980 °C (b) and for the GaAs IFQDs (c). The data were taken at the maximum excitation intensity while remaining in the $\chi^{(3)}$ regime for the respective sample, corresponding to < 0.1 excitons excited per QD on average. The peak of the excitation spectrum was tuned to be resonant with the maximum amplitude of the QD inhomogeneous distribution. The excitation and detection polarizations were adjusted for a cross-linearly polarized sequence (HVVH), and the temperature of all samples was 10 K. Figures 6.4(a) and 6.4(b) both feature a peak inhomogeneously-broadened along the diagonal (D) and a similar peak red-shifted along $\hbar\omega_t$ (B). For the GaAs IFQDs shown in Fig. 6.4(c), two diagonal peaks are observed and correspond to the nonlinear optical response from the QDs (D_{QDs}) and from the disordered QW (D_{QW}). Both diagonal peaks feature a peak red-shifted along $\hbar\omega_t$ similar to the InAs samples. The peaks labeled B for all samples are consistent with being a bound biexciton, as has been previously observed in 2D spectra of GaAs QWs [144] and will be verified using simulations discussed in sub-Section 6.3.1. Horizontal slices taken at the maximum diagonal peak amplitude are shown in the inset to each figure.

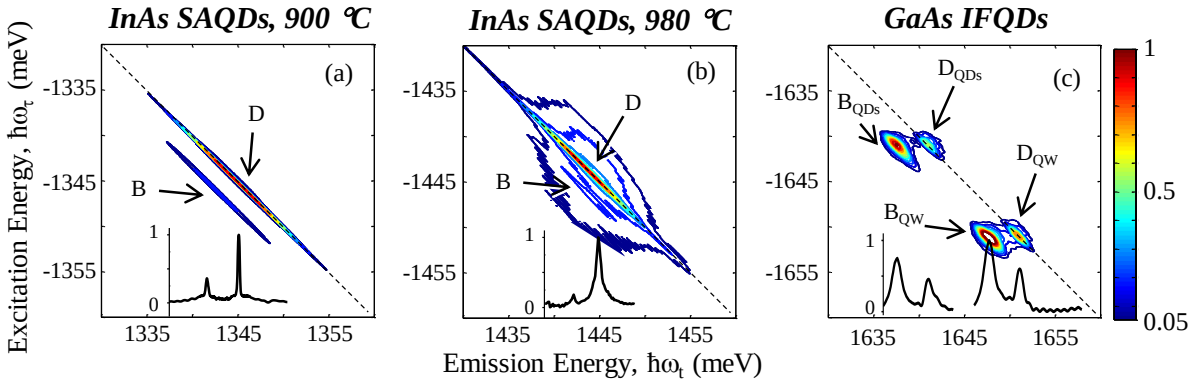

Figure 6.4: Normalized rephasing one-quantum amplitude spectra for the InAs SAQDs annealed at (a) 900 °C and (b) 980 °C and for (c) the GaAs IFQDs. The spectra were taken for a sample temperature of 10 K, cross-linear polarization (HVVH) and for maximum intensity while remaining in the $\chi^{(3)}$ regime. Peaks labeled "D" are signatures of trions and/or unbound two-excitons, whereas peaks labeled "B" are bound biexcitons.

Cross-linear polarization is used to enhance the relative amplitude of the biexciton with respect to the diagonal peak since the quantum pathways for the exciton resonance are not dipole transition allowed. Since contributions from the $|g\rangle \rightarrow |H\rangle$ transition are not expected for this polarization sequence, the peaks labeled "D" must originate from other nonlinearities. In addition to the bound biexciton, a FWM signal at the exciton resonance in a QW for HVVH polarization has been previously observed and attributed to local field effects, EID and unbound two-exciton correlations [156, 248], which are the likely mechanisms contributing to the diagonal peak D_{QW} in Fig. 6.4(c). For the GaAs IFQDs, both EID effects (discussed in the previous Section) and unbound two-quantum coherences (discussed in sub-Section 6.3.2) are observed, which give rise to the peak D_{QDs}.

The many-body interactions giving rise to EID and unbound two-quantum correlations are absent for the InAs SAQDs, indicating that the peaks labeled "D" must originate from a different mechanism. Through measurements of Δ_{FSS} (discussed in the next Section), we determine that all QDs in the ensemble are characterized by an anisotropic confinement potential and the

anisotropy is aligned along the same crystal axes. Since no exciton response is expected for an HVVH polarization sequence, the remaining spectral amplitude on the diagonal is a signature of the trion nonlinear response from QDs that contain a resident charge carrier. In charged QDs, optical excitation can only create an electron-hole pair along one of the circularly-polarized transitions $|+1\rangle$ or $|-1\rangle$, after which the pair can interact with the resident charge carrier to form a singlet trion. The trion response appears as an inhomogeneously-broadened peak on the diagonal for this polarization sequence. For charged QDs, biexcitons cannot be optically excited for the excitation pulse bandwidth used in these experiments because of Pauli blocking.

All three samples exhibit biexciton peaks red-shifted along the emission energy axis $\hbar\omega_t$ by the biexciton binding energy, Δ_B. An advantage of using 2DCS to investigate biexciton properties in QDs is apparent from Fig. 6.4: the binding energy can be measured for the entire ensemble simultaneously, which cannot be done for other linear and nonlinear techniques. The measured Δ_B are shown as a function of emission energy relative to the energy of the maximum diagonal peak amplitude in Fig. 6.5(a) for the InAs SAQDs annealed at 900 °C (blue squares) and 980 °C (red squares) and in Fig. 6.5(b) for the GaAs IFQDs (blue circles) and QW (red circles). For both InAs QD samples, the biexciton binding energy is constant for the entire ground state inhomogeneous distribution and is equal to 3.30 ± 0.02 meV and 2.61 ± 0.03 meV for the 900 °C and 980 °C samples, respectively. Changes in the biexciton binding energy with emission energy appear in the 2D spectra as a tilt of the biexciton peak relative to the diagonal dashed line. With increasing emission energy, $\Delta_{B,QDs}$ increases from 3.3 to 3.8 meV, whereas $\Delta_{B,QW}$ decreases over a similar range.

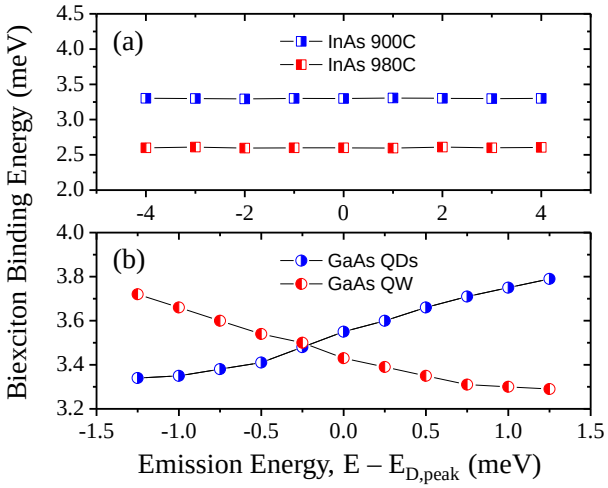

Figure 6.5: Emission energy dependence (measured relative to the maximum amplitude of the diagonal peak) of the biexciton binding energies for (a) the InAs SAQDs annealed at 900 °C (blue squares) and 980 °C (red squares) and (b) for the GaAs IFQDs (blue circles) and QW (red circles).

Inhomogeneity of 10-15 meV in the InAs SAQDs is comparable to the exciton binding energy; therefore it is essential to determine how and if Coulomb interactions dictating biexciton renormalization are affected by changes in QD size (emission energy). The effects of confinement on the binding energy have been studied extensive in the past decade [86, 45, 84, 85]. In these studies, the biexciton binding energy is typically shown to decrease with increasing exciton emission energy at a rate ranging from 0.025 to 0.1, and perhaps more importantly for quantum electronics applications, large dot-to-dot scatter of the data exists in the literature. Using a form of 2D spectroscopy that allows for the investigation of individual QDs, Kasprzak and Langbein have observed a nearly constant binding energy $\Delta_B = 4.9 \pm 0.2$ meV for $\sim$ 50 GaAs IFQDs formed from a 5 nm wide GaAs QW [249]; however their dot-to-dot uncertainty is similar to the overall change in the binding energy shown in Fig. 6.5(b).

Using the configuration interaction model described in Chapter 2, Schliwa *et al.* explained the binding energy dependence on localization as arising primarily from two competing mechanisms [84]: direct pair-wise Coulomb interactions, analogous to a Hartree-Fock mean-field approximation, and Coulomb correlations beyond the mean-field limit. As shown in Fig. 2.6 in Chapter 2, only

when Coulomb correlations are considered is $\Delta_B > 0$. The relative strength of the correlations decreases when the number of bound states within the QD decreases, which can occur for a large fractional decrease in the QD size. For changes in the QD size such that the single-particle energy levels shift, but the total number of confined levels in the dot remains the same, changes in the relative strength of Coulomb correlations is expected to be small. As depicted in the simulated results shown in Figs. 6.1(b) and 6.1(c), the binding energies are predicted to be more sensitive to the number of confined hole levels than the number of confined electron levels.

The constant binding energy for the InAs SAQDs can be explained in the above context. The QD size distribution is large enough to introduce inhomogeneity of $\approx 10 - 15$ meV; however size fluctuations only shift the resonant energies, whereas the number of confined levels in the QDs remains the same for the entire ensemble. Consequently, the biexciton binding energy is independent of the confinement potential. The negligible dot-to-dot scatter of the binding energy is likely a result of thermal annealing. A $\approx 7\%$ lattice mismatch between GaAs and InAs introduces a significant amount of strain in the system, which is not entirely relieved through the formation of SAQDs. In unannealed samples, strain can give rise to built-in piezoelectric fields, whose strength can vary dot-to-dot. Abbarchi *et al.* have suggested that strain is the primary source of scatter in the data for a given sample, and they have found that in GaAs QD samples formed by droplet epitaxy, the strain is eliminated and the scatter in the biexciton binding energy is reduced [85]. For the InAs SAQDs samples we have investigated, post-growth thermal annealing results in In/Ga diffusion and leads to an indium gradient across the QD, which reduces the InAs/GaAs lattice mismatch [250] as well as the built-in fields that can impact the multi-particle interactions.

Determining the effects of localization and disorder in the GaAs IFQD sample requires different theoretical treatment since electrons and holes are only weakly localized in the QDs. First-principles Monte Carlo simulations by Filinov *et al.* indicate that for a given QW width, introducing a single monolayer (ML) width fluctuation will force electrons and holes to spatially overlap until the ML lateral dimensions reach a critical size, at which point the multi-particle binding energies are at a maximum and the inter-particle distances a minimum [251]. Upon further increase of

the ML size, the inter-particle distances increase and the binding energies decrease until the ML fluctuation size is large enough such that the particles are considered to be confined in a single-ML-wider QW. Our observations are consistent, at least qualitatively, with their calculations. In regions of the QW where the fluctuation lateral dimensions are small, the exciton and biexciton are only weakly localized by the disorder. For these excitonic states, the biexciton binding energy increases with fluctuation size (decreasing exciton recombination energy), which is consistent with the observed trend for $\Delta_{B,QW}$ in Fig. 6.5(b) for the QW biexciton. In regions of the QW where the fluctuations are large enough such that excitons are confined in the QDs, an increase in the QD size (decrease in the recombination energy) would decrease the binding energy, also consistent with the trend for $\Delta_{B,QDs}$ in Fig. 6.5(b) for the QD biexciton peak.

6.3.1 OBE Analysis

In addition to the biexciton binding energy, quantitative information regarding the exciton $\rightarrow$ biexciton dephasing rate, correlations between fluctuations of the exciton and biexciton states, and the distribution of biexciton binding energies at any particular recombination energy can be extracted from the 2D spectra. Insight into these processes is obtained by comparing the measured spectra to simulations based on a perturbative expansion of the density matrix similar to the calculations discussed in Chapter 3 and derived in Appendix B (the simulations follow a similar approach derived in Ref. [89]). Results from the calculations are shown in this sub-Section for the InAs SAQD sample annealed at 900 °C, but calculations have also been performed for the other samples and the results are simply quoted. Briefly, the OBEs are analytically-solved to third-order in the applied field using Dirac delta-function pulses in time. A two-dimensional Gaussian distribution is used for the exciton and biexciton transitions with inhomogeneous line widths δ_X and δ_B, respectively. Correlations between fluctuations in the ground-state $\rightarrow$ exciton and exciton $\rightarrow$ biexciton transition energies are characterized through a correlation coefficient R, where perfect correlation corresponds to $R = 1$. Perfect correlation implies that the biexciton energy is uniquely defined for a specific exciton energy, whereas for $R < 1$, a distribution of biexciton energies exists.

To model the diagonal peak, which arises from the trion nonlinear response, it is assumed that only a single circularly-polarized transition is accessible in the charged QD; thus only the quantum pathways associated with singly-excited states along this transition are considered (since Pauli-blocking inhibits multi-exciton excitation in a charged QD for the excitation bandwidth used in the experiments). A positive biexciton binding energy, $\Delta_B > 0$, is used for the calculations. The homogeneous line width of the trion transition is adjusted to match the cross-diagonal line width, whereas the biexciton line width is varied for reasons discussed below.

Results from the simulation are shown in Fig. 6.6. The spectral features are different than those from the examples in Chapter 3 for a few reasons. First, inhomogeneity was neglected in Chapter 3 but is included in Fig. 6.6. Second, all the possible quantum pathways are considered in Chapter 3, whereas in the simulations presented here, only the pathways contributing to the biexciton and trion peaks are considered for neutral QDs and charged QDs, respectively. Lastly, usually $\Delta_B \gg \Delta_{FSS}$, which, for a homogeneously-broadened system, would result in only a single biexciton peak appearing in the 2D spectrum of a neutral QD. When including inhomogeneity and the nonlinear response from charged QDs, two inhomogeneously-broadened peaks appear in the spectrum, as shown in Fig. 6.6 for various simulation parameters.

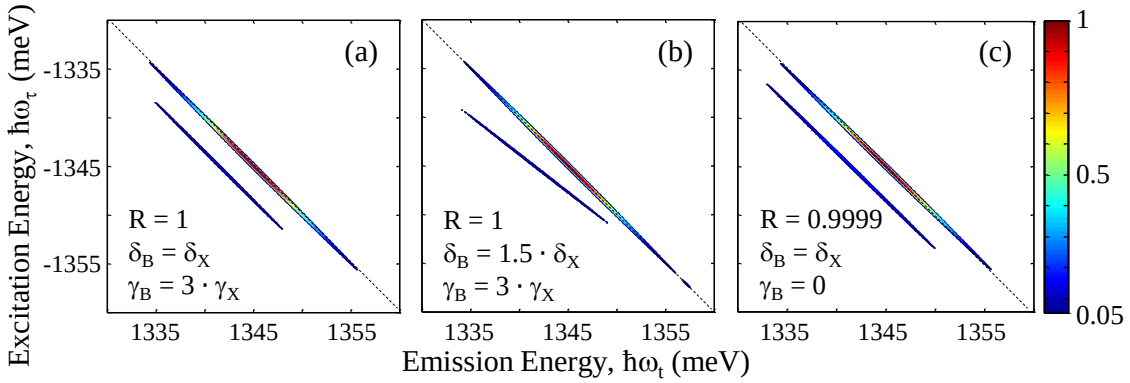

Figure 6.6: Simulations based on analytical solutions to the OBEs demonstrate the effects of exciton-biexciton correlations, inhomogeneity and dephasing on the biexciton nonlinear response in a 2D rephasing one-quantum spectrum. The exciton (γ_X) and biexciton (γ_B) dephasing rates, exciton (δ_X) and biexciton (δ_B) inhomogeneous line widths, and the correlation coefficient (R) are set to: (a) $R = 1$, $\delta_B = \delta_X$ and $\gamma_B = 3 \cdot \gamma_X$; (b) $R = 1$, $\delta_B = 1.5 \cdot \delta_X$ and $\gamma_B = 3 \cdot \gamma_X$; and (c) $R = 0.9999$, $\delta_B = \delta_X$ and $\gamma_B = 0$.

The simulations demonstrate that the model accurately reproduces the measured spectrum for $R \geq 0.9999$, $\delta_B = \delta_X$ and $\gamma_B \leq 3 \cdot \gamma_X$. To illustrate the effects of inhomogeneity on the coherent nonlinear response, Fig. 6.6(b) shows a 2D spectrum for $R = 1$, $\delta_B = 1.5 \cdot \delta_X$ and $\gamma_B = 3 \cdot \gamma_X$. Increasing the biexciton inhomogeneous line width relative to that of the exciton results in a tilt of the biexciton peak – indicating that the binding energy decreases with increasing emission energy. This can be understood by considering correlation of the exciton and biexciton transition energy fluctuations. For $R \ll 1$, a distribution of biexciton binding energies will exist at each exciton emission energy and a round biexciton peak will appear in the 2D spectrum. However, for $R = 1$, an increase in the exciton transition energy corresponds to a deterministic proportional increase in the biexciton transition energy, according to

$$\omega_B - \omega_B^0 = \alpha \cdot \left(\omega_X - \omega_X^0\right), \tag{6.1}$$

where $\omega_B - \omega_B^0$ and $\omega_X - \omega_X^0$ are the changes in biexciton and exciton transition frequencies,

respectively, about their center frequency. This expression leads to the relation

$$\delta_B = \alpha \cdot \delta_X. \tag{6.2}$$

For $\alpha > 1$, an increase in the exciton transition energy corresponds to a larger increase in the biexciton transition energy, and as a result, the biexciton peak appears tilted in the 2D spectrum.

Distinguishing between the effects of correlation and dephasing is more subtle, since both increasing γ_B and decreasing R broaden the biexciton cross-diagonal line width. A lower limit on R is estimated by setting $\gamma_B = 0$ and decreasing R to 0.9999, shown in Fig. 6.6(c), which matches the measured cross-diagonal line width. For $R < 1$, a distribution of exciton $\rightarrow$ biexciton transition energies exists and consequently the biexciton peak is broadened along the cross-diagonal direction. Since γ_B is necessarily greater than zero, this gives a lower limit on R for the InAs SAQDs annealed at 900 °C. A similar analysis for the InAs SAQD sample annealed at 980 °C and for the GaAs IFQDs and QW yield minimum R coefficients of 0.99, 0.97 and 0.95, respectively. A value of $R \geq 0.99$ for both the InAs SAQD samples – indicating essentially no scatter of the biexciton binding energy at a given exciton emission energy – is attributed to thermal annealing, which relieves strain and minimizes the built-in piezoelectric fields that can alter the optical properties from dot-to-dot. Weaker confinement in the GaAs QDs reduces the correlation coefficient to $R = 0.97$.

6.3.1.1 Signature of the $\chi^{(5)}$ Biexciton Nonlinear Response

By increasing the excitation intensity to drive the system beyond the $\chi^{(3)}$ regime, an additional spectral feature (B_U), too weak to be observed in the TI-FWM signal, appears red-shifted by Δ_B along the *excitation* energy axis in the 2D rephasing one-quantum spectrum of the 900 °C InAs SAQD sample, shown in Fig. 6.7(a) for an average power of 15 mW/beam (1×10^{13} photons·pulse^{-1}·cm^{-2}) using HVVH polarization. The spectrum also features the bound biexciton (B_L) and trion ($X+$) peaks that are present in the low-excitation-intensity spectrum in Fig. 6.4(a). A power dependence of the amplitudes, shown in Fig. 6.7(c), indicates that B_U increases with intensity as $P^{5/2}$, which suggests that it arises from the $\chi^{(5)}$ biexciton nonlinear optical response.

This six-wave mixing signal radiates in the FWM direction only for nonlinear interactions in which one of the pulses, A, B or C, acts three times. For excitation below 5 mW/beam (3.3×10^{12} photons·pulse^{-1}·cm^{-2}), B_U is absent and the $X+$ and B_L amplitudes follow $P^{3/2}$, confirming that the experiments are performed in the $\chi^{(3)}$ regime at low power.

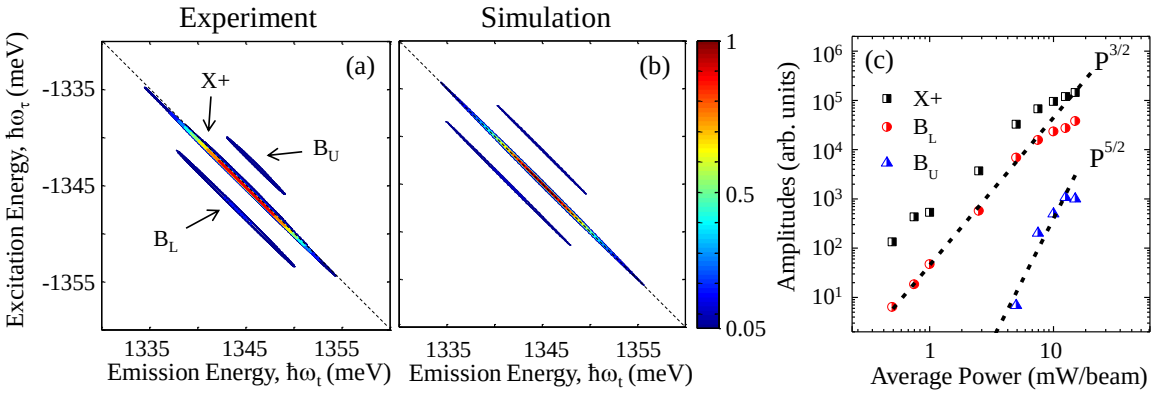

Figure 6.7: Experimental and simulated normalized rephasing one-quantum spectra are shown for HVVH polarization in (a) and (b), respectively. The power dependence of the peak amplitudes in (c) indicates that the trion ($X+$) and biexciton (B_L) peaks arise from the $\chi^{(3)}$ response, whereas the peak B_U is attributed to the $\chi^{(5)}$ biexciton response.

Additional evidence supporting our identification of the $\chi^{(5)}$ biexciton peak is provided by extending the OBE simulations discussed in this section to fifth-order in the applied field. Parameters similar to those used for the third-order response are used for the calculations, with the difference that one of the pulses acts three times. The third- and fifth-order quantum pathways contributing to the biexciton nonlinear response are represented by the double-sided Feynman diagrams shown in Fig. 6.8 for an HVVH polarization sequence. Only a single Feynman diagram contributes to the biexciton $\chi^{(3)}$ response, as indicated in Fig. 6.8(a). The diagram demonstrates that the system evolves with frequencies ω_0 and $\omega_0 - \Delta_B/\hbar$ during τ and t, respectively, corresponding to peak B_L that is red-shifted along $\hbar\omega_t$ by Δ_B. The $\chi^{(5)}$ biexciton nonlinear response can be constructed from a total of 12 quantum pathways; however only three pathways in which pulse A acts three

times, depicted in Figs. 6.8(b)-(d), contribute to peak B_U. The diagrams indicate that the system evolves with frequencies $\omega_0 - \Delta_B/\hbar$ and ω_0 during τ and t, respectively, consistent with peak B_U red-shifted along the excitation energy axis $\hbar\omega_\tau$ by Δ_B. Analytical solutions to the OBEs including the fifth-order effects are shown in Fig. 6.7(b). Excellent agreement with the data is obtained using similar parameters for peak B_U as are used for peak B_L.

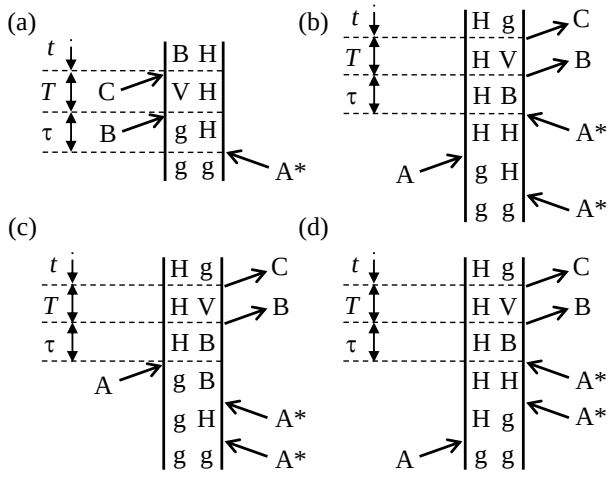

Figure 6.8: Double-sided Feynman diagrams representing the quantum pathways contributing to (a) the $\chi^{(3)}$ response and (b)-(d) the $\chi^{(5)}$ response of the bound biexciton.

The TI-FWM signal from this sample for the HVVH sequence does indeed show exciton-biexciton quantum beats, but with a frequency proportional to the emission energy difference between the $X+$ and B_L peaks. If strong enough, the $\chi^{(5)}$ biexciton contribution could be distinguished in the TI-FWM signal as a beat with frequency corresponding to the energy separation between peaks B_U and B_L [252]. Although signatures of the $\chi^{(5)}$ biexciton response are absent from the TI-FWM signal, these results demonstrate the sensitivity of 2DCS to clearly and unambiguously measure weak higher-order nonlinearities. Further separation of the $\chi^{(3)}$ and $\chi^{(5)}$ pathways could be accomplished using a variation of nonlinear spectroscopy that isolates the six-wave mixing signal [116, 115] in combination with higher-order multi-dimensional spectroscopy [110].

6.3.2 Two-Quantum Coherences in GaAs IFQDs

A two-quantum 2D spectrum, for which the conjugated pulse is incident on the sample last, is particularly sensitive to the effects of many-body interactions on the coherent nonlinear optical response, since the signal for this pulse time ordering is non-zero only if there are interactions between excitons. Two-quantum spectra have been used to investigate the microscopic mechanisms governing bound biexcitons and unbound, but correlated, two-excitons in GaAs QWs [199, 218]; however two-quantum coherences have not been probed previously in QDs using 2DCS. Since nonlinearities associated with phase-space filling do not contribute for the two-quantum pulse sequence, weak nonlinearities associated with exciton-exciton interactions can be investigated. Surprisingly, no two-quantum signal is measured for either InAs QD sample, which is unexpected since it is clear that interactions between excitons leads to biexciton formation and spectrally-shifted peaks in the 2D rephasing one-quantum spectrum. The absence of a two-quantum signal could be due to either a fast dephasing time between the ground state and the two-quantum state (which is either a bound biexciton or unbound, correlated two-exciton state), or the signal-to-noise ratio could be too small to detect the signal. On the other hand, a two-quantum signal is observed for the GaAs IFQDs, and preliminary two-quantum spectra are shown in Fig. 6.9. The excitation intensity is adjusted so that the signal is in the $\chi^{(3)}$ regime, and the excitation and detection polarization is set to co-circular (LLLL) and cross-circular (LRRL) for the top and bottom rows, respectively. The spectra on the left in both rows are taken using the full excitation spectral bandwidth, whereas the middle and right figures are acquired with the excitation spectrum progressively filtered to avoid excitation at the QW resonance energy.

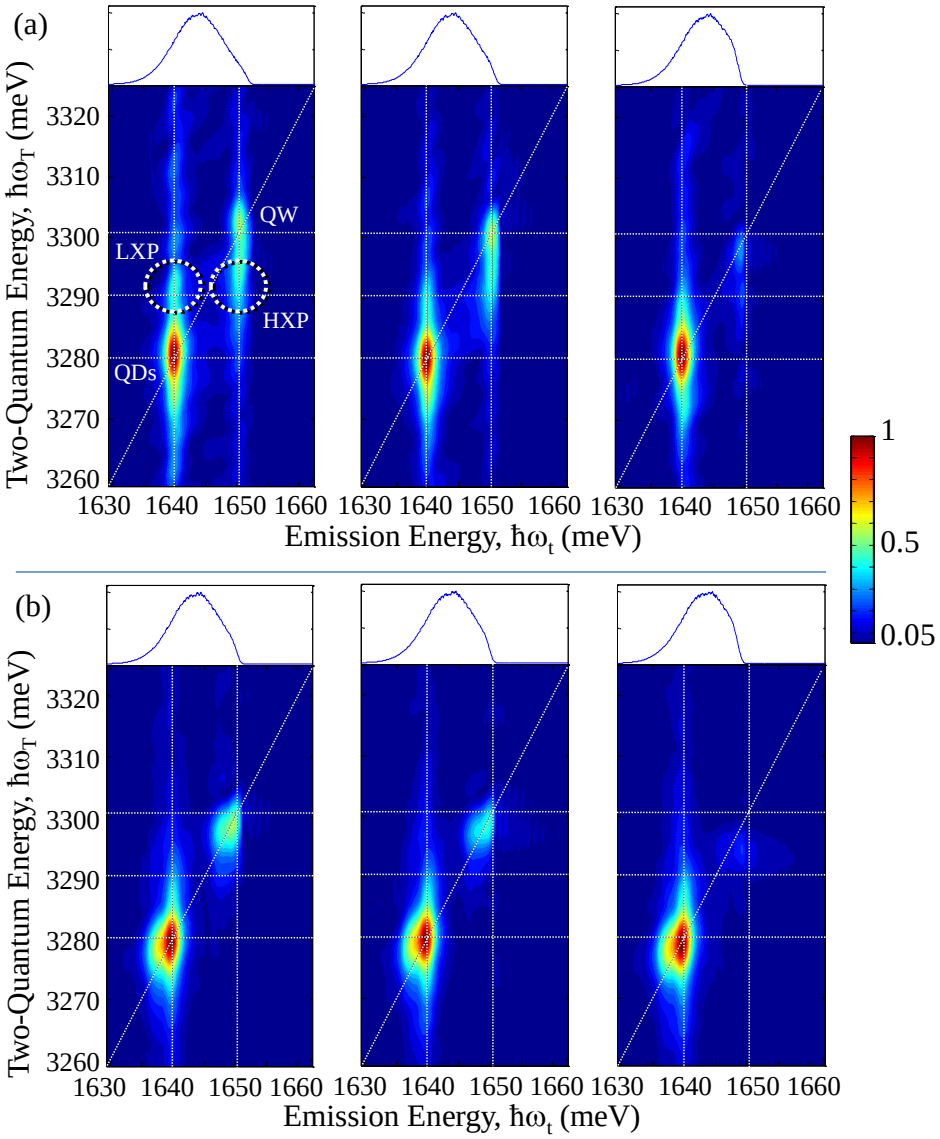

Figure 6.9: Two-quantum amplitude spectra are shown for (a) co-circular (LLLL) and (b) cross-circular (LRRL) polarization schemes. The excitation spectrum is shown above each 2D spectrum. In (a), the QW, LXP and HXP amplitudes decrease as the excitation pulses are filtered so that their spectral overlap with the QW resonance decreases, while the QD amplitude remains unchanged. In (b), cross peaks are absent and only the QW amplitude decreases when spectrally-filtering the excitation pulses.

Each spectrum in the top row features two peaks on the diagonal line ($\hbar\omega_T = 2 \cdot \hbar\omega_t$). These peaks correspond to unbound, but correlated, two-excitons in the QDs and in the QW. Interestingly,

cross peaks are present at the QD + QW two-quantum energy the QD and QW emission energies, which indicates that the QD and QW excitons are correlated. When using a LRRL polarization scheme, as shown in the bottom row in Fig. 6.9, the unbound two-quantum peaks appear on the diagonal red-shifted along both energy axes, which is attributed to the allowed formation of bound biexcitons comprised of opposite-spin excitons. Moreover, the QW–QD cross peaks are absent for this polarization scheme. The amplitudes of each peak are shown in Figs. 6.10(a) and 6.10(b) for LLLL and LRRL polarization, respectively. The cross peak amplitudes are shown after subtracting the amplitude measured on the opposite side of the diagonal peak to eliminate contributions from the diagonal peaks.

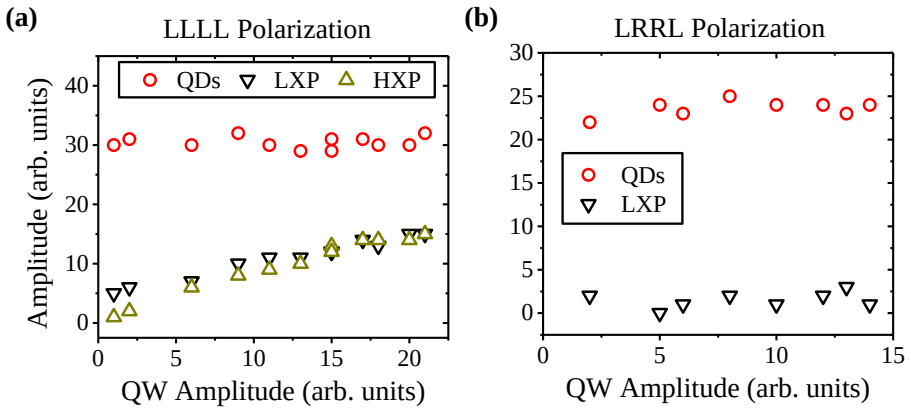

Figure 6.10: The QDs (red circles), LXP (black upside-down triangles) and HXP (green triangles) amplitude dependence on the QW amplitude, which is varied by spectrally-filtering the excitation pulses. For co-circular polarization shown in (a), the QD amplitude remains unchanged, whereas the LXP and HXP decrease with QW amplitude. For cross-circular polarization shown in (b), the QD amplitude remains unaffected by changes in the QW amplitude, and the LXP (and HXP, not shown) amplitude is at the background level.

Previous experiments and calculations of two-quantum spectra from GaAs QWs demonstrated that the dominant contribution to the signal was the interaction of the exciton interband coherence with the mean-field present from other excitons [199]. Moreover, two-quantum coherent

coupling between heavy-hole and light-hole excitons was observed and also attributed primarily to the mean-field. Our observations of two-quantum coherent coupling between QD and QW excitons only for co-circular polarization might suggest that the QW–QD correlations are governed primarily by their mean-field interactions. A comparison of the real and imaginary components of the signal to microscopic calculations is necessary to establish the dominant microscopic interactions giving rise to the two-quantum signal. However, we can determine the dominant many-body effects arising from the microscopic interactions by simulating the 2D spectrum using the analytical OBE simulations discussed in Chapter 3, for a six-level system, shown in Fig. 6.11(a). The energy scheme consists of a ground state ($|g\rangle$), singly-excited QD ($|D\rangle$) and QW ($|W\rangle$) exciton states, doubly-excited states representing two-exciton correlations in the QDs ($|2D\rangle$) and QW ($|2W\rangle$), and a doubly-excited QW–QD correlated state ($|DW\rangle$). A bound biexciton is ignored since the excitation pulses and detected signal were co-circularly polarized. Such a level diagram is equivalent to two four-level systems through a Hilbert space transformation [93, 219, 226]. In the absence of interaction effects, quantum pathways involving the doubly-excited states destructively interfere with pathways associated with interactions between the singly-excited states so that only nonlinearities associated with the individual singly-excited transitions contribute to the signal. Interactions in the system are modeled by breaking the equivalence of the doubly- and singly-excited states by changing the two-exciton $\rightarrow$ exciton optical properties, such as the energies, dephasing rates, or transition dipole moments, compared to the ground state $\rightarrow$ exciton transitions. Experimental and calculated spectra are shown in Figs. 6.11(b) and 6.11(c), respectively.

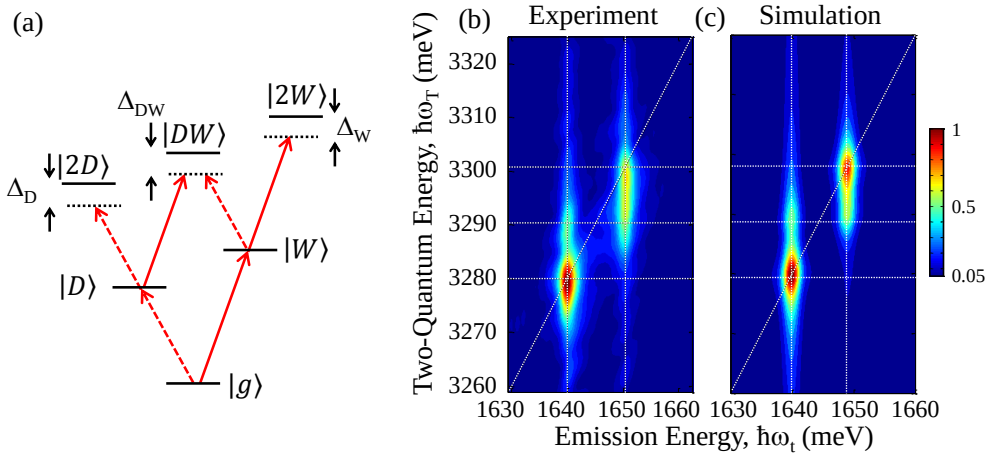

Figure 6.11: (a) Six-level energy scheme used to simulate the measured two-quantum 2D spectrum shown in (b), which was obtained using co-circularly polarized excitation and detection. The energy scheme consists of a single ground state ($|g\rangle$), QD ($|D\rangle$) and QW ($|W\rangle$) exciton states, QD ($|2D\rangle$) and QW ($|2W\rangle$) two-exciton states, and a mixed QW–QD two-exciton state ($|DW\rangle$). The simulated spectrum is shown in (c).

Excellent agreement between the simulation and experiment can be obtained by introducing a renormalization of the two-exciton energies on the order of tens of μeV. The energy shift of each state breaks the equivalence of the doubly- and singly-excited transitions, giving rise to the two-quantum signal. The parameters used in the simulation are not unique, though – excitation-induced dephasing effects will also generate a two-quantum signal. However, these two effects will produce different peak line shapes in the real and imaginary components of the spectrum. Measurements of the complex signal with correct phase is an interesting area of future research and should reveal the dominant coherent interaction effects between QW and QD excitons.

6.4 Electron-Hole Exchange Interaction: Exciton Fine-Structure

The exchange-interaction-mediated fine-structure splitting, Δ_{FSS}, between the two lowest exciton states $|H\rangle$ and $|V\rangle$ has been widely-studied for both fundamental and applied reasons. From an application standpoint, QDs are promising candidates to form the building blocks for

large-scale entangled-photon pair generation. The polarization of photon pairs emitted through cascaded radiative decay of the biexciton state is determined by the intermediate exciton state. In an ideal QD with $\Delta_{FSS} = 0$, the polarization of the photon emitted from the biexciton $\rightarrow$ exciton transition has been shown to be entangled with the polarization of the photon emitted from the exciton $\rightarrow$ ground state transition [253], forming the state $(|H_B H_X\rangle + |V_B V_X\rangle)/\sqrt{2})$, where H and V are the polarization states of the two photons. Splitting of the $|H\rangle$ and $|V\rangle$ states provides "which path" information with respect to the energy of the photons, preventing polarization entanglement. Thus, significant effort is being expended in the pursuit of scalable arrays of QDs with a Δ_{FSS} as close to zero as possible. QDs whose Δ_{FSS} is smaller than the radiative line width of either the $|H\rangle$ or $|V\rangle$ transition can exhibit polarization entanglement, however the degree to which the photons are entangled is maximum for zero splitting. Manipulation of Δ_{FSS} has been achieved using numerous methods, such as application of an in-plane magnetic field [253] and external electric fields in combination with applied mechanical strain [254].

From a fundamental perspective, the dominant microscopic mechanisms that are responsible for the splitting are still under debate [85]. The influence of QD morphology on Δ_{FSS} has been investigated in single dots using photoluminescence [44, 85, 143, 166, 250] or by spectrally averaging the ensemble nonlinear response using time-integrated FWM techniques [45]. These studies have shown that Δ_{FSS} typically decreases with increasing emission energy (decreasing confinement) at a rate ranging from 0.25 to 2 μeV/meV. Moreover, it is generally believed that anisotropy in the confinement potential responsible for non-zero Δ_{FSS} tends to orient $|H\rangle$ and $|V\rangle$ along the [110] and $[1\bar{1}0]$ crystal axes for samples grown along the [001] direction. Elongation and piezo-electric fields are thought to be responsible for the anisotropy [143], both of which are sensitive to the amount of strain in the sample.

In this Section, our efforts to investigate the influence of confinement on Δ_{FSS} in the InAs SAQD sample annealed at 900 °C using 2DCS are discussed (similar experimental parameters were used as in the previous Section). Using 2DCS, Δ_{FSS} can be measured for an entire QD ensemble simultaneously by monitoring the temporal evolution of the non-radiative coherence between $|H\rangle$

and $|V\rangle$. The non-radiative $|H\rangle - |V\rangle$ coherence, which has no optical dipole moment, can be probed optically by coherently exciting the $|g\rangle - |H\rangle$ and $|g\rangle - |V\rangle$ transitions using either two orthogonal linearly-polarized pulses or a single circularly-polarized pulse. We choose to work in the $|H\rangle$ and $|V\rangle$ basis and generate the non-radiative $|H\rangle - |V\rangle$ coherence using the rephasing timing sequence for which the conjugated pulse A arrives at the sample first, followed by pulses B and C. Referring back to the double-sided Feynman diagrams in Fig. 3.10, pulse A, which is polarized along $|H\rangle$, generates an optical coherence along the $|g\rangle - |H\rangle$ transition. Pulse B is incident on the sample after a time $\tau = 200$ fs to avoid coherent artifacts and pulse time-ordering ambiguities and is linearly polarized along $|V\rangle$, so that it generates a coherence along the $|g\rangle - |V\rangle$ transition. The two optical coherences are equivalent to a non-radiative coherence between $|H\rangle$ and $|V\rangle$ that oscillates during T with a frequency equal to $\Delta_{FSS}/\hbar$. Pulse C, linearly polarized along $|H\rangle$, converts this non-radiative coherence back to a coherence along $|g\rangle - |V\rangle$, which radiates along the FWM signal direction and is recorded while the delay T is scanned. The signal is Fourier transformed with respect to T to generate the zero-quantum spectrum, which is shown in Figs. 6.12(a)-(c) for polarization sequences HVHV, VHVH and HHHH, respectively.

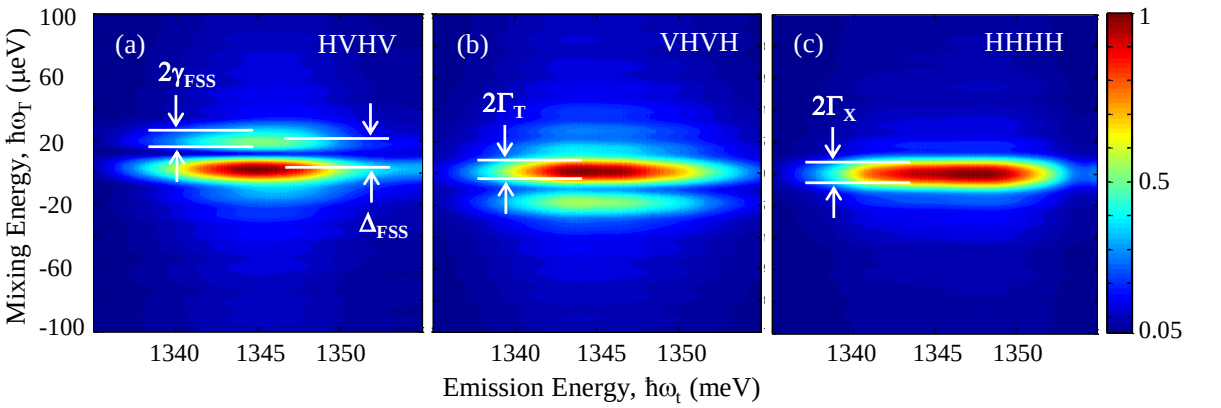

Figure 6.12: Normalized rephasing zero-quantum amplitude spectrum for (a) HVHV, (b) VHVH and (c) HHHH polarization sequences. For HVHV and VHVH polarizations, the spectra feature an $|H\rangle - |V\rangle$ coherence peak at $+\Delta_{FSS}$ and $-\Delta_{FSS}$ along $\hbar\omega_T$, respectively, and a trion peak at $\hbar\omega_T = 0$. Only a single peak dominated by the exciton nonlinear response is observed for HHHH polarization.

The spectrum in Fig. 6.12(a) features a peak at zero mixing energy that is inhomogeneously-broadened along $\hbar\omega_t$, which is attributed to the trion nonlinear response since no quantum pathways exist for the exciton for an HVHV polarization scheme. Being at zero mixing energy, the trion is in either a ground- or excited-state population during T, and the line width along $\hbar\omega_T$ is a measure of the trion population decay rate. The spectrum also features a peak a $\hbar\omega_T \approx 19$ μeV, which stems from the $|H\rangle - |V\rangle$ coherence that oscillates with frequency $\omega_{VH} = \omega_V - \omega_H$ during T. The spectrum shown in Fig. 6.12(b) demonstrates that upon switching the polarization sequence to VHVH, for which during T the non-radiative coherence oscillates with frequency $\omega_{HV} = -\omega_{VH}$, the $|H\rangle - |V\rangle$ coherence peak resonant energy switches sign, as expected for an anisotropic confinement axis aligned along the same crystal axis for all the QDs. When using an HHHH polarization sequence, shown in Fig. 6.12(c), the $|H\rangle - |V\rangle$ coherence disappears and the spectrum features a single peak at zero mixing energy. The amplitude of this peak increases by over an order of magnitude compared to the zero-mixing-energy peak in the other spectra, which is attributed to the allowed exciton coherent pathways for this polarization that dominate the nonlinear response.

6.4.1 Exciton Fine-Structure Splitting and Radiative Line Widths

Quantitative information regarding the radiative line widths and Δ_{FSS} is obtained by fitting slices taken along $\hbar\omega_T$ to either a double $\sqrt{Lorentzian}$, as shown as the solid line in Fig. 6.13(a) for HVHV at an emission energy of 1345 meV, or a single $\sqrt{Lorentzian}$ for HHHH. The exciton and trion population decay rates, Γ_X and Γ_T, respectively, and the $|H\rangle - |V\rangle$ coherence dephasing rate, γ_{FSS}, are obtained from the half width at half maximum of the fits to the corresponding peaks [112]. Δ_{FSS} is the difference between the energies corresponding to the maximum amplitude of the two peaks in either the HVHV or VHVH spectra. Line widths and splitting obtained from the fits are shown in Fig. 6.13(b) for emission energies within the FWHM of the inhomogeneous distribution. With increasing (decreasing) emission energy (confinement), Δ_{FSS} decreases at a rate of 0.1 μeV/meV. For the ensemble, $\Gamma_X \approx 5.8 \pm 0.5$ μeV, $\Gamma_T \approx 5.2 \pm 0.4$ μeV and $\gamma_{FSS} \approx 5.7 \pm 0.3$ μeV. Both Γ_T and Γ_X increase with increasing emission energy, although the changes are within the estimated uncertainties in the line widths.

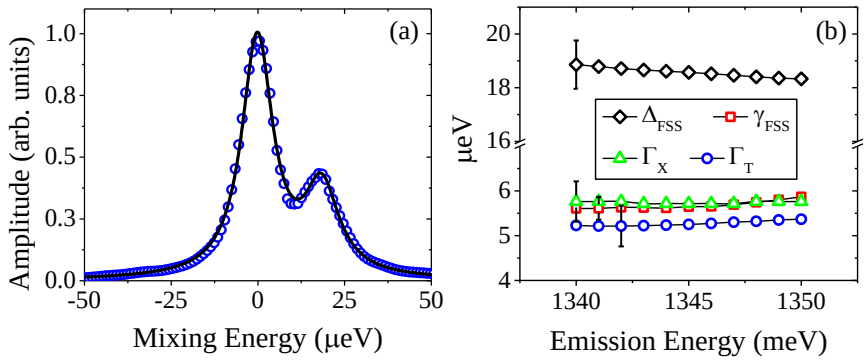

Figure 6.13: (a) A slice (points) taken along $\hbar\omega_T$ at an emission energy of 1345 meV is fit to a double $\sqrt{Lorentzian}$ (solid line) for HVHV polarization. (b) Exciton fine-structure splitting (Δ_{FSS}), the $|H\rangle - |V\rangle$ coherence dephasing rate (γ_{FSS}) and the exciton (Γ_X) and trion (Γ_X) population decay rates are shown as a function of the exciton emission energy.

The population decay rates shown in Fig. 6.13(b) for the exciton and trion indicate that the radiatively limited ZPL widths are $\gamma_X \approx 2.9$ μeV and $\gamma_T \approx 2.6$ μeV, respectively, which

are consistent with FWM studies of samples with similar confinement reported in the literature [45, 150]. Recall that the measured low-temperature exciton and trion ZPL widths for this sample are 12 ± 1 μeV and 8 ± 2 μeV, respectively. The fact that $\gamma_X > \Gamma_X/2$ and $\gamma_T > \Gamma_T/2$ verifies that significant pure dephasing exists in this sample even at low temperature, independent of excitation density. The decrease of Δ_{FSS} with increasing emission energy is consistent with results in the literature for samples with similar confinement [250, 45, 255], although our measured rate at which the splitting decreases is relatively smaller, likely a result of the thermal annealing. This is an interesting result, since it implies that essentially all of the QDs in the sample exhibit to the same Δ_{FSS}, which could perhaps be exploited for large-scale generation of entangled-photon pairs through the application of external fields or strain.

6.4.2 Transition Energy Fluctuation Correlations

The dephasing rate of the $|H\rangle - |V\rangle$ coherence, γ_{FSS}, is equal to Γ_X within experimental uncertainties. This result suggests that not only does a single Δ_{FSS} characterize the exciton fine-structure splitting at a particular resonance energy, but that fluctuations in the $|H\rangle$ and $|V\rangle$ transition energies are correlated. To quantify the level of correlation, the dephasing rate, γ_{FSS}, can be related to the population decay and dephasing rates of the individual $|g\rangle - |H\rangle$ and $|g\rangle - |V\rangle$ optical transitions by [201, 256]

$$\gamma_{FSS} = 1/2 \cdot (\Gamma_{X,H} + \Gamma_{X,V}) + \gamma^p_{FSS}, \tag{6.3}$$

where γ^p_{FSS} is the contribution from pure dephasing mechanisms and is defined as

$$\gamma^p_{FSS} = \gamma^p_H + \gamma^p_V - 2 \cdot R \cdot (\gamma^p_H \cdot \gamma^p_V)^{1/2}. \tag{6.4}$$

In the above expression, γ^p_H and γ^p_V are the pure dephasing rates of states $|H\rangle$ and $|V\rangle$, respectively, and the coefficient R represents the level of correlation between fluctuations in the transition energies of the two states. As shown in the inset to Fig. 6.14, a coefficient $R = 1$

corresponds to a simultaneous energy fluctuation of states $|H\rangle$ and $|V\rangle$ with equal amplitude. Correlated scattering preserves the $|H\rangle - |V\rangle$ coherence – but not the interband optical coherence of the individual transitions – and leads to $\gamma_{FSS} = 1/2 \cdot (\Gamma_{X,H} + \Gamma_{X,V}) = \Gamma_X$ for $\Gamma_{X,H} = \Gamma_{X,V}$ and $\gamma_H^p = \gamma_V^p$ (which is the case for this sample). For uncorrelated scattering, where $R = 0$, the additional dephasing beyond the radiative limit is simply the sum of the dephasing rate of the individual transitions. Anti-correlated scattering ($R = -1$) occurs when the two transitions experience simultaneous and opposite-amplitude transition energy fluctuations and results in the maximum dephasing rate of the $|H\rangle - |V\rangle$ coherence.

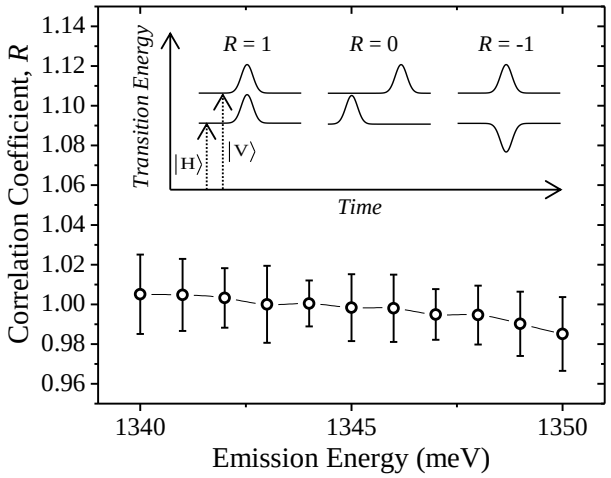

Figure 6.14: Coefficient R representing the level of correlation between transition energy fluctuations of states $|H\rangle$ and $|V\rangle$, shown as a function of emission energy. The inset is a schematic diagram illustrating the effects of correlated ($R = 1$), uncorrelated ($R = 0$) and anti-correlated ($R = -1$) scattering events.

Since the experimentally determined γ_{FSS} is nearly equal to Γ_X, $R \approx 1$ and the exciton states exhibit nearly perfectly correlated scattering. R is determined by inserting the measured line widths into Eqns. 6.3 and 6.4 and is shown in Fig. 6.14. The slight decrease with increasing emission energy stems from the increase in γ_{FSS} since γ_X and Γ_X are independent of emission energy. The slight decrease could arise from an extension of the exciton wave functions into the

barriers for smaller QDs, which could cause the $|H\rangle$ and $|V\rangle$ states to no longer experience similar transition energy scattering events. One might suspect that with increasing temperature, exciton-phonon interactions could reduce the level of correlation. Investigating the temperature dependence of R could provide a deeper understanding into the mechanisms that govern correlation between the bright exciton states and is an interesting direction for future experiments.

Chapter 7

Quantum Well – Quantum Dot Incoherent Population Transfer in GaAs IFQDs

Charge carrier transfer in low-dimensional semiconductor heterostructures occurs in a wide-range of material systems that are technologically relevant. For example, the principle operation of continuous-wave and mode-locked lasers with QD-based active media relies on optical or electrical injection of charge carriers into the wetting layer, after which they relax to the lowest energy confined states in the QDs. QD-based lasers offer a number of advantages compared to those based on bulk or QW active media, including temperature-insensitivity, low current threshold, low noise, enhanced gain over a broad wavelength range and complex gain dynamics that enable novel lasing modes [49, 257], all of which are sensitive to the relaxation dynamics of the injected carriers. Charge transfer dynamics are also important for light-harvesting, where, for example, high energy photons generate electron-hole pairs in highly-excited, weakly-confining states of the QD. The high-energy carriers can relax to lower energy states through the emission of phonons, or energy in excess of the band gap can be harnessed to generate multiple electron-hole pairs from a single photon [78]. Understanding the dynamics associated with charge transfer between states is crucial for increasing the efficiency of enhanced energy conversion processes.

The GaAs IFQD sample is a model system to study population transfer between localized and delocalized states. Because the QW–QD energy separation is smaller than the excitation laser spectral bandwidth, the nonlinear optical response of both the QW and QDs can be simultaneously probed. Moreover, the population transfer and decay rates are slow compared to the duration of the pulses, i.e. the change in population is negligible during the light-matter interaction, but fast

compared to the maximum achievable pulse delays in the 2DCS experiment, enabling complete characterization of the population relaxation dynamics. In this Chapter, incoherent exciton population transfer dynamics between confined states in the GaAs IFQDs and delocalized states in the underlying QW are studied by recording rephasing one-quantum spectra for various delays T. In Section 7.1, 2D rephasing one-quantum spectra revealing incoherent QW–QD exciton population transfer are presented. Procedures for determining transfer rates and amplitudes are discussed and the temperature dependence of the extracted values are shown. A model describing the coupling is introduced in Section 7.2. In Section 7.3, the data are simulated using a rate equation analysis based on the model presented in Section 7.2, and the main conclusions from the simulations are highlighted.

7.1 Measuring QW – QD Population Transfer Dynamics

It is clear from the two-quantum 2D spectra shown in the previous Chapter that QW and QD excitons are coherently coupled through an excitation-induced shift or dephasing mechanism. The coupling strength, however, is too weak for features associated with coherent QW–QD interactions to appear in the rephasing zero- and one-quantum spectra, which are dominated by nonlinearities associated with phase-space filling. Figure 7.1(a) shows a normalized rephasing one-quantum spectrum for a sample temperature of 35 K and for a delay between pulses B and C of $T = 5$ ps. The spectrum is qualitatively similar to the low temperature spectra of this sample shown in the previous Chapters, where the coherent nonlinear optical response of the QD (X_{QDs}) and QW (X_{QW}) excitons appears on the diagonal dashed line, and the QW biexciton peak (B_{QW}) appears red-shifted along the emission energy axis by the QW biexciton binding energy. Quantum pathways associated with the system being in a ground or excited state population after the first two pulses do not accumulate phase during the delay T, but instead decay through interband recombination or non-radiative relaxation. Since the phase does not evolve during T for these processes, population transfer dynamics can be studied by recording 2D rephasing spectra for increasing delay T. Normalized spectra are shown in Figs. 7.1(b)-(c) for T increasing from 20 ps to 100 ps, also

acquired for a sample temperature of 35 K. The maximum amplitudes of the spectra relative to the spectrum taken at $T = 5$ ps are shown on the respective color bars. At short times, the QW and QD peaks dominate the spectrum and are inhomogeneously broadened along the diagonal. With increasing delay T, radiative recombination and population transfer processes decrease the amplitudes of these peaks. Moreover, the peak shapes become more symmetric, which indicates loss of correlation between the exciton excitation and emission energies during T. The appearance of cross peaks at long T reveals incoherent exciton population transfer between the QW and QDs, which would otherwise be concealed in one-dimensional linear and nonlinear spectroscopies. A relaxation peak (RP) appears at the excitation energy of the QW and emission energy of the QDs, revealing incoherent QW $\rightarrow$ QD population relaxation and localization. Thermal activation of QD excitons is observed at longer T as an excitation peak (EP) at the excitation energy of the QDs and emission energy of the QW. The round line shapes of the cross peaks indicate that there is no correlation between the QW and QD energies during the population transfer process.

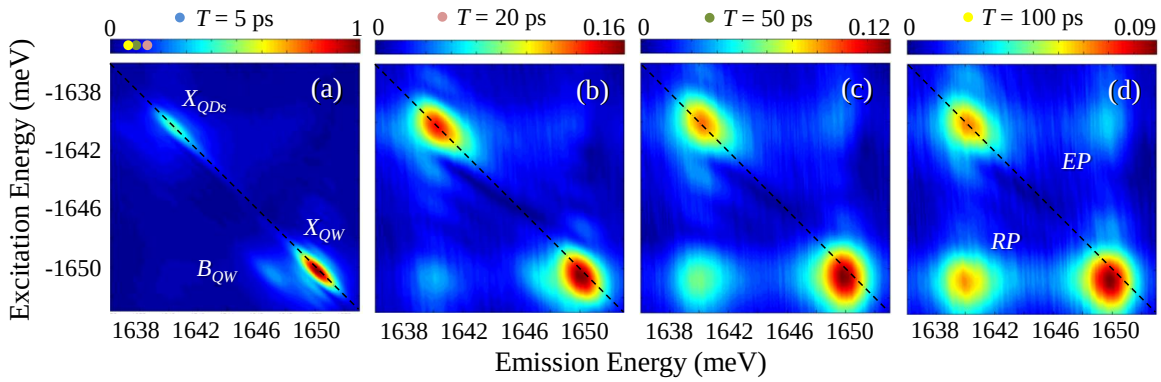

Figure 7.1: QW (X_{QW}) and QD (X_{QDs}) excitons, QW biexciton (B_{QW}), QW $\rightarrow$ QD relaxation (RP) and QD $\rightarrow$ QW excitation (EP) peaks are observed in the normalized 2D rephasing one-quantum spectra for increasing delay T. The sample temperature is 35 K for all spectra. The maximum amplitude of each spectrum relative to the $T = 5$ ps spectrum is shown on the color bar.

The extent to which QW–QD population transfer occurs is quantified by integrating each peak within a square region of ± 3 meV about the peak center, encompassing $> 95\%$ of the feature.

The background is removed by subtracting the line integral of the enclosing region. Integrating each peak, as opposed to simply using the maximum amplitude, provides insight into the coupling mechanisms between the QW and QD ensemble. Migration and tunneling of excitons – resulting in spectral diffusion that broadens the peaks at long delay T – will not transfer the exciton population outside of the integration region. Thus any contributions to the decay of the integrated signal stem from radiative recombination, non-radiative scattering process, spin relaxation between the bright $|\pm 1\rangle$ and dark $|\pm 2\rangle$ states, and QW–QD population transfer. The integrated RP (EP) values are divided by the X_{QW}+RP (X_{QDs}+EP) values in order to properly determine the degree to which excitons excited in the QW (QDs) have transferred to the QDs (QW).

The QW and QD peaks decay bi-exponentially with T, shown using a logarithmic vertical scale in Figs. 7.2(a) and 7.2(b), respectively, for a sample temperature of 35 K. Growth of the RP and EP is shown in Figs. 7.2(c) and 7.2(d), respectively. The RP and EP data are modeled using a fit function proportional to $[1 - \exp(-\Gamma \cdot T)]$. The T-dependence experiments are repeated for sample temperatures ranging from 6 - 50 K, and the temperature dependence of the decay and growth rates extracted from the fits are shown in Figs. 7.2(e)-(h) for the QW, QDs, RP and EP, respectively. Both the QW and QD fast and slow relaxation rates are on the order of 0.1 and 0.01 ps^{-1}, respectively. At temperatures less than 10 K, the RP growth rate is comparable to the QW and QD slow decay rates, and it becomes twice as fast at higher temperatures. The EP is only observed at temperatures higher than 35 K, and its growth rate is < 0.01 ps^{-1}. The observation of an EP at temperatures < 50 K is in contrast to SAQDs exhibiting stronger confinement, where phonon-assisted excitation of excitons out of the QDs occurs at much higher temperatures [258]. The temperature dependence of the ratio of the slow and fast decay fit amplitudes are shown in Figs. 7.2(i) and 7.2(j) for the QW and QDs, respectively, and for the RP and EP growth fit amplitudes in Figs. 7.2(k) and 7.2(j), respectively. The QW and QD fit amplitude ratios decrease with increasing temperature, indicating an enhancement of their respective population decay within the first 10 ps. The RP fit amplitude decreases from unity to $\approx 1/2$ with increasing temperature, while the EP fit amplitude increases to $\approx 1/2$ at 50 K.

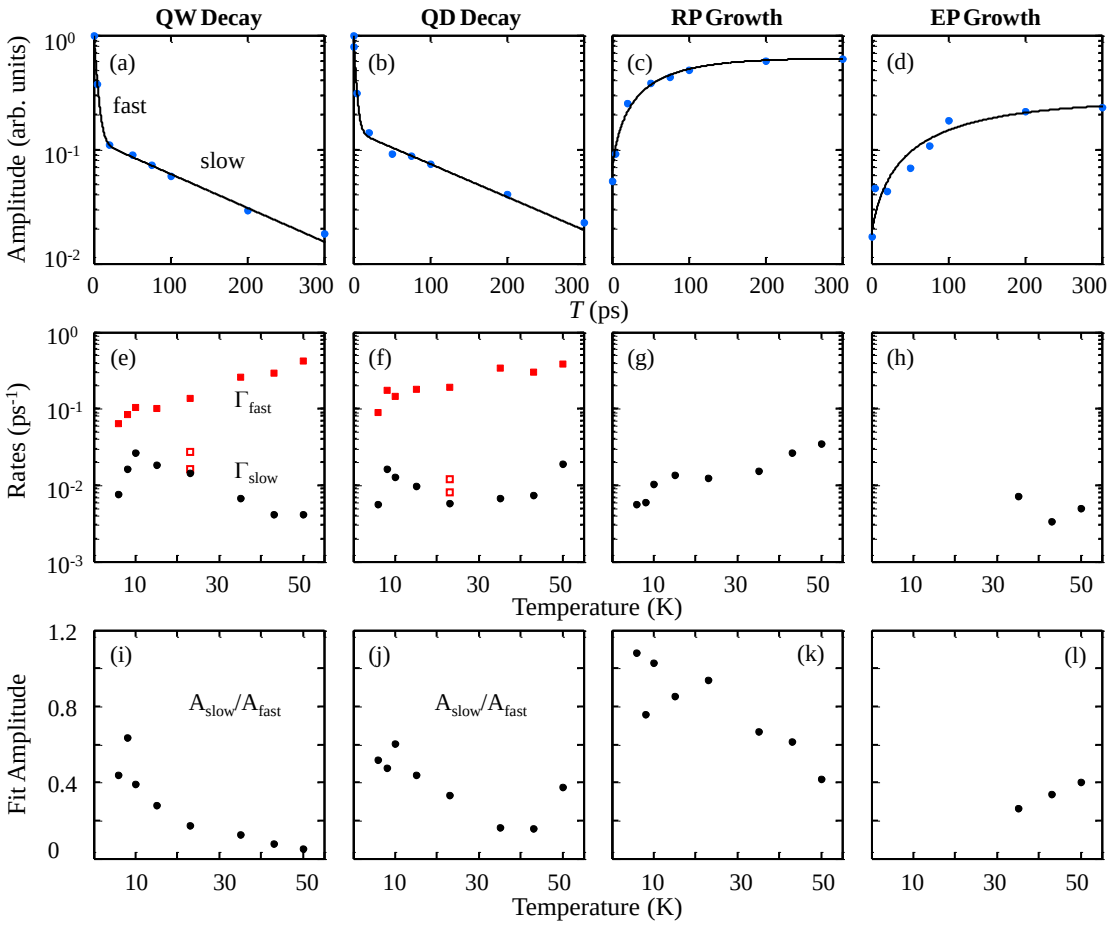

Figure 7.2: Bi-exponential decay of the integrated (a) QW and (b) QD peaks and growth of the (c) RP and (d) EP with T for a sample temperature of 35 K. Temperature dependence of the rates extracted from the fits are shown in (e)-(h). Under high excitation conditions, the QW and QD peaks exhibit a single exponential decay with delay T with a decay rate indicated by the open squares in (e) and (f). These rates converge to the low-excitation slow decay rates for decreasing excitation photon density. Panels (a)-(h) are plotted on a logarithmic vertical scale. The last row shows the temperature dependence of the ratio of the QW (i) and QD (j) bi-exponential fit amplitudes and the RP (k) and EP (l) growth fit amplitudes.

7.2 Modeling QW – QD Population Transfer

The essential features observed in Fig. 7.1 can be captured using a simplified energy scheme for the QW and QD states, which is shown in Fig. 7.3(a). Even though the two-quantum spectra in the previous Chapter revealed that excitons in the QDs and QW interact coherently, this type of coupling is weak compared to incoherent population transfer. Thus we model the QW and QD ground state transitions as two separate two-level systems that are coupled only by exciton population transfer. Both the QW and QD exciton states, each of which is comprised of a spin $\pm 3/2$ heavy-hole and a spin $\pm 1/2$ electron, can be described by their total spin quantum numbers, resulting in four states with spin projections ± 1 and ± 2, as depicted in Fig. 7.3(b). Since the goal of this experiment is to establish the dominant QW–QD incoherent population transfer phenomena, we ignore any exchange interaction effects that can couple and energetically-split the $|\pm 1\rangle$ and $|\pm 2\rangle$ states, and instead consider a simplified system in which optical excitation can create QW and QD excitons in the dipole transition allowed $|\pm 1\rangle$ bright states, which are degenerate.

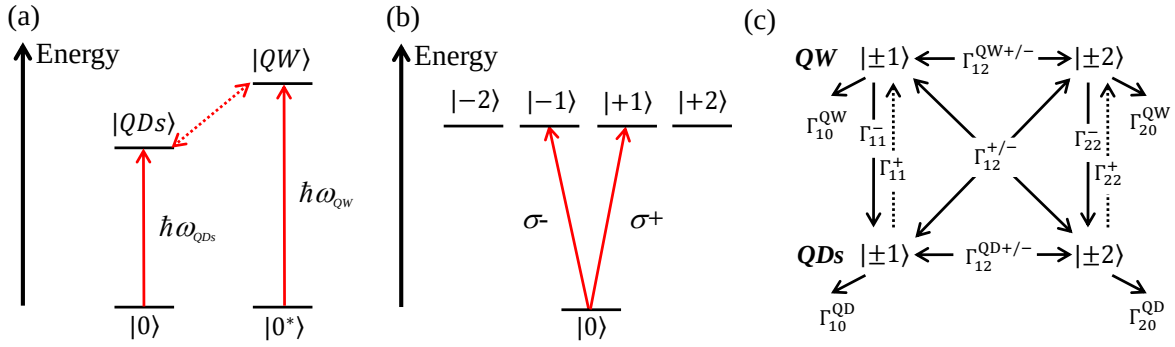

Figure 7.3: (a) Approximation of the QW and QD states as two separate two-level systems that are coupled by incoherent population transfer. The lowest energy QW and QD states are comprised of optically-active $|\pm 1\rangle$ bright states and optically-inactive $|\pm 2\rangle$ dark states, as shown in (b). (c) Proposed model capturing all possible coupling channels between the QW and QD states. Transfer rates between the QW and QD states are labeled as $\Gamma_{ij}^{+/-}$, where the + (-) corresponds to excitation (relaxation) and i (j) corresponds to the initial (final) state. Electron/hole spin flips transfer the exciton between the $|\pm 1\rangle$ and $|\pm 2\rangle$ states at a rate of $\Gamma_{12}^{\mathrm{QW}+/-}$ for the QW and $\Gamma_{12}^{\mathrm{QD}+/-}$ for the QDs. QW/QD radiative and non-radiative population decay to the ground state occurs at a rate of $\Gamma_{i0}^{\mathrm{QW/QD}}$, where i is either 1 or 2 depending on the exciton spin state.

All possible coupling channels between the QW and QD excitons are shown in Fig. 7.3(c). Excitons can decay through radiative recombination or non-radiative processes, such as scattering from defects or exciton-exciton Auger scattering. Alternatively, the $|\pm 1\rangle$ excitons can couple to the dipole forbidden $|\pm 2\rangle$ dark states through electron or hole spin flips. For example, the $|+1\rangle$ state is comprised of a $-1/2$ spin electron and a $-3/2$ spin heavy-hole [1] . An electron spin flip takes the exciton from the $|+1\rangle$ state to the $|+2\rangle$ state, whereas a hole spin flip would couple the $|+1\rangle$ and $|-2\rangle$ states. Reverse spin-flip processes can return the excitons from the $|\pm 2\rangle$ states back to $|\pm 1\rangle$. In the limit that these processes are fast compared to recombination, a quasi-equilibrium population distribution of the bright and dark states will form, and the decay of this distribution is

[1] here we define the exciton spin projection, $J_{Z,X}$, in terms of the electron and hole spin projections, $J_{Z,e}$ and $J_{Z,h}$, respectively, as $J_{Z,X} = J_{Z,e} - J_{Z,h}$

reflected in the slow decay rate of the QW and QD populations. The slow decay rates are limited by recombination and non-radiative scattering, slower spin-flip processes, and QW–QD incoherent population transfer. QW excitons can relax directly into QD states through phonon scattering and emission or indirectly through multiple spin flip scattering events. Cross-coupling between QW and QD bright and dark states involves phonon-assisted population transfer in addition to a spin-flip event. Indirect coupling involving more than one path in Fig. 7.3(c) occurs at a rate that is a multiplicative combination of the rates of each process; thus the likelihood of population transfer occurring via multiple paths decreases as the number of paths involved increases. On the other hand, QD excitons can be excited to the QW states along the reverse paths of the QW $\rightarrow$ QD relaxation.

7.3 Rate Equation Analysis

The QW–QD population transfer dynamics are modeled using a system of rate equations. The goal of the proposed model is not to encompass all QW and QD intra-actions, but instead connect the population transfer phenomena to coupling between the states depicted in Fig. 7.3(c). The model incorporates radiative and non-radiative decay, coupling between bright and dark exciton states and population transfer between QW and QD exciton states. Despite the simplified model, excellent agreement with the results is obtained, providing insight into the coupling dynamics in the sample. Rate equations describing the coupling channels shown in Fig. 7.3(c) are given by the expressions in Eqn. 7.1. The exciton population in the QW is given by $\mathrm{N}_{\pm \mathrm{i}}^{\mathrm{QW}}$ and in the QDs by $\mathrm{N}_{\pm \mathrm{i}}^{\mathrm{QD}}$. $\mathrm{G}_{\mathrm{i}}^{\mathrm{QW/QD}}$ determines the number of available states in the QW or QDs and is given by $(1 - \mathrm{N}_{\pm \mathrm{i}}^{\mathrm{QW/QD}} / \mathrm{N}_{max}^{\mathrm{QW/QD}})$, where i is the spin state.

$$
\begin{aligned}
\dot{\mathrm{N}}_{\pm 1}^{\mathrm{QW}} &= -\left(\Gamma_{10}^{\mathrm{QW}} + \Gamma_{12}^{\mathrm{QW}-}\mathrm{G}_{2}^{\mathrm{QW}} + \Gamma_{11}^{-}\mathrm{G}_{1}^{\mathrm{QD}} + \Gamma_{12}^{-}\mathrm{G}_{2}^{\mathrm{QD}}\right)\mathrm{N}_{\pm 1}^{\mathrm{QW}} + \left(\Gamma_{11}^{+}\mathrm{N}_{\pm 1}^{\mathrm{QD}} + \Gamma_{12}^{\mathrm{QW}+}\mathrm{N}_{\pm 2}^{\mathrm{QW}} + \Gamma_{12}^{+}\mathrm{N}_{\pm 2}^{\mathrm{QD}}\right)\mathrm{G}_{1}^{\mathrm{QW}} \\
\dot{\mathrm{N}}_{\pm 2}^{\mathrm{QW}} &= -\left(\Gamma_{20}^{\mathrm{QW}} + \Gamma_{12}^{\mathrm{QW}+}\mathrm{G}_{1}^{\mathrm{QW}} + \Gamma_{22}^{-}\mathrm{G}_{2}^{\mathrm{QD}} + \Gamma_{12}^{-}\mathrm{G}_{1}^{\mathrm{QD}}\right)\mathrm{N}_{\pm 2}^{\mathrm{QW}} + \left(\Gamma_{22}^{+}\mathrm{N}_{\pm 2}^{\mathrm{QD}} + \Gamma_{12}^{\mathrm{QW}-}\mathrm{N}_{\pm 1}^{\mathrm{QW}} + \Gamma_{12}^{+}\mathrm{N}_{\pm 1}^{\mathrm{QD}}\right)\mathrm{G}_{2}^{\mathrm{QW}} \\
\dot{\mathrm{N}}_{\pm 1}^{\mathrm{QD}} &= -\left(\Gamma_{10}^{\mathrm{QD}} + \Gamma_{12}^{\mathrm{QD}-}\mathrm{G}_{2}^{\mathrm{QD}} + \Gamma_{11}^{+}\mathrm{G}_{1}^{\mathrm{QW}} + \Gamma_{12}^{+}\mathrm{G}_{2}^{\mathrm{QW}}\right)\mathrm{N}_{\pm 1}^{\mathrm{QD}} + \left(\Gamma_{11}^{-}\mathrm{N}_{\pm 1}^{\mathrm{QW}} + \Gamma_{12}^{\mathrm{QD}+}\mathrm{N}_{\pm 2}^{\mathrm{QD}} + \Gamma_{12}^{-}\mathrm{N}_{\pm 2}^{\mathrm{QW}}\right)\mathrm{G}_{1}^{\mathrm{QD}} \\
\dot{\mathrm{N}}_{\pm 2}^{\mathrm{QD}} &= -\left(\Gamma_{20}^{\mathrm{QD}} + \Gamma_{12}^{\mathrm{QD}+}\mathrm{G}_{1}^{\mathrm{QD}} + \Gamma_{22}^{+}\mathrm{G}_{2}^{\mathrm{QW}} + \Gamma_{12}^{+}\mathrm{G}_{1}^{\mathrm{QW}}\right)\mathrm{N}_{\pm 2}^{\mathrm{QD}} + \left(\Gamma_{22}^{-}\mathrm{N}_{\pm 2}^{\mathrm{QW}} + \Gamma_{12}^{\mathrm{QD}-}\mathrm{N}_{\pm 1}^{\mathrm{QD}} + \Gamma_{12}^{-}\mathrm{N}_{\pm 1}^{\mathrm{QW}}\right)\mathrm{G}_{2}^{\mathrm{QD}}. \quad (7.1)
\end{aligned}
$$

Almost all parameters in Eqn. 7.1 can be directly related to the rates extracted from the 2D spectra. The combined radiative and non-radiative recombination decay rates $\Gamma_{10}^{\mathrm{QW/QD}}$ are the measured slow decay rates, Γ_{slow}, and the bright-to-dark coupling rates $\Gamma_{12}^{\mathrm{QW/QD\text{-}}}$ are the measured fast decay rates, Γ_{fast}, in Fig. 7.2. Γ_{11}^{-} is related to the measured RP growth rate and Γ_{11}^{+} is related to the measured EP growth rate. The cross-coupling rates $\Gamma_{12}^{+/-}$ equal $\Gamma_{11}^{+/-} \times \Gamma_{12}^{\mathrm{QW/QD}+/-}$. The sum of the rates contributing to the RP and EP in the model are set equal to the measured growth rates of the peaks, given in Figs. 7.2(g) and 7.2(h), respectively. Dipole selection rules prevent radiative decay of the dark states, thus $\Gamma_{20}^{\mathrm{QW/QD}}$ reflects non-radiative decay processes and is fixed to be an order of magnitude less than $\Gamma_{10}^{\mathrm{QW/QD}}$ in order to best match the population at long times. The dark state QW–QD coupling rates $\Gamma_{22}^{+/-}$ are set equal to $\Gamma_{11}^{+/-}$. The dark-to-bright spin flip rates $\Gamma_{12}^{\mathrm{QW}+}$ and $\Gamma_{12}^{\mathrm{QD}+}$ are adjusted between 0.035 – 0.045 ps^{-1} and 0.065 – 0.07 ps^{-1}, respectively, in order to match the amount of initial population decay at short time. Because a low photon density is used, the exciton states are expected to be far from saturation and $\mathrm{N}_{\mathrm{max}}^{\mathrm{QW/QD}}$ is fixed at an order of magnitude larger than the initial population in each state. The system of rate equations are solved and the solutions (solid lines) are shown in Fig. 7.4 with the measured population amplitude (points) taken at 35 K. The free parameters in the equations are the dark state decay rates $\Gamma_{20}^{\mathrm{QW/QD}}$ and dark-to-bright state spin flip rates $\Gamma_{12}^{\mathrm{QW/QD}+}$. The rates are consistent with detailed balance at the highest temperature, when QW $\leftrightarrow$ QD coupling is significant and the system is in a quasi-equilibrium state. Departure from detailed balance at low temperature is not surprising because the exciton populations decay before equilibrium is reached.

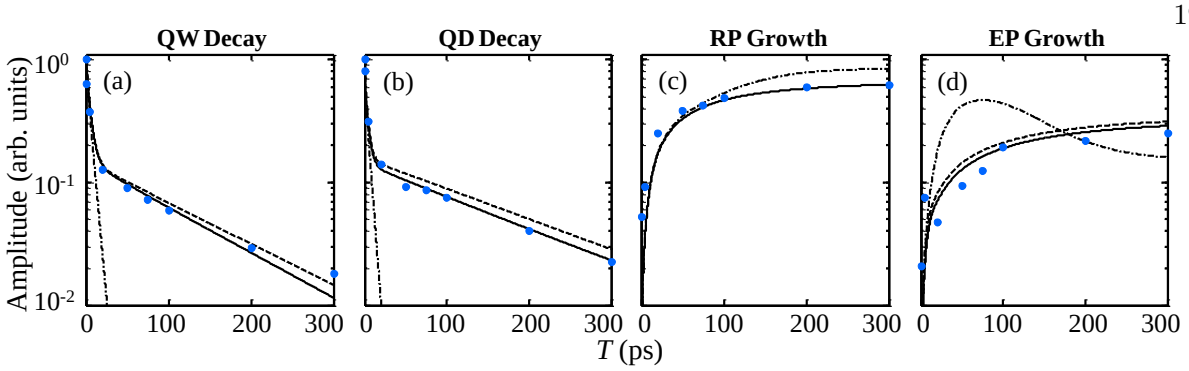

Figure 7.4: Measured population amplitudes (points) and results from the rate equation analysis (solid lines) are shown for the (a) QW, (b) QDs, (c) RP and (d) EP. The rates used in the rate equation analysis are obtained from the measurements except for $\Gamma_{12}^{\mathrm{QW/QD+}}$ and $\Gamma_{20}^{\mathrm{QW/QD}}$, which are adjusted to obtain best agreement between the model and data. Results from the model with $\Gamma_{20}^{\mathrm{QW/QD}}$ (dashed line) and $\Gamma_{12}^{\mathrm{QW/QD+}}$ (dashed-dotted line) equal to zero are also shown.

Agreement between the model and the measurements shown in Fig. 7.4 allows us to draw several conclusions regarding the primary decay and QW–QD coupling mechanisms. To match the QW and QD bi-exponential decay, a population transfer mechanism is required such that a quasi-equilibrium distribution is established between multiple states – otherwise, the population will simply decay at with a rate similar to Γ_{fast} (dashed-dotted line in Fig. 7.4). It is well-established that QW exciton-bound hole spin relaxation occurs on a picosecond timescale due to confinement-enhanced electron-hole exchange [259], and this mechanism is attributed to the fast decay of the QW population. Excitons initially in the $|\pm 1\rangle$ bright states can hole-spin-flip to the $|\mp 2\rangle$ dark states, after which they can non-radiatively decay or spin flip back to the bright states. The onset of the slow decay occurs after formation of a quasi-equilibrium between excitons in the bright and dark states. Exciton population relaxation in QDs is expected to occur more slowly than in QWs because the discrete density of states suppresses many of the effective scattering mechanisms [151, 260]. However, the mechanisms responsible for fast spin relaxation in QWs have been found to be effective for excitons weakly-localized in GaAs IFQDs [261]. Coupling between the exciton spin states through electron or exciton spin flips can contribute to population decay, but these relaxation

processes occur on a much slower time scale compared to Γ_{fast} and are therefore combined with other slow processes in the rate $\Gamma_{10}^{\mathrm{QD}}$ in the model. The similarity between the QW and QD fast population decay suggests that the same exciton-bound hole spin flip mechanisms in the QW are prevalent in the IFQDs as well. This mechanism is included in the model through the terms with rates $\Gamma_{12}^{\mathrm{QD\text{-}}}$. The increase of Γ_{fast} with temperature for the QW and QDs is consistent with previous studies on temperature dependence of hole spin lifetimes in narrow GaAs QWs [262, 263].

With increasing excitation photon density, the QW and QD populations exhibit a single bi-exponential behavior, and the decay rates converge toward a single slow decay rate Γ_{slow}, as shown by the open square symbols in Figs. 7.2(e) and 7.2(f) for a sample temperature of 23 K. This behavior is modeled by setting the maximum number of states $\mathrm{N}_{\mathrm{max}}^{\mathrm{QW/QD}}$ equal to the initial population bright states, which saturates the number of available states $\mathrm{G}_{\mathrm{i}}^{\mathrm{QW/QD}}$. While exciton-exciton Auger scattering increases with excitation density, including this mechanism in the model by introducing terms proportional to $\Gamma_{\mathrm{Auger}} \cdot \mathrm{N}_{\mathrm{i}}^{\mathrm{QW/QD}}$ has an opposite effect – the QW and QD population decay is characterized by a single exponential with a rate that converges towards the fast decay rate Γ_{fast}. Therefore, the observation of a bi-exponential decay suggests that exciton-exciton Auger scattering is negligible for the excitation conditions used in the experiments and that the number of available states greatly exceeds the initial exciton populations.

The ratio of the slow and fast exponential fit amplitudes for the QW and QDs, shown in Figs. 7.2(i) and 7.2(j), respectively, are $\approx 1/2$ for sample temperatures ≤ 10 K, and then decrease with increasing temperature. Since both ground and excited state population terms contribute to the nonlinear response, the initial QW and QD populations should not decay below 1/2 their initial values (since ground state quantum pathways cannot spin flip to dark states). The decrease of the amplitude ratio below 1/2 at higher temperature indicates that additional relaxation mechanisms beyond our model influence the fast dynamics. One possible mechanism could be scattering of excitons to high-momentum states outside of the light-cone, which is known to contribute to a decrease in photoluminescence yield from resonantly excited excitons in QWs [264]. To account for the initial population decay below a relative amplitude of 1/2, we adjust the dark-to-bright

spin flip rates $\Gamma_{12}^{\mathrm{QW/QD+}}$ to match the data. This is justified because the dominant contribution to the QW–QD coupling giving rise to the RP and EP in the model is the direct bright-to-bright transition, which depends on the number of QW and QD excitons in the bright states irrespective of the mechanisms governing their population or decay. The dashed-dotted line in Fig. 7.4 shows the populations when the rates $\Gamma_{12}^{\mathrm{QW/QD+}}$ equal zero, which highlights the significance of the dark-to-bright transfer mechanism for obtaining a bi-exponential decay and reproducing the behavior of RP and EP growth. At long T, the QW and QD populations decay primarily through radiative and non-radiative recombination, exciton and electron spin flips and coupling between the QW and QD states. In the model, the dark state decay rates $\Gamma_{20}^{\mathrm{QW/QD}}$ are set to be an order of magnitude smaller than those for the bright states since the dark states decay non-radiatively. Setting these rates equal to zero, depicted in Fig. 7.4 by the dashed lines, the model underestimates the QW and QD population slow decay rates, the RP is essentially unaffected and the EP growth rate and amplitude increase.

Although the QW and QD can couple through any of the paths indicated in Fig. 7.3(c), the likelihood of a given process occurring decreases with an increasing number of paths involved, since the rates of each path are multiplied to determine the total coupling rate. The most likely QW $\rightarrow$ QD exciton transfer path is directly between the bright $|\pm 1\rangle$ states, which requires acoustic phonon emission for energy and momentum conservation. A possible exciton-phonon coupling mechanism is the following: zero-momentum excitons initially in the QW acquire momentum by scattering from the phonon population, after which they relax to the QD states while emitting one or multiple phonons with the necessary energy and momentum. Because the momentum distribution of excitons in the QDs is centered about zero with a non-zero width $\mathbf{\Delta k}$, QW excitons with zero initial momentum can also lose 10 meV of energy and relax into the QD states via phonon emission. Additionally, the 10 meV energy separation between the QW and QDs can be overcome through a cascaded process involving dark excited states in the QDs [265, 266]. With increasing temperature, the RP exponential fit amplitude decreases from unity at 6 K, indicating that essentially the entire population at long T relaxes to the bright QD states, to 0.4 at 50 K. Although the QW

$\rightarrow$ QD relaxation rate increases with temperature, the process itself becomes inhibited and only approximately half of the initial QW population relaxes to the bright QD states. The decay from unity to 0.4 is attributed to an increase in the QW population decay to the dark QD states. As the bright-to-dark-state exciton-bound hole spin-flip rate $\Gamma_{12}^{\text{QW-}}$ increases with temperature, the QW–QD cross-coupling relaxation rate also increases such that at high temperature, QW excitons in the bright states decay equally to the bright and dark QD states.

Excitation from the QDs to the QW states involves similar paths as the QW relaxation processes in Fig. 7.3(c); however, the physical mechanisms are quite different. Since excitons in the QDs must overcome the 10 meV confinement potential, the EP is only expected to appear at higher temperature where phonon-assisted activation processes can occur. The QD $\rightarrow$ QW activation process is observed only for sample temperatures at 35 K and above, at which significant acoustic phonon population with energy $\geq$ 10 meV exists. While multiphonon activation is possible, the absence of the EP at lower temperatures indicates that QD $\rightarrow$ QW excitation likely arises from a single-phonon process. Similarly to the QW $\rightarrow$ QD RP fit amplitude, the increase in the hole-spin-flip rate $\Gamma_{12}^{\text{QD-}}$ with temperature suggests that at higher temperature, the EP fit amplitude will approach 1/2 because QD excitons will couple to either the bright or dark QW states with equal probability. Best agreement between the model and data is obtained when including terms with the cross-coupling rates $\Gamma_{12}^{+/-}$ and the QW–QD dark state coupling rates $\Gamma_{22}^{+/-}$, so that the sum of the rates contributing to the RP and EP features are equal to the measured growth rates.

The ability of 2DCS to separate quantum pathways is evident from these experiments and analysis. Using one-dimensional linear or nonlinear spectroscopies, the population dynamics could not be accurately modeled, since the overlapping quantum pathways would inhibit extraction of the amplitudes and decay rates. As mentioned in Chapter 5, performing a similar experiment probing population transfer between the exciton ground and first excited states in the InAs SAQDs and applying a similar rate equation analysis would allow one to unambiguously and quantitatively establish the transfer rates and probabilities. Morever, the mechanisms governing energy transfer dynamics in numerous other material systems, such as light-harvesting complexes [187] and col-

loidal nanocrystals designed for multi-exciton generation [135] have been widely debated. Perhaps by performing this type of experiment and analysis, in conjunction with other types of 2DCS experiments discussed in this Thesis thus far, one can better understand and quantify incoherent and coherent energy transfer to design highly-efficient solar energy conversion devices.

Chapter 8

Conclusion

Establishing the connection between morphology and the electronic and optical properties of semiconductor QDs is important for a variety of fields, including solar energy conversion, quantum information, and the generation and detection of classical and quantum states of light, to name a few. Successful implementation of QD-based technologies relies on the ability to grow and prepare QDs with specific properties in a controlled manner. Controlled fabrication has been difficult to achieve since the QD properties are sensitive to the size, shape, strain, confinement and material composition, which can vary dot-to-dot. The focus of this Thesis has been to investigate how the strength and nature of multi-particle interactions, which determine the electronic and optical properties, are influenced by the QD structure and material composition. Optical two-dimensional coherent spectroscopy (2DCS) is a powerful technique for studying interaction effects on the coherent optical response of inhomogeneously-broadened ensembles. 2DCS is based on three-pulse four-wave mixing spectroscopy with the enhancement of interferometric stabilization of the pulse delays, enabling a two-dimensional Fourier transform of the signal to be taken with respect to two of the time delays. By coherently tracking the signal phase, the nonlinear optical response can be unfolded onto two frequency dimensions, allowing for better isolation of the numerous quantum pathways contributing to the signal that are not sufficiently separated using one-dimensional techniques. Moreover, effects from heterogeneity, such as variation in the resonance energy, exciton fine-structure splitting and biexciton binding energy, have distinct signatures in the 2D spectra. By performing a series of experiments in which the pulse time ordering, excitation and detection

polarization states, sample temperature and material composition are varied, we are able to better understand the connection between morphology and the optical and electronic properties of the QDs. Comparison of the results to simulations reveals the role interaction-effects play in the coherent nonlinear optical response.

This thesis begins with a discussion of the fundamental physics of electrons in semiconductors, whose electronic and optical properties are modified by quantum confinement. A discussion of microscopic many-body calculations reported in the literature aids in developing an intuitive understanding of how Coulomb effects modify the properties of the relevant energy levels in the system. Strong Coulomb interactions result in distinct optical dipole transition selection rules, which we have used to isolate specific quantum pathways that contribute to the coherent nonlinear optical response. We have shown that by using specific polarizations of the excitation pulses and detecting a specific polarization component of the signal, the nonlinear optical response of excitons, biexcitons and trions can be unambiguously isolated.

The first set of experiments discussed in this thesis focused on investigating the effects of exciton-phonon interactions on the spectral line shapes obtained from rephasing one-quantum experiments. Analytical solutions to the optical Bloch equations were used to derive expressions for fitting the spectral line shapes, from which the half-width-at-half-maximum provides a measure of the homogeneous line width. The results reveal that excitons in GaAs IFQDs couple weakly with phonons through an elastic interaction mechanism. The dependence of the homogeneous line widths on the sample temperature and emission energy indicate that excitons confined in smaller QDs couple more strongly to phonons. Compared to GaAs IFQDs, the exciton-phonon interaction strength in strongly-confining InAs SAQDs is significantly enhanced, which is revealed by a distinct spectral line shape that is attributed to phonon-assisted transitions between energy levels with different phonon occupation numbers. A comparison of the low-temperature line widths to the population decay rates indicate that the homogeneous line widths of excitons in the GaAs IFQD sample are radiatively-limited, whereas significant pure dephasing still exists in the InAs SAQDs. The line width temperature dependence for excitons in this sample is reproduced using a model

that incorporates both exciton-phonon and exciton-carrier interactions, for which the latter are responsible for low-temperature line width broadening beyond the radiative limit.

Using a certain excitation and detection polarization sequence, the nonlinear response of biexcitons and trions can be isolated in order to investigate confinement effects on Coulomb interactions. Interestingly, for the InAs SAQDs, which exhibit an inhomogeneous line width of ≈ 15 meV, the biexciton binding energy is the same for all dots in the ensemble. Comparison of this result to calculations reported in the literature reveal that the Coulomb effects responsible for biexciton renormalization are independent of the details of confinement for these samples. In contrast, the biexciton binding energy increases by ≈ 0.5 meV across the 2 meV inhomogeneous line width of the GaAs IFQDs. Thus, even though the GaAs IFQD sample is more homogeneous than the InAs SAQD samples, the Coulomb interactions responsible for exciton-exciton interactions are more sensitive to changes in the confinement potential. By increasing the excitation intensity, we are also able to drive the nonlinear response of the InAs SAQD sample beyond the $\chi^{(3)}$ regime to probe for higher-order nonlinearities. An isolated feature appears in the 2D spectrum under high excitation conditions and is attributed to the $\chi^{(5)}$ nonlinear optical response of the biexciton.

Coulomb interactions are also manifest in coupling of the two lowest exciton spin states, which results in mixing and an energetic splitting between them. Using a specific pulse time ordering and excitation and detection polarization sequence, we have measured this splitting for all dots in the InAs SAQD ensemble simultaneously with a spectral resolution limited only by the maximum pulse delay achievable with the apparatus. The data reveal that fluctuations in the transition energies of the two lowest exciton transitions are nearly perfectly correlated. Moreover, similar to the biexciton binding energy, the state splitting is essentially independent of the QD size, which has interesting implications for applications discussed in the next Section.

We have also studied interactions between excitons localized in the GaAs IFQDs and excitons delocalized in the underlying QW. The exciton transitions can be described using a model comprised of two separate two-level systems that are coupled through incoherent population transfer between the excited states. By performing a series of 2DCS experiments in which incoherent

population dynamics can be probed, we have characterized the population decay rates of QW and QD excitons, as well as the population transfer dynamics between them. The dynamic incoherent coupling is modeled using a set of rate equations that require exciton-bound hole spin flips between optically active and inactive states, radiative and non-radiative decay and incoherent QW–QD coupling to reproduce the data. Coherent interactions between QW and QD excitons, which are too weak to be observed in the rephasing spectra, are revealed through two-quantum 2D experiments. Additional experiments and calculations are currently underway, which will help identify the microscopic interactions responsible for the coherent coupling.

8.1 Outlook

The results presented in this Thesis demonstrate the advantages provided by using 2DCS to probe QD ensembles. Applying the technique to a wide-range of material systems beyond those presented here will provide a more comprehensive picture into the effects of QD morphology on the electronic and optical properties. Modifications to the experimental apparatus will also enable new types of experiments with additional tools for manipulating the QD properties, some of which are described below.

8.1.1 Dephasing and Relaxation of Excited Exciton States

The QW–QD population transfer experiments discussed in Chapter 7 can be used to investigate coupling between the exciton ground and first excited states in the InAs SAQDs. The broad homogeneous line width of the excited state exciton at low temperature, shown in Chapter 5, is reproduced by introducing terms in the model that account for phonon-assisted relaxation from the excited state to the ground state. This mechanism, however, is only inferred from the data. Directly measuring this population transfer mechanism by performing rephasing one-quantum experiments for various delays T would provide an unambiguous and quantitative measurement of the decay rate and amplitude of this process. This experiment will require a mode-locked laser with a spectral bandwidth FWHM of at least 25 meV; thus the mode-locked ti:sapphire laser will

not suffice. A second generation 2DCS apparatus that has recently been completed, discussed in Appendix D, will provide the necessary tunability and bandwidth to perform this experiment.

8.1.2 Field Effects on Optical and Electronic Properties

An interesting set of experiments can be performed by using 2DCS to monitor the effects of external magnetic and/or electric fields on the electronic and optical properties of the QDs. For instance, by applying an in-plane magnetic field in combination with an electric field or applied stress, researchers have demonstrated that Δ_{FSS} can be tuned to zero [254]. This aspect has garnered significant interest in recent years, since a QD with Δ_{FSS} less than the radiative line width has been shown to produce polarization-entangled photon pairs via biexciton-exciton cascaded emission [253]. Since all the dots in the InAs SAQD sample studied in this thesis exhibit essentially the same Δ_{FSS}, perhaps by applying the appropriate external fields, one might be able to demonstrate generation of entangle-photon pairs from an ensemble of dots. This experiment would likely require a new sample to be grown that is also strongly thermally-annealed but does not contain a large fraction of charged QDs.

Coupling between QDs has also attracted much interest for quantum information applications. Resonant tunnel coupling of charge carriers or excitons between neighboring QDs can be tuned using an external electric or magnetic field, which has been exploited for qubit gating operations [71]. The spectral response of tunnel-coupled QDs is distinct from the uncoupled case, which might produce unique fingerprints in a 2D spectrum. Heterogeneity will likely wash out any coupling effects in the 2D spectra of coupled QD ensembles, thus a 2DCS scheme that is sensitive to the nonlinear response from a few dots will be necessary. Alternatively, instead of resonant tunnel coupling between adjacent dots, the dots can couple through an electric field enhanced dipole-dipole interaction, which does not require the energies of the coupled QDs to be degenerate [72]. Moreover, it is well-established that QDs grown in adjacent layers, but separated by thin barriers, spatially-align along the growth direction and their resonant energies are correlated [58]. Thus by using a pre-pulse to excite a sub-ensemble of the bottom QD layer while using 2DCS to probe the

ensemble of the top layer or both layers, or by performing a two-color 2DCS experiment, ensemble interaction effects can be studied. The coupling strength can be varied through the applied field, which can enhance or reduce the dipole moment of excitons in the bottom QDs depending on the relative field polarization.

8.1.3 Pre-Pulse 2DCS: Quantum Optics of Quantum Dot Ensembles

A pre-pulse-pump and 2DCS-probe experiment could also be used to perform quantum optics experiments on an ensemble of QDs. For instance, Rabi flopping has been demonstrated in single QDs by pumping the exciton transition and monitoring the photocurrent [66]. The photocurrent has been shown to oscillate for increasing pump pulse area with a period corresponding to the Rabi frequency. Arbitrary optical rotation of the exciton about the Bloch sphere can be achieved by performing a similar experiment using multiple optical pulses [267]; however coherent control has yet to be demonstrated for an array of dots. 2DCS is ideally-suited to probe for population inversion induced by a strong pre-pulse for an ensemble of dots. By taking advantage of the dipole selection rules, one can use a pre-pulse to generate an exciton population in one of the exciton fine-structure states in the InAs SAQD sample. Furthermore, using a specific excitation pulse polarization sequence, one can generate spectrally isolated features that only appear if a significant exciton population is excited by the pre-pulse. Since nearly all QDs in the sample exhibit nearly equal radiative line widths, they should also exhibit similar Rabi frequencies. Thus, with a strong enough pre-pulse intensity, one should be able to invert a significant portion of the ensemble and use 2DCS to probe for inversion beyond the classical limit of a maximum excited-state/ground-state ratio of 1/2.

8.1.4 Carrier Multiplication in Colloidal Nanocrystals

The desire for efficient and inexpensive photovoltaics (PVs) has stimulated significant research on novel materials and solar energy conversion schemes that would enable devices to operate beyond the Shockley-Queisser limit. One such approach is the generation of multiple electron-hole

pairs (excitons) from a single photon, a process known as carrier multiplication (CM). While CM is inefficient in bulk materials, an increase in efficiency in nanocrystals was proposed in 2002 [75] and demonstrated 2004 using PbSe QDs [78]. Subsequent studies have shown that CM occurs in nanostructures of various compositions and shapes, including PbS, Si, InP, and CdTe QDs and more recently PbSe nanorods. CM has been studied using transient pump-probe or time-resolved photoluminescence spectroscopies, which rely on the detection of fast Auger decay signatures of multi-excitons. Comparison of the early-time multi-exciton amplitude compared to the late-time single-exciton background provides a measure of the CM efficiency. By tuning the pump photon energy, the efficiency and energy threshold for CM can be established. Although it is widely-accepted that confinement-enhanced Coulomb interactions lead to higher CM efficiencies, the mechanism responsible for this phenomenon has been difficult to establish. Several ideas have been proposed, including impact ionization (a reverse Auger process), coherent superpositions between single and multiple-exciton states, and multi-exciton generation through virtual excitation of the high-energy exciton state. 2DCS is ideally-suited to investigate the role of these many-body interactions in the CM process, since the technique is sensitive to weak interaction effects in inhomogeneously-broadened ensembles. The proposed mechanisms can be tested using the different types of 2D experiments described throughout this Thesis. For instance, one can probe for coherent superpositions between single and multi-exciton states using multi-quantum multi-dimensional spectroscopy for which peaks will appear in the spectra only if this process contributes to CM. Moreover, using a high-energy pre-pulse to generate electron-hole pairs, one can use 2DCS to probe for CM by looking for Pauli-blocking effects at the lowest-energy exciton resonance. Compared to the conventional detection methods, the excellent signal-to-noise and rapid data acquisition times of 2DCS might provide additional advantages for characterizing the CM efficiency and threshold.

Appendix A

2D Spectroscopy of CdSeTe/ZnS Colloidal Quantum Dots

Semiconductor colloidal nanocrystals exhibit rich and complex electronic structure, which is manifest in the linear and nonlinear optical response. Quantum confinement effects on the electronic and optical properties of nanocrystals have been studied for over three decades [10, 11, 268, 269], with heightened interest in recent years owing to the discovery and characterization of carrier multiplication (CM) in colloidal QDs (CQDs) [78, 135]. From a technical standpoint, compared to epitaxially-grown QDs, CQDs have garnered significant interest owing to the low fabrication cost, simplicity of colloidal synthesis and the relative ease at which quantum confinement effects can be tuned through engineering the size, shape and material composition. As a consequence of the tunable electronic and optical properties and novel quantum phenomena such as CM, CQDs are being explored for a host of applications including photovoltaics [76, 79], laser technology [50] and cavity quantum electrodynamics [270]. A key for exploiting the tunable properties of CQDs is connecting the complexity of the multi-particle interactions to the CQD morphology.

Understanding interactions among the confined particles in CQDs has proven to be difficult because the multitude of transitions in the CQDs are often degenerate, or nearly so, and the optical spectra are dominated by inhomogeneous broadening. A theoretical analysis of the excitonic energy level structure indicates that in spherically-symmetric CQDs, the band-edge exciton transition is eight-fold degenerate. The degeneracy is lifted and the transition is split into five levels when considering the effects of shape asymmetry, the intrinsic crystal field and the electron-hole exchange interaction [271]. The energy spacing and ordering of the levels, as well as the oscillator strength,

strongly depend on the CQD size, shape and material composition.

Recently, multi-exciton interaction effects on the electronic structure and optical properties of CQDs have been probed using optical 2DCS, which has proven to be particularly useful for studying CQDs with extensive inhomogeneous broadening. Harel *et al.* have measured the ultrafast dynamics of electronic coupling between the exciton states and have provided evidence of exciton-exciton interaction effects in the spectra [97]. The presence of exciton-exciton interactions have also been deduced from the spectral line shapes [272]. In this Appendix, we present our preliminary work investigating the homogeneous line width of the lowest exciton transition in CQDs. We studied CdSeTe/ZnS core-shell CQDs (Nano Optical Materials, sample # QD800) that were suspended in a toluene solvent. The manufacturer-specified core diameter is 6.3 nm and shell thickness is 1.8 nm. The solution was kept at room temperature in a precision cell micro cuvette made from IR quartz with a 1 mm cell thickness (NSG Precision Cells, model # 30IR1). The measured optical density (using base e, solid blue line) and the photoluminescence intensity (dashed line) are shown in Fig. A.1. The photoluminescence is centered at 1550 meV with a FWHM of $\approx$ 150 meV. Although maximum excitation occurs at higher energies, the excitation laser spectrum is tuned resonant with the photoluminescence peak in order to avoid excitation of any excited-state transitions.

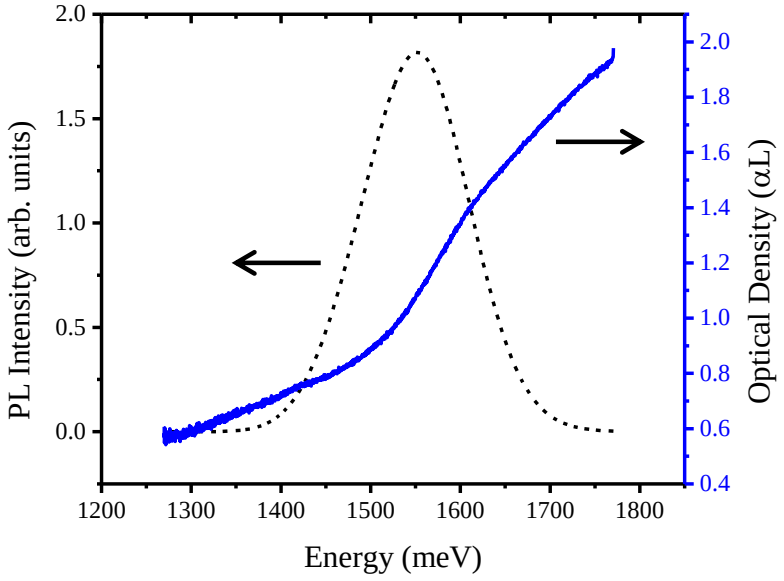

Figure A.1: Room temperature photoluminescence (dashed line) and optical density (base e, solid line) for the CdSeTe/ZnS CQDs. The sample was excited using a 633 nm HeNe laser to generate the photoluminescence spectrum.

A normalized rephasing one-quantum 2D spectrum is shown in Fig. A.2(a). The 2D experiments were performed using co-linear excitation and detection and an excitation photon density of 1×10^{12}·photons·pulse^{-1}·cm^{-2}. The spectrum features a peak on the diagonal with an inhomogeneous line width limited by the laser spectrum. A cross-diagonal slice (points) taken at 1550 meV is shown in Fig. A.2(b). The line shape comprises the ZPL and phonon sidebands are absent. The ZPL shape is fit with a $\sqrt{Lorentzian}$ function (solid line) whose HWHM gives a ZPL width of $\gamma = 11 \pm 3$ μeV, where the estimated uncertainty was determined by repeating the experiment multiple times.

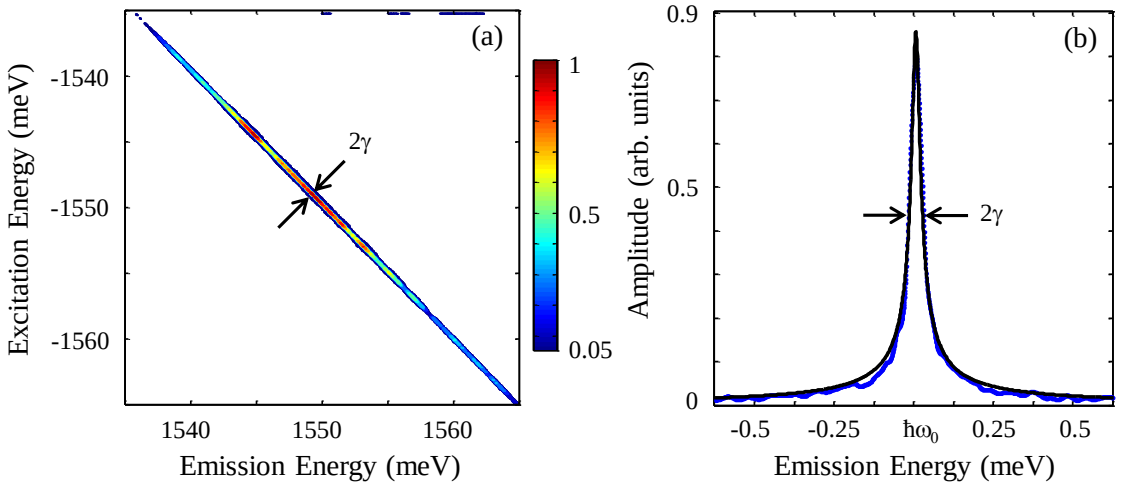

Figure A.2: (a) Normalized rephasing one-quantum amplitude spectrum of the room temperature CdSeTe/ZnS core-shell CQDs acquired using co-linear polarization. (b) A cross-diagonal slice (points) taken at 1550 meV is fit with a $\sqrt{Lorentzian}$ function (solid line) whose HWHM gives a ZPL width of 11 ± 3 μeV.

Recall that the ZPL widths from the GaAs IFQDs and InAs SAQDs are ≈ 30 μeV and ≈ 10 μeV, respectively, at 10 K. The ZPL width measured for the CdSeTe/ZnS CQDs is similar to that of the InAs dots, but remarkably, at room temperature. ZPL widths reported in the literature for CdSe/ZnS CQDs are similar to our measured value, however only at cryogenic temperatures [273, 274, 275, 276]. At elevated temperatures, the reported ZPL width is orders of magnitude larger and the dephasing is dominated by the mechanism giving rise to the phonon sidebands. The absence of phonon sidebands and the narrow ZPL we observe is quite promising for enabling room temperature QD-devices that require long coherence times.

To properly understand the origin of the narrow ZPL, a systematic study of the nonlinear optical response must be performed, including an investigation of the influence of temperature, excitation density and excitation and detection polarization states. Moreover, the radiative lifetime of the bright ground state exciton in CdSe/ZnS is ≈ 10 ns [277], indicating that even the ZPL width we have measured is not radiatively-limited. Furthermore, the dark state transitions have longer radiative lifetimes, which makes interpretation of the results presented in this Appendix dif-

ficult without performing a systematic series of 2D experiments. Because of the long lifetimes, the population likely does not fully decay between sequential sets of pulses, which are separated by 13 ns. Thus, the experiments should also be performed while stirring the samples to introduce a fresh ensemble of CQDs for each set of pulses. By systematically repeating this experiment for various experimental conditions, insight into the relevant dephasing mechanisms can be obtained. Additionally, the second generation 2DCS apparatus discussed in Appendix D offers several advantages, including a lower repetition rate, higher pulse energy, greater tunability and a larger bandwidth, all of which will facilitate 2DCS experiments investigating the dephasing and interaction mechanisms in CQDs.

Appendix B

Perturbative Expansion of the Optical Bloch Equations

The optical Bloch equations (OBEs) can be perturbatively solved by inserting lower orders of the density matrix into the higher order expressions, where each order is an integral over the next lower order, as indicated in Eqn. 3.20. The calculation described in this Appendix is based on the work of Yajima and Taira [201] and Cundiff [89]. We consider the four-level system relevant for the epitaxial QDs, shown in Fig. B.1(a). Recall that the nonlinear optical response for the biexciton can be enhanced relative to the exciton when using an HVVH polarization scheme in the rephasing time ordering, which is shown in Fig. B.1(b). For this polarization sequence, the conjugated pulse A^* is incident on the sample first and generates a coherence between states $|g\rangle$ and $|H\rangle$. After a time τ, the second pulse B impinges the sample and creates a coherence between states $|g\rangle$ and $|V\rangle$, which appears as a zero-quantum coherence between states $|V\rangle$ and $|H\rangle$. After a time T, pulse C is incident on the sample to drive the zero-quantum coherence into a coherence between states $|B\rangle$ and $|H\rangle$, which radiates during the emission time t as the FWM signal to return the system to an $|H\rangle\langle H|$ population state. This sequence is depicted in the double-sided Feynman diagram in Fig. B.1(c).

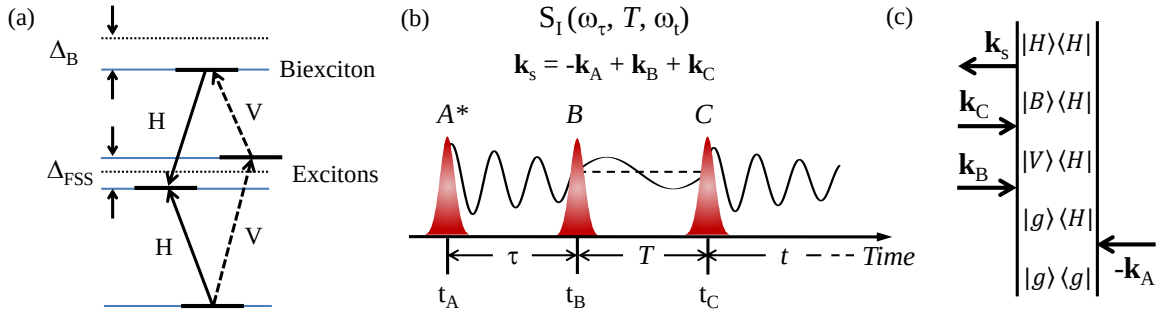

Figure B.1: (a) The four-level energy diagram for a neutral epitaxially-grown QD with an asymmetric confinement potential. The exciton states $|H\rangle$ and $|V\rangle$ are separated by Δ_{FSS}, and the bound two-exciton (biexciton) is shown with a positive binding energy, Δ_B. The rephasing pulse sequence (b) and the double-sided Feynman diagram (c) for the OBE calculation.

For this pulse sequence and polarization scheme, the expressions shown in Fig. 3.5 are used to form the third order density matrix element $\rho_{BH}^{(3)}$,

$$\begin{aligned}\rho_{BH}^{(3)} =& \frac{i\mu_{BV}}{2\hbar}\cdot e^{i\mathbf{k}_C\cdot\mathbf{r}}\int_{-\infty}^{t} dt''' e^{-i\left(\omega_{BH}-i\gamma_{BH}\right)\left(t-t'''\right)}\hat{E}_C\left(t'''\right)e^{-i\omega_C t'''} \\ &\times\frac{i\mu_{VG}}{2\hbar}\cdot e^{i\mathbf{k}_B\cdot\mathbf{r}}\int_{-\infty}^{t'''} dt'' e^{-i\left(\omega_{VH}-i\gamma_{VH}\right)\left(t'''-t''\right)}\hat{E}_B\left(t''\right)e^{-i\omega_B t''} \\ &\times\frac{-i\mu_{GH}}{2\hbar}\cdot e^{-i\mathbf{k}_A\cdot\mathbf{r}}\int_{-\infty}^{t''} dt' e^{-i\left(\omega_{GH}-i\gamma_{GH}\right)\left(t''-t'\right)}\hat{E}_A^*\left(t'\right)e^{i\omega_A t'}\cdot\rho_{GG}^{(0)},\end{aligned} \tag{B.1}$$

where the field is given by $E_j(t) = \hat{E}_j(t)\exp(-i\omega_j t)$ for $j = A, B, C$. The transition frequency, dipole moment and dephasing rate between states $|j\rangle$ and $|k\rangle$ are defined as ω_{jk}, μ_{jk} and γ_{jk}, respectively. Equation B.1 can be simplified by defining $\mathbf{k}_S = -\mathbf{k}_A + \mathbf{k}_B + \mathbf{k}_C$ and grouping terms, leading to the expression

$$\begin{aligned}\rho_{BH}^{(3)} =&\rho_{GG}^{(0)}\frac{-i\mu_{BV}\mu_{VG}\mu_{GH}}{8\hbar^3}e^{i\mathbf{k}_S\cdot\mathbf{r}}e^{-i\left(\omega_{BH}-i\gamma_{BH}\right)t}\\ &\times\int_{-\infty}^{t}dt'''\cdot e^{-i\left(\omega_C-\omega_{BH}+\omega_{VH}\right)t'''}\cdot e^{\left(\gamma_{BH}-\gamma_{VH}\right)t'''}\cdot\hat{E}_C\left(t'''\right)\\ &\times\int_{-\infty}^{t'''}dt''\cdot e^{-i\left(\omega_B-\omega_{VH}+\omega_{GH}\right)t''}\cdot e^{\left(\gamma_{VH}-\gamma_{GH}\right)t''}\cdot\hat{E}_B\left(t''\right)\\ &\times\int_{-\infty}^{t''}dt'\cdot e^{i\left(\omega_A+\omega_{GH}\right)t'}\cdot e^{\left(\gamma_{GH}\right)t'}\cdot\hat{E}_A^*\left(t'\right).\end{aligned}\tag{B.2}$$

In the limit that the pulses are short compared to the system dynamics and the pulse delays, we can approximate the field envelopes as Dirac delta function pulses in time. In this case, the integrals can be easily evaluated in Eqn. B.2 using the expression $\hat{E}_j(t)=\tilde{E}_j\cdot\delta(t-t_j)$, where t_j is the arrival time of pulse E_j for $j=A,B,C$. Setting the field frequencies all equal to ω and inserting the above expression for the field envelopes into Eqn. B.2 gives

$$\begin{aligned}\rho_{BH}^{(3)} =&\rho_{GG}^{(0)}\frac{-i\mu_{BV}\mu_{VG}\mu_{GH}}{8\hbar^3}e^{i\mathbf{k}_S\cdot\mathbf{r}}e^{-i\left(\omega_{BH}-i\gamma_{BH}\right)t}\\ &\times e^{-i\left(\omega-\omega_{BH}+\omega_{VH}\right)t_C}\cdot e^{\left(\gamma_{BH}-\gamma_{VH}\right)t_C}\cdot\tilde{E}_C\\ &\times e^{-i\left(\omega-\omega_{VH}+\omega_{GH}\right)t_B}\cdot e^{\left(\gamma_{VH}-\gamma_{GH}\right)t_B}\cdot\tilde{E}_B\\ &\times e^{i\left(\omega+\omega_{GH}\right)t_A}\cdot e^{\left(\gamma_{GH}\right)t_A}\cdot\tilde{E}_A^*\cdot\Theta\left(t-t_C\right)\Theta\left(t_C-t_B\right)\Theta\left(t_B-t_A\right),\end{aligned}\tag{B.3}$$

where $\Theta(t)$ is the Heaviside theta function. If we let $\rho_{BH}^{(3)}=\hat{\rho}_{BH}^{(3)}\exp(-i\omega t)$ and define $t\equiv t-t_C$, $T\equiv t_C-t_B$ and $\tau\equiv t_B-t_A$, then Eqn. B.3 can be re-written as

$$\begin{aligned}\hat{\rho}_{BH}^{(3)} =&\rho_{GG}^{(0)}\frac{-i\mu_{BV}\mu_{VG}\mu_{GH}}{8\hbar^3}e^{i\mathbf{k}_S\cdot\mathbf{r}}\tilde{E}_A^*\tilde{E}_B\tilde{E}_C\cdot\Theta\left(t\right)\Theta\left(T\right)\Theta\left(\tau\right)\\ &\times e^{-\gamma_{BH}t-\gamma_{VH}T-\gamma_{HG}\tau-i\omega_{VH}T}e^{i\left(\omega-\omega_{BH}\right)t}\cdot e^{-i\left(\omega-\omega_{HG}\right)\tau},\end{aligned}\tag{B.4}$$

where we have taken advantage of the fact that $\gamma_{GH}=\gamma_{HG}$ and $\omega_{GH}=-\omega_{HG}$. The third-order macroscopic polarization, $\hat{P}^{(3)}$, is obtained by taking the trace of $\hat{\rho}_{BH}^{(3)}$ with the dipole moment operator, μ. To account for an inhomogeneous distribution of frequencies, this result can be integrated over a two-dimensional distribution function for ω_{BH} and ω_{HG}:

$$\hat{P}^{(3)}_{BH} = N \int_{-\infty}^{\infty} \int_{-\infty}^{\infty} \mu_{BH} \cdot \hat{\rho}^{(3)}_{BH} \cdot g\left(\omega_{BH}, \omega_{HG}\right) d\omega_{BH} d\omega_{HG}, \tag{B.5}$$

where N is the number of dipoles per unit volume and $g(\omega_{BH}, \omega_{HG})$ is the distribution function, for which we choose to use a two-dimensional Gaussian,

$$g\left(\omega_{BH}, \omega_{HG}\right) = \frac{\sqrt{a_{11}a_{22} - a_{12}^2}}{\pi} e^{\left[a_{11}\left(\omega_{BH}-\omega^c_{BH}\right)^2 - 2a_{12}\left(\omega_{BH}-\omega^c_{BH}\right)\left(\omega_{HG}-\omega^c_{HG}\right) + a_{22}\left(\omega_{HG}-\omega^c_{HG}\right)^2\right]}, \tag{B.6}$$

centered at frequencies ω^c_{BH} and ω^c_{HG}. The parameters a_{11}, a_{12} and a_{22} are useful for evaluating the integrals. To provide physical insight, they can be recast as

$$\begin{aligned} R &= \frac{a_{12}}{\sqrt{a_{11}a_{22}}} \\ \delta\omega_{BH} &= \sqrt{ln\left(2\right)\frac{a_{22}}{a_{11}a_{22} - a_{12}^2}} \\ \delta\omega_{HG} &= \sqrt{ln\left(2\right)\frac{a_{11}}{a_{11}a_{22} - a_{12}^2}}, \end{aligned} \tag{B.7}$$

where R is the correlation coefficient and $\delta\omega_{BH}$ ($\delta\omega_{HG}$) is the half-width at half-maximum of the distribution along the ω_{BH} (ω_{HG}) axis. Perfect correlation between ω_{BH} and ω_{HG} corresponds to $R = 1$, whereas by $R = 0$ describes no correlation. Evaluating the integral in Eqn. B.5 yields

$$\begin{aligned} \hat{P}^{(3)}_{BH} =& \rho^{(0)}_{GG} \frac{-i\mu_{BH}\mu_{BV}\mu_{VG}\mu_{GH}}{8\hbar^3} e^{i\mathbf{k}_S\cdot\mathbf{r}} \tilde{E}^*_A \tilde{E}_B \tilde{E}_C \cdot \Theta\left(t\right)\Theta\left(T\right)\Theta\left(\tau\right) \\ &\times e^{-i\left(\omega-\omega^c_{HG}\right)\tau} \cdot e^{i\left(\omega-\omega^c_{BH}\right)t} \cdot e^{-\gamma_{BH}t - \gamma_{VH}T - \gamma_{HG}\tau - i\omega_{VH}T} \\ &\times e^{-1/4ln(2)\left[\left(\delta\omega_{HG}\tau\right)^2 - 2R\delta\omega_{HG}\delta\omega_{BH}\tau t + \left(\delta\omega_{BH}t\right)^2\right]}. \end{aligned} \tag{B.8}$$

This expression can be inserted into Eqn 3.22 to calculate the radiated electric field due to the third-order polarization. A similar derivation can be performed for the other Feynman diagrams presented in Chapter 3. Alternatively, the parameters in Eqn. B.8 can be replaced by those associated with the corresponding Feynman diagram, since the diagrams in general will result

in a similar expression. The total two-dimensional time-domain signal is Fourier-transformed with respect to the varied delays to generate a two-dimensional spectrum. For the $\chi^{(5)}$ nonlinear response in which one of the pulses acts three times to generate a six-wave mixing signal in the FWM phase matched direction, this derivation can also be easily adapted. The general expression will be the same since additional time delays need not be considered, although the nonlinear response will be proportional to $i\mu^6 E^5/32\hbar^5$, where each μ and E in this expression represents a single vertex of the Feynman diagram.

Appendix C

Alignment Procedure for the MONSTRs

This Appendix outlines the alignment procedure for the first generation JILA-MONSTR. Alignment of the second generation apparatus is performed using a similar procedure, although not all the steps are necessary due to the inclusion of corner cube retro-reflectors on the translation stages. Meticulous alignment is crucial for a few reasons: 1) If the beams are not properly aligned onto the translation stages, then their wavevectors will vary while the stages are scanned. This effect will gradually reduce the beam overlap at the sample, leading to an artificially fast decay of the FWM signal; 2) The stabilization and stepping algorithm requires excellent overlap of the HeNe beams at the diagnostic output, which cannot be achieved without precise alignment; and 3) When properly aligned, the day-to-day alignment of the experimental setup is minimal. For instance, as of writing this Thesis, we have not had to re-align the MONSTR for over three years. The only alignment necessary is to adjust the pointing of the Ti:sapphire and HeNe lasers into the MONSTR, which is relatively straightforward. The alignment procedure is separated into five sections: 1) Initial beam alignment into the bottom deck of the MONSTR; 2) alignment of the bottom deck; 3) alignment of the top deck; 4) closing the MONSTR; and 5) aligning the two decks with respect to each other.

The components used for the MONSTR experimental setup are the following:

- HeNe laser $\rightarrow$ from *CVI Melles Griot*, part # 25 LHP 171-249
- Mirrors $\rightarrow$ either $1/2''$ or $1''$ diameter protected silver

- Beam splitters → $1''$ diameter, 1 mm thick FABS low-dispersion beam splitters from *CVI Melles Griot*
- Compensation plates → windows made from the same substrate as the FABS beam splitters, double-side anti-reflection coated
- PZT → ring piezo-electric actuators from *Piezomechanik GMBH*, part # HPCH150/6−2/2
- Dichroic mirrors → both from *CVI Melles Griot*, part #'s LWP-0-R-633-T-800-PW-2025-C and LWP-45-Rp-633-Tp-800-PW-1025-C
- B-M1 and T-M1 mirror mounts → from *Newport Corporation*, part # SS100-R3H
- Translation stages → from *Aerotech Inc*, AXIS-X/Y/Z are all model # ALS130H-050-PLUS and AXIS-U is model # ALS135-200-PLUS
- Translation stage controller → *Aerotech Inc* NPAQ drive rack and Lab-VIEW integrated A3200 motion controller software
- The remainder of the mounts on the bottom and top decks are custom made by the JILA machine shop
- The decks are made from cast aluminum, have a mass of 19 kg each and are precision machined using a computer numerical control (CNC) mill
- The piezo actuators are controlled using JILA-built piezo drivers, servo loop filters, amplifiers and silicon photodiode detectors.

C.1 Initial Beam Alignment into the Bottom Deck (refer to Fig. C.1)

1.1 Using mirrors O-M1, O-M2 and O-M4, align the Ti:sapphire beam to the JILA-MONSTR input, adjusting to the proper height and leaving enough space to place apertures and the Ti:sapphire/HeNe dichroic mirror (O-DM1) on the optical table.

1.2 Place O-DM1 into the Ti:sapphire beam path at 45° relative to the beam propagation as shown in Fig. C.1, and adjust the HeNe beam path using the HeNe kinematic mount and O-M3 to co-propagate with the Ti:sapphire beam.

1.3 Re-align the Ti:sapphire beam through the apertures located at B-A1 and B-A2 by adjusting mirrors O-M2 and O-M4. Placing a photodiode behind the set of apertures helps to maximize the power through the apertures.

1.4 Re-align the HeNe beam through apertures B-A1 and B-A2 by adjusting the HeNe kinematic mount and mirror O-M3. The beams should now both be co-propagating into the bottom deck assembly. If the HeNe is not mounted using a kinematic holder, then another mirror in addition to O-M3 can be used to help with adjustment, although it is not necessary.

1.5 Place apertures A1 and A2 in the Ti:sapphire/HeNe beam paths. When the entire alignment procedure is complete, these apertures can facilitate day-to-day alignment.

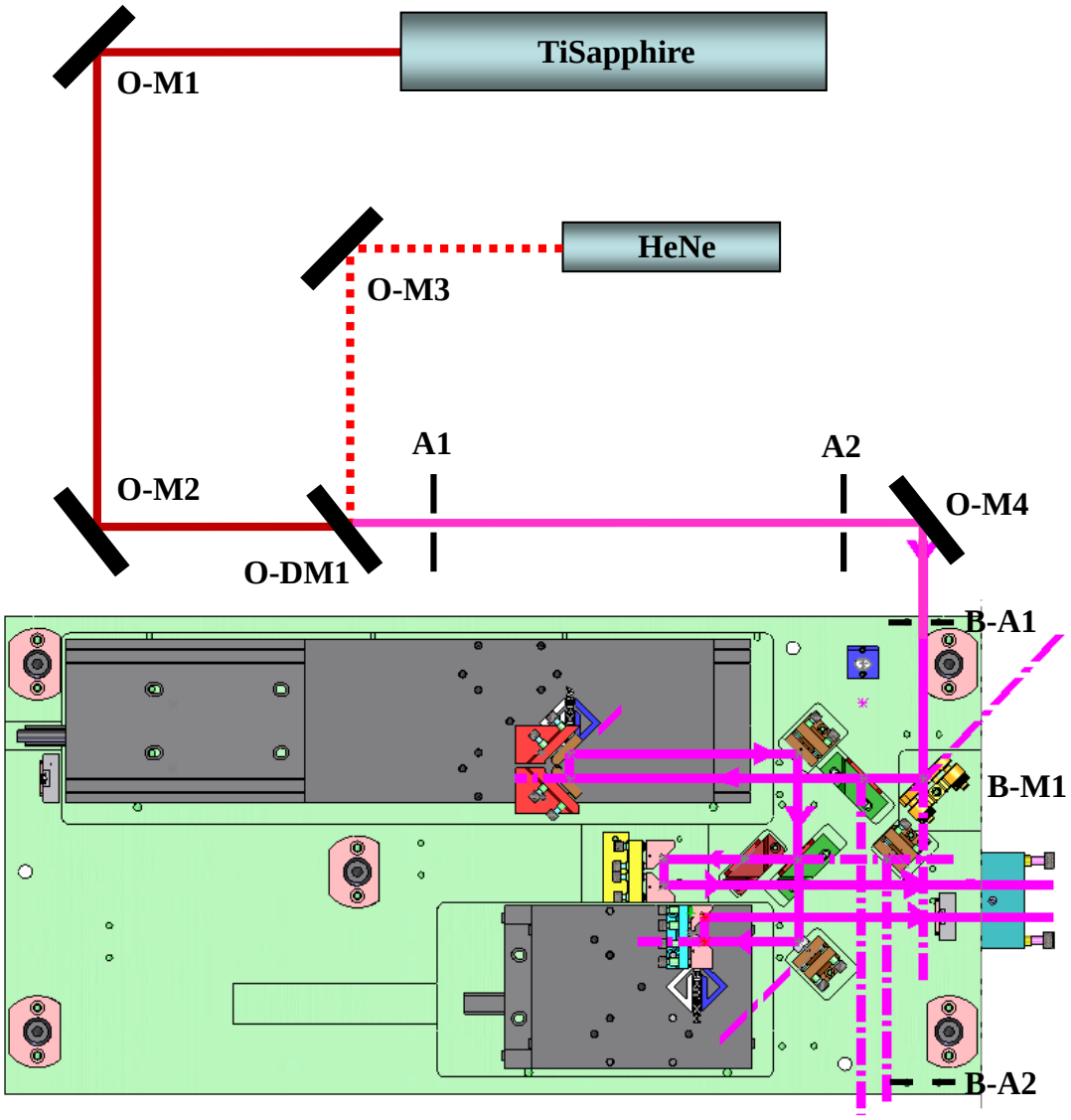

Figure C.1: Layout of external optics aligning the beams into the bottom deck of the MONSTR. Definitions: M – mirror; DM – dichroic mirror; A – aperture.

C.2 Bottom Deck Assembly Alignment (refer to Fig. C.2)

2.1 For alignment purposes, block the Ti:sapphire laser and use only the HeNe.

2.2 Install the translation stages. Alignment pins have been inserted to ensure that the stage motion is parallel to the side of the bottom deck.

(a) At this point, use the software provided by *Aerotech* to check that the stages are operating correctly, i.e. minimal in-position jitter, accurate position, minimal move-and-settle times.

(b) After the alignment of the bottom deck is completed, the HeNe errors signals should be used as a more accurate diagnostic of the translation stage performance. For instance, monitor the HeNe fringes at the diagnostic detector while repeatedly stepping one of the stages a specified distance corresponding to a certain number of HeNe fringes.

2.3 Attach B-M1 and crudely align the reflection through apertures B-A3 an B-A4.

(a) Adjust the tilt using the horizontal and vertical adjustors on B-M1 until the beam passes through aperture B-A4.

(b) Close aperture B-A3 and check alignment of the beam. Adjust the corner vertically- and horizontally-coupled tilt knob – this will ultimately translate the beam horizontally.

(c) Repeat steps (a) and (b) until the beam passes cleanly through both apertures.

2.4 Attach B-BS1 and horizontally-center the reflected beam through the PM1 position.

2.5 Attach PM1 to deflect the beam vertically. Take the necessary safety measures to contain the reflected beam. Because the mount has no kinematic adjustors, place thin shim wedges underneath the mount to obtain vertical propagating of the beam.

2.6 Check the parallelism of the input beam onto he AXIS-U stage.

(a) Place a photodiode behind the aperture B-A4.

(b) Mount a razor blade on the stage. Without any obstruction of the beam by the blade, measure the total signal on the photodiode.

(c) With the razor blade mounted horizontally and the stage at its forward-most position (towards the front of the MONSTR, farthest away from aperture B-A4, block the

beam so that the signal at the photodiode is one-half the maximum amplitude. Scan the stage either using the computer control or by hand. If the photodiode signal amplitude increases, then the angle between the normal of the mirror in B-M1 and the reflected beam is greater than 45°. Adjust the B-M1 actuators counter-clockwise to compensate. Repeat this process until the beam is passing through both apertures and the amplitude on the photodiode does not vary when the stage is translated through its entire travel range (termed "flattening" the beam).

(d) Repeat (c) with the razor blade mounted vertically. Note that the stage is slightly bowed so that perfect alignment cannot be achieved. Perform the alignment near the position corresponding to time-zero of the pulse delays.

2.7 Attach B-RR1-M2 on the AXIS-U stage.

(a) Attach two apertures onto the optical table, with the farthest distance possible between them.

(b) Move the stage such that the beam is passing through the first aperture. The vertical tilt actuator on the B-RR1-M2 will have to be adjusted.

(c) Open the first aperture and adjust the horizontal tilt actuator so that the beam passes through the second aperture.

(d) Close the first aperture and move the stage until the beam passes through.

(e) Repeat steps (c) and (d) until the beam propagates through both apertures simultaneously.

2.8 Attach B-RR1-M1 on the AXIS-U stage. Attach B-M2 to the bottom deck.

2.9 Using B-RR1-M1 and B-M2, coarsely align the beam through apertures B-A5 and B-A6.

2.10 Place a razor blade in front of a photodiode detector placed behind the B-A6 aperture.

(a) Open both B-A5 and B-A6 apertures. Similar to step 2.6, scan the stage and adjust the horizontal and vertical tilt adjustors on B-RR1-M1 to flatten the beam.

(b) Close the apertures and adjust B-M2 in order to align the beam through them.

(c) If the vertical pointing of the beam is incorrect, then adjust the vertical actuator on B-RR1-M2 to raise or lower the beam in B-RR1-M1. Then repeat steps (a) and (b). Keep in mind that the horizontal and vertical adjustments are slightly coupled, so steps (a), (b) and (c) will have to be iterated.

2.11 Attach beam splitter mount B-BS2 and adjust the reflection through aperture B-A7.

2.12 Attach compensator plate mount B-CP1 and B-RR2 onto the bottom deck and align the reflection through aperture B-A8.

(a) Note that the pointing of this beam might be incorrect. The pointing will be adjusted and aligned to the other bottom deck beam after it has been properly aligned.

2.13 Attach B-PZT1 to the bottom deck and align the reflection through the apertures B-A9 and B-A10.

2.14 Finely adjust the beam onto the AXIS-Z stage using the procedure outlined in step 2.6.

2.15 Place B-RR3 onto the AXIS-Z stage and align the reflection through aperture B-A11.

2.16 Place a razor blade in front of a photodiode behind aperture B-A11.

(a) Open aperture B-A11. Similar to step 2.6, scan the stage and adjust the horizontal and vertical tilt actuators on the B-RR3 output mirror to flatten the beam.

(b) Close aperture B-A11 and adjust the B-RR3 input mirror to align the beam through the aperture.

(c) Iterate steps (a) and (b) until the beam is flattened and passing through aperture B-A11. Keep in mind that because the mounts slightly couple the horizontal and vertical

adjustments, (a) and (b) will have to be iterated between the horizontal and vertical alignment. This beam is now referred to as the Tracer beam.

2.17 The other bottom deck beam, now referred to as beam C, can be aligned to the Tracer beam.

2.18 Using a 1" square pattern (printed and taped level to a mirror mount, for example), adjust the pointing of beam C so that the beam overlaps with the lower-left corner of the pattern (when looking at the pattern in the propagation direction) when the pattern is placed close to the MONSTR and as far away as possible. Since the Tracer beam has been properly aligned, the pattern placement can be established by ensuring that the Tracer beam is on the lower-right corner of the pattern for both positions. Adjust the tilt actuators on the input and output mirrors of B-RR2 to obtain correct alignment of beam C.

2.19 The relative alignment of beam C to the Tracer beam can be checked by measuring the cross-correlation of the Ti:sapphire beams with a BBO crystal.

(a) Place an aperture in each of the beam paths, leaving enough room for a focusing lens and BBO crystal.

(b) Insert a $3''$ diameter focusing lens into the beam paths, and adjust the lens position so that the beams travel through the apertures after focusing.

(c) Insert the BBO crystal and adjust its alignment so that three frequency-doubled beams appear – two for the nonlinear interaction of the individual beams and a third for the interaction involving both of them. The power of the three frequency-doubled beams should be equal to each other – if this is not the case, the overlap of the beams is not sufficient and the alignment of beam C needs to be adjusted by repeating step 2.18. Then block the Ti:sapphire beam for the remainder of the bottom deck alignment.

2.20 Attach B-M3 to the bottom deck.

2.21 Attach the $2''$ diameter DCM1 to the front of the bottom deck assembly and align the HeNe reflection back into the MONSTR.

(a) Block beam C before DCM1 so that it is not reflected back into the MONSTR. Adjust DCM1 so that the Tracer beam at the HeNe diagnostic output port does not walk when translating the AXIS-Z stage.

(b) Unblock beam C. Beam C and the Tracer beam should overlap and collinearly propagate after B-M3. If this is not the case, then the alignment of the Tracer beam, beam C or DCM1 is not correct. When translating the AXIS-Z stage, oscillations in the interference pattern of the Tracer and beam C should be observed, and the beams should not walk.

(c) When translating the AXIS-U stage, the HeNe interference patterns at the diagnostic output should be walk nor should the interference patterns change. If they do, then either the Tracer, beam C or DCM1 needs to be re-aligned.

2.22 At this point, proper alignment will result in the output Tracer and C beams collinearly propagating along the lower two corners of a $1''$ box and the HeNe diagnostic outputs should also be collinearly propagating with high-visibility interference fringes apparent at all locations along the beam paths. If both of these conditions are not achieved, it is crucial that the beams be re-aligned before closing the MONSTR.

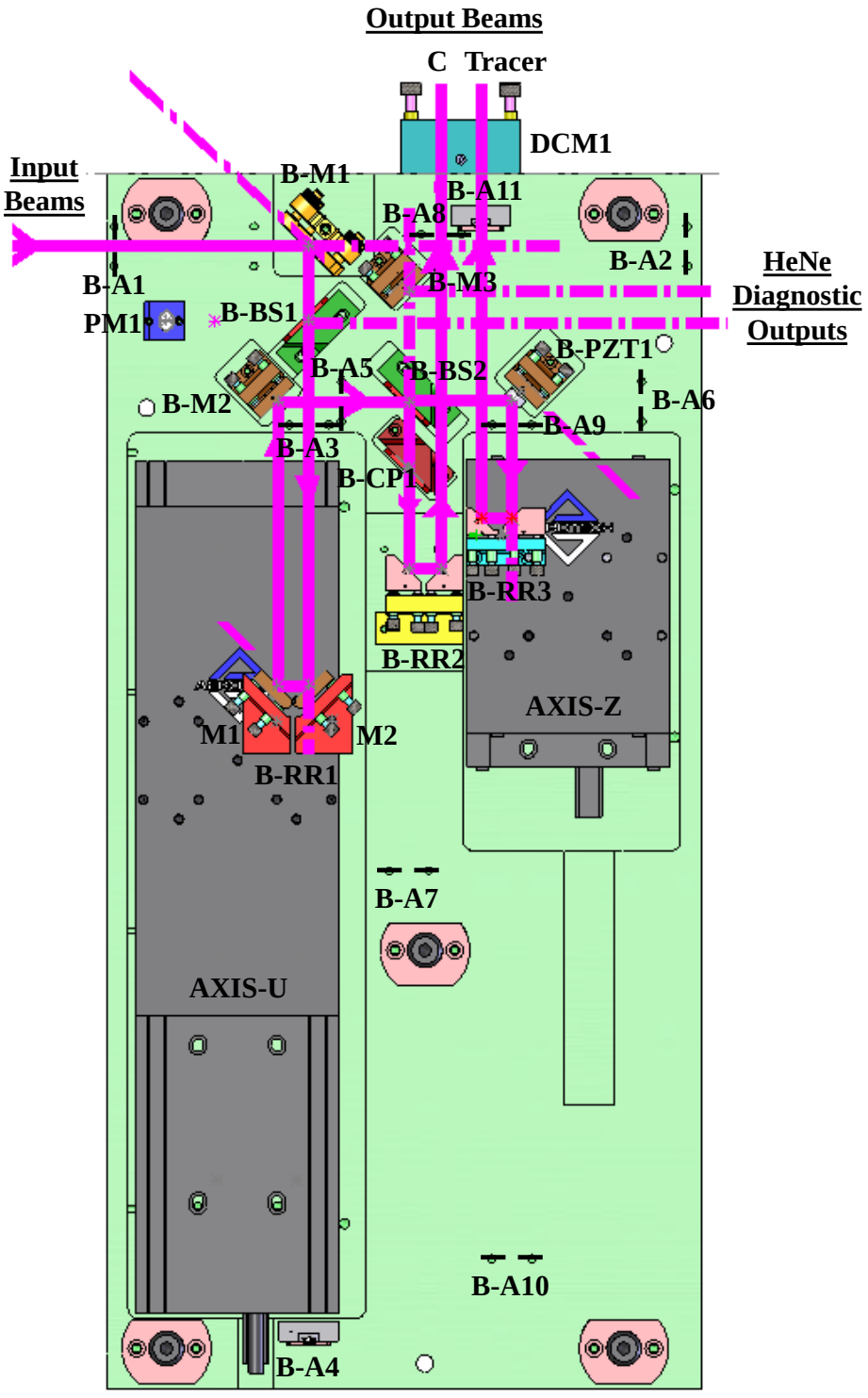

Figure C.2: Layout of the bottom deck assembly. Definitions: M – mirror; DM – dichroic mirror; A – aperture; BS – beam splitter; CP – compensation plate; PM – periscope mirror; RR – retro-reflector mount; PZT – mirror mounted on a piezo-electric actuator; AXIS – translation stage.

C.3 Top Deck Assembly Alignment (refer to Fig. C.3)

3.1 Secure the top deck on the optical table, and use a mirror on a flip mount to direct the collinearly propagating Ti:sapphire and HeNe beams to the input of the top deck assembly. Block the Ti:sapphire beam.

3.2 Install the translation stages and verify proper performance as outlined in step 2.2.

3.3 Ensure that no optical components have been installed on the top deck. Align the input HeNe through apertures T-A1 and T-A2.

3.4 Attach T-M1 to the top deck and align the reflection through apertures T-A3 and T-A4 as outlined in step 2.3.

3.5 Attach T-RR1 and T-PZT1 to the top deck.

3.6 Align the input and output mirrors of T-RR1 so that the beam is centered on the mirror on T-PZT1.

3.7 Align the reflection from T-PZT1 through the apertures T-A5 and T-A6, using the procedure outlined in step 2.3.

3.8 Attach T-PZT2, T-BS1 and T-CP1 to the top deck.

3.9 Loosen the fasteners of T-BS1 and adjust the position so that the reflection off the beam splitter propagates through apertures T-A7 and T-A8 while ensuring that the beam passes through the beam splitter towards T-PZT2 cleanly.

3.10 Attach T-CP2 to the top deck.

3.11 Measure the input beam parallelism relative to the AXIS-Y stage using the procedure outlined in step 2.6. Flatten the beam using T-PZT1 and T-BS1.

3.12 Attach T-RR2 to the AXIS-Y stage and align the output through aperture T-A9.

3.13 Place a razor blade and photodiode after T-A9 and use the procedure outlined in step 2.16 for flattening the beam output from the AXIS-Y stage.

3.14 Attach T-PZT2 to the top deck and align the reflection through the apertures T-A10 and T-A11 using the procedure in step 2.3.

3.15 Measure the input beam parallelism relative to the AXIS-X stage using the procedure outlined in step 2.6. Flatten the beam using T-PZT2.

3.16 Attach T-RR3 to the AXIS-X stage and align the beam output through the aperture T-A12.

3.17 Place a razor blade and photodiode after aperture T-A12 and use the method outlined in step 2.16 for flattening the beam output from the AXIS-X stage.

3.18 Perform the cross-correlation measurement between beams A and B using the BBO crystal as outlined in step 2.19.

3.19 Attach the $2''$ DCM1 to the front of the top deck. Do not adjust the alignment of DCM1.

(a) Check that the reflected beams do not walk when moving the translation stages, that the beams are collinearly propagating, and that excellent interference is obtained for all locations along the beam paths.

(b) If the conditions in (a) are not achieved, the alignment of beams A and B needs to be checked.

3.20 Attach PM2 to the top deck.

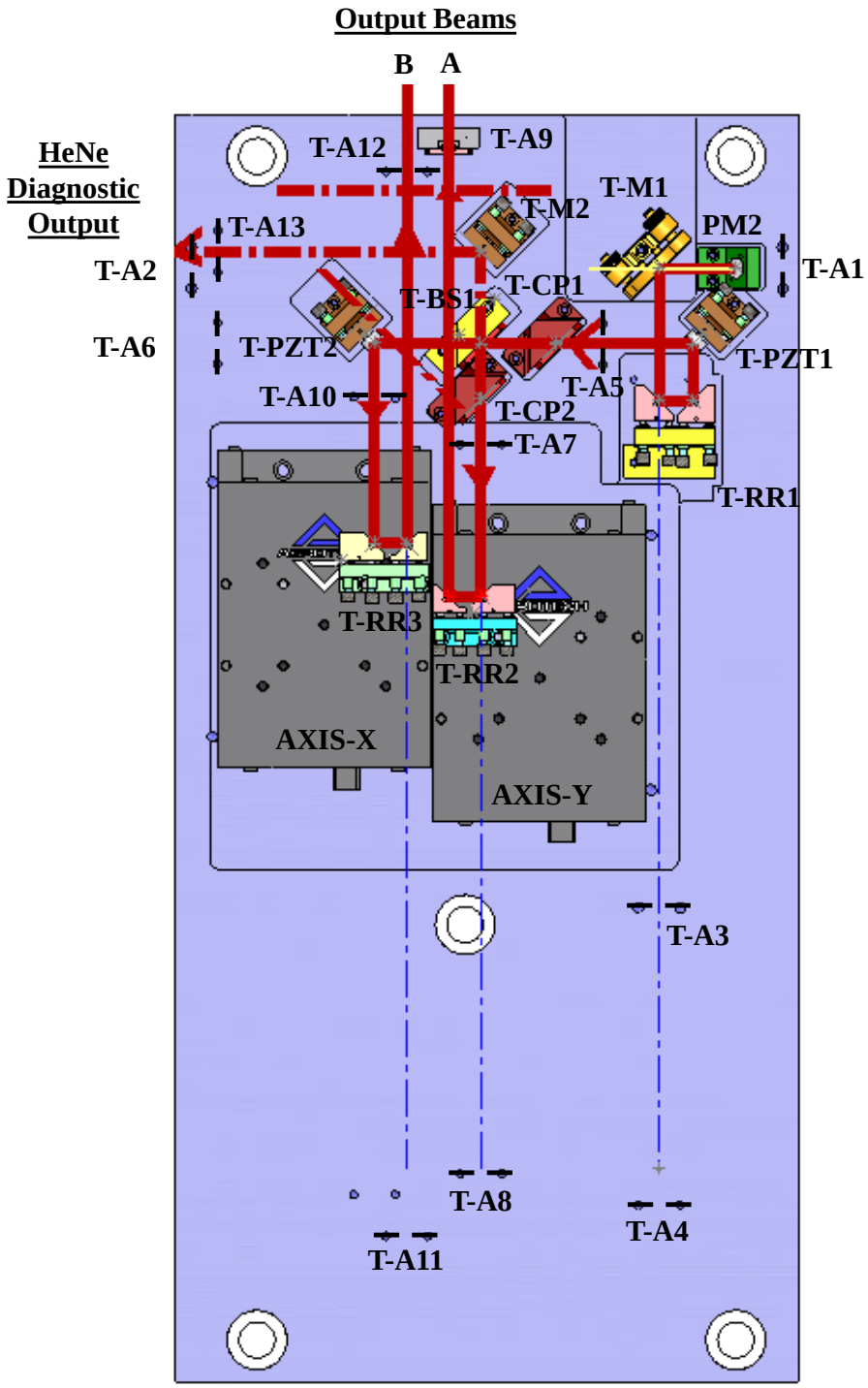

Figure C.3: Layout of the top deck assembly. Definitions: M – mirror; A – aperture; BS – beam splitter; CP – compensation plate; PM – periscope mirror; RR – retro-reflector mount; PZT – mirror mounted on a piezo-electric actuator; AXIS – translation stage.

C.4 Closing the JILA MONSTR

4.1 Ensure that the Ti:sapphire and HeNe beams are correctly aligned to the input of the bottom deck. Make sure that all apertures have been removed from both deck assemblies. Double check that PM2 has been installed. Block the laser beams.

4.2 Place lab-jacks near the bottom deck.

4.3 Fasten the handles to the top deck. Flip over the top deck and rest the handles on the lab-jacks so that the top deck is now resting above the bottom deck.

4.4 Grease the posts on the bottom deck with molybdenum ("molly") grease. Slowly lower the lab-jacks so that the top deck is lowered onto the bottom deck. If the top deck becomes stuck, slowly extend the lab-jacks to loosen the deck, and then continue lowering the deck.

(a) Note that at the time this Thesis was written, we had plans to modify the top deck so that the lab-jacks were incorporated into the design instead of being an auxiliary tool.

4.5 Once the top deck is resting on top of the bottom decks, securely fasten it with the bolts.

4.6 Attach DCM1 to the front of the MONSTR.

C.5 Alignment of the Joined Top and Bottom Assemblies

5.1 At this point the Ti:sapphire and HeNe beams should be aligned properly into the bottom deck assembly. Due to the weight of the top deck, the MONSTR might shift after joining the two decks.

(a) If this is the case, check that the Tracer and beam C propagate along the lower two corners of a $1''$ box.

(b) Adjust O-M1 and O-M2 for the Ti:sapphire laser (kinematic mount and O-M3 for the HeNe laser) to correct for any deviations.

(c) Adjust the apertures A1 and A2 so that the Ti:sapphire and HeNe beams are propagating through them.

5.2 Align the top deck to the bottom deck.

(a) Adjust T-M1 and T-PZT1 so that beams A and B are propagating along the top corners of the $1''$ box. Proper alignment should result in all four beams propagating along the four corners of the box at all locations along the beam propagation paths.

(b) Check that when translating the stages, none of the beams walk.

(c) Check that excellent HeNe interference patterns are obtained at the HeNe diagnostic outputs.

(d) A more precise way to check for proper alignment is to set up the all-optical phase-retrieval and field-correlation diagnostics.

(i) Insert the lens used for focusing the beams onto the sample.

(ii) Insert the collimating lens, and make sure that the collimated beams also propagate along the four corners of a box (note that we use a 15 cm focal lens focusing lens and 10 cm focal length collimating lens, thus the output box size is smaller than the input).

(iii) Insert the single-side anti-reflection coated window that is used for the all-optical phase-retrieval procedure, and image the focus onto the all-optical CCD camera.

(iv) Scan the translation stages to find time-zero between beam pairs A–B, A–C and C–Tracer. The interference pattern from each pair should have a similar spatial period. At this point, all four beams should produce a grid-pattern (see Ref. [228]). If this pattern is visible and the beams directly after the MONSTR are on the four corners of a $1''$ box, then the MONSTR should be aligned properly.

Appendix D

Second-Generation JILA MONSTR

The first generation JILA MONSTR has facilitated 2DCS experiments of a wide-range of material systems, including epitaxially-grown GaAs, InGaAs and CdTe QWs, GaAs and InAs QDs, CdSeTe/ZnS core-shell CQDs, and potassium and rubidium vapors. The experimental setup has several constraints, however, that limit the types of materials that can be studied. For example, the maximum τ and T delays are ≈ 333 ps and ≈ 1.3 ns, respectively, which limits the maximum population decay and dephasing times that can be probed. Moreover, the Ti:sapphire laser system limits the materials that can be studied to those with resonances within the range of $\approx 700 - 1000$ nm. The laser FWHM spectral bandwidth is also ≤ 15 nm, depending on the operating wavelength. Thus the system can probe for coupling between resonances that are separated by 15 nm or less. The laser gain profile and repetition rate (76 MHz) also limits the maximum pulse energy at the sample to ≈ 200 pJ. A more subtle constraint of the high repetition rate shot-to-shot accumulation effects. For instance, if the population decay rate of an optical transition is less than the laser repetition frequency, the system population would not decay to the ground state between subsequent sets of pulses and artifacts might appear in the 2D spectra. For these reasons, we have developed a second generation 2DCS experimental setup that is designed to overcome many of these limitations. The new experimental setup will enable 2DCS of a wide-range of material systems that could not be previously studied, such as CQDs relevant for photovoltaic applications, GaN-based nanostructures, light-harvesting complexes, atomic molecules and polymers.

The second generation JILA MONSTR is based on the design of the first generation model

with a few modifications, which are depicted in the computer-aided design images of the bottom and top deck assemblies in Fig. D.1. Specifically, the AXIS X and Z translation stages have been replaced with *Aerotech Inc* model # ANT130-060-L-25DU-PLUS, which provides 6 cm of travel, and AXIS Y and U with model # ANT130-160-L-25DU-PLUS, which provides 16 cm of travel. The new models have superior stability and stepping precision specifications compared to the previous versions. Morever, the beams double-pass the AXIS Y and U stages, which enables a maximum delay of $\approx$ 2 ns for τ and T. Compared to the original translation stages, the new stages have superior specifications for the accuracy, repeatability and stability performance. We have found, however, that the accuracy in the stage movement is marginally sufficient for the 2DCS experiments. After fine-tuning the gain parameters of the servo feedback loops built in to the stages, in-position stability comparable to the original stages is achieved. On the other hand, we have yet to find any parameters that lead to sufficiently accurate and repeatable motion when the stages are commanded to travel a relative distance greater than $\lambda_{HeNe} = 632$ nm (corresponding to an undersampling ratio of 4). Thus, in order to perform the 2DCS experiments using an undersampling ratio greater than 4, the stages must be incrementally stepped a maximum distance of 632 nm and the movement corrected between increments. An alternative stepping algorithm we are currently developing involves counting the number of HeNe fringe zero-crossings at the error signal diagnostic detector in real time and compensating the stage movement accordingly.

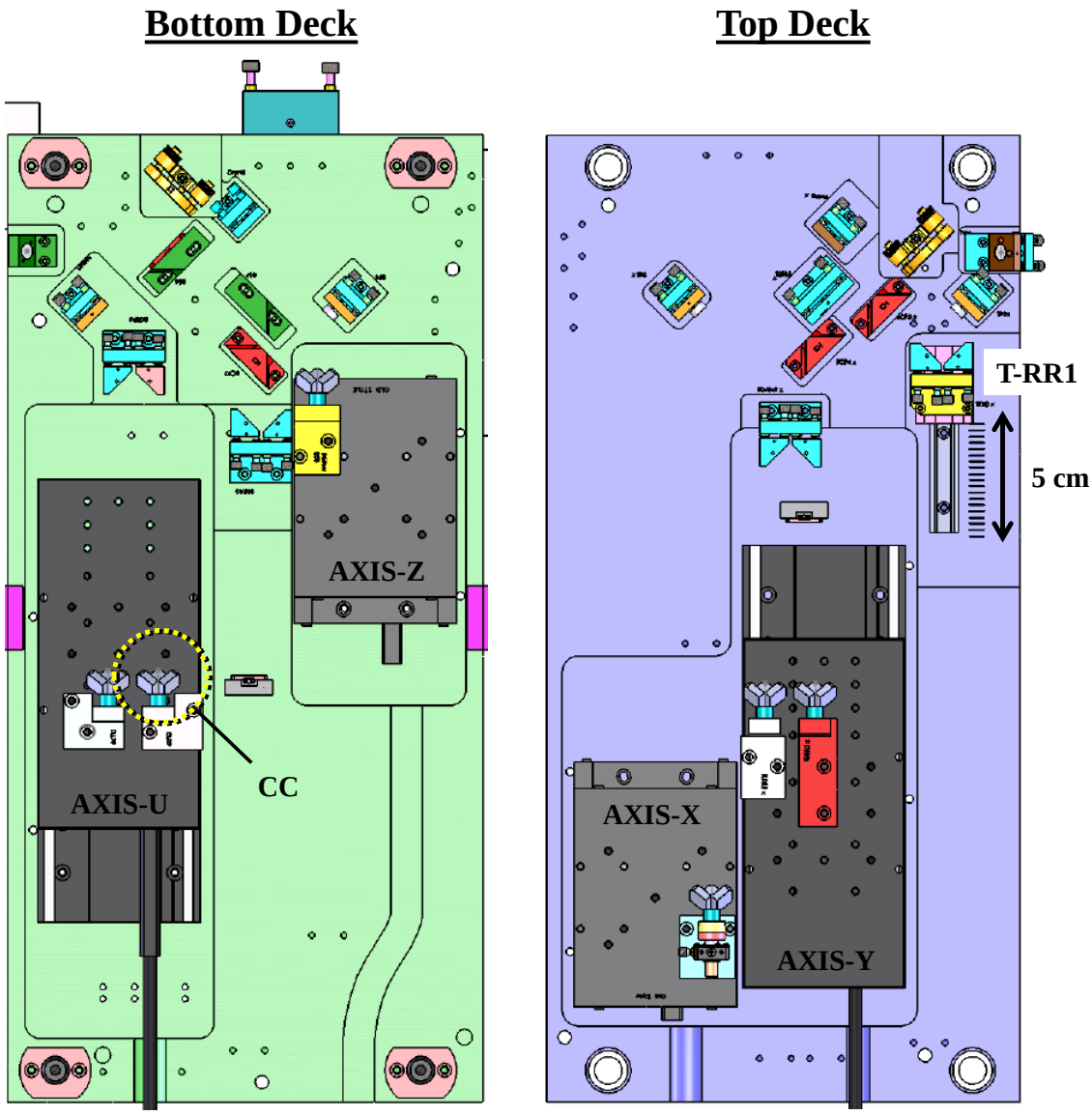

Figure D.1: Layout of the bottom and top deck assemblies. Definitions: RR – retro-reflector; CC – corner cube; AXIS – translation stage.

The retro-reflector T-RR1 on the top deck has been mounted on a 5 cm rail and carriage system, shown in Fig. D.2(a), to enable a maximum $-\tau$ delay (i.e., for the S_{III} time-ordering) of up to $\approx$ 330 ps. Zero delay between the pulses is achieved when the AXIS X and Y stages are $\approx$ 0.5 cm from their maximum rear-most position and the AXIS Z and U stages $\approx$ 0.5 cm from their forward-most position. Thus to achieve $\approx$ 330 ps delay for $-\tau$, the T-RR1 mount is moved

5 cm towards the rear of the MONSTR while the AXIS X and Y stages are moved forward 5 cm and 2.5 cm, respectively. To account for any irregularities in the flatness of the stage motion, the two-mirror retro-reflectors mounted on the stages in the original design have been replaced with 1" clear aperture corner cubes from *PLX Inc* made from protected silver mirrors (model # HM-10-1E). The corner cube on the AXIS-X stage is mounted on a *Thorlabs* two-axis translation mount with 2 mm of total travel along each axis (model # SCP-05), shown in Fig. D.2(b), to facilitate alignment after joining the top and bottom deck assemblies. The remaining optical components are similar to those in the original design.

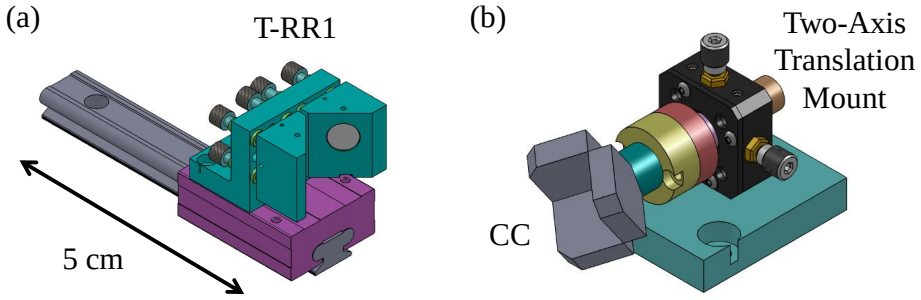

Figure D.2: (a) Top deck retro-reflector (T-RR1) mounted on a rail and carriage with a maximum travel distance of 5 cm. (b) Corner cube (CC) mounted on a two-axis translator.

The Ti:sapphire laser system used for the 2DCS experiments in the original design has been replaced with a regenerative amplifier (*Coherent* model # 9000PV) that is seeded with pulses from a Ti:sapphire laser (*Coherent* Micra). The amplifier operates at a 250 kHz repetition rate and outputs an average power of ≈ 1.5 W, thus providing ≈ 6 μJ energy per pulse. The output of the amplifier can be used as the input for a visible optical parametric amplifier (OPA, *Coherent* model # 9400) that can output pulses with 80 nJ energy in a tunable wavelength range from 480-700 nm (the signal output) and 933-2300 nm (the idler output). Additional outputs from the OPA include a super-continuum white light beam and a frequency-doubled beam stemming from second harmonic generation of the regenerative amplifier seed pulse. The output of the regenerative amplifier can instead be used to pump an infrared OPA (*Coherent* model # 9800) that provides pulses with

160 nJ energy in a tunable wavelength range of 1200-1600 nm (the signal output) and 1600-2400 nm (the idler output). Either the output of the Micra mode-locked oscillator, the regenerative amplifier output, or any of the beams from the OPAs can be used as the input for the second generation JILA MONSTR. Since the optics in the MONSTR are designed for a wavelength range of 700-1000 nm, operation beyond this range will result in the output beams from the MONSTR having unequal average power. In most instances this disparity can be compensated by adjusting the half-wave plates and linear polarizers in the polarization optics assembly (see Fig. 4.1). The attenuated pulse energies will still likely be greater than the typical pulse energies required for $\chi^{(3)}$ experiments, which usually range from 10-200 pJ per pulse for optical densities below 1 (αL in base e, where α is the absorption coefficient and L the sample thickness). If sufficient pulse energy cannot be obtained, the optics can be replaced with those with the appropriate coatings, which requires re-alignment of the MONSTR as described in Appendix C.

Bibliography

[1] H. M. Manasevit, "Single-crystal gallium arsenide on insulating substrates," Applied Physics Letters **12**, 156 (1968).

[2] A. Y. Cho and J. R. Arthur, "Molecular beam epitaxy," Progress in Solid-State Chemistry **10**, 157 (1975).

[3] L. Esaki and R. Tsu, "Superlattice and negative differential conductivity in semiconductors," IMB Journal of Research and Development **14**, 61 (1970).

[4] R. Tsu and L. Esaki, "Tunneling in a finite superlattice," Applied Physics Letters **22**, 562 (1973).

[5] R. Dingle, A. C. Gossard, and W. Wiegmann, "Direct observation of superlattice formation in a semiconductor heterostructure," Physical Review Letters **34**, 1327 (1975).

[6] R. Chin, N. Holonyak, B. A. Vojak, K. Hess, and R. D. a. Dupuis, "Temperature dependence of threshold current for quantum well AlGaAs/GaAs heterostructure laser diodes," Applied Physics Letters **36**, 19 (1980).

[7] Y. Arakawa and H. Sakaki, "Multidimensional quantum well laser and temperature dependence of its threshold current," Applied Physics Letters **40**, 939 (1982).

[8] W. J. Skocpol, L. D. Jackel, E. L. Hu, R. E. Howard, and L. A. Fetter, "One-dimensional localization and interaction effects in a narrow (0.1-μm) silicon inversion layers," Physical Review Letters **49**, 951 (1982).

[9] A. I. Ekimov and A. A. Onushchenko, "Quantum size effect in three-dimensional microscopic semiconductor crystals," Letters to the Journal of Experimental and Theoretical Physics **34**, 345 (1981).

[10] L. E. Brus, "A simple model for the ionization potential, electron affinity, and aqueous redox potentials of small semiconductor crystallites," Journal of Chemical Physics **79**, 5566 (1983).

[11] L. E. Brus, "Electron-electron and electron-hole interactions in small semiconductor crystallites: the size dependence of the lowest excited electronic state," Journal of Chemical Physics **80**, 4403 (1984).

[12] M. A. Reed, R. T. Bate, K. Bradshaw, W. M. Duncan, W. R. Frensley, J. W. Lee, and H. D. Shih, "Spatial quantization in GaAs-AlGaAs multiple quantum dots," Journal of Vacuum Science and Technology B **4**, 358 (1986).

[13] M. A. Reed, J. N. Randall, R. J. Aggarwal, R. J. Matyi, T. M. Moore, and A. E. Wetsel, "Observation of discrete electronic states in a zero-dimensional semiconductor nanostructure," Physical Review Letters **60**, 535 (1988).

[14] K. Kash, A. Scherer, J. M. Worlock, H. G. Craighead, and M. C. Tamargo, "Optical spectroscopy of ultrasmall structures etched from quantum wells," Applied Physics Letters **49**, 1043 (1986).

[15] H. Temkin, G. J. Dolan, M. B. Panish, and S. N. G. Chu, "Low-temperature photoluminescence from InGaAs/InP quantum wires and boxes," Applied Physics Letters **50**, 413 (1987).

[16] W. Hansen, T. P. Smith, K. Y. Lee, J. A. Brum, C. M. Knoedler, J. M. Hong, and D. P. Kern, "Zeeman bifurcation of quantum-dot spectra," Physical Review Letters **62**, 2168 (1989).

[17] M. Tewordt, H. Asahi, V. J. Law, R. T. Syme, M. J. Kelly, D. A. Ritchie, A. Churchill, J. E. F. Frost, R. H. Hughest, and G. A. C. Jones, "Resonant tunneling in coupled quantum dots," Applied Physics Letters **60**, 595 (1992).

[18] B. Meurer, D. Heitmann, and K. Ploog, "Single-electron charging of quantum-dot atoms," Physical Review Letters **68**, 1371 (1992).

[19] M. Field, C. G. Smith, M. Pepper, D. A. Ritchie, J. E. F. Frost, G. A. C. Jones, and D. G. Hasko, "Measurements of Coulomb blockade with a noninvasive voltage probe," Physical Review Letters **70**, 1311 (1993).

[20] R. C. Ashoori, H. L. Stormer, J. S. Weiner, L. N. Pfeiffer, K. W. Baldwin, and K. W. West, "N-electron ground state energies of a quantum dot in magnetic field," Physical Review Letters **71**, 613 (1993).

[21] S. Schmidtt-Rink, D. A. B. Miller, and D. S. Chemla, "Theory of the linear and nonlinear optical properties of semiconductor microcrystallites," Physical Review B **35**, 8113 (1987).

[22] L.-W. Wang and A. Zunger, "Electronic structure pseudopotential calculations of large ($\tilde{1}$000 atoms) Si quantum dots," Journal of Physical Chemistry **98**, 2158 (1994).

[23] G. W. Bryant, "Excitons in quantum boxes: correlation effects and quantum confinement," Physical Review B **37**, 8763 (1988).

[24] A. Kumar, S. T. Laux, and F. Stern, "Electron states in a GaAs quantum dot in a magnetic field," Physical Review B **42**, 5166 (1990).

[25] K. Brunner, U. Bockelmann, G. Abstreiter, M. Walther, G. Böhm, G. Tränkle, and G. Weimann, "Photoluminescence from a single GaAs/AlGaAs quantum dot," Physical Review Letters **69**, 3216 (1992).

[26] K. Brunner, G. Abstreiter, G. Böhm, G. Tränkle, and G. Weimann, "Sharp-line photoluminescence and two-photon absorption of zero-dimensional biexcitons in a GaAs/AlGaAs structure," Physical Review Letters **73**, 1138 (1994).

[27] D. Gammon, E. S. Snow, and D. S. Katzer, "Excited state spectroscopy of excitons in single quantum dots," Applied Physics Letters **67**, 2391 (1995).

[28] D. Gammon, E. S. Snow, B. V. Shanabrook, D. S. Katzer, and D. Park, "Homogeneous linewidths in the optical spectrum of a single Gallium Arsenide quantum dot," Science **273**, 87 (1996).

[29] D. Gammon, E. S. Snow, B. V. Shanabrook, D. S. Katzer, and D. Park, "Fine structure splitting in the optical spectra of single GaAs quantum dots," Physical Review Letters **76**, 3005 (1996).

[30] E. R. Glaser, B. R. Bennett, B. V. Shanabrook, and R. Magno, "Photoluminescence studies of self-assembled InSb, GaSb, and AlSb quantum dot heterostructures," Applied Physics Letters **68**, 3614 (1996).

[31] V. Esch, B. Fluegel, G. Khitrova, H. M. Gibbs, X. Jiajin, K. Kang, S. W. Koch, L. C. Liu, S. H. Risbud, and N. Peyghambarian, "State filling, Coulomb, and trapping effects in the optical nonlinearity of CdTe quantum dots in glass," Physical Review B **42**, 7450 (1990).

[32] T. Rajh, O. I. Micic, and A. J. Nozik, "Synthesis and characterization of surface-modified colloidal CdTe quantum dots," Journal of Physical Chemistry **97**, 11 999 (1993).

[33] C. Gourgon, B. Eriksson, L. S. Dang, H. Mariette, and C. Vieu, "Photoluminescence of CdTe/ZnTe semiconductor wires and dots," Journal of Crystal Growth **138**, 590 (1994).

[34] N. Magnea, "ZnTe fractional monolayers and dots in a CdTe matrix," Journal of Crystal Growth **138**, 550 (1994).

[35] V. Calvo, P. Lefebvre, J. Allegre, A. Bellabchara, H. Mathieu, Q. X. Zhao, and N. Magnea, "Evidence of the ordered growth of monomolecular ZnTe islands in CdTe/(Cd,Zn)Te quantum wells on a nominal (001) surface," Physical Review B **53**, 16 164 (1996).

[36] J. Y. Marzin, J. M. Gerard, A. Izrael, D. Barrier, and G. Bastard, "Photoluminescence of single InAs quantum dots obtained by self-organized growth on GaAs," Physical Review Letters **73**, 716 (1994).

[37] Y. Nabetani, T. Ishikawa, S. Noda, and A. Sasaki, "Initial growth stage and optical properties of a three-dimensional InAs structure on GaAs," Journal of Applied Physics **76**, 347 (1994).

[38] W. Seifert, N. Carlsson, M. Miller, M.-E. Pistol, L. Samuelson, and L. R. Wallenberg, "In-situ growth of quantum dot structures by the stranski-krastanow growth mode," Progress in Crystal Growth and Characterization of Materials **33**, 423 (1996).

[39] I. N. Stranski and L. Krastanow, "Zur theorie der orientierten ausscheidung von ionenkristallen aufeinander," Abhandlungen der Mathematisch-Naturwissenschaftlichen Klasse IIb. Akademie der Wissenschaften Wien **146**, 797 (1938).

[40] L. Goldstein, F. Glas, J. Y. Marzin, M. N. Charasse, and G. Le Roux, "Growth by molecular beam epitaxy and characterization of InAs/GaAs strained-layer superlattices," Applied Physics Letters **47**, 1099 (1985).

[41] K. H. Schmidt, G. Medeiros-Ribeiro, M. Oestreich, P. M. Petroff, and G. H. Döhler, "Carrier relaxation and electronic structure in InAs self-assembled quantum dots," Physical Review B **54**, 11 346 (1996).

[42] S. Tarucha, D. G. Austing, T. Honda, R. J. van der Hage, and L. P. Kouwenhoven, "Shell filling and spin effects in a few electron quantum dot," Physical Review Letters **77**, 3613 (1996).

[43] D. I. Lubyshev, P. P. González-Borrero, E. Marega Jr., E. Petitprez, N. La Scala Jr., and P. Basmaji, "Exciton localization and temperature stability in self-organized InAs quantum dots," Applied Physics Letters **68**, 205 (1996).

[44] M. Bayer, G. Ortner, O. Stern, A. Kuther, A. A. Gorbunov, A. Forchel, P. Hawrylak, S. Fafard, K. Hinzer, T. L. Reinecke, S. N. Walck, J. P. Reithmaier, F. Klopf, and F. Schäfer, "Fine structure of neutral and charged excitons in self-assembled In(Ga)As/(Al)GaAs quantum dots," Physical Review B **65**, 195 315 (2002).

[45] W. Langbein, P. Borri, U. Woggon, V. Stavarache, D. Reuter, and A. D. Wieck, "Control of fine-structure splitting and biexciton binding in InGaAs quantum dots by annealing," Physical Review B **69**, 161 301(R) (2004).

[46] P. Borri, W. Langbein, S. Schneider, U. Woggon, R. L. Sellin, D. Ouyang, and D. Bimberg, "Ultralong dephasing time in InGaAs quantum dots," Physical Review Letters **87**, 157 401 (2001).

[47] H. Shoji, K. Mukai, N. Ohtsuka, M. Sugawara, T. Uchida, and H. Ishikawa, "Lasing at three-dimensionally quantum-confined sublevel of self-organized InGaAs quantum dots by current injection," IEEE Photonics Technology Letters **7**, 1385 (1995).

[48] D. Bimberg, N. N. Ledentsov, M. Grundmann, N. Kirstaedter, O. G. Schmidt, M. H. Mao, V. M. Ustinov, A. Y. Egorov, A. E. Zhukov, P. S. Kopév, Z. I. Alferov, S. S. Ruvimov, U. Gosele, and J. Heydenreich, "InAs-GaAs quantum pyramid lasers: in situ growth, radiative lifetimes and polarization properties," Japanese Journal of Applied Physics **35**, 1311 (1996).

[49] R. Mirin, A. Gossard, and J. Bowers, "Room temperature lasing from InGaAs quantum dots," Electronics Letters **32**, 1732 (1996).

[50] V. I. Klimov, A. A. Mikhailovsky, S. Xu, A. Malko, J. A. Hollingsworth, C. A. Leatherdale, H.-J. Eisler, and M. G. Bawendi, "Optical gain and stimulated emission in nanocrystal quantum dots," Science **290**, 314 (2000).

[51] L. Bakueva, S. Musikhin, M. A. Hines, T.-W. F. Chang, M. Tzolov, G. D. Scholes, and E. H. Sargent, "Size-tunable infrared (1000-1600 nm) electroluminescence from PbS quantum-dot nanocrystals in a semiconductor polymer," Applied Physics Letters **82**, 2895 (2003).

[52] D. Pan, E. Towe, and S. Kennerly, "Normal-incidence intersubband (In,Ga)As/GaAs quantum dot infrared photodetectors," Applied Physics Letters **73**, 1937 (1998).

[53] G. Konstantatos, I. Howard, A. Fischer, S. Hoogland, J. Clifford, E. Klem, L. Levina, and E. H. Sargent, "Ultrasensitive solution-cast quantum dot photodetectors," Nature **442**, 180 (2006).

[54] P. Michler, A. Kiraz, C. Becher, W. V. Schoenfeld, P. M. Petroff, L. Zhang, E. Hu, and A. Imamoglu, "A quantum dot single-photon turnstile device," Science **290**, 2282 (2000).

[55] O. Benson, C. Santori, M. Pelton, and Y. Yamamoto, "Regulated and entangled photons from a single quantum dot," Physical Review Letters **84**, 2513 (2000).

[56] C. Santori, D. Fattal, J. Vuckovic, G. S. Solomon, and Y. Yamamoto, "Indistinguishable photons from a single-photon device," Nature **419**, 594 (2002).

[57] R. Hanbury Brown and R. Q. Twiss, "A test of a new type of stellar interfeometer on Sirius," Nature **178**, 1046 (1956).

[58] G. S. Solomon, J. A. Trezza, A. F. Marshall, and J. S. Harris Jr., "Vertically aligned and electronically coupled growth induced InAs islands in GaAs," Physical Review Letters **76**, 952 (1996).

[59] N. H. Bonadeo, J. Erland, D. Gammon, D. Park, D. S. Katzer, and D. G. Steel, "Coherent optical control of the quantum state of a single quantum dot," Science **282**, 1473 (1998).

[60] D. P. DiVincenzo, "Quantum Computation," Science **270**, 255 (1995).

[61] M. Atatüre, J. Dreiser, A. Badolato, A. Högele, K. Karrai, and A. Imamoglu, "Quantum-dot spin-state preparation with near-unity fidelity," Science **312**, 551 (2006).

[62] H. Kamada, H. Gotoh, J. Temmyo, T. Takagahara, and H. Ando, "Exciton Rabi oscillation in a single quantum dot," Physical Review Letters **87**, 246 401 (2001).

[63] X. Li, Y. Wu, T. H. Stievater, D. G. Steel, D. Gammon, D. S. Katzer, D. Park, C. Piermarocchi, and L. Sham, "An all-optical quantum gate in a semiconductor quantum dot," Science **301**, 809 (2003).

[64] M. Kroutvar, Y. Ducommun, D. Heiss, M. Bichler, D. Schuh, G. Abstreiter, and J. J. Finley, "Optically programmable electron spin memory using semiconductor quantum dots," Nature **432**, 81 (2004).

[65] D. Press, T. D. Ladd, B. Zhang, and Y. Yamamoto, "Complete quantum control of a single quantum dot spin using ultrafast optical pulses," Nature **456**, 218 (2008).

[66] A. Zrenner, E. Beham, S. Stufler, F. Findeis, M. Bichler, and G. Abstreiter, "Coherent properties of a two-level system based on a quantum-dot photodiode," Nature **418**, 612 (2002).

[67] J. M. Elzerman, R. Hanson, L. H. Willems van Beveren, B. Witkamp, L. M. K. Vandersypen, and L. P. Kouwenhoven, "Single-shot read-out of an individual electron spin in a quantum dot," Nature **430**, 431 (2004).

[68] R. Hanson, L. H. Willems van Beveren, I. T. Vink, J. M. Elzerman, W. J. M. Naber, F. H. L. Koppens, L. P. Kouwenhoven, and L. M. K. Vandersypen, "Single-shot readout of electron spin states in a quantum dot using spin-dependent tunnel rates," Physical Review Letters **94**, 196 802 (2005).

[69] M. Bayer, P. Hawrylak, K. Hinzer, S. Fafard, M. Korkusinski, Z. R. Wasilewski, O. Stern, and A. Forchel, "Coupling and entangling of quantum states in quantum dot molecules," Science **291**, 451 (2001).

[70] H. J. Krenner, M. Sabathil, E. C. Clark, A. Kress, D. Schuh, M. Bichler, G. Abstreiter, and J. J. Finley, "Direct observation of controlled coupling in an individual quantum dot molecule," Physical Review Letters **94**, 057 402 (2005).

[71] J. R. Petta, A. C. Johnson, J. M. Taylor, E. A. Laird, A. Yacoby, M. D. Lukin, C. M. Marcus, M. P. Hanson, and A. C. Gossard, "Coherent manipulation of coupled electron spins in semiconductor quantum dots," Science **309**, 2180 (2005).

[72] T. Unold, K. Mueller, C. Lienau, T. Elsaesser, and A. D. Wieck, "Optical control of excitons in a pair of quantum dots coupled by the dipole-dipole interaction," Physical Review Letters **94**, 137 404 (2005).

[73] M.-K. So, C. Xu, A. M. Loening, S. S. Gambhir, and J. Rao, "Self-illuminating quantum dot conjugates for in vivo imaging," Nature Biotechnology **24**, 339 (2006).

[74] C.-Y. Zhang, H.-C. Yeh, M. T. Kuroki, and T.-H. Wang, "Single-quantum-dot-based DNA nanosensor," Nature Materials **4**, 826 (2005).

[75] A. J. Nozik, "Spectroscopy and hot electron relaxation dynamics in semiconductor quantum wells and quantum dots," Annual Review of Physical Chemistry **52**, 193 (2001).

[76] A. J. Nozik, "Quantum dot solar cells," Physica E **14**, 115 (2002).

[77] G. Nair, L.-Y. Chang, S. M. Geyer, and M. G. Bawendi, "Perspective on the prospects of a carrier multiplication nanocrystal solar cell," Nano Letters **11**, 2145 (2011).

[78] R. D. Schaller and V. I. Klimov, "High efficiency carrier multiplication in PbSe nanocrystals: implications for solar energy conversion," Physical Review Letters **92**, 186 801 (2004).

[79] M. C. Beard, "Multiple exciton generation in semiconductor quantum dots," Journal of Physical Chemistry Letters **2**, 1282 (2011).

[80] M. S. Skolnick and D. J. Mowbray, "Self-assembled semiconductor quantum dots: fundamental physics and device applications," Annual Review of Materials Research **34**, 181 (2004).

[81] E. Dekel, D. Gershoni, E. Ehrenfreund, D. Spektor, J. M. Garcia, and P. M. Petroff, "Multiexciton spectroscopy of a single self-assembled quantum dot," Physical Review Letters **80**, 4991 (1998).

[82] M. Braskén, M. Lindberg, D. Sundholm, and J. Olsen, "Full configuration interaction calculations of electron-hole correlation effects in strain-induced quantum dots," Physical Review B **61**, 7652 (2000).

[83] M. Wimmer, S. V. Nair, and J. Shumway, "Biexciton recombination rates in self-assembled quantum dots," Physical Review B **73**, 165 305 (2006).

[84] A. Schliwa, M. Winkelnkemper, and D. Bimberg, "Few-particle energies versus geometry and composition of InGaAs/GaAs self-organized quantum dots," Physical Review B **79**, 075 443 (2009).

[85] M. Abbarchi, T. Kuroda, T. Mano, K. Sakoda, C. A. Mastrandrea, A. Vinattieri, M. Gurioli, and T. Tsuchiya, "Energy renormalization of exciton complexes in GaAs quantum dots," Physical Review B **82**, 201 301 (2010).

[86] A. S. Lenihan, M. V. Gurudev Dutt, D. G. Steel, S. Ghosh, and P. Bhattacharya, "Biexcitonic resonance in the nonlinear optical response of an InAs quantum dot ensemble," Physical Review B **69**, 045 306 (2004).

[87] P. Borri and W. Langbein, "Four-wave mixing dynamics of excitons in InGaAs self-assembled quantum dots," Journal of Physics: Condensed Matter **19**, 295 201 (2007).

[88] M. Koch, J. Feldmann, G. von Plessen, E. O. Göbel, P. Thomas, and K. Köhler, "Quantum beats versus polarization interference: an experimental distinction," Physical Review Letters **69**, 3631 (1992).

[89] S. T. Cundiff, "Effects of correlation between inhomogeneously broadened transitions on quantum beats in transient four-wave mixing," Physical Review A **49**, 3114 (1994).

[90] M. Wegener, D. S. Chemla, S. Schmitt-Rink, and W. Schäfer, "Line shape of time-resolved four-wave mixing," Physical Review A **42**, 5675 (1990).

[91] H. Wang, K. Ferrio, D. G. Steel, Y. Z. Hu, R. Binder, and S. W. Koch, "Transient nonlinear optical response from excitation induced dephasing in GaAs," Physical Review Letters **71**, 1261 (1993).

[92] J. M. Shacklette and S. T. Cundiff, "Nonperturbative transient four-wave-mixing line shapes due to excitation-induced shift and excitation-induced dephasing," Journal of the Optical Society of America B **20**, 764 (2003).

[93] K. Bott, O. Heller, D. Bennhardt, S. T. Cundiff, P. Thomas, E. J. Mayer, G. O. Smith, R. Eccleston, J. Kuhl, and K. Ploog, "Influence of exciton-exciton interactions on the coherent optical response in GaAs quantum wells," Physical Review B **48**, 17 418 (1993).

[94] S. T. Cundiff, A. D. Bristow, M. E. Siemens, H. Li, G. Moody, D. Karaiskaj, X. Dai, and T. Zhang, "Optical 2-D Fourier transform spectroscopy of excitons in semiconductor nanostructures," IEEE Journal of Selected Topics in Quantum Electronics **18**, 318 (2012).

[95] R. R. Ernst, G. Bodenhausen, and A. Wokaun, Principles of nuclear magnetic resonance in one and two dimensions (Oxford University Press, 1987).

[96] S. Mukamel, D. Abramavicius, L. Yang, W. Zhuang, I. V. Schweigert, and D. V. Voronine, "Coherent multidimensional optical probes for electron correlations and exciton dynamics: from NMR to X-rays," Accounts of Chemical Research **42**, 553 (2009).

[97] E. Harel, S. M. Rupich, R. D. Schaller, D. V. Talapin, and G. S. Engel, "Measurement of electronic splitting in PbS quantum dots by two-dimensional nonlinear spectroscopy," Physical Review B **86**, 075 412 (2012).

[98] G. Moody, M. E. Siemens, A. D. Bristow, X. Dai, A. S. Bracker, D. Gammon, and S. T. Cundiff, "Exciton relaxation and coupling dynamics in a GaAs/AlGaAs quantum well and quantum dot ensemble," Physical Review B **83**, 245 316 (2011).

[99] G. Moody, M. E. Siemens, A. D. Bristow, X. Dai, D. Karaiskaj, A. S. Bracker, D. Gammon, and S. T. Cundiff, "Exciton-exciton and exciton-phonon interactions in an interfacial GaAs quantum dot ensemble," Physical Review B **83**, 115 324 (2011).

[100] J. Kasprzak, B. Patton, V. Savona, and W. Langbein, "Coherent coupling between distant excitons revealed by two-dimensional nonlinear hyperspectral imaging," Nature Photonics **5**, 123 (2011).

[101] G. Moody, R. Singh, H. Li, I. A. Akimov, M. Bayer, D. Reuter, A. D. Wieck, and S. T. Cundiff, "Fifth-order nonlinear optical response of excitonic states in an InAs quantum dot ensemble measured with two-dimensional spectroscopy," Physical Review B **87**, 045 313 (2013).

[102] G. Moody, R. Singh, H. Li, I. A. Akimov, M. Bayer, D. Reuter, A. D. Wieck, A. S. Bracker, D. Gammon, and S. T. Cundiff, "Influence of confinement on biexciton binding in semiconductor quantum dot ensembles measured with two-dimensional spectroscopy," Physical Review B **87**, 041 304(R) (2013).

[103] G. Moody, R. Singh, L. H., I. A. Akimov, M. Bayer, D. Reuter, A. D. Wieck, and S. T. Cundiff, "Correlation and dephasing effects on the non-radiative coherence between bright excitons in an InAs QD ensemble measured with 2D spectroscopy," Solid State Communications **163**, 65 (2013).

[104] T. Zhang, C. Borca, X. Li, and S. T. Cundiff, "Optical two-dimensional Fourier transform spectroscopy with active interferometric stabilization," Optics Express **13**, 7432 (2005).

[105] C. N. Borca, T. Zhang, X. Li, and S. T. Cundiff, "Optical two-dimensional Fourier transform spectroscopy of semiconductors," Chemical Physics Letters **416**, 311 (2005).

[106] X. Li, T. Zhang, C. N. Borca, and S. T. Cundiff, "Many-body interactions in semiconductor probed by optical two-dimensional Fourier transform spectroscopy," Physical Review Letters **96**, 057 406 (2006).

[107] T. Zhang, I. Kuznetsova, T. Meier, X. Li, R. P. Mirin, P. Thomas, and S. T. Cundiff, "Polarization-dependent optical two-dimensional Fourier transform spectroscopy of semiconductors," Proceedings to the National Academy of Sciences **104**, 14 227 (2007).

[108] X. Dai, A. D. Bristow, D. Karaiskaj, and S. T. Cundiff, "Two-dimensional Fourier-transform spectroscopy of potassium vapor," Physical Review A **82**, 052 503 (2010).

[109] X. Dai, M. Richter, H. Li, A. D. Bristow, C. Falvo, S. Mukamel, and S. T. Cundiff, "Two-dimensional double-quantum spectra reveal collective resonances in an atomic vapor," Physical Review Letters **108**, 193 201 (2012).

[110] H. Li, A. D. Bristow, M. E. Siemens, G. Moody, and S. T. Cundiff, "Unraveling quantum pathways using optical three-dimensional Fourier-transform spectroscopy," Nature Communications **4**, 1390 (2013).

[111] A. D. Bristow, D. Karaiskaj, X. Dai, T. Zhang, C. Carlsson, K. R. Hagen, R. Jimenez, and S. T. Cundiff, "A versatile platform for multidimensional spectroscopy," Review of Scientific Instruments **80**, 073 108 (2009).

[112] M. E. Siemens, G. Moody, H. Li, A. D. Bristow, and S. T. Cundiff, "Resonance lineshapes in two-dimensional Fourier transform spectroscopy," Optics Express **18**, 17 699 (2010).

[113] U. Bockelmann and G. Bastard, "Phonon scattering and energy relaxation in two-, one-, and zero-dimensional electron gases," Physical Review B **42**, 8947 (1990).

[114] A. Berthelot, I. Favero, G. Cassabois, C. Voisin, C. Delalande, P. Roussignol, R. Ferreira, and J. M. Gérard, "Unconventional motional narrowing in the optical spectrum of a semiconductor quantum dot," Nature Physics **2**, 759 (2006).

[115] S. R. Bolton, U. Neukirch, L. J. Sham, D. S. Chemla, and V. M. Axt, "Demonstration of sixth-order Coulomb correlations in a semiconductor single quantum well," Physical Review Letters **85**, 2002 (2000).

[116] D. B. Turner and K. A. Nelson, "Coherent measurements of high-order electronic correlations in quantum wells," Nature **466**, 1089 (2010).

[117] M. A. Cusack, P. R. Briddon, and M. Jaros, "Electronic stucture of InAs/GaAs self-assembled quantum dots," Physical Review B **54**, R2300 (1996).

[118] L. R. C. Fonseca, J. L. Jimenez, J. P. Leburton, and R. M. Martin, "Self-consistent calculation of the electronic structure and electron-electron interaction in self-assembled InAs-GaAs quantum dot structures," Physical Review B **57**, 4017 (1998).

[119] G. Bester, S. Nair, and A. Zunger, "Pseudopotential calculation of the excitonic fine structure of million-atom self-assembled InGaAs/GaAs quantum dots," Physical Review B **67**, 161 306 (2003).

[120] H. Jiang and J. Singh, "Strain distribution and electronic spectra of InAs/GaAs self-assembled dots: an eight-band study," Physical Review B **56**, 4696 (1997).

[121] C. Pryor, "Eight-band calculations of strained InAs/GaAs quantum dots compared with one-, four-, and six-band approximations," Physical Review B **57**, 7190 (1998).

[122] O. Stier, M. Grundmann, and D. Bimberg, "Electronic and optical properties of strained quantum dots modeled by 8-band k.p theory," Physical Review B **59**, 5688 (1999).

[123] P. Meystre and M. Sargent, Elements of Quantum Optics (Springer, 2007), 4th edn.

[124] N. W. Ashcroft and N. D. Mermin, Solid State Physics (Brooks Cole, 1976), 1st edn.

[125] J. C. Slater and G. F. Koster, "Simplified LCAO method for the periodic potential problem," Physical Review **94**, 1498 (1954).

[126] R. J. Elliot, "Intensity of optical absorption by excitons," Physical Review **108**, 1384 (1957).

[127] D. S. Chemla and J. Shah, "Many-body and correlation effects in semiconductors," Nature **411**, 549 (2001).

[128] J. Shah, Ultrafast spectroscopy of semiconductors and semiconductor nanostructures (Spring Series in Solid-State Sciences, 1999), 2nd edn.

[129] J. Frenkel, "On the transformation of light into heat in solids, I," Physical Review **37**, 17 (1931).

[130] J. Frenkel, "On the transformation of light into heat in solids, II," Physical Review **37**, 1276 (1931).

[131] G. H. Wannier, "The structure of electronic excitation levels in insulating crystals," Physical Review **52**, 191 (1937).

[132] Ioffe Physico-Technical Institute (1998-2001), http://www.ioffe.ru/SVA/NSM/.

[133] M. Fox, Optical properties of solids (Oxford University Press, 2010), 2nd edn.

[134] H. Castella and J. W. Wilkins, "Splitting of the excitonic peak in quantum wells with interfacial roughness," Physical Review B **58**, 16 186 (1998).

[135] V. I. Klimov, "Spectral and dynamical properties of multiexcitons in semiconductor nanocrystals," Annual Review of Physical Chemistry **58**, 635 (2007).

[136] P. W. Fry, I. E. Itskevich, D. J. Mowbray, M. S. Skolnick, J. J. Finley, J. A. Barker, E. P. O'Reilly, L. R. Wilson, I. A. Larkin, P. A. Maksym, M. Hopkinson, M. Al-Khafaji, J. P. R. David, A. G. Cullis, G. Hill, and J. C. Clarck, "Inverted electron-hole alignment in InAs-GaAs self-assembled quantum dots," Physical Review Letters **84**, 733 (2000).

[137] J. Tommila, A. Schramm, T. V. Hakkarainen, M. Dumitrescu, and M. Guina, "Size-dependence properties of single InAs quantum dots grown in nanoimprint lithography patterned GaAs pits," Nanotechnology **24**, 235 204 (2013).

[138] S. Sanguinetti, K. Watanabe, T. Tateno, M. Gurioli, P. Werner, M. Wakaki, and N. Koguchi, "Modified droplet epitaxy GaAs/AlGaAs quantum dots grown on a variable thickness wetting layer," Journal of Crystal Growth **253**, 71 (2003).

[139] J. Singh, Physics of Semiconductors and Their Heterostructures (McGraw-Hill Education, 1993).

[140] G. A. Narvaez, G. Bester, and A. Zunger, "Excitons, biexcitons, and trions in self-assembled (In,Ga)As/GaAs quantum dots: recombination energies, polarization, and radiative lifetimes versus dot height," Physical Review B **72**, 245 318 (2005).

[141] J. Shumway, A. Franceschetti, and A. Zunger, "Correlation versus mean-field contributions to excitons, multiexcitons, and charging energies in semiconductor quantum dots," Physical Review B **63**, 155 316 (2001).

[142] H. W. van Kesteren, E. C. Cosman, W. A. J. A. van der Poel, and C. T. Foxon, "Fine structure of excitons in type-II GaAs/AlAs quantum wells," Physical Review B **41**, 5283 (1990).

[143] R. Seguin, A. Schliwa, S. Rodt, K. Pötschke, U. W. Pohl, and D. Bimberg, "Size-dependent fine-structure splitting of self-organized InAs/GaAs quantum dots," Physical Review Letters **95**, 257 402 (2005).

[144] A. D. Bristow, D. Karaiskaj, X. Dai, R. P. Mirin, and S. T. Cundiff, "Polarization dependence of semiconductor exciton and biexciton contributions to phase-resolved two-dimensional Fourier-transform spectra," Physical Review B **79**, 161 305 (2009).

[145] S. T. Cundiff, "Coherent spectroscopy of semiconductors," Optics Express **16**, 4639 (2008).

[146] L. Besombes, K. Kheng, L. Marsal, and H. Mariette, "Acoustic phonon broadening mechanism in single quantum dot emission," Physical Review B **63**, 155 307 (2001).

[147] G. Ortner, D. R. Yakovlev, M. Bayer, S. Rudin, T. L. Reinecke, S. Fafard, Z. R. Wasilewski, and A. Forchel, "Temperature dependence of the zero-phonon linewidth in InAs/GaAs quantum dots," Physical Review B **70**, 201 301 (2004).

[148] E. Peter, J. Hours, P. Senellart, A. Vasanelli, A. Cavanna, J. Bloch, and J. M. Gerard, "Phonon sidebands in exciton and biexciton emission from a single GaAs quantum dot," Physical Review B **69**, 041 307 (2004).

[149] X. Fan, T. Takagahara, J. Cunningham, and H. Wang, "Pure dephasing induced by exciton-phonon interactions in narrow GaAs quantum wells," Solid State Communications **108**, 857 (1998).

[150] P. Borri, W. Langbein, U. Woggon, V. Stavarache, D. Reuter, and A. D. Wieck, "Exciton dephasing via phonon interactions in InAs quantum dots: dependence on quantum confinement," Physical Review B **71**, 115 328 (2005).

[151] T. Takagahara, "Theory of exciton dephasing in semiconductor quantum dots," Physical Review B **60**, 2638 (1999).

[152] E. A. Muljarov and R. ZImmermann, "Dephasing in quantum dots: quadratic coupling to acoustic phonons," Physical Review Letters **93**, 237 401 (2004).

[153] R. C. C. Leite, J. Shah, and J. P. Gordon, "Effect of electron-exciton collisions on the free-exciton linewidth in epitaxial GaAs," Physical Review Letters **23**, 1332 (1969).

[154] L. Schultheis, J. Kuhl, A. Honold, and C. W. Tu, "Ultrafast phase relaxation of excitons via exciton-exciton and exciton-electron collisions," Physical Review Letters **57**, 1635 (1986).

[155] A. Honold, L. Schultheis, J. Kuhl, and C. W. Tu, "Collision broadening of two-dimensional excitons in a GaAs single quantum well," Physical Review B **40**, 6442 (1989).

[156] Y. Z. Hu, R. Binder, S. W. Koch, S. T. Cundiff, H. Wang, and D. G. Steel, "Excitation and polarization effects in semiconductor four-wave-mixing spectroscopy," Physical Review B **49**, 14 382 (1994).

[157] H. C. Schneider, W. W. Chow, and S. W. Koch, "Excitation-induced dephasing in semconductor quantum dots," Physical Review B **70**, 235 308 (2004).

[158] M. Lorke, T. R. Nielsen, J. Seebeck, P. Gartner, and F. Jahnke, "Influence of carrier-carrier and carrier-phonon correlations on optical absorption and gain in quantum-dot systems," Physical Review B **73**, 085 324 (2006).

[159] W. Q. Q., A. Muller, P. Bianucci, E. Rossi, Q. K. Zue, T. Takagahara, C. Piermarocchi, A. H. MacDonald, and C. K. Shih, "Decoherence processes during optical manipulation of excitonic qubits in semiconductor quantum dots," Physical Review B **72**, 035 306 (2005).

[160] J. Kasprzak and W. Langbein, "Four-wave mixing from individual excitons: intensity dependence and imaging," Physica Status Solidi (B) **246**, 820 (2009).

[161] J. Feldmann, S. T. Cundiff, M. Zrzberger, G. Böhm, and G. Abstreiter, "Carrier capture into InAs/GaAs quantum dots via multiple optical phonon emission," Journal of Applied Physics **89**, 1180 (2001).

[162] L. Zhang, T. F. Boggess, D. G. Deppe, D. L. Huffaker, O. B. Shchekin, and C. Cao, "Dynamic response of 1.3-um-wavelength InGaAs/GaAs quantum dots," Applied Physics Letters **76**, 1222 (2000).

[163] F. Adler, M. Geiger, A. Bauknecht, F. Scholz, H. Schweizer, M. H. Pilkuhn, B. Ohnesorge, and A. Forchel, "Optical transitions and carrier relaxation in self assembled InAs/GaAs quantum dots," Journal of Applied Physics **80**, 4019 (1996).

[164] J. Hegarty, M. D. Sturge, C. Weisbuch, A. C. Gossard, and W. Wiegmann, "Resonant Rayleigh scattering form an inhomogeneously broadened transition: a new probe of the homogeneous linewidth," Physical Review Letters **49**, 930 (1982).

[165] S. T. Cundiff and D. G. Steel, "Coherent transient spectroscopy of excitons in GaAs-AlGaAs quantum wells," IEEE Journal of Quantum Electronics **28**, 2423 (1992).

[166] A. Greilich, M. Schwab, T. Berstermann, T. Auer, R. Oulton, D. R. Yakovlev, and M. Bayer, "Tailored quantum dots for entangled photon pair creation," Physical Review B **73**, 045 323 (2006).

[167] R. Leon, Y. Kim, C. Jagadish, M. Gal, J. Zou, and D. J. H. Cockayne, "Effects of interdiffusion on the luminescence of InGaAs/GaAs quantum dots," Applied Physics Letters **69**, 1888 (1996).

[168] K. Kuroda, T. Kuroda, K. Watanabe, T. Mano, K. Sakoda, G. Kido, and N. Koguchi, "Final-state readout of exciton qubits by observing resonantly excited photoluminescence in quantum dots," Applied Physics Letters **90**, 051 909 (2007).

[169] A. Muller, E. B. Flagg, P. Bianucci, X. Y. Wang, D. G. Deppe, W. Ma, J. Zhang, G. J. Salamo, M. Xiao, and C. K. Shih, "Resonance fluorescence from a coherently driven semiconductor quantum dot in a cavity," Physical Review Letters **99**, 187 402 (2007).

[170] I. J. Luxmoore, N. A. Wasley, A. J. Ramsay, A. C. T. Thijssen, R. Oulton, M. Hugues, S. Kasture, V. G. Achanta, A. M. Fox, and M. S. Skolnick, "Interfacing spins in an InGaAs quantum dot to a semiconductor waveguide circuit using emitted photons," Physical Review Letters **110**, 037 402 (2013).

[171] S. Stufler, P. Machnikowski, P. Ester, M. Bichler, V. M. Axt, T. Kuhn, and A. Zrenner, "Two-photon Rabi oscillations in a single InGaAs/GaAs quantum dot," Physical Review B **73**, 125 304 (2006).

[172] A. J. Ramsay, R. S. Kolodka, F. Bello, P. W. Fry, W. K. Ng, A. Tahraoui, H. Y. Liu, M. Hopkinson, D. M. Whittaker, A. M. Fox, and M. S. Skolnick, "Coherent response of a quantum dot exciton driven by a rectangular optical pulse," Physical Review B **75**, 113 302 (2007).

[173] A. J. Ramsay, S. J. Boyle, R. S. Kolodka, J. B. B. Oliveira, J. Skiba-Szymanska, H. Y. Liu, M. Hopkinson, A. M. Fox, and M. S. Skolnick, "Fast optical preparation, control, and readout of a single quantum dot spin," Physical Review Letters **100**, 197 401 (2008).

[174] S. Michaelis de Vasconcellos, S. Gordon, M. Bichler, T. Meier, and A. Zrenner, "Coherent control of a single exciton qubit by optoelectornic manipulation," Nature Photonics **4**, 545 (2010).

[175] J. Berry, M. J. Stevens, R. P. Mirin, and K. L. Silverman, "High-resolution spectral hole burning in InGaAs/GaAs quantum dots," Applied Physics Letters **88**, 061 114 (2006).

[176] T. H. Stievater, X. Li, D. G. Steel, D. Gammon, D. S. Katzer, D. Park, C. Piermarocchi, and L. J. Sham, "Rabi oscillations of excitons in single dots," Physical Review Letters **87**, 133 603 (2001).

[177] I. A. Akimov, J. T. Andrews, and F. Henneberger, "Stimulated emission from the biexciton in a single self-assembled II-VI quantum dot," Physical Review Letters **96**, 067 401 (2006).

[178] E. D. Kim, K. Truex, Y. Wu, A. Amo, X. Xu, D. G. Steel, A. S. Bracker, D. Gammon, and L. J. Sham, "Picosecond optical spectroscopy of a single negatively charged self-assembled InAs quantum dot," Applied Physics Letters **97**, 113 110 (2010).

[179] Y. Tanimura and S. Mukamel, "Two-dimensional femtosecond vibrational spectroscopy of liquids," Journal of Chemical Physics **99**, 9496 (1993).

[180] M. L. Cowan, B. D. Bruner, N. Huse, J. R. Dwyer, B. Chugh, E. T. J. Nibbering, T. Elsaesser, and R. J. D. Miller, "Ultrafast memory loss and energy redistribution in the hydrogen bond network of liquid H2O," Nature **434**, 199 (2005).

[181] J. D. Hybl, A. W. Albrecht, S. M. Gallagher Faeder, and D. M. Jonas, "Two-dimensional electronic spectroscopy," Chemical Physics Letters **297**, 307 (1998).

[182] D. A. Blank, L. J. Kaufman, and G. R. Fleming, "Fifth-order two-dimensional Raman spectra of CS2 are dominated by third-order cascades," Journal of Chemical Physics **111**, 3105 (1999).

[183] M. C. Asplund, M. T. Zanni, and R. M. Hochstrasser, "Two-dimensional infrared spectroscopy of peptides by phase-controlled femtosecond vibrational photon echoes," Proceedings of the National Academy of Sciences **97**, 8219 (2000).

[184] M. T. Zanni, S. Gnanakaran, J. Stenger, and R. M. Hochstrasser, "Heterodyned two-dimensional infrared spectroscopy of solvent-dependent conformations of acetylproline-NH2," Journal of Physical Chemistry B **105**, 6520 (2001).

[185] T. Brixner, J. Stenger, H. M. Vaswani, M. Cho, R. E. Blankenship, and G. R. Fleming, "Two-dimensional spectroscopy of electronic couplings in photosynthesis," Nature **434**, 625 (2005).

[186] C. Y. Wong, R. M. Alvey, D. B. Turner, K. E. Wilk, D. A. Bryant, P. M. G. Curmi, R. J. Silbey, and G. D. Scholes, "Electronic coherence lineshapes reveal hidden excitonic correlations in photosynthetic light harvesting," Nature Chemistry **4**, 396 (2012).

[187] V. Tiwari, W. K. Peters, and D. M. Jonas, "Electronic resonance with anticorrelated pigment vibrations drives photosynthetic energy transfer outside the adiabatic framework," Proceedings of the National Academy of Sciences **110**, 1203 (2013).

[188] P. F. Tekavec, G. A. Lott, and A. H. Marcus, "Fluorescence-detected two-dimensional electronic coherence spectroscopy by acousto-optic phase modulation," Journal of Chemical Physics **127**, 214 307 (2007).

[189] D. B. Turner, P. Wen, D. H. Arias, K. A. Nelson, H. Li, G. Moody, M. E. Siemens, and S. T. Cundiff, "Persistent exciton-type many-body interactions in GaAs quantum wells measured using two-dimensional optical spectroscopy," Physical Review B **85**, 201 303 (2012).

[190] W. P. Aue, E. Bartholdi, and R. R. Ernst, "Two-dimensional spectrscopy. Application to nuclear magnetic resonance," Journal of Chemical Physics **64**, 2229 (1976).

[191] G. Bodenhausen, R. Freeman, G. A. Morris, and D. L. Turner, "NMR spectra of some simple spin systems studied by two-dimensional Fourier transformation of spin echoes," Journal of Magnetic Resonance **31**, 75 (1978).

[192] B. Vogelsanger and A. Bauder, "Two-dimensional microwave Fourier transform spectroscopy," Journal of Chemical Physics **92**, 4101 (1990).

[193] D. Suter, H. Klepel, and J. Mlynek, "Time-resolved two-dimensional spectroscopy of optically driven atomic sublevel coherences," Physical Review Letters **67**, 2001 (1991).

[194] I. Noda, "Two-dimensional infrared spectroscopy," Journal of American Chemical Society **111**, 8116 (1989).

[195] O. Golonzka, M. Khalil, N. Demirdoven, and A. Tokmakoff, "Vibrational anharmonicities revealed by coherent two-dimensional infrared spectroscopy," Physical Review Letters **86**, 2154 (2001).

[196] X. Zhu, M. S. Hybertsen, and P. B. Littlewood, "Quantum beats in photon echo from four-wave mixing," Physical Review Letters **73**, 209 (1994).

[197] V. Lyssenko, J. Erland, I. Balslev, H.-H. Pantke, B. S. Razbirin, and J. M. Hvam, "Nature of nonlinear four-wave-mixing beats in semiconductors," Physical Review B **48**, 5720 (1993).

[198] A. Euteneuer, E. Finger, M. Hofmann, W. Stolz, T. Meier, P. Thomas, S. W. Koch, W. W. Rühle, R. Hey, and K. Ploogy, "Coherent excitation spectroscopy on inhomogeneous exciton ensembles," Physical Review Letters **83**, 2073 (1999).

[199] D. Karaiskaj, A. D. Bristow, L. Yang, X. Dai, R. P. Mirin, S. Mukamel, and S. T. Cundiff, "Two-quantum many-body coherences in two-dimensional Fourier-transform spectra of exciton resonances in semiconductor quantum wells," Physical Review Letters **104**, 117 401 (2010).

[200] K. Leo, M. Wegener, J. Shah, D. S. Chemla, E. O. Göbel, T. C. Damen, S. Schmitt-Rink, and W. Schäfer, "Effects of coherent polarization interactions on time-resolved degenerate four-wave mixing," Physical Review Letters **65**, 1340 (1990).

[201] T. Yajima and Y. Taira, "Spatial optical parametric coupling of picosecond light-pulses and transverse relaxation effect in resonant media," Journal of the Physical Society of Japan **47**, 1620 (1979).

[202] L. Lepetit, G. Chériaux, and M. Joffre, "Linear techniques of phase measurement by femtosecond spectral interferometry for applications in spectroscopy," Journal of the Optical Society of America B **12**, 2467 (1995).

[203] S. Mukamel, Principles of nonlinear optical spectroscopy (Oxford University Press, 1995).

[204] L. Yang, I. V. Schweigert, S. T. Cundiff, and S. Mukamel, "Two-dimensional optical spectroscopy of excitons in semiconductor quantum wells: Liouville-space pathway analysis," Physical Review B **75**, 125 302 (2007).

[205] R. W. Boyd, Nonlinear Optics (Academic Press, 2002), 2nd edn.

[206] V. M. Axt and A. Stahl, "A dynamics-controlled truncation scheme for the hierarchy of density matrices in semiconductor optics," Zeitschrift für Physik B **93**, 195 (1994).

[207] M. Z. Maialle and L. J. Sham, "Interacting electron theory of coherent nonlinear response," Physical Review Letters **73**, 3310 (1994).

[208] C. Sieh, T. Meier, A. Knorr, F. Jahnke, P. Thomas, and S. W. Koch, "Influence of carrier correlations on the excitonic optical response including disorder and microcavity effects," European Physical Journal B **11**, 407 (1999).

[209] M. O. Scully and M. S. Zubairy, Quantum Optics (Cambridge University Press, 1997).

[210] J. D. Hybl, A. Albrecht Ferro, and D. M. Jonas, "Two-dimensional Fourier transform electronic spectroscopy," Journal of Chemical Physics **115**, 6606 (2001).

[211] T. Brixner, I. V. Stiopkin, and G. R. Fleming, "Tunable two-dimensional femtosecond spectroscopy," Optics Letters **29**, 884 (2004).

[212] M. L. Cowan, J. P. Ogilvie, and R. J. D. Miller, "Two-dimensional spectroscopy using diffractive optics based phased-locked photon echoes," Chemical Physics Letters **385**, 184 (2004).

[213] J. Kim, S. Mukamel, and G. D. Scholes, "Two-dimensional electronic double-quantum coherence spectroscopy," Accounts of Chemical Research **42**, 1375 (2009).

[214] K. Gundogdu, K. W. Stone, D. B. Turner, and K. A. Nelson, "Multidimensional coherent spectroscopy made easy," Chemical Physics **341**, 89 (2007).

[215] J. A. Myers, K. L. M. Lewis, P. F. Tekavec, and J. P. Ogilvie, "Two-color two-dimensional Fourier transform electronic spectroscopy with a pulse-shaper," Optics Express **16**, 17 420 (2008).

[216] J. A. Davis, L. V. Dao, M. T. Do, P. Hannaford, K. A. Nugent, and H. M. Quiney, "Noninterferometric two-dimensional Fourier-transform spectroscopy of multilevel systems," Physical Review Letters **100**, 227 401 (2008).

[217] V. Volkov, R. Schanz, and P. Hamm, "Active phase stabilization in Fourier-transform two-dimensional infrared spectroscopy," Optics Letters **30**, 2010 (2005).

[218] K. W. Stone, K. Gundogdu, D. B. Turner, X. Li, S. T. Cundiff, and K. A. Nelson, "Two-Quantum 2D FT Electronic Spectroscopy of Biexcitons in GaAs Quantum Wells," Science **324**, 1169 (2009).

[219] G. Nardin, G. Moody, R. Singh, T. M. Autry, H. Li, F. Morier-Genoud, and S. T. Cundiff, "Coherent coupling in an asymmetric double InGaAs quantum well," *in preparation* .

[220] I. Kuznetsova, T. Meier, S. T. Cundiff, and P. Thomas, "Determination of homogeneous and inhomogeneous broadening in semiconductor nanostructures by two-dimensional Fourier-transform optical spectroscopy," Physical Review B **76**, 153 301 (2007).

[221] S. M. Gallagher Faeder and D. M. Jonas, "Phase-resolved time-domain nonlinear optical signals," Physical Review A **62**, 033 820 (2000).

[222] A. Tokmakoff, "Two-dimensional line shapes derived from coherent third-order nonlinear spectroscopy," Journal of Physical Chemistry A **104**, 4247 (2000).

[223] K. Kwac and M. Cho, "Molecular dynamics simulation study of N-methylacetamide in water. II. Two-dimensional infrared pump-probe spectra," Journal of Chemical Physics **119**, 2256 (2003).

[224] K. Lazonder, M. S. Pshenichnikov, and D. A. Wiersma, "Easy interpretation of optical two-dimensional correlation spectra," Optics Letters **31**, 3354 (2006).

[225] K. Nagayama, P. Bachmann, K. Wuthrich, and R. R. Ernst, "The use of cross-sections and of projections in two-dimensional NMR spectroscopy," Journal of Magnetic Resonance **31**, 133 (1978).

[226] G. Moody, I. A. Akimov, H. Li, R. Singh, D. R. Yakovlev, G. Karczewski, T. Wojtowicz, M. Bayer, and S. T. Cundiff, "Exciton-trion coherent interactions in a CdTe/CdMgTe quantum well," *in preparation* .

[227] D. B. Turner, K. W. Stone, K. G. Gundogdu, and K. A. Nelson, "The coherent optical laser beam recombination technique (COLBERT) spectrometer: coherent multidimensional spectroscopy made easier," Review of Scientific Instruments **82**, 081 301 (2011).

[228] A. D. Bristow, D. Karaiskaj, X. Dai, and S. T. Cundiff, "All-optical retrieval of the global phase for two-dimensionalFourier-transform spectroscopy," Optics Express **16**, 18 017 (2008).

[229] C. Dorrer, N. Belabas, J.-P. Likforman, and M. Joffre, "Spectral resolution and sampling issues in Fourier-transform spectral interferometry," Journal of the Optical Society of America B **17**, 1795 (2000).

[230] R. Trebino, K. W. DeLong, D. N. Fittinghoff, J. N. Sweetser, M. A. Krumbügel, and D. J. Kane, "Measuring ultrashort laser pulses in the time-frequency domain using frequency-resolved optical gating," Review of Scientific Instruments **68**, 3277 (1997).

[231] P. F. Tian, D. Keusters, Y. Suzaki, and W. S. Warren, "Femtosecond phase-coherent two-dimensional spectroscopy," Science **300**, 1553 (2003).

[232] S.-H. Shim, D. B. Strasfeld, Y. L. Ling, and M. T. Zanni, "Automater 2D IR spectroscopy using a mid-IR pulse shaper and application of this technology to the human islet amyloid polypeptide," Proceedings of the National Academy of Sciences **104**, 14 197 (2007).

[233] C. E. Shannon, "Communication in the presence of noise," Proceedings of the Institute of Radio Engineers **37**, 10 (1949).

[234] A. Vagov, V. M. Axt, and T. Kuhn, "Electron-phonon dynamics in optically excited quantum dots: exact solution for multiple ultrashoft laser pulses," Physical Review B **66**, 165 312 (2002).

[235] R. F. Schnabel, R. Zimmermann, D. Bimberg, H. Nickel, R. Lösch, and W. Schlapp, "Influence of exciton localization on recombination line shapes: InGaAs/GaAs quantum wells as a model," Physical Review B **46**, 9873 (1992).

[236] K. Leosson, J. R. Jensen, W. Langbein, and J. M. Hvam, "Exciton localization and interface roughness in growth-interrupted GaAs/AlAs quantum wells," Physical Review B **61**, 10 322 (2000).

[237] W. Borri, P .and Langbein, E. A. Muljarov, and R. Zimmermann, "Dephasing of excited-state excitons in InGaAs quantum dots," Physica Status Solidi (B) **243**, 3890 (2006).

[238] I. E. Itskevich, S. I. Rybchenko, I. I. Tartakovskii, S. T. Stoddart, A. Levin, P. C. Main, L. Eaves, M. Henini, and S. Parnell, "Stark shift in electroluminescence of individual InAs quantum dots," Applied Physics Letters **76**, 3932 (2000).

[239] S.-S. Li and J.-B. Xia, "Quantum-confined Stark effects of InAs/GaAs self-asembled quantum dot," Journal of Applied Physics **88**, 7171 (2000).

[240] H. Htoon, D. Kulik, O. Baklenov, A. L. Holmes, T. Takagahara, and C. K. Shih, "Carrier relaxation and quantum decoherence of excited states in self-assembled quantum dots," Physical Review B **63**, 241 303 (2001).

[241] A. Barenco and M. A. Dupertuis, "Quantum many-body states of excitons in a small quantum dot," Physical Review B **52**, 2766 (1995).

[242] S. V. Nair and T. Takagahara, "Theory of exciton pair states and their nonlinear optical properties in semiconductor quantum dots," Physical Review B **55**, 5153 (1997).

[243] A. Wojs and P. Hawrylak, "Exciton-exciton interactions in highly excited quantum dots in a magnetic field," Solid State Communications **100**, 487 (1996).

[244] S. Rodt, A. Schliwa, K. Pötschke, F. Guffarth, and D. Bimberg, "Correlation of structural and few-particle properties of self-organized InAs/GaAs quantum dots," Physical Review B **71**, 155 325 (2005).

[245] H. F. Hess, E. Betzig, T. D. Harris, L. N. Pfeiffer, and K. W. West, "Near-Field Spectroscopy of the Quantum Constituents of a Luminescent System," Science **264**, 1740 (1994).

[246] J. R. Guest, T. H. Stievater, X. Li, J. Cheng, D. G. Steel, D. Gammon, D. S. Katzer, D. Park, C. Ell, A. Thränhardt, G. Khitrova, and H. M. Gibbs, "Measurement of optical absorption by a single quantum dot exciton," Physical Review B **65**, 241 310 (2002).

[247] L. C. Andreani, G. Panzarini, and J. M. Gérard, "Vacuum-field Rabi splitting for quantum boxes in micropillar cavities?" Physical Status Solidi (A) **178**, 145 (2000).

[248] W. Langbein and J. M. Hvam, "Biexcitonic Bound and Continuum States of Homogeneously and Inhomogeneously Broadened Exciton Resonances," Physical Status Solidi (A) **190**, 167 (2002).

[249] J. Kasprzak and W. Langbein, "Coherent response of individual weakly confined exciton-biexciton systems," Journal of the Optical Society of America B **29**, 1766 (2012).

[250] A. I. Tartakovskii, M. N. Makhonin, I. R. Sellers, J. Cahill, A. D. Andreev, D. M. Whittaker, J.-P. R. Wells, A. M. Fox, D. J. Mowbray, M. S. Skolnick, K. M. Groom, J. Steer, H. Y. Liu, and M. Hopkinson, "Effect of thermal annealing and strain engineering on the fine structure of quantum dot excitons," Physical Review B **70**, 193 303 (2004).

[251] A. V. Filinov, C. Riva, F. M. Peeters, Y. E. Lozovik, and M. Bonitz, "Influence of well-width fluctuations on the binding energy of excitons, charged excitons, and biexcitons in GaAs-based quantum wells," Physical Review B **70**, 035 323 (2004).

[252] T. F. Albrecht, K. Bott, T. Meier, A. Schulze, M. Koch, S. T. Cundiff, J. Feldmann, W. Stolz, P. Thomas, S. W. Koch, and E. O. Göbel, "Disorder mediated biexcitonic beats in semconductor quantum wells," Physical Review B **54**, 4436 (1996).

[253] R. M. Stevenson, R. J. Young, P. Atkinson, K. Cooper, D. A. Ritchie, and A. J. Shields, "A semiconductor source of triggered entangled photon pairs," Nature **439**, 179 (2006).

[254] R. Trotta, E. Zallo, C. Ortix, P. Atkinson, J. D. Plumhof, J. van den Brink, A. Rastelli, and O. G. Schmidt, "Universal recovery of the energy-level degeneracy of bright excitons in InGaAs quantum dots without structure symmetry," Physical Review Letters **109**, 147 401 (2012).

[255] D. J. P. Ellis, R. M. Stevenson, R. J. Young, A. J. Shields, P. Atkinson, and D. A. Ritchie, "Control of fine-structure splitting of individual InAs quantum dots by rapid thermal annealing," Applied Physics Letters **90**, 011 907 (2007).

[256] A. G. V. Spivey, C. Borca, and S. T. Cundiff, "Correlation coefficient for dephasing of light-hole excitons and heavy-hole excitons in GaAs quantum wells," Solid State Communications **145**, 303 (2008).

[257] M. Feng, K. L. Silverman, R. P. Mirin, and S. T. Cundiff, "Dark pulse quantum dot diode laser," Optics Express **18**, 13 385 (2010).

[258] T. V. Torchynska, "Exciton capture and thermal escape in InAs dot-in-a-well laser structures," Superlattices and Microstructures **45**, 349 (2009).

[259] M. Z. Maialle, E. A. Andrada e Silva, and L. J. Sham, "Exciton spin dynamics in quantum wells," Physical Review B **47**, 15 776 (1993).

[260] A. V. Khaetskii and Y. V. Nazarov, "Spin-dephasing processes in semiconductor quantum dots," Physica E **6**, 470 (2000).

[261] T. H. Stievater, X. Li, T. Cubel, D. G. Steel, D. Gammon, D. S. Katzer, and D. Park, "Measurement of relaxation between polarization eigenstates in single quantum dots," Applied Physics Letters **81**, 4251 (2002).

[262] S. Adachi, T. Miyashita, S. Takeyama, Y. Takagi, and A. Tackeuchi, "Exciton spin dynamics in GaAs quantum wells," Journal of Luminescence **72-74**, 307 (1997).

[263] R. Ferreira and G. Bastard, "Hole "spin" relaxation in semconductor quantum wells," Europhysics Letters **23**, 439 (1993).

[264] A. Vinattieri, J. Shah, T. C. Damen, D. S. Kim, L. N. Pfeiffer, M. Z. Maialle, and L. J. Sham, "Exciton dynamics in GaAs quantum wells under resonant excitation," Physical Review B **50**, 10 868 (1994).

[265] B. Ohnesorge, M. Albrecht, J. Oshinowo, A. Forchel, and Y. Arakawa, "Rapid carrier relaxation in self-assembled InGaAs/GaAs quantum dots," Physical Review B **54**, 11 532 (1996).

[266] V. Savona and W. Langbein, "Realistic heterointerface model for excitonic states in growth-interrupted GaAs quantum wells," Physical Review B **74**, 075 311 (2006).

[267] E. Poem, O. Kenneth, Y. Kordiano, Y. Benny, S. Khatsevich, J. E. Avron, and D. Gershoni, "Optically induced rotation of an exciton spin in a semiconductor quantum dot," Physical Review Letters **107**, 087 401 (2011).

[268] R. Rossetti, S. Nakahara, and L. E. Brus, "Quantum size effects in the redox potentials, resonance Raman spectra, and electronic spectra of CdS crystallites in aqueous solution," The Journal of Chemical Physics **79**, 1086 (1983).

[269] D. Duonghong, J. Ramsden, and M. Grätzel, "DDynamic of interfacial electron-transfer processes in colloidal semiconductor systems," Journal of American Chemical Society **104**, 2977 (1982).

[270] N. Le Thomas, U. Woggon, O. Schöps, M. V. Artemyev, M. Kazes, and U. Banin, "Cavity QED wih semiconductor nanocrystals," Nano Letters **6**, 557 (2006).

[271] A. L. Efros, M. Rosen, M. Kuno, M. Nirmal, D. J. Norris, and M. G. Bawendi, "Band-edge exciton in quantum dots of semiconductors with a degenerate valence band: dark and bright exciton states," Physical Review B **54**, 4843 (1996).

[272] J. Bylsma, P. Dey, J. Paul, S. Hoogland, E. H. Sargent, J. M. Luther, M. C. Beard, and D. Karaiskaj, "Quantum beats due to excitonic ground-state splitting in colloidal quantum dots," Physical Review B **86**, 125 322 (2012).

[273] P. Palinginis, S. Tavenner, M. Lonergan, and H. Wang, "Spectral hole burning and zero phonon linewidth in semiconductor nanocrystals," Physical Review B **67**, 201 307 (2003).

[274] L. Biadala, T. Louyer, P. Tamarat, and B. Lounis, "Direct observation of the two lowest exciton zero-phonon lines in single CdSe/ZnS nanocrystals," Physical Review Letters **103**, 037 404 (2009).

[275] L. Coolen, X. Brokmann, P. Spinicelli, and J.-P. Hermier, "Emission characterization of a single CdSe-ZnS nanocrystal with high temporal and spectral resolution by photon-correlation Fourier spectroscopy," Physical Review Letters **100**, 027 403 (2008).

[276] F. Masia, N. Accanto, W. Langbein, and P. Borri, "Spin-flip limited exciton dephasing in CdSe/ZnS colloidal quantum dots," Physical Review Letters **108**, 087 401 (2012).

[277] O. Labeau, P. Tamarat, and B. Lounis, "Temperature dependence of the luminescence lifetime of signle CdSe/ZnS quantum dots," Physical Review Letters **90**, 257 404 (2003).